Micromachining technologies for future Cochlear Implants

Human Ear, Materials and Micro-technologies

Micromachining technologies for future Cochlear Implants

Human Ear, Materials and Micro-technologies

Proefschrift

ter verkrijging van de graad van doctor
aan de Technische Universiteit Delft,
op gezag van de Rector Magnificus prof. ir. K. C. A. M. Luyben,
voorzitter van het College voor Promoties,
in het openbaar te verdedigen op 15 september 2015 om 15:00 uur

door

NISHANT SHANKAR LAWAND
Master of Science in Mechatronics
Aachen University of Applied Sciences, Duitsland
Geboren te Satara, India

This dissertation has been approved by the:
promotor's: Prof. dr. P. J. French and Prof. dr. ir. J. H. M. Frijns
copromotor: Dr. ir. J. J. Briaire

Composition of the doctoral committee:

Rector Magnificus	chairman (Technische Universiteit Delft)
Prof. dr. P. J. French	promotor (Technische Universiteit Delft)
Prof. dr. ir. J. H. M. Frijns	promotor (Leiden University Medical Centre)
Dr. ir. J. J. Briaire	copromotor (Leiden University Medical Centre)

Independent members:

Dr. P. Boyle	Advanced Bionics Corporation, USA/UK
Prof. dr. K. Mottaghy	Universitätsklinikum, RWTH, Aachen, Germany
Prof. dr. G. Q. Zhang	Technische Universiteit Delft
Prof. dr. ir. W. A. Serdijn	Technische Universiteit Delft
Prof. dr. J. Dankelman	Technische Universiteit Delft (reserve member)

Cover Title: Micromachining technologies for future Cochlear Implants
Human Ear, Materials and Micro-technologies.
Cover design by: Sayali Balasaheb Jadhav
Photo credentials: Annelies te Selle

The research project, Smart Cochlear Implants (Smac-*it*) was financially supported by the Dutch Technology Foundation (STW) under the SmartSiP program and by Advanced Bionics Corporation, CA, USA.

ISBN: 978-94-6259-835-5

॥ श्री ॥

To my amazing parents (Lawand and Jadhav family)
and to my soulmate Sayali

। विद्याधनं सर्व-धन-प्रधानम । व्ययेन वृद्धिः संचयनेन नाशः ॥
। समाजस्य सर्वस्य संवर्धनाय । आबालवृद्धान ध्रुवतांनयेत तत् ॥
। कल्याण- सौख्य सततं समृद्धमे । अखण्डितं विश्वहिताय सिध्येत ॥

— पंडित वसंतराव गाडगीळ

"Knowledge is the greatest wealth of all. It increases when it is spread among others and decreases when selfishly kept to oneself. This wealth is for the welfare and happiness of the human beings to preserve ones stability in the society. Knowledge gained should fulfill the welfare of the world forever."

Table of Contents

Summary

Micromachining technologies for future Cochlear Implants

By: Nishant Shankar Lawand

Our ears, the tiny organs sitting on the either sides of our head, have quite a few surprises in store for us. If observed carefully, the inner ear (cochlea) is precisely packed in a very small space which enables listening very cleverly in sound levels varying from the slightest whisper to that of an explosion, with its dynamic compressor capability and a frequency analyser bone. The cochlea is efficiently equipped with a series of filter banks with a highly sophisticated analogue-to-digital converter intelligently coupled to our brain. Due to evolution, human being was separated from the rest of the species. The cognitive abilities and their derived intelligence gave them an ability to do new innovative inventions for the benefit of the society where they live. One of the bold inventions which helps the deaf people to bring back their sense of hearing is the Cochlear Implant (CI). This technology has been developed and will be enhanced in future as new concepts and technologies are unfolded. The aim of this thesis was to realise new manufacturing technologies to build CI electrode arrays which will replace the traditional tailored manual process. The idea was to demonstrate a concept prototype of a microfabricated CI electrode array which serves as a foundation for the future product development.

A CI is an implantable device that bypasses the non-functional inner ear and directly stimulates the hearing nerves with electric currents by the help of wires (electrode array) thus enabling deaf people to experience sound again. With the existing CI wiring technology, CI's are unable to cover the audible frequency spectrum for lower frequencies due to its limited insertion depths into the cochlea, and the number of electrodes are limited. Furthermore the material instability in the harsh perilymph environment limits the life time of the device. Keeping this issues in mind, as a first step the anatomical features of the human ear were studied and described in chapter 2. A brief investigation of the different aspects of the CI electrode array and the various possible Micro-Electrical Mechanical Systems (MEMS) micromachining techniques are described in chapter 3.

In chapter 4 an extensive investigation was performed to identify suitable materials. For the electrodes TiN was selected due to its high stability in harsh

S conditions. It was also able to withstand much higher current density (2.8 mA/μm²) than aluminium (Al: a commonly used material in IC technology), which failed due to electromigration in comparison with TiN. TiN performed well under the accelerated harsh environment durability tests at high temperatures (around 70 °C).

The microelectrode array (MEA) design process (chapter 5) and fabrication was done in stages. The first generation completely flexible MEA was designed and fabricated. These devices were further improved with the development of the second generation "Flexi-Stiff" MEA device. Various electrode design configurations were investigated and the embedded design was chosen. This was chosen due to its lower electric field spread and fewer microfabrication processing steps. A novel microfabrication process was developed for the second generation devices using new materials and advanced processing steps. These devices consist of two thin (10 μm) polyimide (PI 2611) substrate layers along with TiN (240 nm) electrode stimulation material. The detailed manufacturing process is described in chapter 6. A unique polymer etching process described in this thesis opens new areas for patterning polyimide thin films, enabling a good metal step coverage.

Assembly and packaging (chapter 7) is important to give a final shape to the device and to protect the potential damageable areas from the corrosive saline environment. The "Flexi-Stiff" MEA design facilitates the assembly, mounting and the packaging of the device on pre-fabricated flexible carriers. Excimer lasering process played an important role in achieving the desired dimensions precisely. The initial electrochemical characterisation (chapter 7) tests performed, proved the working capabilities during *in-vitro* experimentation. The results indicate that the charge densities (150 μC/cm²) delivered by "Flexi-Stiff" MEA devices are well under the non-damaging zone as per the Shanon plot. This plot is normally used to indicate the safe stimulation parameters for different electrode–stimulation materials. *In-vivo* (Guinea Pig) testing demonstrated the basic device functionality in animals. The "Flexi-Stiff" MEA device was able to exhibit a required balance between the flexible and stiff behaviour during the intracochlear insertion and removal process in Guinea Pigs. Additionally the device handled sufficient current to elicit a neural response. Also along with the stimulation process, a neural response was measured back by the same MEA which is comparable to the electrode designs used in CI recipients.

Another application of the electrode stimulation material was discussed in chapter 8 where the traditional gate material (Al+1%Si) was replaced by TiN to build BiCMOS devices. The fabrication process is robust and the experiments performed showed good transistor characteristics. This approach will allow some simple electronics to be included at the electrode site, this allowing the number of electrodes to be increased without creating a wiring problem. Therefore this approach showed a

possible step towards future on-chip heterogeneous integration in the MEA to build hybrid devices.

The currently available CI devices are limited by the fact that they are unable to penetrate far into the cochlea and the number of electrodes cannot be greatly increased. In this thesis a new microfabrication process with non-traditional materials has been developed for manufacturing miniature microelectrode arrays for future CI's. This process will allow a considerable increase in the number of electrodes and an improvement in functionality. *In-vitro* and *in-vivo* measurements have shown that this approach has a great potential for the development of a new generation cochlear implants (CI's).

Samenvatting

Microtechnologie voor toekomstige cochleaire implantaten

Door: Nishant Shankar Lawand

Onze oren, de kleine organen aan weerskanten van ons hoofd, hebben voor ons een aantal verassingen in petto. Bij zorgvuldige observatie blijkt dat het binnenoor (cochlea) heel precies is opgeborgen in een zeer kleine ruimte, en het op slimme wijze mogelijk maakt om te luisteren bij geluidsniveaus variërend van zacht gefluister tot dat van een explosie, met zijn vermogen tot dynamische compressie en een bot dat frequenties analyseert.

De cochlea is hiertoe op doelmatige wijze uitgerust met rijen filters voorzien van een zeer geraffineerde analoog-digitaalomzetter die op intelligente wijze is gekoppeld met onze hersenen. Dank zij de evolutie zijn mensen zich gaan onderscheiden van de rest van de schepselen. De cognitieve vermogens en de daarvan afgeleide intelligentie verschaft hen de mogelijkheid van "uitvinden" ten voordele van de samenleving waarin zij zich bevinden. Een van de krachtige uitvindingen die dove mensen helpt om hun gehoorvermogen terug te krijgen is het Cochleaire Implantaat (CI). Deze technologie is ontwikkeld en zal in de toekomst worden versterkt door de komst van nieuwe concepten en technologieën. Het doel van dit proefschrift was het realiseren van nieuwe vervaardigingstechnologieën om CI elektrode-arrays te bouwen op een wijze die het traditionele handwerk kan vervangen. Het idee was om een concept prototype te demonstreren van zo'n CIU elektrode-array dat is vervaardigd met microtechnologie en dat als basis kan dienen voor toekomstige productontwikkeling.

Een CI is een inplanteerbaar instrument dat een rondweg vormt voor het niet-functionerende binnenoor en direct de gehoorzenuwen stimuleert met elektrische stromen met behulp van draden (electrode array) en op deze wijze dove mensen in staat stelt om weer geluid waar te nemen. Met de bestaande CI bedradingstechnologie zijn CIs niet in staat om het laagfrequent gebied van het hoorbare spectrum te bedekken, hetgeen een gevolg is van de beperkte insteekdiepte in de cochlea en het beperkte aantal electroden dat kan worden gebruikt. Verder beperkt materiaalinstabiliteit in de ruwe omgeving met perilymfe vloeistof de levensduur van het instrument . Met deze tekortkomingen in het achterhoofd zijn als eerste stap de anatomische kenmerken van het menselijke oor bestudeerd en

S

beschreven in hoofdstuk 2. De verschillende aspecten van een CI elektrode-array en de verschillende mogelijke MEMS (Micro Electrical Mechanical Systems) microtechnieken zijn beschreven in hoofdstuk 3.

In hoofdstuk 4 wordt een uitgebreid onderzoek beschreven dat is uitgevoerd om de geschikte materialen te vinden. Voor de electroden werd TiN uitgekozen vanwege zijn hoge stabiliteit in een ruwe omgeving. De materiaal kan een veel hogere stroomdichtheid weerstaan (2.8 mA/μm^2) dan aluminium (Al: is in IC technologie een veelgebruikt materiaal) dat tekortschoot vanwege elektromigratie. Verder bleek TiN bestand tegen de zware versnelde-levensduurtesten uitgevoerd bij hoge temperaturen (ongeveer 70 ^{O}C).

Het ontwerpproces van het microelektrode-array (MEA) (hoofdstuk 5) en de fabricage daarvan is uitgevoerd in fasen. Een eerste generatie volledig flexibel MEA werd ontworpen en vervaardigd. Deze instrumenten werden verder verbeterd door de ontwikkeling van de tweede generatie "Flexi-Stiff" MEA instrumenten. Voor het electrode ontwerp daarvan werden verschillende configuraties onderzocht, waarna het "embedded" ontwerp werd uitgekozen. De voorkeur voor dit ontwerp werd ingegeven vanwege de lagere spreiding van het elektrische veld en het geringere aantal fabricagestappen. Voor de tweede-generatie instrumenten werd nieuw microfabricageprocesontwikkeld, waarbij gebruik gemaakt wordt van nieuwe materialen en geavanceerde processtappen. Deze instrumenten bestaan uit twee dunne (10 µm) polyimide (PI 2611) substraatlagen, met TiN (240 nm) materiaal voor de stimulatie-elektroden. Het uitgebreide fabricageproces is beschreven in hoofdstuk 6. Een uniek polymeer_etsproces, dat beschreven is in dit proefschrift, opent nieuwe perspectieven voor het vormen van patronen met Polyimide (PI) dunne filmen, zodat een goede "stapbedekking" van metalen wordt verkregen.

Samenstelling en verpakking (hoofdstuk 7) is van belang om het ontwerp zijn uiteindelijke vorm te geven en om kwetsbare delen te beschermen tegen mogelijke schadelijke invloeden van de corrosieve zoute omgeving. Het "Flexi-Stiff" MEA ontwerp vergemakkelijkt samenstelling en montage van het instrument op een geprefabriceerde flexibele dragers. Het excimeerlaser-proces speelde een belangrijke rol om de gewenste afmetingen nauwkeurig te bereiken. Eerste experimenten voor elektrochemische karakterisatie (hoofdstuk 7) lieten de gebruiksmogelijkheden zien voor in-vitro experimenten. De resultaten wijzen uit dat de ladingsdichtheden (150 µC/cm2) opgewekt in de "Flexi-Stiff" prototypen nog ruim binnen de grenzen voor schadevrij gebruik liggen, zoals aangegeven in de Shanon plot. Deze plot wordt gewoonlijk gebruikt om de veiligheidsmarges aan te geven voor stimulatieparameters voor verschillende materialen voor electrostimulatie. In-vivo testen uitgevoerd met cavia's lieten de functionaliteit zien van het basisinstrument bij gebruik in proefdieren. Het Flexi-Stiff" MEA instrument toonde de benodigde balans tussen een

flexibiliteit en stevigheid gedurende het proces van intra-cochleaire inbrenging en verwijdering in cavia's. Bovendien bleek het instrument in staat om voldoende stroom te kunnen opwekken en verwerken om een neurale respons te kunnen veroorzaken. Tegelijkertijd met het stimulatieproces werd een neurale respons gemeten met hetzelfde MEA, zoals dat ook gebeurt bij de ontwerpen gebruikt in CI ontvangers.

In hoofdstuk 8 wordt als andere toepassing van stimulatie-elektrodematerialen de mogelijkheid besproken om TiN te gebruiken als gate materiaal voor BiCMOS componenten, als alternatief voor het traditionele gate-materiaal. Het fabricageproces is robuust en de experimenten lieten goede transistorkarakteristieken zien. Deze benadering maakt het mogelijk om eenvoudige elektronica aan te brengen op de plaats van de electroden, zodat het aantal electroden kan worden uitgebreid zonder dat daarbij bedradingsproblemen ontstaan. Daarom laat deze benadering een mogelijke stap zien naar toekomstige heterogene integratie van basiselektronica in het MEA in hybride (on-chip) ontwerpen.

De momenteel verkrijgbare CI instrumenten worden beperkt doordat ze niet diep genoeg in de cochlea aangebracht kunnen worden en dat het aantal elektroden onvoldoende is. Dit proefschrift beschrijft een nieuwe microfabricage-proces waarbij nieuwe niet-traditionele materialen zijn gebruikt ten behoeve van de vervaardiging van miniatuur elektrode-arrays voor toekomstige CI's. Dit proces maakt het mogelijk om het aantal elektroden aanzienlijk uit te breiden en om hun functionaliteit te verbeteren. *In-vitro* en *in-vivo* beproevingen hebben laten zien dat deze benadering grote mogelijkheden biedt voor de ontwikkeling van een nieuwe generatie cochleaire implantaten (CI's).

"सारांश"

विषय: श्रवण दोषांवरील उपायांसाठी आगामी सूक्षतम तंत्रज्ञान

संशोधक: निशांत शंकर लावंड

आपले दोन कान हे मानवी शरीराचे अत्यंत महत्वपूर्ण तसेच नाजूक अवयव ! हे दिसायला जरी लहान अवयव असले तरीही यांची रचना खरोखर थक्क करणारी व वैशिष्टयपूर्ण अशी आहे. श्रवण क्षमतेच्या दृष्टीने कानाच्या आतला भाग म्हणजेच आंतर्कान अतिशय लहान जागेत चपलखपणे बसलेला आहे. लहानशी कुजबुज ते महास्फोटातील फरक हा खुबीने आणि तात्काळ समजून घेतो. हा एका विशेष प्रकारच्या मऊसर हाडाचा प्रकार आहे. हे हाड जणू आपल्या मेंदूशी अत्युच्च तंत्रज्ञानाने जोडलेले आहे जे अत्याधुनिक संगणकापेक्षाही कित्येक पटीने वेगाने कार्य करते. त्याद्वारे सलग ध्वनीलहरींचे अंकात्मक पृथक्करण केले जाते. सजीव सृष्टीच्या उत्क्रांतीच्या प्रदीर्घ कालखंडात मनुष्य प्राण्याच्या विकासामध्ये इतर सजीवांच्या तुलनेत फार मोठे बदल होत गेले. त्यातील अत्यंत महत्वाचा बदल म्हणजे मनुष्य प्राण्याच्या मेंदूचा प्रचंड वेगाने झालेला विकास! आपल्या अवतीभवती घडणा-या विविध घटनांचे निरीक्षण, आकलन व विश्लेषण करण्याची वैचारीक क्षमता म्हणजेच 'बुध्दिमत्ता' आपल्या मेंदू मध्ये विकसीत झाली आणि या बुध्दिमत्तेच्या बळावर मानवाने अनेक नवनवीन शोध लावले. ज्ञानाची आसक्ती व मानवी गरजांची परिपूर्ती करण्याची आवश्यकता यातूनच विज्ञानाची प्रगती होत गेली.

मानवाने समाजाच्या उन्नतीसाठी बरेच शोध लावले. अशा अनेक शोधांमध्ये "श्रवणदोषावरील अंर्तगत सूक्ष्मयंत्रे" याचा ठळकपणे उल्लेख करावा लागेल. या यंत्राच्या सहाय्याने पूर्णत: अथवा अंशत: बहि-या असलेल्या व्यक्तींना आपली श्रवणशक्ती पुनश्च प्राप्त होऊ शकते व अश्या व्यक्ती इतर सर्वसामान्य व्यक्तींप्रमाणे ऐकू शकतात. अशा प्रकारचे उपकरण बनवण्याचे तांत्रिक कौशल्य यापूर्वी पुष्कळ विकसीत झाले आहे. सदर संशोधनाचा मुख्य उद्देश हा आधुनिक उत्पादन तंत्रज्ञानाचा वापर करून विद्युतभारीत सूक्ष्मतम यंत्रे Cochlear Implant (C.I.) – कानाचे वैद्यकीय उपकरण विकसित करणे हा आहे. त्यायोगे पारंपारिक तंत्रज्ञान व मानवी हस्तक्षेपाला पर्याय म्हणून सूक्ष्म विद्युत्घटांच्या रचनेत तांत्रिक कौशल्य विकसित करण्यावर भर देण्यात आला. अशा आधुनिक तंत्रज्ञानाचा वापर करून भविष्यकाळात उत्तम गुणवत्तेच्या श्रवणयंत्रांचे व्यावसायिक तत्वांवर उत्पादन होण्याचा मार्ग सुकर होण्यासाठी वैज्ञानिक माहिती व तांत्रिक कौशल्याचा पाया घालण्याच्या दृष्टीने या प्रबंधातील संशोधन उपयुक्त ठरेल.

श्रवणक्षमतेच्या दृष्टीने सध्या वापरात असलेल्या श्रवणयंत्राच्या तंत्रज्ञानाला काही मर्यादा आहेत. त्यातील प्रमुख मर्यादा म्हणजे या उपकरणांना मनुष्य प्राण्याच्या ध्वनीपटलावरील ऐकू येऊ शकणा-या लहान कंपनांची मर्यादा आहे. या उपकरणांत वापरण्यात आलेल्या घटकपदार्थांची अस्थिरता, दिर्घकालीन वापराचे शरीरावर होणारे दुष्परीणाम हाही एक चिंतेचा विषय ठरतो. श्रवणयंत्र वापरात असताना संबधित व्यक्तीला वेळप्रसंगी अवतीभवतीच्या कर्कश आवाजाचा सामना करावा लागतो. त्याचा विपरीत परिणाम उपकरणातील घटकपदार्थांवर होत असतो. सध्याच्या उपकरणातील ही एक लक्षणीय त्रुटी अथवा मर्यादा आहे. या सर्व बाबी नजरेसमोर ठेवून मानवी कानाच्या शरीरशास्त्रीय वैशिष्टयांची अभ्यासपूर्ण माहिती प्रकरण २ मध्ये दिली आहे. प्रबंधाच्या प्रकरण ३ मध्ये विद्युतभारीत सूक्ष्मतम यंत्राची अंर्तगत रचना तसेच त्याच्या निर्मितीच्या सूक्ष्मतंत्र कौशल्यांबाबत सविस्तर चर्चा केली आहे.

संशोधनाच्या पुढील टप्प्यातील महत्वाचा भाग म्हणजे विद्युतभारीत सूक्ष्मयंत्रामधील सध्या वापरात येत असलेल्या घटकपदार्थांना समर्थ पर्याय म्हणून नवीन पदार्थाचा शोध घेणे की जो प्रयोगशाळेमध्ये स्वच्छ वातावरणात

स

बनवता येईल व जो वातावरणातील कमालीच्या बदलाचा यशस्वीपणे सामना करून दीर्घकाळ टिकण्याच्या कसोटीला पात्र ठरेल. या गोष्टी लक्षात ठेवून विविध पर्यायी पदार्थांचा प्रयोगशाळेत सखोल शास्त्रीय अभ्यास करण्यात आला व त्यातून अंतिमतः टिटॅनियम नायट्राईड हा पदार्थ उच्च दाबाच्या विद्युतप्रवाहाचा सामना यशस्वीपणे करू शकतो असे निश्कर्षित झाले. तसेच वातावरणीतील तापमानाच्या मोठ्या बदलामुळेदेखील या पदार्थाच्या टिकाऊपणावर फारसा परिणाम होत नाही (प्रकरण ४). अत्युच्च विद्युतलहरी, टिकाऊपणा, उच्चतम तापमान , जैविक सुसंगती इत्यादी परीक्षांमध्ये टिटॅनियम नायट्राईड पात्र ठरले. या परीक्षांमध्ये अल्यूमिनियम हा पदार्थ विविध कसोट्यांमध्ये अपात्र ठरला. प्रकरण ५ मध्ये विद्युतभारीत सूक्ष्मतम यंत्राची अंतर्गत रचना, (मायक्रो-इलेक्ट्रोड) त्याचा आराखडा व तयार करण्याची प्रक्रिया ऊर्फ निर्मिती याबाबत सखोल चर्चा केली आहे. या मायक्रो-इलेक्ट्रोड्सची नवीन रचना व निर्मिती याबाबतचे संशोधनकार्य मुख्यत्वे दोन टप्प्यांमध्ये करण्यात आले. पूर्णपणे लवचिक ("फ्लेक्सिबल") आणि टणक ("स्टीफ") मायक्रो-इलेक्ट्रोड्सची रचना व निर्मिती हा पहिला टप्पा होता. त्यातील त्रुटींचा अभ्यास करण्यात आला व त्याच्या आधारे सुधारणा करून दुस-या पिढीतील "लवचिक तसेच टणक" ('फ्लेक्सि-स्टिफ') उपकरण बनविण्यात यश आले. विविध इलेक्ट्रोड्सचा अभ्यास करून एकत्रित अशी रचना करण्यात आली. याद्वारे कमीत कमी विद्युतभार तसेच उत्पादनाच्या कमीत कमी प्रक्रिया अमलांत आणल्या आहेत. दुस-या पिढीतील उपकरणासाठी अत्याधुनिक "एल्स कुई" प्रयोगशाळेत उच्चतम निर्मिती पद्धत तयार करण्यात आली. या उपकरणात "**पॉलिइमाईड सबस्ट्रेट**" सह टिटॅनियम नायट्राईड चे दोन पातळ पापुद्रे आहेत. एका सँडवीज सदृश हा प्रकार भासतो. त्याच्या निर्मितीचे विश्लेषण प्रकरण ६ मध्ये सविस्तररित्या केले आहे. प्रचलीत पद्धतीपेक्षा नियोजित पद्धतीचे फायदे या प्रकरणात सविस्तररित्या स्पष्ट केले आहेत. तसेच या पद्धतीमुळे '**पॉलिइमाईड**' पुनर्रचनेवरील संशोधनाची बरीच दालने उघडण्यात आलेली आहेत. दिसायला सुबक व वापरावयास सुलभ असे श्रवणयंत्र बनवणे ही निर्मितीच्या शेवटच्या टप्प्यातील बाबही खूप महत्वाची आहे. जुळवा जुळव आणि वेष्टनाचे आवरण, त्यातील एक महत्वाचा टप्पा ठरतो. हे करीत असताना पराकोटीच्या विषम हवामानातील बदलामुळे आतील कोणत्याही सुट्या भागास धोका पोहचू नये याची काळजी घेण्यास प्राधान्य द्यावे लागते. या सर्व बाबी विचारात घेवून लवचिक परंतु टणक अशा नविन संकल्पनेमुळे आवरणाची हाताळणी, जोडणी, तसेच पॅकेजींग (आविष्टन) च्या खर्चात बचत होते तसेच सोयीस्कर ठरते. लेझर किरणांमुळे पॉलिइमाईडचे आकारमान अचूकपणे मोजण्यास तसेच काटेकोर कापण्यास मदत होते. त्यायोगे उपकरणाचे आकारमान अचूकपणे साधता येऊ शकते. प्राथमिक रासायनिक चाचण्यांमध्ये लवचिक, टणक तसेच टिकाऊ पदार्थ यशस्वी झाला. याबाबतची सविस्तर माहीती प्रकरण ७ मध्ये दिली आहे. प्रकरण ८ मध्ये इलेक्ट्रोड उत्तेजनाच्या विविध उपयोगांविषयी विवेचन करण्यात आले आहे. भविष्यात विद्युतभारीत सूक्ष्मतम यंत्रांच्या इलेक्ट्रोड्स वर विविध सूक्ष्म ईलेक्ट्रॉनिक उपकरणे जोडली जाऊ शकतात. या पुढील काळातील या विषयाशी निगडित संशोधन तसेच निर्मिती तंत्रज्ञानाचा विकास याचे बळावर या समस्यांवर मात करता येईल.

सध्याच्या विद्युतभारीत सूक्ष्मतम उपकरणांना कमी कंपन संख्यांविषयी मर्यादा आहेत. या संशोधनात अशा मर्यादांविषयी विश्लेषण करून त्यावर उपाय सुचवण्यात आले आहेत. हे उपाय जैविक सुसंगत उपकरणांबरोबरच त्यांच्या सुयोग्य निर्मितीवर भर देतात. हे तंत्रज्ञान पुढे विकसित करून त्याच्याद्वारे विद्युतभारीत सूक्ष्मतम यंत्राचे नमुने विविध चाचण्यांद्वारे बहुउद्देशिय उत्पादन क्षेत्रात विकसित केले जाऊ शकतात. या पुढील पायरी म्हणजे प्राण्यांवरील चाचण्या. त्या निरीक्षणावरून उपकरणाची जैविक कसोटी पार पडु शकते. अशा आवश्यक व आवाहनात्मक कसोटी नंतर मनुष्याच्या उपयोगासाठी दालने उघडली जाऊ शकतात. त्यामुळे जनसामान्यांमध्ये याचा वापर करण्याआधी काही सखोल संशोधन आवश्यक आहे. या सर्व कामाचा 'बीजसंशोधन' म्हणून वापर करून भविष्यकाळात अनेक नवीन उपकरणे विकसित केली जातील व त्यातूनच मानवी वापरासाठी उत्तम कार्य करणारी व व्यापारी तत्वांवर बनवलेली श्रवणयंत्रे बाजारात उपलब्ध होतील यात शंकाच नाही. या प्रबंधातील संशोधन हे या दृष्टीने पुढे टाकलेले एक पाऊल !!

Chapter 1
Introduction

It's not that I'm smart, it's just that I stay with problems longer.
Albert Einstein (Theoretical Physicist)

This is an introduction chapter briefing with some aspects related to hearing and its common losses associated with human beings. The state-of-the art hearing assistance devices will be introduced briefly. In a later section, the Smac-it (Smart Cochlear Implants) project will be described in detail with more focus on the part dealt for the development of the cochlear micro-electrode arrays (MEAs). This chapter ends with a thesis organization giving information on the individual chapters which covers the research goals addressed under the Smac-it project.

1 Introduction

1.1 Hearing and deafness

Human beings are privileged by the ability to differentiate between a significant range of sounds from the understanding a smallest whisper to the warmth of a conversation, from the complexity of a symphony to the roar of a stadium [1]. Hearing is a process which occurs when sound is transmitted from the outer pinna down the ear canal, through the middle ear and then to the inner ear. The inner ear which is anatomically referred as cochlea is a tiny coiled, snail like structure which is embedded inside a bone that houses the sense organ of hearing (organ of Corti). This organ of hearing lies on a membrane (basilar membrane) across the length of the cochlear coil. This membrane responds to the entered sound of different frequencies by selectively vibrating various sections of the membrane, thus acting as a sound filter. High frequency sound vibrations are detected at the entrance of the cochlear coil near the opening from the middle ear called the round window. The low frequencies which travel inside the cochlear coil vibrates the tip or the other end of the cochlea [2]. The organ of Corti of the inner ear consists of very miniature cells with hairs that protrude into a gelatinous membrane. These hair cells which responds to sound in terms of mechanical movement (back and forth) which translates the vibrations into electrical signals. This is as a result of the physical and chemical changes occurring at these hair cells. The produced electrical signals stimulate the hearing nerves which in turn causes patterns of excitation. These excitation patterns are transmitted to the auditory cortex where they are interpreted as sound. These electrical patterns are further processes as pitch and loudness along with meaningful signals such as speech [2]. This ability of the human being to recognize small differences in sounds, noise, speech etc. from cochlea's capacity to distinguish between different frequencies and to inform us about the tones present with their amplitudes is referred as hearing process. This process normally occurs in human beings who do not experience any kind of hearing imperfections.

Deafness on the other hand can be disturbing. In human beings gradually losing the functionality of the hair cells results in a progressive sensorineural hearing loss. Due to this sound heard is distorted imposing a requirement of sound amplification which is high enough to vibrate the hair cells in order to respond for their intended functionality. In situations where most of the hair cell population is lost, the sound amplification process performed by hearing devices (e.g. hearing aid) would not satisfy the person to hear speech, as physically the organ to excite the remaining hearing nerves is absent [2]. Hearing loss in the elderly people can result in a painful and prolonged disaffection from family, friends and colleagues. In youngsters hearing loss is seen increasing in an alarming rate. Evidence suggests that loud rock music along with increased use of portable radios with earphones may be responsible for

this phenomenon. A loud rock concert (115 dB and above) with 15 minutes per day exposure without any protection can lead to progressive hearing loss [3]. Infants may encounter hearing loss due to perinatal infections and especially due to genetic disorder in children which may affect one child in a thousand. Children who are hard of hearing hinders their intellectual development process which is restored back once this problem is addressed and solved correctly.

Hearing plays and important role in our psychological well-being in which a social context is normally established in a normal routine conversation occurring within family and colleagues. A sudden or a progressive hearing loss with family and colleagues may cause the weakening of social connection leaving the affected person disturbingly lonely and may lead to depression or even suicide. Our hearing is an important aspect of our auditory system which acts efficiently in giving warnings in difficult situations by subconsciously informing us about the environment, for e.g. another person's existence or approach in nearby vicinity, alarm to fire signals or ambulance sirens etc. Deafness may leave a person with an ominous sense of vulnerability to unheard environmental changes [1]. Often hearing loss is accompanied with another symptom termed as tinnitus or ringing in the ears which can frustrate, depress and even madden the victims. Most tinnitus, however is idiopathic: its cause in uncertain. Some drugs trigger the conditions for e.g. some antimalarial drugs related to quinine and aspirin at the high dosages used in the treatment of rheumatoid arthritis are notorious for this. Often, tinnitus occurs at high frequencies to which a damaged ear is no longer sensitive. In this case tinnitus may reflect hypersensitivity in the deafferented central nervous system [1]. In order to solve hearing loss problems various approved and tested medical devices are present which addresses to solve the different types of hearing loss problems.

1.2 Auditory Prostheses (State-of-the art)

As mentioned earlier that various auditory prostheses (for e.g. Hearing Aid: HA, cochlear implant: CI) are being used by people with hearing deficiency to solve their problems as per the degree of deafness. Out of which cochlear implants (CI's) is one of the medical implant device which have significantly extended its function and performance in the last decade through its improvement in technology and its application by addressing to a broad range of hearing related disorders. Auditory sensation realization can be induced by various physical principles as sketched out in Figure 1.1. In a normal hearing process as explained in the earlier section, the sound in terms of acoustic energy, is converted into mechanical vibrations and then further into electric neural signals. For a hearing impaired person different devices are required depending upon the type and the degree of hearing loss. People at the initial

stages of hearing loss for whom the mechanical amplification process of the ear/cochlea is not operative then this functionality can be replaced by hearing aids. The hearing aid which is an electroacoustic device senses the surrounding sound and amplifies it for the user (first arrow in Figure 1.1). For a certain degree of hearing loss where more amplification without any acoustic feedback is required, sound can be converted directly into mechanical vibrations which stimulates the middle ear by an middle ear implant (second arrow in Figure 1.1).

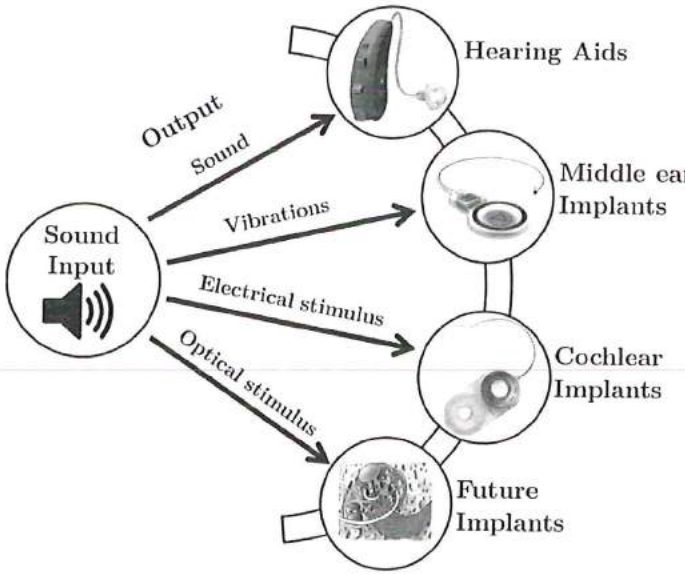

Figure 1.1 Various paths to auditory system stimulation. Hearing aids (*Image courtesy: Siemens, www.siemens.com*), Middle ear implant (*Image courtesy: MedEl, www.medel.com*). Cochlear Implants (*Image courtesy: Advanced Bionics Corporation, www.advancedbioncis.com*), Optical stimulation (*Image courtesy: www.optoiq.com*) [4,9] and Optogenetic stimulation [5,6].

In cases of people experiencing severe–to–profound hearing loss where the cochlea losses its working capability to convert sound into electrical neural signal, in those cases the traditional CI's bypasses the normal hearing path and directly stimulate the residual auditory nerve by converting sound into electrical pulses (third arrow in Figure 1.1). Recently researchers have found optical way of stimulation as an alternative to the electrical stimulation process. Here two strategies for driving auditory neurons were followed: infrared neural stimulation pioneered by Richter *et al.* [4] and the other is optogenetic stimulation used in auditory research where a viral vector is used to introduce rhodopsin into the nerves in order to enhance light sensitivity. For e.g. channelrhodopsin 2 (ChR2) for enabling blue light-driven activity of spiral ganglion neurons (SGNs), cochlear nucleus and auditory cortex neurons or halorhodopsin cochlear nucleus and auditory cortex neurons for inhibiting cochlear

nucleus neurons [5,6] (Figure 1.1). This technique has yet to prove its capability. In the following sections we will talk on hearing assistance devices/auditory prostheses (HA and CI) which makes uses of the first and the third conversion principles.

1.2.1 Hearing Aid (HA)

HA is nothing but a sound amplifier. It's primary function is to amplify sound to such a level that a hearing-impaired person can detect it and most importantly make effective use of the acoustic signals being generated [7]. Although amplification being its main function, different levels of hearing damage and associated complexities of frequency & temporal perception places varying demands on the Hearing Instrument (HI) design. Looking at the progress in HI technology in the past few years, HI still only partially compensate for hearing loss and do not correct it completely [7].

The state-of-the art HI contains various components out which the main important components are its electrostatic transducer, the microphone and the receiver of the device. A normal HA contains a microphone to pick up the surrounding acoustic sound/signal and converts it into an electrical signal. This electrical signal is then modified by an amplifier depending upon the hearing loss requirement, and feeds this amplified signal to the HA receiver. The receiver then converts this amplified electrical signal back into a sound signal, tailored to the needs of the hearing-impaired person. HI are available in several different styles Figure 1.2 (a): behind-the-ear (BTE), receiver-in-the-Canal (RIC), in-the-ear (ITE), in-the-canal (ITC), completely-in-canal (CIC) or body worn hearing instruments. For all these instruments, sound amplification is the primary function therefore the vital components used in building the HI are similar. However, due to different styles the differences occur in component packaging and appearance. A HI consists of the following basic components (Figure 1.2 (b)) with its intended function:

1) Microphone: Captures the external acoustic signals from the environment and converts it into an electrical signal. Conversion of one form of energy (acoustic) to another form (electric).
2) Amplifier: Amplifies or increases the strength of the electrical signal received from the microphone. In this conversion process it will also alter the balance of the sound, usually giving more emphasis to high-frequency sounds and weak sounds than it does to low-frequency sounds and intense sounds.
3) Battery: Supplying power supply to all the components of the HI.
4) User controls: Used for adjusting output, amplification and frequency response etc., of the HI. These can be adjusted by the user itself or by an expert hearing health care professional (dispenser).
5) Receiver: Also referred to as speaker which converts back the electrical signal to an acoustic signal.

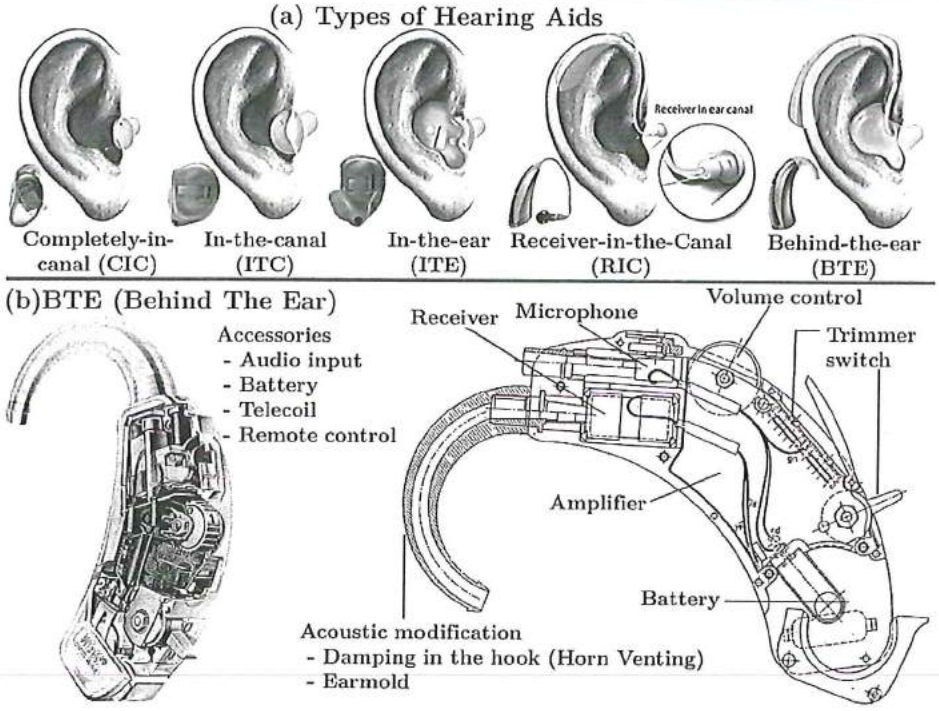

Figure 1.2 (a) Different types of HA; (b) Details of a particular HA (BTE) with component placements (*Image courtesy: Phonak AG, www.phonak.com* [7]).

One type of HI; BTE from a HI manufacturer (Phonak AG) shows all the detail fundamental placement of the components present inside the device (Figure 1.2 (b)). BTE HI shell is designed in such a manner that it always strives hard to achieve the smallest possible size and the best cosmetic appearance within the constraints imposed by the components to be used inside the HI [7].

1.2.2 Cochlear Implants (CI's)

Unlike a typical HA which is worn externally, CI's are therapeutic electronic devices which are surgically placed inside the inner ear (cochlea), which directly stimulate the auditory nerves in response to a sound. In doing so this device bypasses the normal path of the hearing process so, this sends audio information to neural parts by conversion of acoustical energy to electrical energy. Electrical currents produced inside the cochlea induce action potentials in the auditory nerve fibres which are transmitted to the auditory cortex of the brain where the sound is interpreted. It bypasses the damaged or the missing hair cells within cochlea that would normally code sound by converting mechanical energy into an electrical neural signal. CI's are beneficial for those people who experience severe–to–profound or

totally hearing impaired loss and could not sufficiently regain the sound perception from the conventional HA. The sole purpose of the HA is to amplify the sound for perception enhancement, whereas the CI's bypass the outer and the middle ear in order to stimulate the auditory nerve endings within the human auditory system.

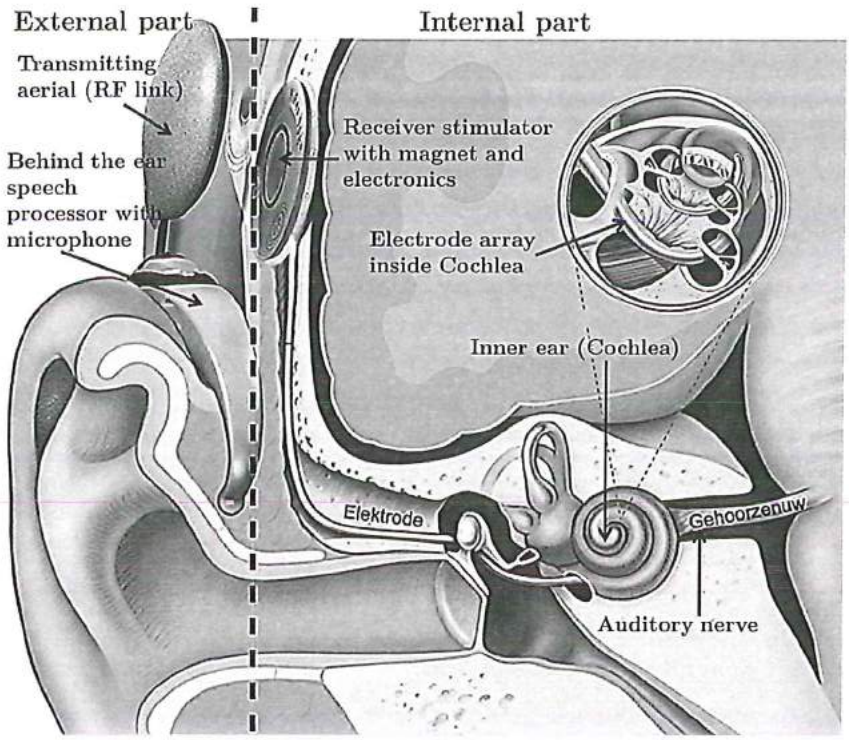

Figure 1.3 Pictorial representation of a human ear with a CI (*Image courtesy: Leiden University Medical Centre and Advanced Bionics Corporation, USA*).

As illustrated in Figure 1.3 a traditional CI consists of an external part worn on the ear and an internal part which is surgically implanted behind the ear with electrodes wires extending and ending inside the inner ear (cochlea). The external part consists directional as well as omnidirectional microphones that picks the environmental sound and converts them into electrical voltages that are send to a small speech processor which is worn behind the ear (pinna) or in some cases a larger, more versatile one attached to a belt or placed in a pocket. The speech processor filters all the received waveform into different frequency bands. The outputs of the filters are referred to a map of the patient's electric current thresholds and comfortable listening levels for the individual electrodes [2]. In order to represent a speech signal for each time instant, a certain code is produced for the stimulus parameters (electrode stimulation site and its respective current level) to be passed

on further. This code along with power is transmitted by radio waves via a circular transmitting aerial (RF link) through the intact skin to the internal part of the receiver-stimulator package which is surgically implanted under the skin inside the mastoid bone. This receiver-stimulator package which receives the codes along with power is responsible for the signal decoding process to produce a pattern of electrical stimulus currents or instructions for controlling the process which is carried by the electrode array (bundle of wires) placed inside the cochlea. These electrode arrays, which are inserted around the circular turns inside the cochlea perform the neural stimulation process by electrically stimulating the auditory nerve fibres, thus transmitting the external acoustical information. A certain pattern of hearing neural activity is the result in response to the produced sound, thus providing a meaningful representation of speech and external environmental sounds. The electrode array is physically lying close but is not attached to the spiral ganglion cells of the cochlea and their peripheral hearing nerve fibres [2].

In the past, it looked nearly impossible to cure the hearing loss. After years of research and development, the modern CI's do the primary function of listening and enable the conception of sound and speech for hearing disabled people. CI's also allow the possibility of communication, development of language skills, and enjoyment through media connectivity such as television, phones and music. The invention of CI devices permitted us to understand that meaningful sound can be send to brain by an electrical impulse. Despite of all the developments so far, there are still many limitations and therefore there is always room for improvement. As an improvement step, a project consortium naming Smac-*it* (**S**mart **C**ochlear **I**mplants) was designed in a joint collaboration within Delft University of Technology (TU Delft) and Leiden University Medical Centre (LUMC) with an industrial partner (Advanced Bionics Corporation®, USA) to address and research various aspects related to CI's. This STW (Dutch Technology Foundation) funded Smac-*it* project (project number: 10056) which is a part of the SMART-SIP programme deals with answering some research questions to solve the drawbacks related to the current CI's by using new materials and new manufacturing techniques.

1.3 Smac-*it* (Smart Cochlear Implants)

Cochlear implants are commonly accepted as therapeutic devices, on the market and have restored hearing to more than 400000 profoundly deaf people worldwide. Users can participate in normal conversation and other situations where the sound environment is relatively clean. However their hearing performance drops dramatically in complex sound environments, causing poor appreciation of music and inability to converse in crowded rooms (cocktail-party effect). Furthermore, the surgical placement of the device remains complex. The bottleneck is delivering more

sound detail is the crudeness of current-state intracochlear electrodes. They are based on classic technology consisting of wires and Platinum contacts in a silicone carrier. Therefore the number of stimulation contacts is limited (+/- 20) compared to the number of neural stimulation sites (+/- 3000), and they are relatively large compared to the small size of the cochlea. Incorrect insertion of the electrode can lead to damage of the cochlear tissues, thus impairing the effectiveness of the implant. The goal of the consortium is to research and develop technologies to address these drawbacks as follows:

1) Miniaturization and increased number of electrodes with low level processing at each electrode.
2) Exploring new material and manufacturing technique to develop microelectrode array (MEA) intended for animal use.
3) Optimise electrode use after implantation using low power electronics and its integration in the overall system.
4) Overall system level optimizations for reliable data transmission for the designed low power analogue electronics.

The main goal of the project is to lay foundation steps by fundamental research for the future development of an improved cochlear implant. The main industrial partner (Advance Bionics Corporation®, USA) being a CI producer will be in an ideal position to further develop the results into possible new products. In addition to the main aim, there are many potential spin-offs from this combined consortium project (Smac-*it*). Many implantable systems can benefit from the software development and low-power electronics and low-level integration.

In order to improve the functionality of the cochlear implants a multi-disciplinary approach is required. In this approach criteria such as: reliability, biological interaction, power limitations and re-configurability span both hardware and software related disciplines are to be considered. Solutions are expected through finding the correct balance between hardware and software. In the Smac-*it* project research consortium the medical (in-vitro and in-vivo experimentation) research was carried out at LUMC and the technological part was realised at TU Delft. At TU Delft the technological research part was divided into three different research groups at the Faculty of Electrical Engineering, Mathematics and Computer Science. The three researchers with their individual research focus is as follows:

1) Electronic Instrumentation Laboratory (EI Lab): The main challenge was to understand and come up with innovative solutions for the problems associated with the CI electrode array. This was achieved by using new microfabrication processing techniques using non-traditional materials.

2) Biomedical Electronics group: Under this research domain of low-power electronics and low level integration, the main goal was to develop a low power analogue integrated circuit for the CI system.
3) Computer Science and Engineering (Parallel and Distributed Systems): Here the research was focused at the overall system level, where software optimization techniques were used for compressed reliable digital data generation and transmission from the external part to the internal part of the CI device.

In this thesis the research journey related only to the EI Lab will be handled since the other two aspects are handled separately in other thesis.

1.3.1 Research at EI Laboratory

In terms of CI electrode array there are important issues addressed and researched under the Smac-*it* project consortium. The design and fabrication of the microelectrode arrays (MEAs) was one of the main tasks of the researcher of EI Lab. In the first phase a rigid probe was made in order to sketch out the manufacturing boundaries and the limitations encountered in terms of material and process capabilities. The second phase moved towards exploring new materials and subsequent microfabrication of a flexible or a combination of rigid and flexible probe which in future will allow the electrode array to bend along the scala tympani (ST) of the cochlea during the electrode array insertion process.

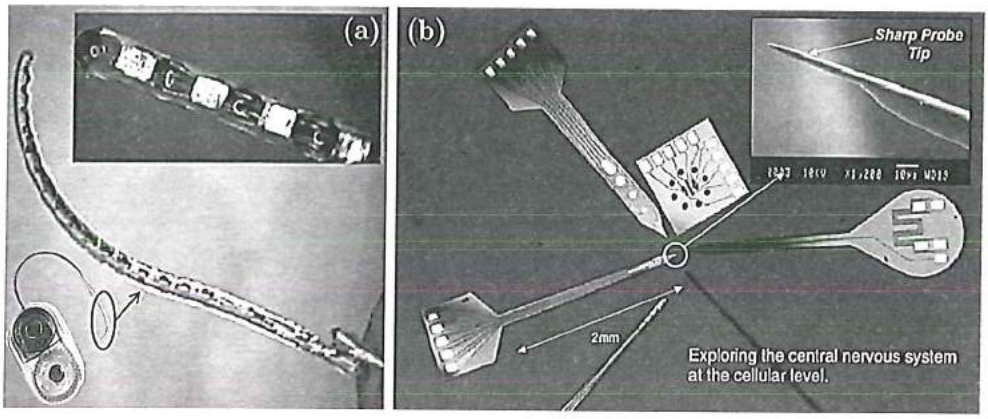

Figure 1.4 (a) A CI electrode array (Clarion High Focus) (*Image courtesy: Advanced Bionics Corporation, USA*); (b) Neural probes from Michigan [8,10].

Characterisation and testing of the microfabricated prototype is an important phase in order to understand the probable feasibility application for the future CI's.

In the clinically used cochlear implant systems the electrode implant array is made of individual wires connecting each of the electrodes contact stimulation site (Figure 1.4 (a)). The use of silicon will enable more functionality to be included adjacent to the electrodes, which will improve performance and remove the need for the wires in the probe. Silicon can be machined to make a fine needle (Figure 1.4 (b)) and also made sufficiently flexible for this application [8]. By shifting the current sources from the casing to the electrode contacts the number of wires through the array could be decreased allowing for far more contacts while maintaining a flexible design. Another additional task was to find a common material which can be utilised for fabricating both the MEA as well as the required electronics in close vicinity of the MEA. By doing this, the wiring problem associated with increasing the number of electrode stimulation sites in the available space, can be solved. The goal was to show a proof of principle (demonstrator) which in future can developed as a product.

1.4 Objectives and outline of the thesis

The key technological challenges to solve the drawbacks of the current CI's mentioned in earlier sections include a) the development and characterisation of a new biocompatible conducting material, b) the adaption and integration of an appropriate polymer to develop the microfabrication process for the MEA, and c) the selection of appropriate packaging material followed by subsequent characterisation techniques of the MEA to satisfy the preliminary requirements.

The objectives of the present thesis are:

- to design and develop a suitable microfabrication technique for fabricating rigid/stiff probes to understand the manufacturing limitations for the further development of the MEA.
- to investigate and study an appropriate electrode stimulation material which can be used along with a suitable polymer to design and optimize a microfabrication process to develop a completely flexible or a combination of a stiff and a flexible MEA.
- to identify and design a suitable mounting, assembly and packaging process for the fabricated MEA followed by subsequent characterisation tests.
- to perform an initial evaluation to build basic electronics by using the same microelectrode material for an application to build a possible hybrid device which can be used to develop the future cochlear implants.

The complete thesis is subdivided into different chapters as follows:

- **Chapter 2** is a short introduction chapter which gives a general anatomical information of the human ear and its normal working. This is followed by a description of the history of the development of the CI's, its working and other medical devices used for different type of hearing loss.
- **Chapter 3** gives an overview of the state-of-the art of CI electrode array and the other different types of MEAs which are at research or commercial level. Later in the chapter, various MEMS based micro-fabrication technologies which were used in developing the MEAs are described.
- **Chapter 4** focuses on the material aspects of the CI electrode array along with the charge transfer methods occurring at the electrode-electrolyte interface. After this a biocompatible electrode material (Titanium Nitride: TiN) is investigated for its further application in manufacturing the MEA.
- **Chapter 5** explains various MEA designs (stiff, flexible and "Flexi-Stiff") and its variations. Microfabrication steps for the stiff probe followed by electric field density distribution analysis performed by finite element analysis (FEA) techniques using multiphysics simulation software (COMSOL®) is mentioned.
- **Chapter 6** goes into the details of the microfabrication procedure adopted for the 1st generation flexible and the 2nd generation "Flexi-Stiff" MEA. A brief overview of different challenges and problems encountered along with the subsequent steps undertaken to solve them are given. These improvement steps were accordingly incorporated in the final process flow in order to optimize the overall microfabrication process for the MEAs.
- **Chapter 7** talks about the assembly, packaging of the MEA device. This is followed by initial *in-vitro* and *in-vivo* experiments done at LUMC and its subsequent discussion with future recommendations to the experiments.
- **Chapter 8** is a demonstrative chapter which exhibits the application of using TiN as a gate material which is common to MEA stimulation material to microfabricate basic electronics. This opens a new research area where the further possible development in combining a simple 5 mask BiCMOS process along with the microfabrication process of the MEA will initiate the next stage to develop an hybrid implant. This approach will allow some simple electronics to be included in MEA, thus allowing increased number of electrodes without creating a wiring problem.

The conclusions and the future outlook is discussed in **Chapter 9**.

1.5 References

1. Kandel, E. R.; Schwartz, J. H.; Jessell, T. M. *Principles of Neural Science*; 2000; Vol. 4.

2. Clark, G. *Cochlear implants: fundamentals and applications*; springer, 2003.

3. American Hearing Research Foundation Noise Induced Hearing Loss http://american-hearing.org/disorders/noise-induced-hearing-loss/.

4. Richter, C.-P.; Matic, A. I.; Wells, J. D.; Jansen, E. D.; Walsh, J. T. Neural stimulation with optical radiation. *Laser Photon. Rev.* **2011**, *5*, 68–80.

5. Moser, T. Optogenetic stimulation of the auditory pathway for research and future prosthetics. *Curr. Opin. Neurobiol.* **2015**, *34C*, 29–36.

6. Hernandez, V. H.; Gehrt, A.; Reuter, K.; Jing, Z.; Jeschke, M.; Mendoza Schulz, A.; Hoch, G.; Bartels, M.; Vogt, G.; Garnham, C. W.; Yawo, H.; Fukazawa, Y.; Augustine, G. J.; Bamberg, E.; Kügler, S.; Salditt, T.; de Hoz, L.; Strenzke, N.; Moser, T. Optogenetic stimulation of the auditory pathway. *J. Clin. Invest.* **2014**, *124*, 1114–29.

7. Vonlanthen, A. *Hearing Instrument Technology for the Hearing Healthcare Professional*; 2000.

8. Wise, K. D.; Sodagar, A. M.; Gulari, M. N.; Perlin, G. E.; Najafi, K. Microelectrodes, Microelectronics, and Implantable Neural Microsystems. *Proc. IEEE* **2008**, *96*, 1184–1202.

9. Zeng, F.-G. *Auditory Prostheses: New Horizons*; Zeng, F.-G.; Popper, A. N.; Fay, R. R., Eds.; Springer Handbook of Auditory Research; Springer New York: New York, NY, 2012; Vol. 39.

10. Wise, K. D.; Anderson, D. J.; Hetke, J. F.; Kipke, D. R.; Najafi, K. Wireless Implantable Microsystems: High-Density Electronic Interfaces to the Nervous System. *Proc. IEEE* **2004**, *92*, 76–97.

Section I

Human Ear, implants and manufacturing

Chapter 2
The Ear, Cochlear Implants and other auditory prosthesis

Applied technology itself is merely an extension of human attributes, which reduces human effort, freeing human from a particular chore or problem.
From the documentary: "Zeitgeist – Addendum"

This chapter will give a brief overview of the human ear's anatomical features and their different subsequent functions in the overall hearing mechanism. It will then dive into different types and degrees of common hearing losses encountered. This will give an understanding to the various types of hearing losses and the causes responsible for creating the same. Later the chapter proceeds with the different therapies associated with the hearing loss. Treatments revolve around FDA approved medical devices which are available in the market. These include different types of bone conduction devices which basically involves sound amplification bypassing the external ear canal and providing this amplified sound to the inner ear (cochlea) via the bone pathway bypassing the traditional acoustic path. A detailed discussion along with a brief history will be done on the Cochlear Implant's which works on the principle of converting sound into electrical signals and channelizing them as per frequency in order to stimulate the auditory neurons inside the cochlea. This is done by means of a tiny electrode array placed inside the scala tympani which is built with individual electrode contact sites stimulating different positions inside the cochlea which represents different audio frequencies. The electrode array will be explained in in the later chapters. The chapter ends with a discussion about devices which are completely implantable and its basic working principles aimed for particular type of hearing loss to assist the patients in their hearing process.

2

2.1 Human Ear anatomy

Human beings are enriched with various senses, viz. smell, taste, touch, pain, vision, hearing and so on. Hearing is an unique ability to recognize sound, which is enabled by the human hearing organ commonly referred to as "ear". Sound normally consists of compressions and rarefactions which are propagated in an elastic medium (air) at approximate speed of 340 m/s. These propagations cause vibrations which are picked up by our ears. The ear is an engineering marvel which consists of its sensory receptors which transduce the sound vibrations with amplitudes as small as the diameter of an atom of gold (0.3 nm) into electrical signals 1000 times faster than photoreceptors can respond to light [1]. These three functions of capturing acoustic signals, converting and transmitting them is performed in combination by the external, middle and the internal ear. In addition to such receptors ear also contains receptors for equilibrium which are responsible for maintaining balance and making oneself aware of the orientation in space [1].

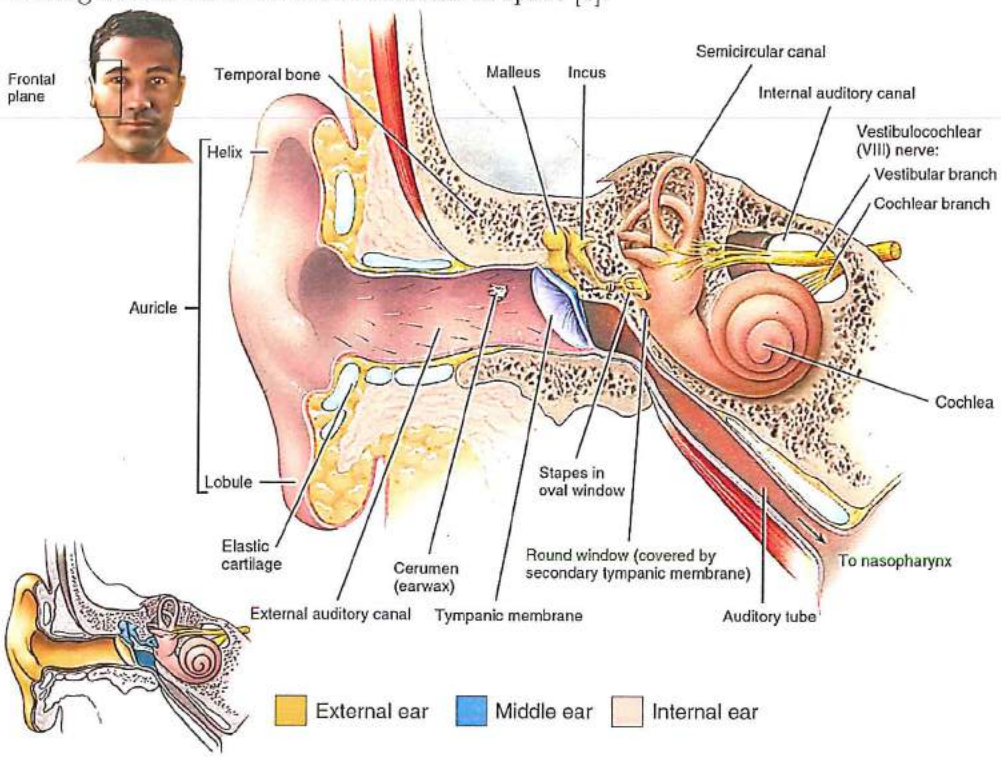

Figure 2.1 Sections of the ear; external, middle and the internal ear (*Adapted and re-printed from* [1]).

The human ear is divided into three major sections: (a) the external ear; which accumulates sound waves from the surroundings and directs it to the other sections, (b) the middle ear by its transformer action transmits the sound vibrations

to the oval window of the inner ear and, (c) the internal ear which is the house of the receptors which convert these vibrations into electrical neural signals which are perceived as sound by the brain. The external and the middle ear functionality are rather simply engineered in comparison to the internal ear functions (hearing and equilibrium) which are extremely complex. We will be briefly covering the different sections of the ear with detailed focus on the cochlea and its functions.

2.1.1 The external, the middle and the internal ear

The components which make up the external (outer) ear are the auricle, the external auditory canal and the ear drum (Figure 2.1). The auricle (pinna) is made of an elastic cartilaginous shaped like flared flap which is covered by the skin and is responsible for the first step of gathering and steering the external sound waves to the sensitive middle and the inner ear. The external auditory canal (EAC) which is approximate 25 mm in length of which $2/3^{rd}$ part is cartilaginous (elastic cartilage) and the remaining $1/3^{rd}$ part is the sensitive bony area (temporal bone) which further leads to the tympanic membrane (TM). The TM or the eardrum is a thin semi-transparent membrane (partition) which acts as a separating medium between the EAC and the middle ear. The middle ear which is nothing but a small air-filled cavity of the temporal bone which on one side is attached to the external ear via. the TM and from one side (internal side) attached to the internal ear by a thin bony portion that contains two small membrane covered openings: the oval window and the round window [1].

The middle ear actually couples the sound energy from the EAC to the inner ear. By the transformer action it performs the function of impedance matching of the EAC to a much higher impedance of the inner ear fluids. The sound will normally reflect in the absence of this transformer action which eventually is transmitted via the TM to the cochlear with the help the auditory ossicles. The auditory ossicles contains the three smallest bones in the body which are referred to as the malleus, the incus and the stapes (Figure 2.2 Middle ear). The malleus ("handle or hammer") which attaches to the internal surface of the TM on one side, on its head side is connected to the incus ("anvil") which in turn is connected to the head of the stapes ("stirrup"). The malleus and the incus are hinged rigidly so that when the top of malleus is pushed by the TM the bones rotate together and accordingly transfer the forces to the stapes. This lever action increases the applied force due to sound vibrations and decreases the velocity. The basal part of the stapes is attached to a flexible window in the wall of the cochlea commonly referred to as the oval window. Below this window another window (round window) is present which is enclosed by a membrane commonly referred to as round window membrane [1].

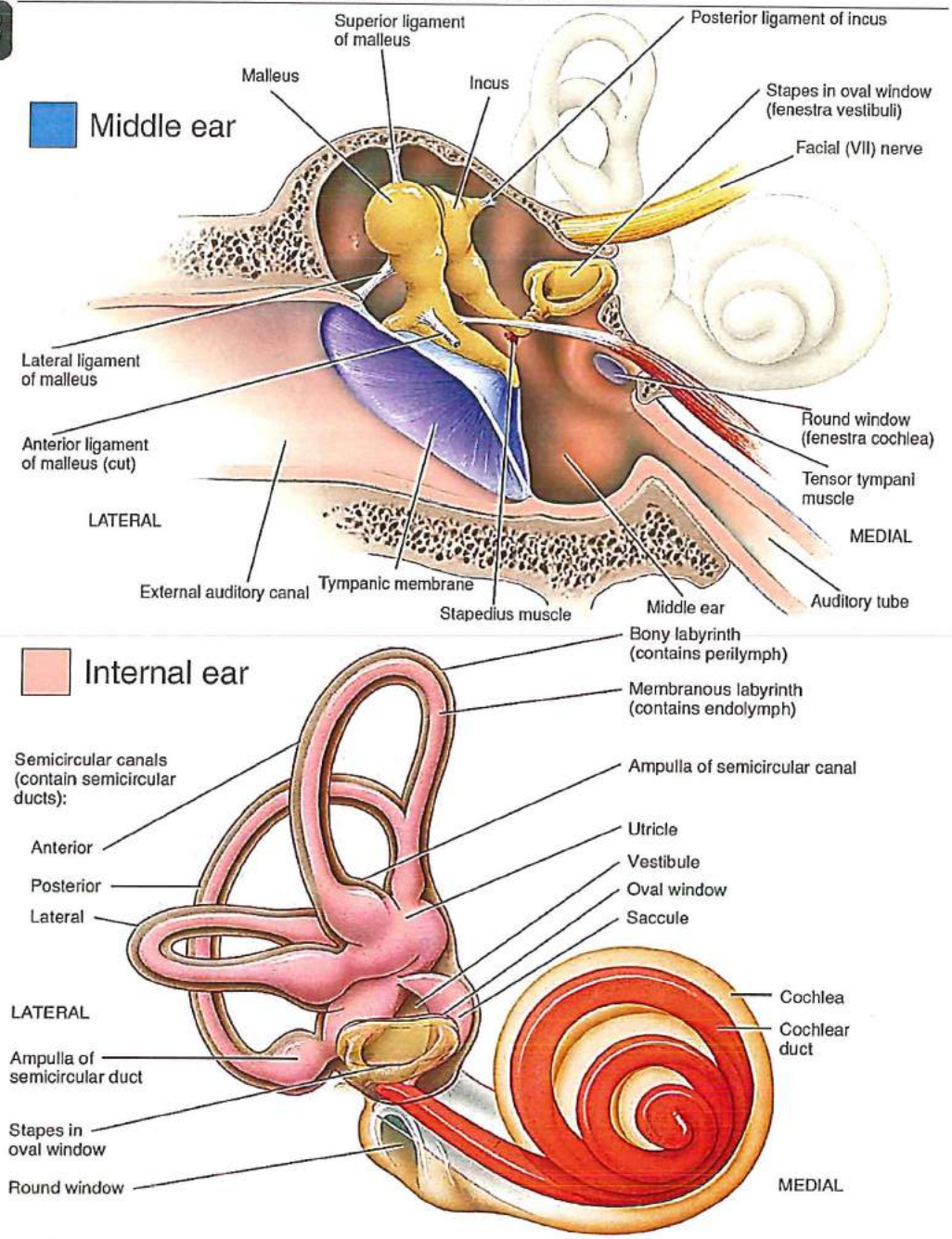

Figure 2.2 Different parts of the middle and the internal ear (*Adapted and re-printed from* [1]).

The internal (inner) ear also referred as labyrinth bone cavity is divided into three main areas; the semi-circular canals, the vestibule and the cochlea. The semi-circular canals and the vestibule which forms the vestibular system is responsible for

motion and balancing purposes while the cochlea is solely responsible for hearing which involves conversion of mechanical energy to electrical energy. The vestibular system consists of three semicircular canals and two vestibular sacs (utricle and saccule). These canals which contains ducts running through them holds the same kind of fluids (perilymph and endolymph) and sensory hair cells as in cochlea. These deliver sensory information about the equilibrium, motion and spatial orientation. The rotational movement is sensed by these semi-circular canals, similarly the two vestibular sacs sense horizontal movement and gravity.

2.1.2 The Cochlea and its functions

Cochlea (Latin: "Snail") is a spiral shaped, conical, bony chamber which extends from the anterior part of the vestibular system and coils for about 2 ½ turns around a bony pillar called the modiolus (Figure 2.3 (a) [2]).

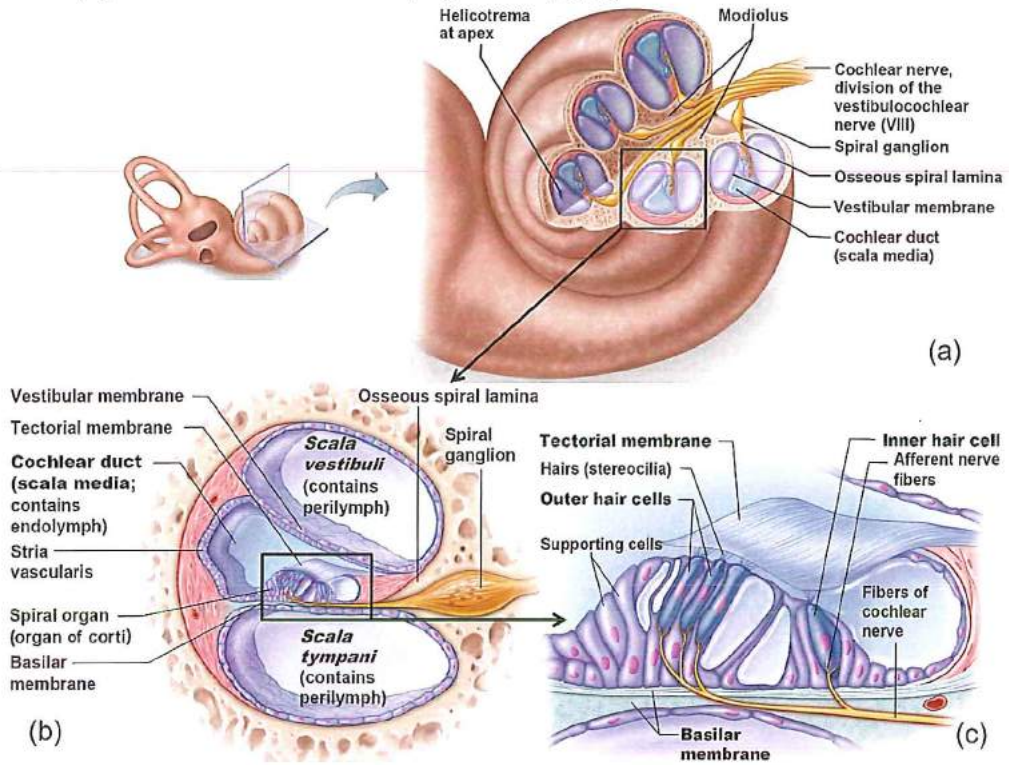

Figure 2.3 Anatomy of the cochlea; (a) Lateral view with wedge-cut section; (b) Enlarged cross-section of the cochlea to show details; (c) Detailed structure of organ of Corti (*Adapted and re-printed from* [2]).

From inside the cochlea a membranous duct (cochlear duct) (Figure 2.3 (b)) runs through the centre from the base and ends at the apex (Helicotrema). This cochlear duct is the place where the sensory receptor organs of hearing, called the spiral organ or the organ of Corti is present (Figure 2.3 (b) & (c)). Sections through the cochlear

duct reveal that it is divided into three channels; scala vestibuli (SV), scala media (SM) and scala tympani (ST). The vestibular membrane (Reissner's membrane: RM) separates the SV from the SM and the basilar membrane (BM) separates the SM from the ST (Figure 2.3 (b) and (c)). The cochlear duct or SM is a membranous labyrinth into the cochlea filled with endolymph. Above SM is the SV, filled with perilymph which lies superior to the cochlear duct is continuous touching the oval window at the bottom and runs until Helicotrema at the apex. The ST channel, filled with perilymph which is below the SM, at the base ends at the round window and similar joining at the apex. The Helicotrema allows fluid to flow from SV to ST and vice versa. Due to vibrations any inward and outward movement of the ossicles (stapes) against the oval window causes the perilymph in the SV to experience a similar back-and-forth motion. The inward motion of the stapes causes a downward movement of the basilar membrane and direct fluid displacement in the ST, with the round window (RW) acting as pressure release point. The basilar membrane is the medium for the travelling wave, and it can be considered as a series of coupled oscillators, collectively more or less acting as a mechanical Fourier transformer [3].

Sounds of high frequencies which creates pressure waves while transmitting via the perilymph of ST during its descend travel also vibrates the BM. BM separates SM from ST is an spiral organ which is a coiled sheet of epithelial cells, including supporting sensory structures and about 16000 hair cells which are the receptors for hearing. There are two distinct groups of hair cells: the inner hair cells (IHC) are arranged in a single row located more closely to the modiolus and the outer hair cells (OHC) are positioned outside of the spiral and arranged in three rows that run along the length of the SM. A human ear has typically about 12000 OHC's and 3500 IHC's [4]. IHC's differ from OHC's in terms of functionality where IHC's takes an active role in converting mechanical vibrations into an electrical neural signal which generates an action potential in the neurons of the cochlear nerve whereas OHC's do not send signals but act as an frequency sensitive amplifier [4]. Each hair cell at its apical tip have 40-80 stereocilia (actually long microvilli) arranged in several rows of graded height. The "hairs" (stereocilia) protrude into the K^+ rich endolymph, and the longest ones are embedded in the overlying, stiff gel-like tectorial membrane (Figure 2.3 (c)). Movement in the BM causes the stereocilia to deflect, leading to a depolarization of the hair cells from its resting potential to its receptor potential. This results in the release of the neurotransmitter L-glutamate in the IHC, producing action potentials in the ganglion cells dendrites connected to these hair cells [5].

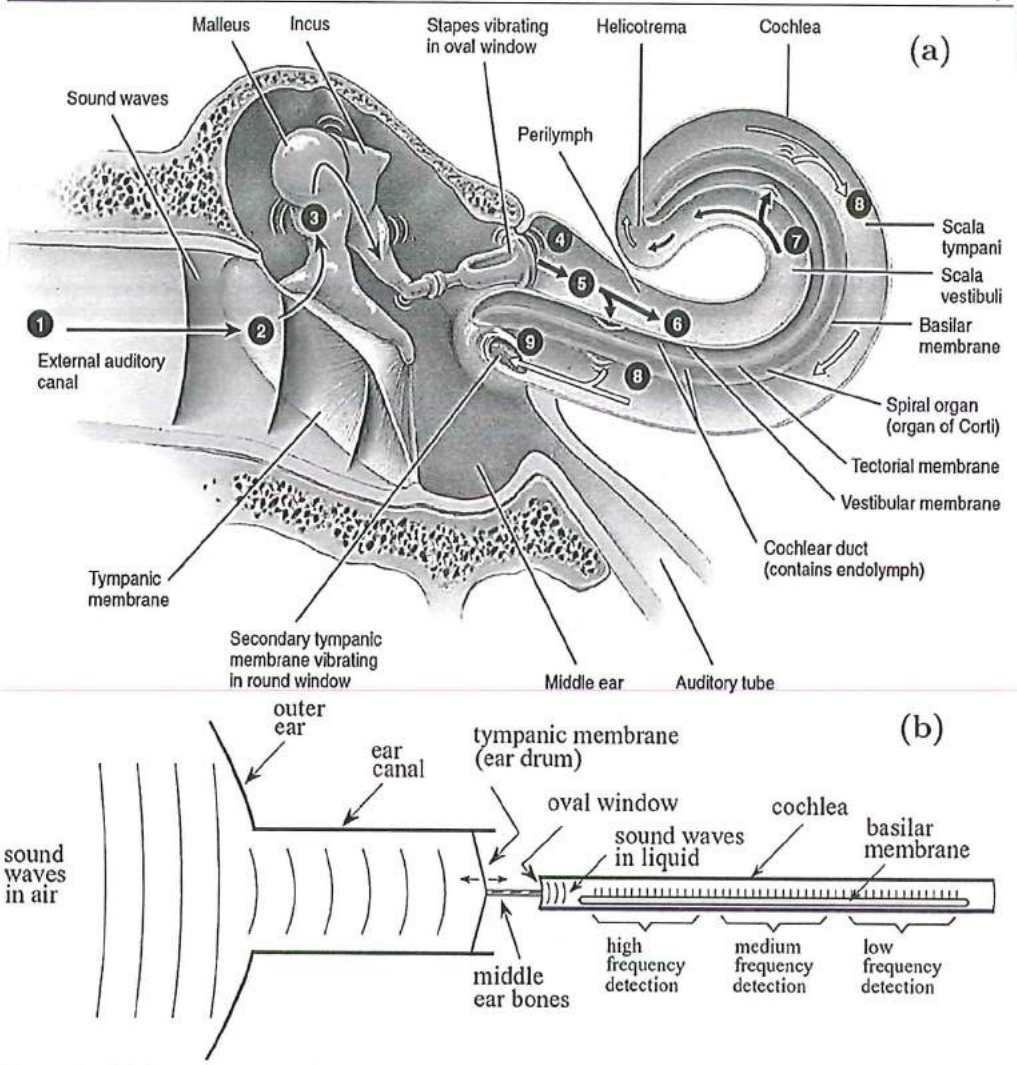

Figure 2.4 (a) Structure and working of a right human ear; (1) Pinna collects sound waves and enter the EAC and (2) channels them to TM (ear drum) where the mechanical energy of sound waves vibrates this thin sheet of tissue in synchronization with the air waveform. (3) The middle ear bones (Malleus, Incus and Stapes) transmit these impedance matched vibrations to (4) the oval window of the fluid filled cochlea. (5, 6, 7, 8) This results in a pressure wave which travels from the base of scala vestibuli (SV) to the apex. This traveling pressure wave vibrates the basilar membrane (BM) which moves the hair cells of the organ of Corti against the tectorial membrane. Due to the varying stiffness of the BM, each hair cell responds to a narrow range of audio frequencies, making the ear a frequency spectrum analyser (b). (9) At the end an combined effect of the Helicotrema and BM pressure waves are transferred to ST resulting in vibrations at the RW membrane in the round window which is opposite and below the oval window. Figure (a): *Adapted and re-printed with permission from* [45] and Figure (b): Functional diagram of the human ear. *Adapted and re-printed with permission from* [46].

This action potential signal is then accordingly transmitted via the auditory nerve

fibres to brainstem which further is delivered to the auditory cortex for further processing. Normally for a single auditory nerve fibre an action potential is generated when a cell's transmembrane pressure is depolarized to a threshold value which results in a triangular spike (Figure 2.5 (e)). These spikes (action potentials) will remain to arise unless and until the neuron remains depolarized beyond its threshold value. The magnitude of this depolarizing current is dependent on the spikes produced per second (firing rate) where greater the current, the quicker is the firing rate. In many cases the magnitude of the resting potential for the hair cells triggers the nearby neurons continuously in the absence of any external auditory stimulus. This is referred to as spontaneous firing rate [6].

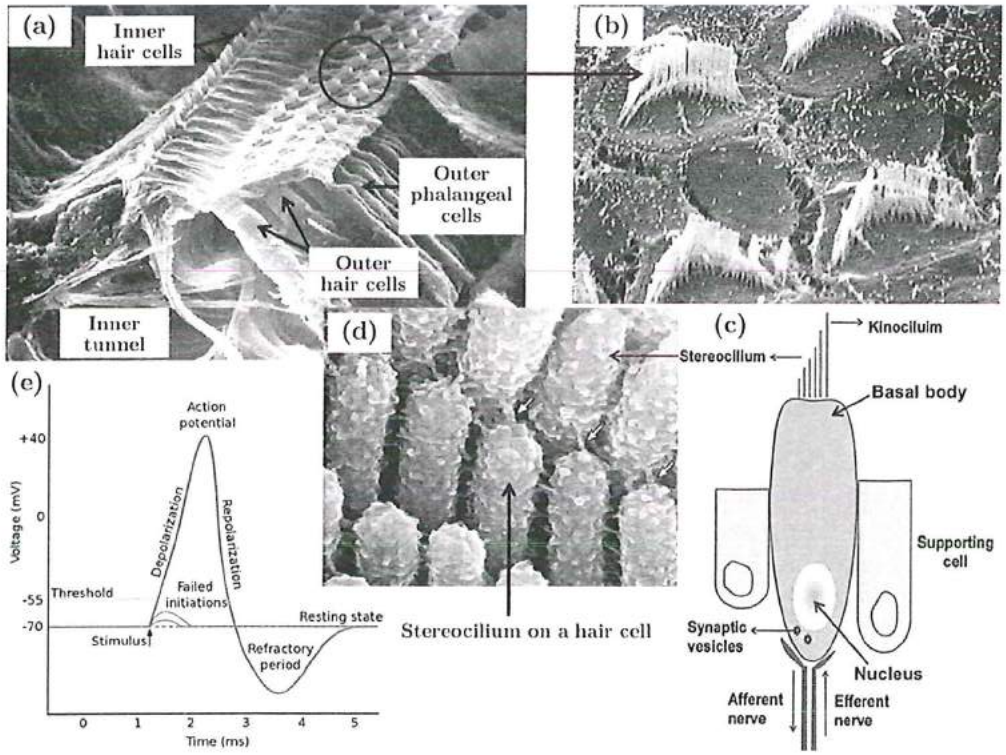

Figure 2.5 (a) Hair cell arrangement in the organ of Corti showing the IHC's and OHC's; (b) Closer look to show the V-shape structure of the OHC's. Surface underneath hair cells is smooth, whereas supporting cells surface is structured with microvilli; (c) Drawing of the sensory epithelium of internal ear showing the hair cell structure. (*Images* (a) and (b) *Adapted and re-printed with permission from* [47] and (c) from [48]); (d) Stereocilia on a hair cell [49]; (e) Illustration of an action potential showing the various phases which occurs after stimulation (*Adapted and re-printed with permission from D. Iberri* [50]).

Basilar membrane (BM) responds in terms of displacements to the different sound frequencies entering the cochlea which are the part of the travelling pressure wave originated from the stapes vibrating on the oval window. The displacement

behaviour of the BM does not only depend on the sound captured by the ear but also relies on the mechanical properties of the BM which change while running from the base to the apex. BM has its maximum displacement where the fibres of the BM are "tuned" to a particular sound frequency. At the base of the cochlea the BM is short and rigid in structure where it is relatively narrowly (100 µm) squeezed with the adjoined supporting cells. Moreover at the apex region BM is less stiff, wider (500 µm), longer and floppy with spaced out more freely along with the supporting cells. This structure leads to have changing mechanical properties thus enabling different sound frequencies to have their specific site on the BM which leads to its subsequent maximum displacement (Figure 2.6) [6]. This characteristics of maximum movement for a particular frequency is termed as "resonance" and frequency dependence for specific site of the BM is termed as "tonotopy". Tonotopical organisation means that the hair cells and their associated neurons spread over the BM responds to a particular frequency (characteristic frequency) of sound which they are most sensitive. At the base where the BM is short and tight in construction resonate in response to high-frequency pressure waves (Figure 2.6) to which they are sensitive. On the other hand at the cochlear apex where the BM is relaxed resonate in time

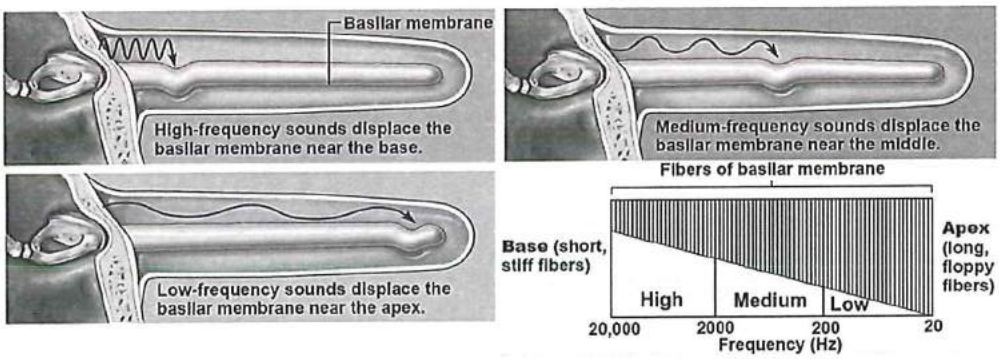

Figure 2.6 Fibre representation with different sound frequencies across the basilar membrane (BM) at different locations. The stiffness of these fibres are tuned for specific regions of BM to vibrate at different frequencies. (*Adapted and re-printed with permission from* [2]).

with lower-frequency waves. As a result, the resonance of the BM mechanically processes the acoustic signals before the signals ever reach the receptors [2]. This behaviour of the BM towards different sound frequencies can be considered as an logarithmic behaviour. This means that each octave is represented by about the same distance on the BM for an uncoiled length of cochlea (approximate 30 mm). This unique material feature of BM enables for translating the sound frequencies with respect to particular sites inside the cochlea. This passive process which contributes to the tonotopic organization of the cochlea can also be observed in dead cochlea [7].

2.2 Understanding types and degrees of hearing loss

Hearing loss is the most common physical disability found in the human beings affecting more than 360 million people (328 million adults and 32 million children's) which is over 5% of the world's population across the globe. In adults hearing loss greater than 40 decibels (dB) in the better hearing ear and 30 dB in children is considered as a disabling hearing loss. Approximately one-third of people over 65 years of age are affected by disabling hearing loss. The prevalence in this age group is greatest in South Asia, Asia Pacific and sub-Saharan Africa [8]. It is estimated that roughly three children per 1000 are born with some kind of hearing loss. Studies have shown that the number is far greater if the children with fluctuating hearing loss (resulting from ear infections such as otitis media, meningitis, rubella), high frequency hearing loss and unilateral hearing loss are included [9,10]. The leading cause for adult hearing loss is age related followed by noise induced hearing loss. Hearing loss makes simple day to day tasks increasingly difficult for e.g. conversations, meetings, phone calls, watching television etc.

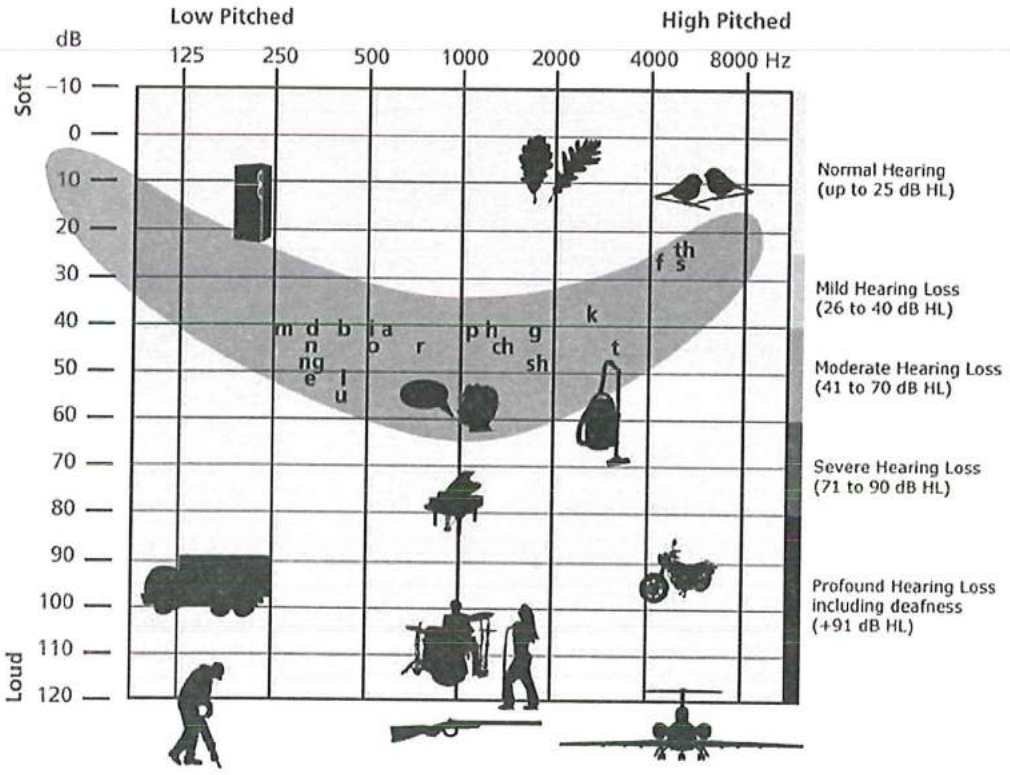

Figure 2.7 A combined audiogram showing different loudness and frequency levels describing the degrees of hearing loss. A "speech banana" is an easy technique to check whether the entire spectrum of speech is still audible and how a person's hearing changes with time. (*Image courtesy: www.phonak.com*).

Normally when describing a hearing loss three aspects are considered: type of hearing loss, degree of hearing loss and configuration of hearing loss. The three types of hearing loss: conductive, sensorineural, and mixed are described as follows:

Conductive hearing loss occurs when sound cannot easily travel through the external ear canal (EAC) to the eardrum and the three tiny bones (ossicles) of the middle ear. This type of hearing loss is caused due to non-functioning EAC or the middle ear thus resulting in an attenuation of the signal arriving at the cochlea, thus making sounds softer and less easy to hear them. This results in the reduction of one of the physical attributes of sound called intensity (loudness), so the energy reaching the inner ear is lower or less intense than that in the original stimulus. Therefore, more energy is required with a conductive hearing loss to hear sound, but once it's loud enough and the mechanical impediment is overcome, the ear works in a normal manner [11]. Generally there are no other extreme consequences to such type of hearing loss. Some of the possible causes for conductive hearing loss are as follows:

- Presence of fluids in the middle ear from colds or allergies.
- Ear infections (otitis media).
- Poor functioning of the Eustachian tube.
- Damage or hole in the ear drum.
- Too much of ear wax (cerumen).
- Foreign external material mitigation in the ear canal.
- Swimmer's ear (external otitis).
- Stiffening of the ossicular chain.
- Malformation of the outer ear, ear canal, or middle ear.

The cause of conductive hearing loss can be identified and treated resulting in a complete or partial improvement in hearing. This type of hearing loss can often be corrected medically by drugs or by surgery. Thereafter hearing aids are effective in correcting the residual hearing loss [11].

Sensorineural hearing loss (SNHL) is the most commonly found permanent type of hearing loss which is caused by damage to, or malfunction of the cochlea or the hearing nerve (neural part) dysfunction leading to a loss of loudness but clarity as well. The malfunction of the cochlea may be due to damage to the organ of Corti, inability of the hair cells to stimulate the nerves of hearing or a metabolic problem in the fluids of the inner ear. The neural or retro-cochlear component can result to a severe damage to the organ of Corti that causes the nerves of hearing to degenerate or it can be an inability of the hearing nerves themselves to convey neurochemical information through the central auditory pathways [11]. This type of hearing loss reduces the ability to hear soft sounds and the sound heard may be unclear or muffled even though the speech is loud enough for normal people. Another common phenomenon for SNHL is the "loudness recruitment" in which the person

experiencing SNHL often perceives high level frequency sounds at the same loudness level as they would have been perceived by a normal listener. In this situation with further increase in the sound level (normally above 90 to 100 dB SPL), the loudness grows more quickly with increased level of stimulation, resulting from the fact that these persons have a reduced dynamic range for a wider range of sound intensities from the surrounding environment [6]. Some of the possible causes for SNHL are listed as below:

- Results due to drugs that are toxic to hearing.
- Hearing loss which runs in the family (genetic or hereditary disorders).
- Aging related hearing loss.
- Head or noise-induced trauma.
- Malformations of the inner ear.
- Tumour in the vicinity of auditory neural structures.
- Overexposure to intense loud noise at concerts, clubs etc.

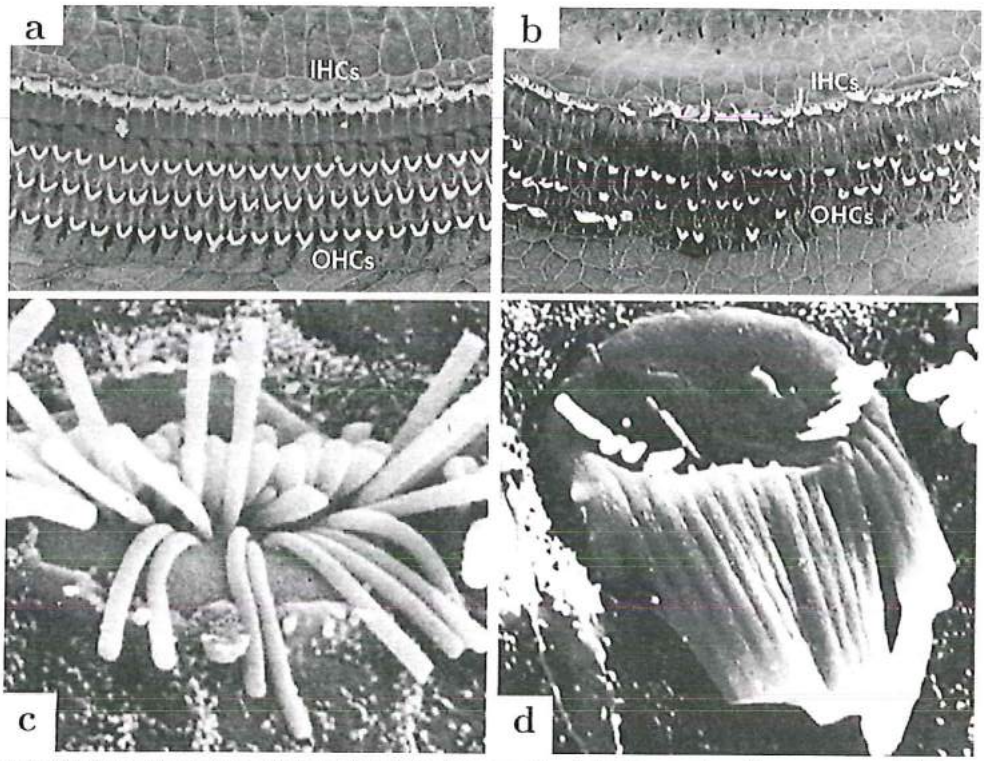

Figure 2.8 Scanning electron micrographs of the (a) normal and (b) damaged cochlear sensory epithelium. In the normal cochlea, the stereocilia of a single row of IHCs and 3 rows of OHCs are present. In the damaged cochlea, hair cells are missing, and stereocilia are abnormal, leading to hearing loss (*Re-printed with permission from E.M.Keithley* [12]). Damage to IHC stereocilia after noise trauma. (c) Floppy stereocilia. (d) Fusion of tallest stereocilia and loss of the shorter ones. (*Adapted and re-printed from* [51]).

From the above mentioned ones the far most prevalent cause of SNHL is the aging of the elements inside the cochlea, and in many of the individuals this is true in the latter half of the life. In the case for mild SNHL it becomes difficult for extracting signals from the noise, as in the "cocktail party effect" [12]. As mentioned earlier SNHL which occurs mainly due to the damage to the internal components of the cochlea. The BM which is responsible for conversion the amplified acoustic signal to electrical neural signal which is done by means of transferring the BM motion with the help of hair cells. This motion transfer which is an combined action of the mechanically active OHC's and the IHC's which convert the stimulus into a neuronal impulse via different synapses with the dendrites of primary auditory neurons. These hair cells and the associated neurons are the most vulnerable components inside the cochlea, the damage to which by the causes mentioned above may lead to permanent hearing loss (Figure 2.8) [12]. The damage to the OHC's and/or IHC's by temporary or permanent structural destructions of the stereocilia or even the hair cells (Figure 2.8) directly affects the chain of acoustic transmission of the cochlea which indirectly affects the total mechanical behaviour response of the BM. In this situation with such non-functioning OHC's and IHC's the BM even though responds to the mechanical membrane, but misses the transduction normally done by hair cells thus leading to an incapable cochlea. Due to this at the end the sound amplification result and the selectivity is reduced for low frequency or soft tones which are hard to detect. Even when speech is loud to hear, it may still be unclear or sound muffled.

Most of the times SNHL cannot be medically or surgically corrected completely. Still in order to assist and solve SNHL to some extent various medical means via drugs or medical assisting devices (middle ear, cochlear implants, hearing aids etc.) help in the hearing process.

Mixed hearing loss is normally observed when a conductive hearing loss occurs in combination with an SNHL. In other words it can be thought of SNHL with a conductive component blanketing completely or a part of the audiometric tested range. Thus, in addition to the irreversible hearing loss caused by an inner ear or auditory nerve disorder, there is also a dysfunction of the middle ear mechanism that makes the hearing worse than the sensorineural loss alone [11].

In such type of hearing loss the conductive component can be medically treated and reversed by the associated hearing loss, but the sensorineural component will most likely be permanent. This permanent loss can be addressed by providing FDA approved auditory prostheses which are available in the market which helps the user in its listening/hearing process but cannot completely fill up or repair the damage caused to the inner important components of the sensory organ (cochlea).

2.3 Hearing loss treatments

As stated earlier that the types of hearing losses mentioned in the earlier sections are often treated with proper drugs or by using medical devices (hearing aids, bone conduction devices, middle ear implants, totally implantable devices, cochlear implants). Some of these devices will be briefly explained in the following sections:

2.3.1 Bone-conduction devices (BCDs) and middle ear implants

BCDs are hearing assisted devices mostly used for conductive type, mixed and single sided hearing losses. BCDs work on the principle of sound conduction by producing vibrations that are produced and transmitted through the skin to the skull bone, and further to the cochlea (the inner ear), bypassing a conductive impairment in the external or middle ear. These BCDs can be non-implantable (conventional BCSs) and semi-implantable, where some part of the devices are implanted. A brief categorization of all the existing BCDs in the market is as shown in Figure 2.9 [13].

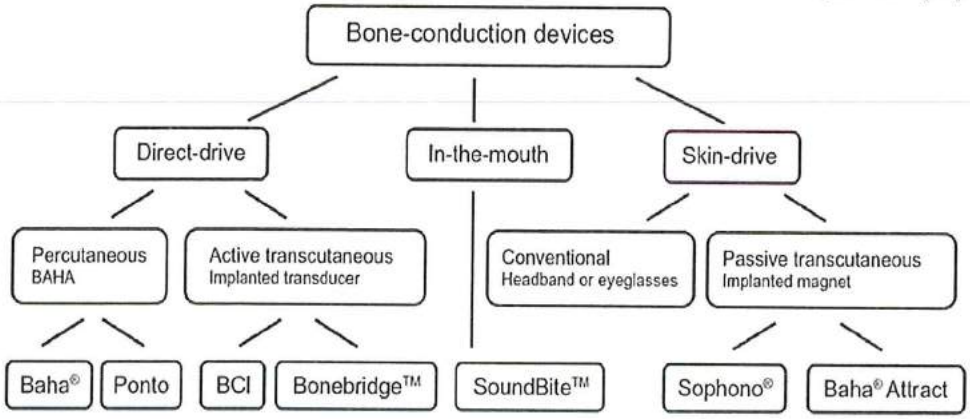

Figure 2.9 Category chart for BCDs. BAHA: Bone-anchored hearing aid, BCI: Bone-conduction implant (*Adapted and re-printed from* [13]).

BCDs can be broadly divided into direct-drive BCDs and skin-drive BCDs. The direct-drive BCDs transfer the sound by vibrations going directly through the skull bone and not via the skin which further can be divided into percutaneous BAHA (Bone-anchored hearing aid) and active transcutaneous devices. On the other hand the skin-drive BCDs do the same procedure but through the skin and then via the bone. These can be similarly divided into conventional and passive transcutaneous BCDs [13]. BAHA is an surgically implanted device which is designed to assist deaf people in their hearing process who encounter with conductive hearing loss, mixed hearing loss or single-sided deafness. The BAHA devices (Baha® BP100 from Cochlear Bone Anchored Solutions AB and Ponto from Oticon Medical) work

basically on the same principle where an external sound processor which includes the microphones along with the necessary electronics. The external environment sound is captured and amplified more effectively than air conduction hearing aids. This amplified sound bypasses the conductive element of the hearing loss by adopting the bony route where the vibrations are delivered directly to the cochlea, with less gain and distortion. This vibration transmission is effectively done via the components (refer Figure 2.10 (b) & (c)) of the device. As per the regulatory directives in the EU and in the USA BAHA devices are regarded as passive devices (Class IIb in EU), whereas a device with implanted transducer (Bonebridge™ from MED-EL Figure 2.11(a)) is regarded as an active device (AIMD in the EU and Class III in USA) [13].

Baha® Attract (Figure 2.10 (a)) is an passive transcutaneous (implanted magnet) skin-drive BCD which consists of a small implant made of titanium which inserted in the bone behind the ear. An implant magnet is attached and is hidden behind the skin which keeps the inner implant in positon. A external sound processor is attached to an external magnet by an appropriate fixation method.

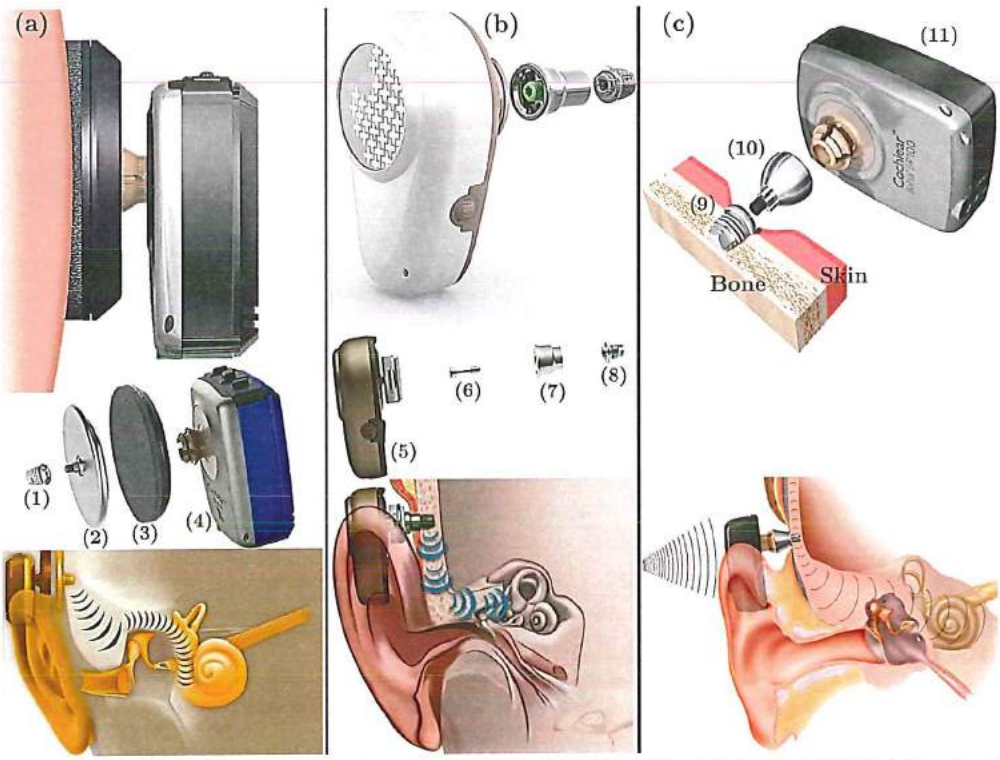

Figure 2.10 (a) Baha®Attract, a passive transcutaneous skin-drive BCD, (1) Implant BI300, (2) Implant BIM400, (3) Magnets, (4) Audio processor; (b and c) Bone-anchored hearing aid, a percutaneous direct-drive BCD; (b) "Ponto" (Oticon Medical, Sweden), (5 and 11) Sound processor with coupling, (6) Screw, (7 and 10) External Abutment, (8 and 9) Titanium implant; (c) Baha® BP100, (*Image courtesy: Oticon Medical and Cochlear Bone Anchored Solutions AB, Sweden* [13,14]).

The external sound is transmitted by means of vibrations from the processor via the magnets to the implant, which then propagates them through the bone to stimulate the inner ear (cochlea) bypassing the outer and the middle ear. To reduce the magnets pressure impact on the skin, for extra comfort the Baha SoftWear™ Pad is attached to the external magnet which comfortably adopts to the shape of the head resulting in even pressure distribution [14].

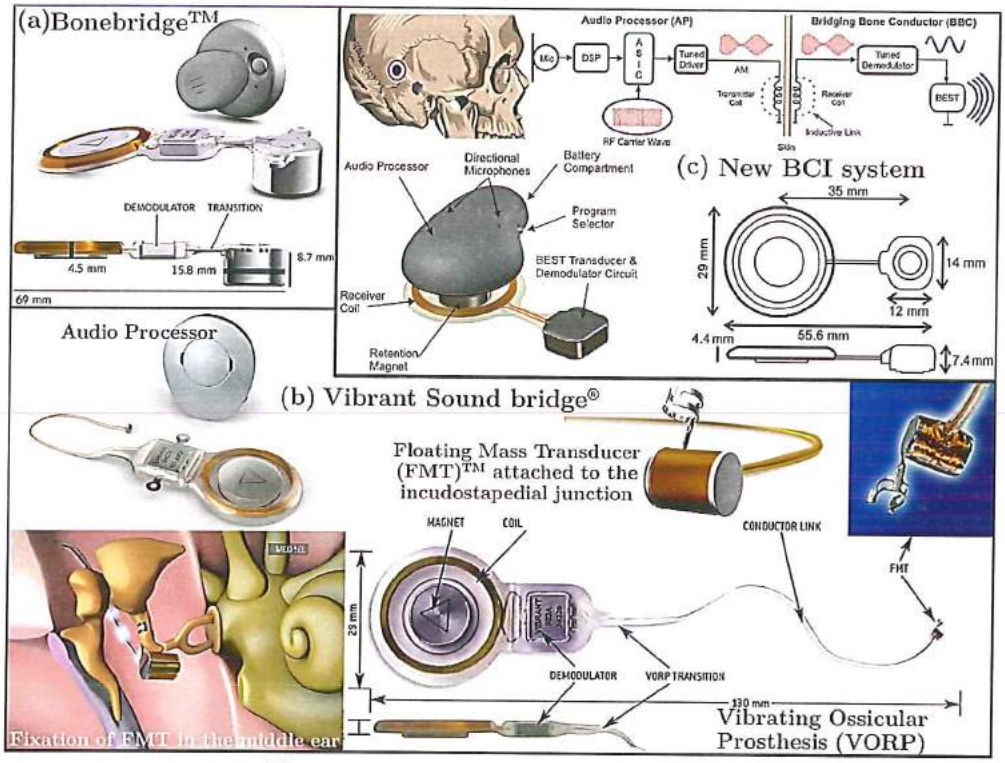

Figure 2.11 (a) Bonebridge™: Direct-drive active transcutaneous BCD; (b) Vibrant Soundbridge® : An ossicular prosthesis as an middle ear implantable hearing system (*Image courtesy, MED-EL corporation; http://www.medel.com/*); (c) New BCI system with only external AP and implanted BBC [17].

Bonebridge™ Figure 2.11 (a) is a direct-drive transcutaneous partially implanted BCD. It consists of an external part (audio processor) and an inner implanted part (bone conduction implant). The processor which contains the microphones, a DSP (digital signal processor), and a battery is normally worn over the skin above the pinna. The implant consists of a receiver coil, an electric demodulator and an active electromagnetic floating mass transducer (FMT). The processed audio signals and the power to drive the FMT in order to vibrate it is done transcutaneously by the processor to the implant via the coils. The FMT (BCI 601) has a diameter of 15.8 mm and a height of 10 mm, 8.7 mm of which is implanted inside the bone by drilling

some space. The weight is approximately 10 grams. The FMT which is placed behind the ear in the mastoid and temporal regions is held by two titanium screws [15]. The vibrations from the FMT are further transferred via the bone pathway to stimulate the inner ear. The main difference between the two BCDs (direct drive: Bonebridge™ and skin-drive: BAHA devices) is the transcutaneous and the percutaneous processor connections, the implant size and the fixation method [15].

Vibrant Soundbridge® (VS) (Figure 2.11 (b)) is a middle ear implant which is used to provide treatment for those deaf patients for whom due to some medical reasons or due to personal dissatisfaction don't use the conventional hearing aids. The VS is a direct-drive middle ear implant which amplifies the mechanical vibrations of the middle ear ossicular chain, thus resulting to provide amplified signals to the cochlea. This is done with the help of a floating mass transducer (FMT) which is surgically fixed to the ossicular chain or sometimes directly onto the round window of the cochlea. This FMT which is driven and is the part of the VORP (Vibrating Ossicular Prosthesis) consists of an internal coil, the magnet for the audio processor and the conductor link. This VORP is the implanted part of the device. This device makes use of the mechanical energy instead of the acoustic signals in order to deliver more accurate and high quality signal to cochlea. The advantage of such direct-driven implants in comparison to conventional hearing aids is that it can provide the acoustic signals without any feedback or occlusion [16]. A new BCI system is researched which consists of an external audio processor (AP) and an implanted unit called the bridging bone conductor (BBC) (Figure 2.11 (c)) [17].

These middle ear implants which are nothing but mechanical or acoustical amplifiers are intended for severe–to–profound SNHL hearing losses. Even though having advantages over conventional hearing aids, these devices are still limited in transmissibility since it needs to travel through the malfunctioned inner ear. Also due to only audible improvement by these devices, the frequency selection which is naturally done by cochlea is missing, thus resulting in reduced speech intelligibility. In this situation for sever to profound hearing losses where the inner ear is incapable to perform its intended functionality, electrical stimulation of the auditory nerve is the only last choice. This is been done for more than 20 years by FDA approved devices called as Cochlear Implants (CI's).

2.4 Cochlear Implants (CI's)

CI's are implantable auditory prosthetic devices designed to regain part of the hearing to adults and children experiencing severe–to–profound SNHL by converting the acoustic input signal into an electrical pattern that is interpreted as sound. A CI does this process by direct electrical stimulation of the auditory nerve. It consists of internal components that are surgically placed and external components that require

fitting and programming. CI's till date are considered the only available successful medical treatment which helps people for severe–to–profound type of hearing loss.

2.4.1 Hearing sensations by electrical stimulation (History)

Regeneration of hearing sensations by electrical stimulation of the auditory nerve fibre can be traced back to 1790 by the inventor of the battery, an Italian scientist Alessandro Volta. With the help of a 50 V battery he demonstrated that by electrical stimulation process a human being can induce different types of sensations such as touch, audio and vision [18]. In his experimentation he inserted a pair of metal rods in his ears which are connected by a battery and expressed his sensations as [19]:

....at this moment when the circuit was completed, I received a shock in the head and after some moments I began to hear a sound or rather a noise in the ears, which I cannot define well: it was some crackling with shocks, as of some paste or tenacious matter was boiling....This disagreeable sensation, which I believed might be dangerous because of the shock in the brain, prevented me from repeating this experiment....

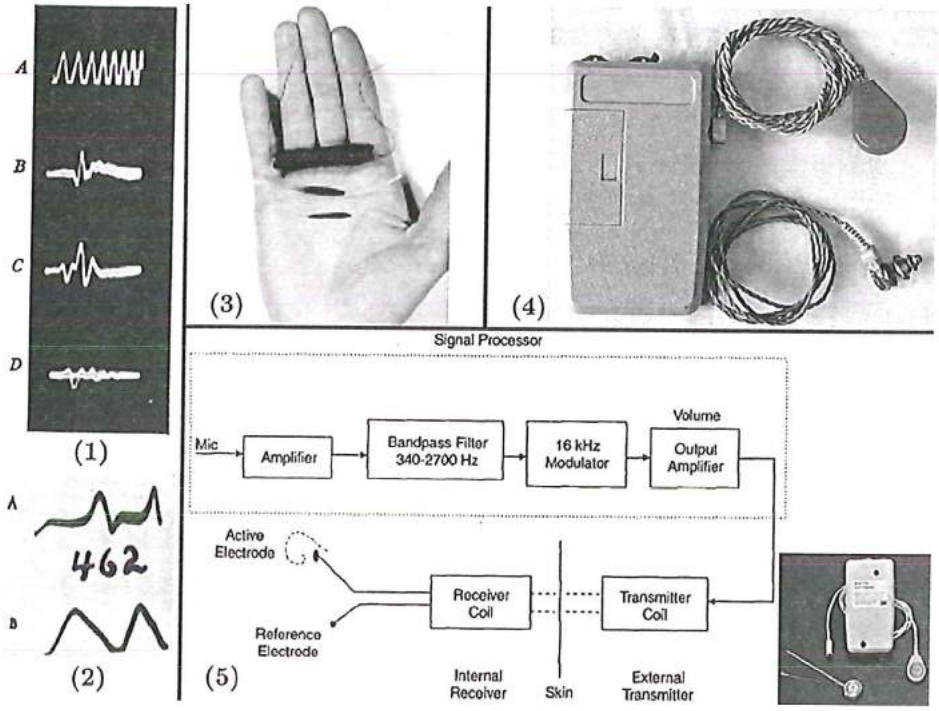

Figure 2.12 (1) Oscillogram of nerve impulses and cochlear response. A. 1000 Hz wave on time scale, B. Nerve impulse from 8th nerve in response to single clicks. C. Response to single clicks as recorded from round window, D. The sane, expect for increase in stimulus strength; (2) Similar oscillogram response to tone of 462 Hz.; (3) First handmade CI system covered in Araldite [19,23]; (4) The House 3M single-channel CI body worn speech processor unit with transmitter coil; (5) Signal processing diagram of the House 3M single-channel CI system (*Image courtesy, http://www.hearingaidmuseum.com/*).

Year	Description of the incident
1790	Alessandro Volta used 50V battery to stimulate his inner ear with an electrical current [18].
1855	Duchenne de Boulonge used alternating current to stimulate his ear.
1935	Hallowell Davis recorded nerve impulses and cochlear responses of animals via oscillograms (Figure 2.12 [20]). Andreev *et al.* demonstrated the first direct evidence of electrical stimulation of the auditory nerve giving hearing sensations in a deaf patient whose middle and inner ears were damaged [21].
1940	Jones *et al.* explained that the mechanisms inducing sound effects are not only due to direct stimulation of auditory nerve but was said that the cochlear microphonic was responsible for the pure tones [22].
1950	Lundberg did the first recorded attempts to stimulate the auditory nerve by sinusoidal current during a neurosurgical operation.
1956	Jack Urban and Dr. W. House designed a workable/wearable implant.
1957	Djourno and Eyries used a handmade receiver made of insulated silver wire around an iron core (approx. 2000 turns) covered in Araldite. The electrode contacts were made of stainless steel, soldered to silver coils (Figure 2.12) [23].
1964 and 1965	Simmons *et al.* implanted a 6-electrode array directly into the modiolus of a volunteer suffering from right ear deafness and progressive hearing loss in the left ear [24].
1972	Dr. William House builds the first wearable signal processor.
1977	Adam Kissiah proposed the fundamental design aspects of a cochlear implant via a patent (US patent 4,063,048) [25].
1978	Dr. Graeme Clark and Dr. Brian Pyman operates the first multi-channel Cochlear Implant [26].
1980	US Food and Drug Administration (FDA) started regulations of CI [27].
1984	The first FDA approved commercial device for adults: *House/3M.*
1985	Cochlear Corp. Nucleus® 1 system approved by USFDA [28].
1989	MED-EL introduced their Comfort CI System [29].
1990	CI's for children above 2 years old approved by FDA.
1996	Advanced Bionics Corp. implant approved by USFDA [30].
2000	Approval of CI implants by FDA for infants above 12 months of age.

Table 1. A brief timeline highlighting the main inventions and the incidents that took place towards the developmet of Cochlear Implants *(Adapted and reprinted with additions from* [31]).

After this experimentation Duchenne de Boulogne, a French neurologist who

hearing. In his experiments he used an alternating current to stimulate his hearing and described what he heard, as a sound like an insect trapped between a glass pane and a curtain [19]. After this in the 1930s many research groups explored the principle of the electrical stimulation of the ear to generate acoustic effects. All these studies where on similar stimulation reports and its phenomenon involved towards the hearing mechanism (Figure 2.12 (1 and 2)) [20]. A brief summary of the number of bold and visionary individual findings which believed that this principle will lead to restoration of hearing for the deaf ones is listed in the Table 1 [31]. Figure 2.13 shows a CI system devloped by the team of University of California at San Francisco. In today's compariosn they were large and cumbersome, but these where the first of its kind devices which were possibly been used outside the laboratory by the patients.

CI's journey from more than 30 years until now demonstrates that these FDA

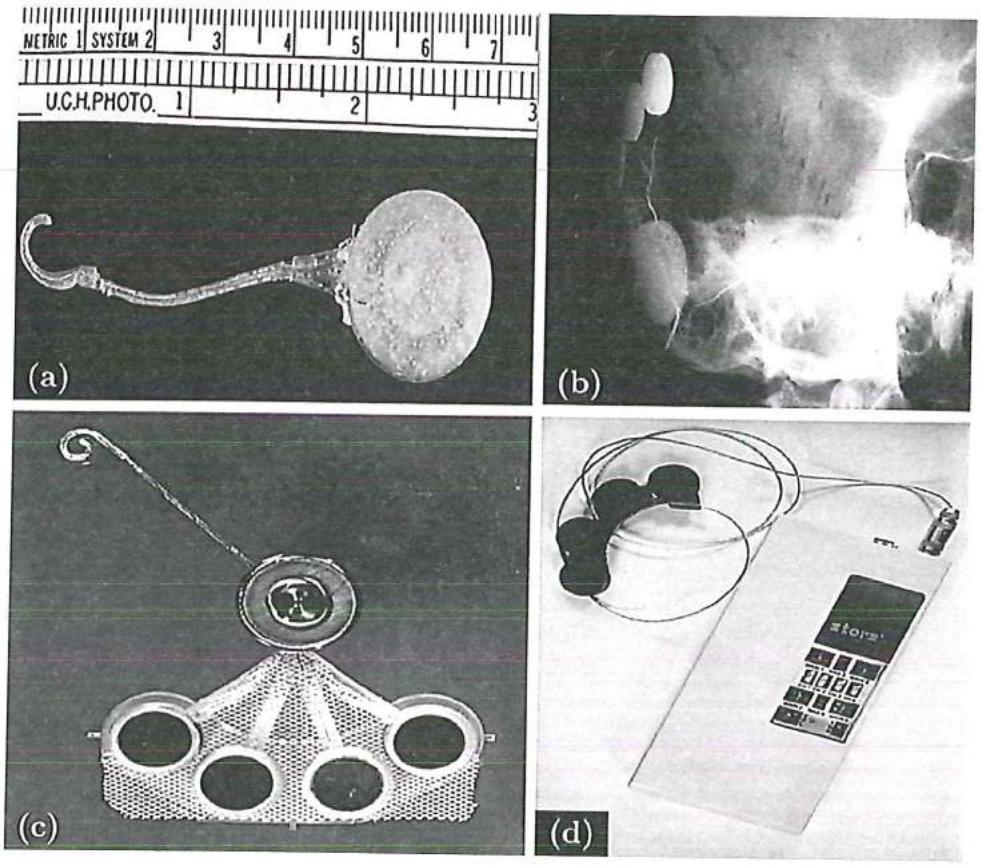

Figure 2.13 The CI designed by Michelson in 1978. (a). The implant of the CI measuring 70 mm in length; (b) Radiographic image of a skull with an implant in place; (c) Internal implant of CI; (d) The external worn part of the CI *(Image courtesy: Adapted from* [52]).

approved medical implants which has become a routine intervention is the only available solution often used to address people with severe–to–profound hearing losses. The modern CI which has a multichannel miniature surgically implanted electrode arrays which convey the external auditory information to the auditory nerve by direct electrical stimulation. In doing so it bypasses the EAC, middle ear and also up to some extent the damaged hair cells inside the cochlea. Moreover the CI electrode array still requires a certain population of auditory nerve fibres or endings in order to convey the acoustic signals thus providing useful hearing sensations to the end user.

2.4.2 Basic structure, components and its functions

The current state-of-art of a CI consists of externally worn (behind the ear) part (Figure 2.14 (a)) and an surgically implanted internal part (Figure 2.14 (b)).

1) External part containing the following items:
   - Microphone/s.
   - Speech processor (encoding).
   - RF (radio frequency) transmitter coil.
   - Extra peripherals for phone, Bluetooth and other device connectivity.

2) Internal part containing the following items:
   - RF receiver.
   - Signal decoding circuitry.
   - Stimulator and its subsequent circuitry.
   - Electric stimulations carried via intracochlear electrode array.

A complete implant with its components is depicted in Figure 2.14. The external part which contains the microphone captures, senses and converts the external sound from the environment into an acoustic signal. This signal will be processed by the speech processor Figure 2.14 (a). This processor performs the function of converting the analogue audio signal from the microphone into different digital electrical signals. Basically a processor consists of many filter banks. These filter banks use band pass filters to extract a range of frequencies corresponding to an electrode. Generally, one can find at least one filter bank for one electrode. The speech processor further conveys the signal through to the RF transmitting coil. The RF transmitter transmits the encoded signal to the internal RF receiver of the implant which is nothing but a receiver RF coil along with an adjacent stimulator circuit. The whole assembly is normally referred to as receiver-stimulator internal implant.

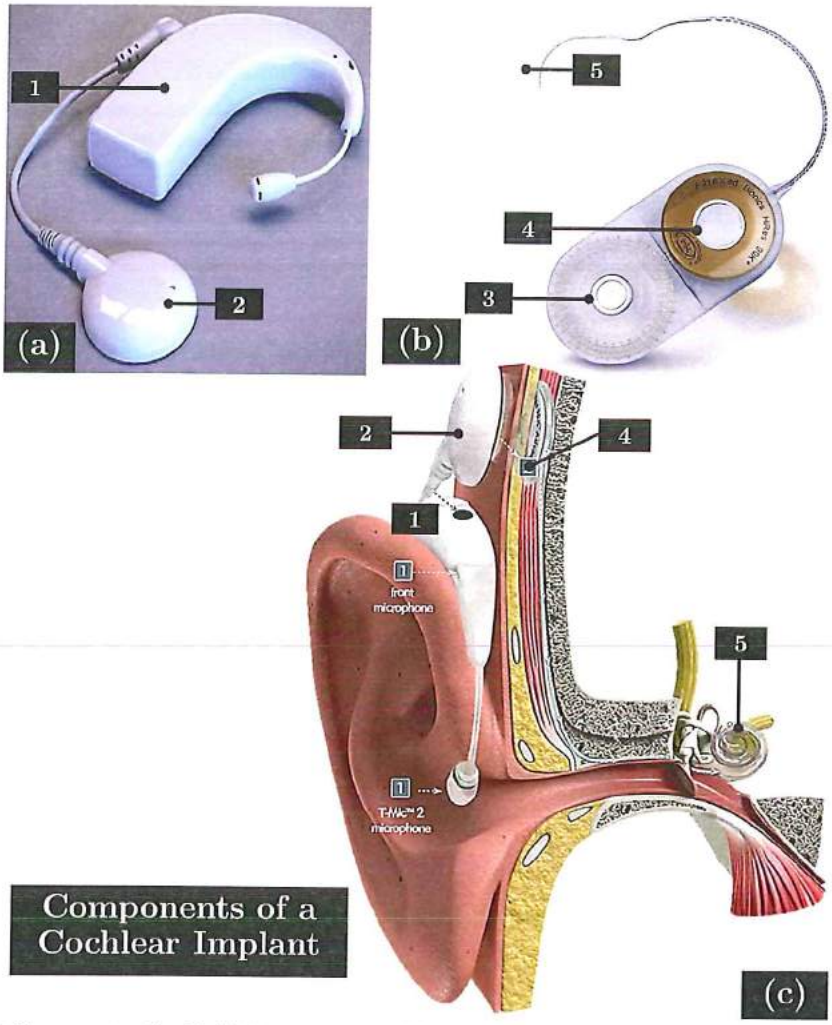

Figure 2.14 Components of a CI (a) External part of the device containing 1. Microphone and a Speech processor, 2. RF transmitter coil; (b) Internal receiver-stimulator with 3. RF receiver coil, 4. Stimulator and 5. Electrode array; (c) CI after implantation in the ear. (*Image courtesy, from Advanced Bionics Corporation* [30].

This part is surgically placed inside the human skull behind the ear and underneath the skin. The receiver decodes the signal received from the signal processor into an electrical stimulation pattern which further travels to the electrode array. This electrode array (Figure 2.14 (b)) is normally positioned in the scala tympani with the help of surgery (cochleostomy) and an insertion through the round window. This electrode array which contains electrode contacts (16 stimulation sites depending upon manufacturer) sites which run along the length of the cochlea (approximate two turns). This electrode array transmit acoustic information by

direct electrical stimulation of the spiral ganglion cells in the modiolus. This signal is further transmitted via the auditory brainstem to the auditory cortex of the brain where sound is perceived.

Currently there are four major CI manufacturers available in the market (Figure 2.15); An Australian based Cochlear Limited, Advanced Bionics in California under Sonova Holdings AG, Switzerland, MED-EL from Austria and Neurelec SA in France which was recently (April, 2013) been acquired by Oticon Medical AB, Sweden (A William Demant Company). A detailed comparison document of these four CI manufacturers can be found on http://cochlearimplanthelp.com/ [32].

Figure 2.15 The present available range of CI speech processors from 4 manufacturers: from left to right: Advanced Bionics – Neptune and Naida CIQ70; Cochlear Corporation Ltd., – Nucleus® 5 Sound Processor; MED-EL – Sonnet Audio Processor; Neurelec (Oticon Medical in 2013) – Saphyr processor.

2.4.3 Signal processing

The natural tonotopical behaviour of the human ear allows us to hear different frequency bands of a sound. When natural hearing is replaced by CI's, it with the help of multichannel electrode array along with its subsequent stimulation sites tries to mimic this natural hearing process. So in this it is very important that the electrode array must be able to allocate the complex input acoustic spectrum over its different channels. This is done in combination with the help of the circuitry in the audio processor as well as the receiver-stimulator internal implant. A typical architecture of the current generation CI's with its different blocks is as shown in Figure 2.16 [33–35]. We will step by step briefly go over each block as follows:

Microphone pre amplifier / Audio Front End (AFE): This unit is the first block which is responsible for sensing the acoustic signals form the environment and converting them into an electrical domain. It is the sensor part of the whole system. This electrical input with a particular dynamic range is fed to an **automatic-gain-control circuit (Broadband AGC)**. AGC compresses this input dynamic range to

a narrower (50 to 60 dB for CI's) internal dynamic range (IDR) at which each of the multichannel processor operate [34]. AGC is necessary for CI's in order to protect the ears from overload. When the incoming signal is too high, it will damage the hearing even further than it already is. Therefore, an AGC is used. It is a device which can adapt its gain to the incoming signal. Thus in this way an amplified signal always has the same output signal level or at least over a certain input range it will be [36]. The signal from the AGC is then fed to different channels, each representing a certain frequency position inside the cochlea. In these channels the signal will be processed to a signal which is suitable for the electrodes. Each channel has its own processing blocks which contains of Bandpass filters, Envelope detectors, Amplitude compressors (Logarithmic dual-slope Analog to Digital: A-to-D converters) and Pulse modulators. The **Bandpass** filters takes care of the selection of the proper frequency for the channel. By filtering out the proper frequency, the electrode corresponding to a particular channel will only be stimulated inside the cochlea when there is a signal been generated for that certain frequency [37].

Envelope detectors are responsible for determining proper power estimation for each channel so they are present in per channel pathway. Mostly it consists of a trans-conducting rectifier, followed by a current-mode peak detector. This together will take care of determining the dc-component of the signal [34]. This DC signal is further fed to the **A-to-D converter** which are logarithmic in nature due the fact

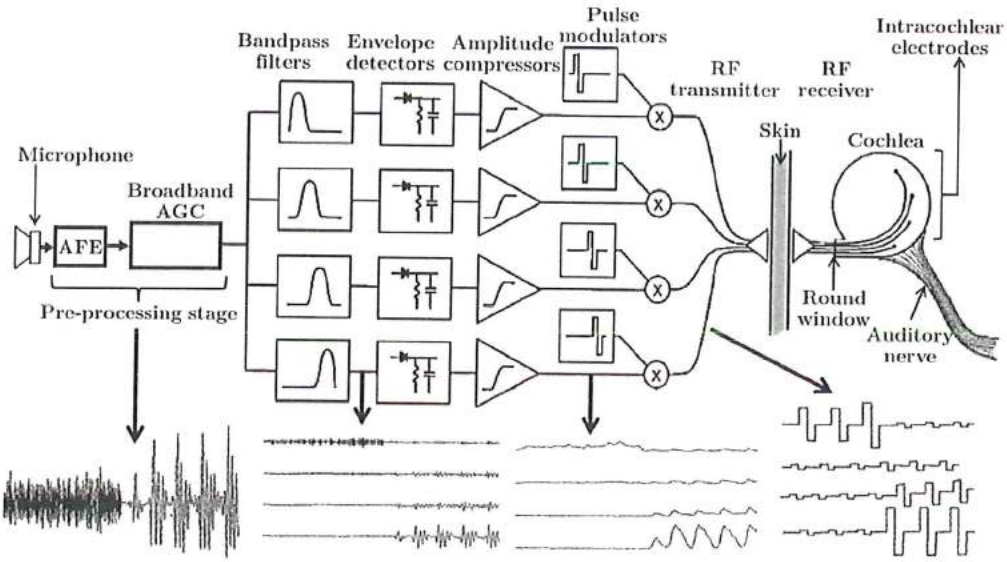

Figure 2.16 An overall architecture of the signal processing for an analog 4 channel CI speech processor; AFE: Audio Front End, AGC: Automatic gain-control. (*Image adapted and revised from* [33–35]).

that the human hearing process also resembles logarithmic behaviour. A normal human being is able to distinguish between 8-50 electrode stimulation steps per

electrode [34,38]. With a 5-bit A-to-D converter 50 steps can be achieved. The A-to-D converter will convert the DC signal of the envelope detector to a certain digital level. These pulse train signals of each channel are modulated with compressed envelope by **pulse modulators.** These modulated signals are transported through the RF transmitter coil (coupled to pulse modulators) to the internal receiver via a skin layer which in turn are further applied with an appropriate voltage to the electrode array contact sites to obtain the desired current levels.

2.5 Fully implantable middle ear auditory prosthesis

Fully implantable devices are alternatives which are developed in order to provide greater comfort to the patients with conductive type of hearing loss bypassing the EAC. In comparison to traditional HA the middle ear devices (MEDs) avoids the limitation of sound transmission by an external microphone, as it resides completely underneath the skin behind the ear [39]. Currently there are two fully implantable MEDs (refer Figure 2.17) which are available in the market. The Carina® implant system from Otologics LLC of Boulder, Colorado, USA and the Esteem® device from Envoy Medical Corporation, Saint Paul, Minnesota, USA. We will be briefly discussing these two devices in this section.

The Otologics MET (Middle Ear Transducer) fully implantable Ossicular stimulator system mainly consists of three primary components; the implant, the battery, its connector, battery charger and a remote control (Figure 2.17 (I)). The implant component of the MET which is under the skin works in conjunction with a charger and a remote control. It consists of a signal processing electronic capsule, a pendant microphone system, the internal battery and an electromechanical transducer. In specific, the electronic package consists of two digital signal processors, control circuitry, battery, radio frequency coil and a magnet [40]. The MET transducer is basically derived from the original transducer which was first investigated by Fredrcikson *et al.* [41]. The basic working of the MET starts with the sound been picked up from the external environment through the skin by an extra sensitive pendant microphone. This is converted into an electrical signal, digitally processed according to the patient's hearing requirements, and conducted down a lead and into the transducer that is mounted in a laser-drilled hole in the body of the incus. The transducer translates the electrical signals into a mechanical motion that directly stimulates the ossicles and enables the wearer to perceive sound. A remote control allows the wearer to turn the implant on and off and to adjust the volume. To use the remote control, the wearer simply holds the remote against the skin over the implant magnet. The charger system consists of the base station, charging coil, and a charger body [40]. Usually the battery charger is plugged into an outlet and the battery fits inside the charger; once charged, the battery may be used to charge

the implant. The device for its functioning requires programming to suit individual needs which is similar to the programming of the traditional digital hearing aids. In addition, the Otologics Programming System provides the ability for extensive testing and diagnostics of the MET Fully Implantable Ossicular Stimulator [42].

Another company St. Croix Medical, Inc. (currently Envoy Medical Corporation) has done a quite extensive research on a semi-implantable hearing device which

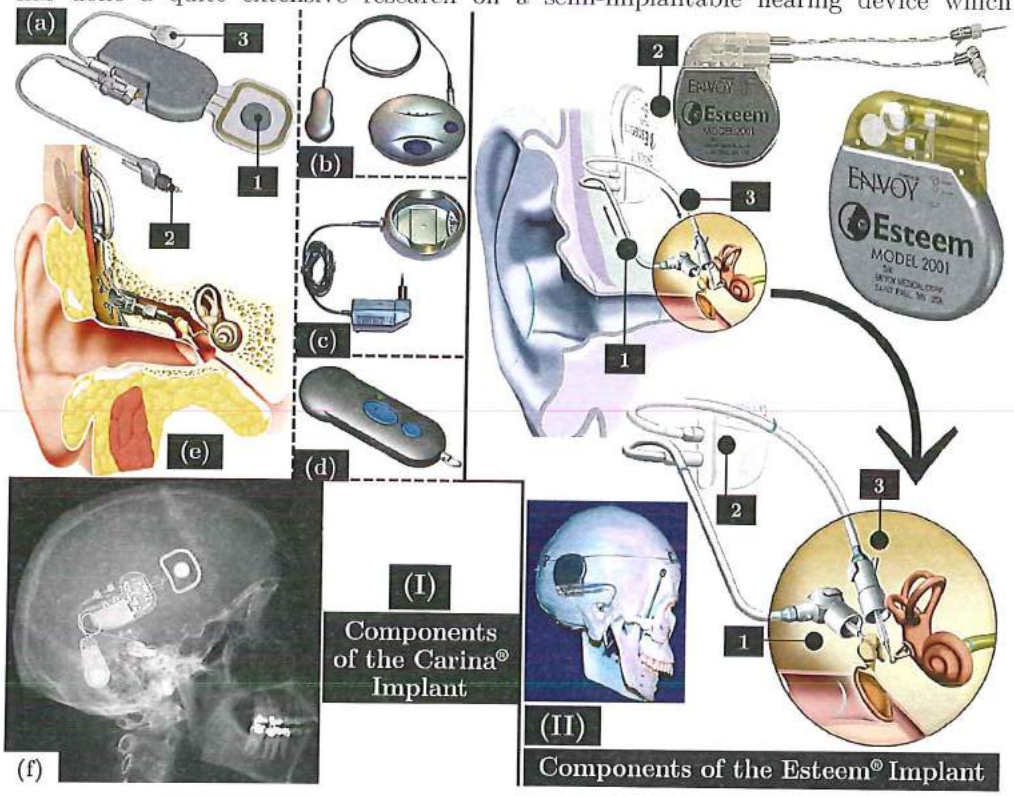

Figure 2.17 (I) The Carina® Implant from Otologics LLC, Colorado, USA: (a) The implant: 1. Receiver coil, 2. Transducer, 3. Microphone, (b) Battery and connector, (c) Battery charger, (d) Remote control, (e) Otologics Middle Ear Transducer TM (METTM) or fully implantable middle hearing device with (f) an MRI scan showing its position; (*Image courtesy* [42] *and http://www.audiologyonline.com/*); (II) The Esteem® device from Envoy Medical Corporation, USA: 1. Piezoelectric sensor and transducer, 2. Sound processor, 3. Driver (piezoelectric transducer) coupled to stapes footplate (*Image courtesy from http://esteemhearing.com/, http://www.audiologyonline.com/ and* [44]).

resulted in a totally implantable piezoelectric device commonly referred to as the envoy® totally implantable hearing system [43]. In 2011 this system did Phase 2 trials as per FDA regulations and has conditionally approved (PMA P090018) totally implantable hearing system for treatment of moderate to severe SNHL. The whole Envoy Esteem system (Figure 2.17 (II)) consists of three implantable components,

external testing/programming instruments, and system accessories. The basic working principle lies with the Piezoelectric transducers which picks/senses the incoming acoustic signals from the tympanic membrane (TM) which in turn drives the stapes [44]. The implantable components are 2 piezoelectric transducers acting as a sensor (Figure 2.17 (II) 1) and a driver (Figure 2.17 (II) 3), and a hermetically sealed titanium dual-channel sound processor (Figure 2.17 (II) 2) (SP). The SP is implanted in the temporal bone similarly as the CI. The SP which receives electrical signals from the sensor, modifies to desired settings and in turn vibrates the stapes by an appropriate signal. A piezoelectric sensor which is interfaced with the incus senses the incoming sound vibrations from the TM. These vibrations which are converted to an electric signal are send to SP which are further fed to another piezoelectric driver where it transforms electric signals back to mechanical vibrations. These vibrations at the stapes induce mechanical waves inside the perilymph of the scala tympani. In the trails demonstrated by Eric M. Kraus [44] in their publication mentions the driver responses to be linear up to 2 V root mean square (Vrms) with harmonic distortion of –40 dB or better at all frequencies greater than 250 Hz. Low distortion permits increasing gain without compromising audibility. The device is capable of generating +55 dB of acoustic gain [44]. The drawback of the Envoy system is that it requires removal of the incus bone. The piezoelectric transducers become the link between the malleus and stapes. Envoy Medical Corporation claims that it is possible to surgically restore the ossicular function of the middle ear by reattachment of the incus bone with a prosthesis. Operationally, the Envoy implant incorporates the eardrum as the microphone, and the malleus detects the mechanical signal. The device does, however, have limited output capabilities that restrict its implantation to patients with mild to moderate hearing loss [40].

2.6 Conclusions

The human ear is responsive and allows a remarkable experience of hearing to a normal human being. Despite of a certain percentage of population partially or totally losing their capability of hearing, due to the continuous efforts, inventions and research being done, brings us one step closer to restore the natural hearing capability. This continuous efforts and will be carried out in future by providing the necessary solutions to the society to help the affected people to restore their hearing process. This chapter which mentions about the totally implantable devices have a promising future which still needs to conquer the hurdles and the technological challenges to provide hearing mechanisms for better living.

2.7 References

1. Torta; Tortora, G. J.; Derrickson, B. H. *Principles of Anatomy and Physiology*; John Wiley & Sons, Incorporated, 2011.

2. Marieb, E. N. *Human Anatomy and Physiology Plus a Brief Atlas of the Human Body Plus MasteringA&P with Pearson EText*; Benjamin-Cummings Publishing Company, 2012.

3. Frijns, J. H. M. *Personal communications from LUMC, Leiden.*; 2015.

4. Dallos, P. The active cochlea. *J. Neurosci.* **1992**, *12*, 4575–4585.

5. Nordang, L.; Cestreicher, E.; Arnold, W.; Anniko, M. Glutamate is the afferent neurotransmitter in the human cochlea. *Acta Otolaryngol.* **2000**, *120*, 359–62.

6. Moore, B. C. J. *Cochlear Hearing Loss: Physiological, Psychological and Technical Issues*; 2007.

7. Johnstone, B. M.; Patuzzi, R.; Yates, G. K. Basilar membrane measurements and the travelling wave. *Hear. Res.* **1986**, *22*, 147–153.

8. World Health Organization Deafness and hearing loss http://www.who.int/mediacentre/factsheets/fs300/en/ (accessed May 30, 2015).

9. Wayner, D. S. *Phonak A.G. , Switzerland.* 2009, pp. 1–20.

10. Vohr, B. Overview: Infants and children with hearing loss-part I. *Ment. Retard. Dev. Disabil. Res. Rev.* **2003**, *9*, 62–4.

11. Phonak Types of hearing loss http://www.phonak.com/ (accessed May 30, 2015).

12. Ryan, A. F. Protection of auditory receptors and neurons: Evidence for interactive damage. *Proc. Natl. Acad. Sci.* **2000**, *97*, 6939–6940.

13. Reinfeldt, S.; Håkansson, B.; Taghavi, H.; Eeg-Olofsson, M. New developments in bone-conduction hearing implants : a review. *Med. Devices Evid. Res.* **2015**, *8*, 79–93.

14. Cochlear Baha® 4 attract system http://www.cochlear.com/.

15. MED-EL Bonebridge http://www.medel.com/int/bonebridge/.

16. MED-EL Vibrant Soundbridge® http://www.medel.com/int/vibrant-soundbridge.

17. Taghavi, H.; Håkansson, B.; Reinfeldt, S.; Eeg-Olofsson, M.; Jansson, K.-J. F.; Håkansson, E.; Nasri, B. Technical design of a new bone conduction implant (BCI) system. *Int. J. Audiol.*

2015, 1–9.

18. Volta, A. On the Electricity Excited by the Mere Contact of Conducting Substances of Different Kinds. *Abstr. Pap. Print. Philos. Trans. R. Soc. London* **1800**, *1*, 27–29.

19. Briaire, J. J.; LUMC Cochlear implants from model to patients, Faculty of Medicine, Leiden University Medical Center (LUMC), Leiden University, 2008.

20. Davis, H. The Electrical Phenomena of the Cochlea and the Auditory Nerve. *J. Acoust. Soc. Am.* **1935**, *6*.

21. Andreev, A. M.; Gersuni, G. V; Volokhov, A. A. On the electrical excitability of the human ear: On the effect of alternating currents on the affected auditory apparatus. *J Physiol USSR* **1935**, *18*, 250–265.

22. Jones, R. C.; Stevens, S. S.; Lurie, M. H. Three Mechanisms of Hearing by Electrical Stimulation. *J. Acoust. Soc. Am.* **1940**, *12*.

23. Djourno, A.; Eyries, C. Auditory prosthesis by means of a distant electrical stimulation of the sensory nerve with the use of an indwelt coiling. *Presse Med.* **1957**, *65*, 1417.

24. Simmons, F. B.; Epley, J. M.; Lummis, R. C.; Guttman, N.; Frishkopf, L. S.; Harmon, L. D.; Zwicker, E. Auditroy nerve: Electrical Stimualtion in man. *Science* **1965**, *148*, 104–6.

25. Kissiah, A. M. Implantable electronic hearing aid 1977.

26. Clark, G. M.; Pyman, B. C.; Bailey, Q. R. The Surgery for multiple-electrode cochlear implantations. *J. Laryngol. Otol.* **1979**, *93*, 215–223.

27. FDA US Food and Drug Administration (FDA) http://www.fda.gov/.

28. Cochlear America Corporation http://www.cochlear.com/wps/wcm/connect/us/home.

29. MED-EL Corporation http://www.medel.com/nl/history/.

30. Advanced Bionics Corporation http://www.advancedbionics.com/com/en/home.html.

31. Moctezuma, A.; Tu, J. An Overview of Cochlear Implant Systems. *BIOE 414, Spring 2011, Univ. Illinois, Urbana-Champaign* 2011, 1–20.

32. Holding, W. D. *Cochlear Implant Comparison Chart*; 2013.

33. Rubinstein, J. T. How cochlear implants encode speech. *Curr. Opin. Otolaryngol. Head Neck Surg.* **2004**, *12*, 444–448.

34. Sarpeshkar, R.; Salthouse, C.; Sit, J. J.; Baker, M. W.; Zhak, S. M.; Lu, T. K. T.; Turicchia, L.; Balster, S. An ultra-low-power programmable analog bionic ear processor. *IEEE Trans. Biomed. Eng.* **2005**, *52*, 711–727.

35. Loizou, P. C. Mimicking the human ear. *Signal Process. Mag. IEEE* 1998, *15*, 101–130.

36. Zeng, F.-G.; Grant, G.; Niparko, J.; Galvin, J.; Shannon, R.; Opie, J.; Segel, P. Speech dynamic range and its effect on cochlear implant performance. *J. Acoust. Soc. Am.* **2002**, *111*, 377–86.

37. Salthouse, C. D.; Sarpeshkar, R. A practical micropower programmable bandpass filter for use in bionic ears. *Solid-State Circuits, IEEE J.* **2003**, *38*, 63–70.

38. Zeng, F.-G.; Shannon, R. V Psychophysical laws revealed by electric hearing. *Neuroreport* **1999**, *10*.

39. Pulcherio, J. O. B.; Bittencourt, A. G.; Burke, P. R.; Monsanto, R. D. C.; de Brito, R.; Tsuji, R. K.; Bento, R. F. Carina® and Esteem®: A Systematic Review of Fully Implantable Hearing Devices. *PLoS One* **2014**, *9*, 1–8.

40. Traynor, R. M.; Fredrickson, J. M. The Future is Here: The Otologics Fully Implantable Hearing System http://www.audiologyonline.com/articles/.

41. Bankaitis, A. U.; Fredrickson, J. M. Otologics Middle Ear Transducer™ (MET™) Implantable Hearing Device: Rationale, Technology, and Design Strategies. *Trends Amplif.* **2002**, *6*, 53–60.

42. Kasic, B. J. F.; Franklin, A. W.; Traynor, R. M. The future of implantable hearing devices: The Otologics fully implantable hearing system. *Europe* **2008**, *61*, 32–33.

43. Kroll, K.; Grant, I. L.; Javel, E. The envoy® totally implantable hearing system, st. Croix medical. *Trends Amplif.* **2002**, *6*, 73–80.

44. Kraus, E. M.; Shohet, J. A.; Catalano, P. J. Envoy Esteem Totally Implantable Hearing System: phase 2 trial, 1-year hearing results. *Otolaryngol. Head. Neck Surg.* **2011**, *145*, 100–9.

45. Tortora, G. J.; Derrickson, B. H. *Principles of Anatomy and Physiology*; 13th Editi.; 2012.

46. Strauss, W. *Digital signal processing*; 2000; Vol. 17.

47. Wagner, R. C. Ear Ultrastructure: Microscopic Anatomy http://www.udel.edu/biology/Wags/histopage/empage/ee/ee.htm (accessed May 20, 2008).

48. Devarajan, K.; Staecker, H.; Detamore, M. S. A review of gene delivery and stem cell based therapies for regenerating inner ear hair cells. *J. Funct. Biomater.* **2011**, *2*, 249–70.

49. Steel, K. P. Human Genetics: Progress in Progressive Hearing Loss. *Science (Vol: 279).* **1998**, *279*, 1870–1871.

50. Iberri, D. Action Potential
http://upload.wikimedia.org/wikipedia/commons/thumb/4/4a/Action_potential.svg/491px-Action_potential.svg.png (accessed May 30, 2015).

51. Slepecky, N. Overview of mechanical damage to the inner ear: noise as a tool to probe cochlear function. *Hear. Res.* **1986**, *22*, 307–321.

52. Eshraghi, A. A.; Nazarian, R.; Telischi, F. F.; Rajguru, S. M.; Truy, E.; Gupta, C. The cochlear implant: historical aspects and future prospects. *Anat. Rec. (Hoboken).* **2012**, *295*, 1967–80.

Chapter 3

Manufacturing technologies

For a successful technology, reality must take precedence over public relations, for nature cannot be fooled.
Richard P. Feynman (Theoretical Physicist)

The traditional manufacturing techniques for flexible Cochlear Implant electrode arrays do not satisfy the increasing demands for improved sound quality and functionality, thus keeping room for improvements, especially for patients at the low end of the performance spectrum. MEMS based manufacturing techniques are one of the promising technologies which makes step to solve the manufacturing hurdles in CI development process and plays a major role in improving the overall functionality of the device. In this chapter a technical overview from the traditional manufacturing of the CI electrode array, to the latest MEMS based manufacturing (microfabrication) technologies used nowadays will be mentioned. All the basic micromachining processes such as photolithography, coating, deposition and growth of thin films, etching etc. will be discussed in detail. This technological overview will sketch the different possibilities which forms the basis to solve the manufacturing technological hurdles coming across in the current manufacturing of the CI electrode array.

3 Manufacturing technologies

3.1 Introduction and development history

The CI electrode arrays provides an efficient interface between the electrical signal of sound and the auditory nervous system. In 1970's multiple-electrode arrays showed more potential than the single-electrode because of their ability to reproduce the coding frequency at respective positions [1]. In 1978, Mercer and White [2] designed the first robust eight-contact monolithic electrode arrays with metallic substrates and test them out into the auditory nerves of anesthetized cats. Initially these arrays were designed as gold-on-silicon combination which further ended up as molybdenum or tungsten substrates with Platinum (Pt) electrodes. Reasonable recordings with low threshold currents were reported by them while placing the electrodes in the inferior colliculus. After this, a group from Stanford built electrode arrays on flexible polymer substrate with iridium as a contact. Iridium (Ir), acting as an functional metal layer was evaporated on Titanium (Ti) which was deposited on spun polyimide where Ti acts as an adhesion layer [3]. These arrays were never used on human subjects.

After few years Raytheon van der Puije [4] exhibited a novel concept of electrode array with several ideas, one of which was the development of a cylindrical electrode array formed around a silicone core. In his paper he mentioned the use of ring electrodes, already introduced by Clark [5]. Van der Puje's array consists of sputtered Ti on polyimide substrate followed by an coating of Pt. Standard lithographic techniques were used to pattern the contacts, metal tracks and wiring pads to distinguish the desired conductors from the substrate [4]. After insulating the array surface with another polyimide layer the flexible structure was rolled using a special die into a cylinder of 0.5 mm diameter whose central hollow part was filled with silicone [4]. In 2002, Berrang *et al.* [6] patented a modiolar-hugging cochlear electrode array design. Figure 6.1 shows a sketch from the U.S. Patent for the device [6] which has many required characteristics of a cochlear electrode array; such as preferred bending direction to approximate the spiral cochlea, hugging of the modiolar wall because of the central beam (10 as in Figure 3.1), and the backbone lying on the side of the lateral wall of cochlea. This array was intended to be a part of a patented idea of a totally implantable cochlear implant [7].

Corbett *et al.* [8] in 1997, and Spelman *et al.* [9] in 1998 attempted to atomize the manufacturing and the production process of CI electrode arrays along with increasing the number and the density of the electrode contacts. A flexible layered array on liquid crystal polymer was developed by Corbett *et al.* [10] at the Advanced Cochlear Systems. The production process can be automated by building them with integrated circuit technologies. For an 72 electrode contacts, seven layers of 25 µm thick liquid crystal polymer were used, each separated by another layer.

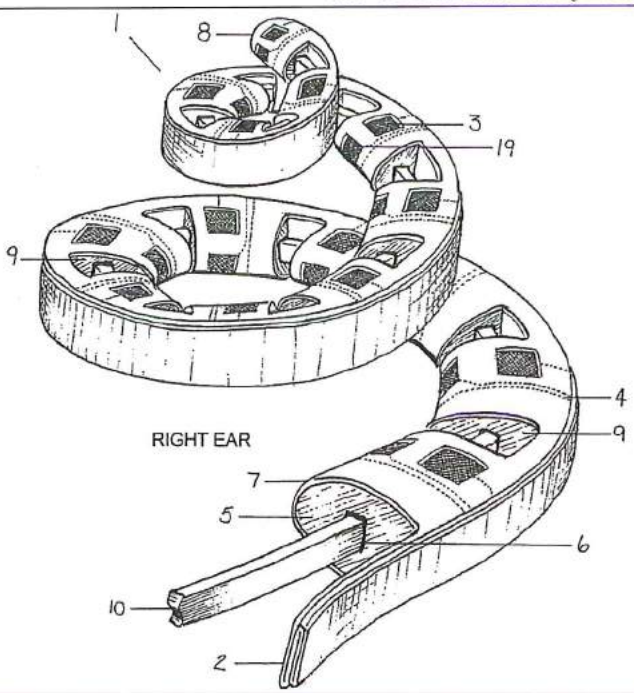

Figure 3.1 Schematics of the electrode array designed by Berrang. The array consists of a silastic core on a polymer substrate. The stiff beam (10) in the centre of the array provides the necessary strength to be placed close to the modiolar wall of the cochlea [6].

Researchers of the Wireless Integrated Microsystems Engineering Research (WIMS²) at the University of Michigan are engaged in researching the CI electrode array domain for high-density, flexibility and new manufacturing techniques to simplify the production process. Bhatti *et al.* [8] developed a 32 site 4-channel high-density intracochlear electrode array. The array contains 180 µm contacts with a pitch of 250 µm. The array combined the MEMS processing technology with active circuitry to realise a thin-film device with a stimulating site density which is three times that of the available commercial systems, delivering 500 µA biphasic current levels with 8-bit resolution and less than 1% charge mismatch.

3.2 CI electrode array: State-of-the art

The success of these CI devices is based on the fact that there are enough auditory nerve fibres left for the stimulation activity performed by the electrode arrays which is placed close to the target neurons. These electrode arrays should provide reliable and repeatable excitation to the neurons of the auditory nerve with a longer duration survival in the tissue vicinity of the cochlea (inner ear). The present CI technology relies on surface stimulation of the cochlear nucleus or auditory nerve stimulation within the scala tympani which is limited by an complex electrode-neural

interface for the transfer of the outer auditory information to the auditory cortex. The electrode arrays has went through a development process.

The commercially available CI electrode array in the market differs in design from manufacturer to manufacturer. The popular FDA approved CI systems used in adults and children are; a) Nucleus Freedom™ 422 implant with slim straight electrode and the Nucleus Freedom™ 24RE with the Contour Advance electrode (Cochlear, Sydney, Australia); b) Synchrony (with rotatable magnet for MRI purposes), Concerto and Concerto Pin (MED-EL Corp., Innsbruck, Austria). Owing to the development of the electrode arrays in the last decade manufacturers are aiming to produce modiolar-hugging electrode arrays. By placing the array in the closer proximity of the spiral ganglion cells gain an theoretic advantage of improved sound quality, speech recognition, and power efficiency [9].

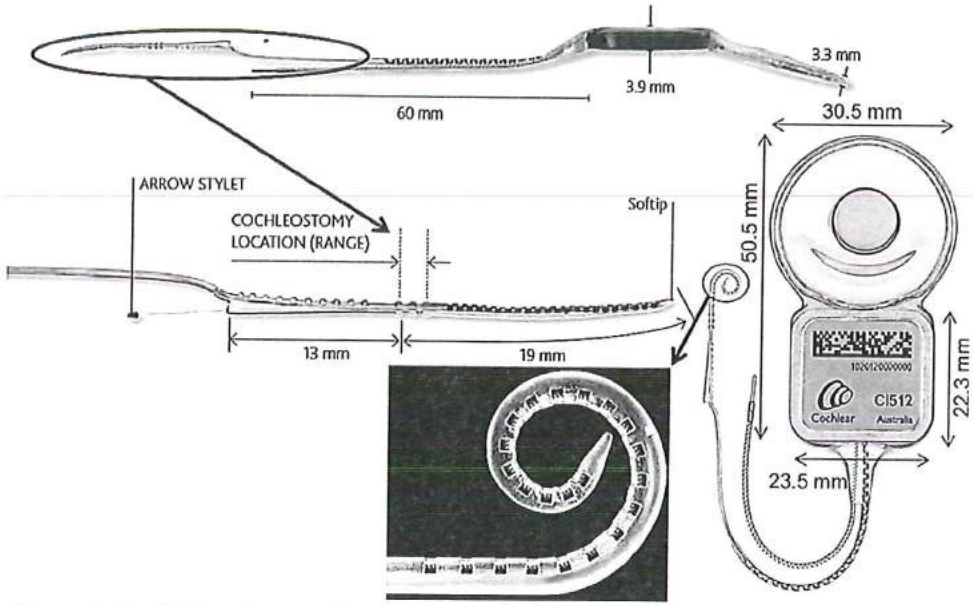

Figure 3.2 The Nucleus CI512 Implant (Cochlear, Sydney, Australia) with major dimensions [53].

The Nucleus CI512 Implant system as shown in Figure 3.2 uses the Contour Advance™ electrode in combination with an AOS (Advance Off-Stylet™) surgical technique and Softip™ electrode to minimise lateral wall insertion force. Results have shown a significant reduction in trauma to the intracochlear structures during the insertion process with the usage of such electrodes in combination of AOS technique [10]. This consists of 32 mm long pre-curved modiolar-hugging electrode with 22 half-banded platinum contact sites held in a straight position with a soft platinum arrow wire stylet. The electrode contacts are arranged in a non-uniform spacing from 0.4 mm to 0.8 mm and spaced over 15 mm active array. The conical shape tapered

silicone elastomer electrode tip is designed to improve the insertion characteristics of the contour electrode and to minimize tip fold-over during the insertion process.

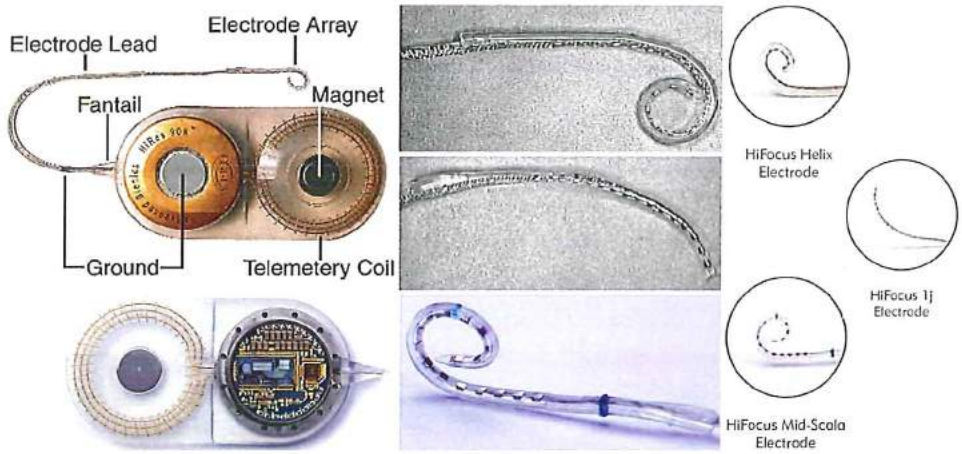

Figure 3.3 HiRes90K implantable part with the electrode family showing the HiFocus Helix, 1j and the Mid-Scala electrode arrays [54].

A white marker as shown in Figure 3.2 which is on the peripheral surface of the electrode, (approx. 11 mm away from the tip) defines the insertion point at which the AOS technique should begin. Similar to the earlier generation Freedom Implant this implant also consists of a ground or reference electrode. This allows monopolar stimulation of all the 22 electrodes in the array, thus reducing the power consumption. The HiRes90K implant from Advanced Bionics as shown in Figure 3.3 is housed in a titanium case with a removable magnet and telemetry coil attached and encased in silastic. The device comes with three electrode array options; the HiFocus Helix and the HiFocus 1j electrodes are of approximate 24.5 mm in length with 16 planar platinum-iridium contacts arranged along the medial surface of the silicone electrode array, the only difference is that the HiFocus 1j electrode array is slightly longer with narrower tip and less curved silicone array designed to insert to a depth of 25 mm. HiFocus Mid-Scala electrode array specially designed for mid-scala placement is the smallest pre-curved electrode is aimed for insertion depth up to 18.5 mm inside the cochlea. The blue indicators as shown in Figure 3.3 ensures the right technique for tool/freehand insertion and proper insertion depth. As mentioned earlier, the manufacturing process/assembly procedure of these electrode arrays been used to-date is still build by hands. A short overview of the general main steps involved in making the Advanced Bionics electrode arrays is depicted in Figure 3.4. The procedure starts with a bundle of Platinum/Iridium (Pt/Ir) electrode wires pre-coated with a polymer which are partially twisted on a mandrel to give the curled structure Figure 3.4 (a). The curled part is inserted into a PTFE

(PolyTetraFluoroEthylene) tubing filled with silicone Figure 3.4 (b). The 16 Pt contacts are mounted on a special metal plate, they are each separated by a defined distance (1.1 mm for HiFocus 1j and 0.85 mm for the helix) as seen in Figure 3.4 (c) and (d). The Pt/Ir wires are then welded onto each separate Pt strip by fixing them on the special metal plate (Figure 3.4 (e) and (f)). Once the each separate wire is been welded to all the 16 Pt contacts then the contact is coated on one side and folded across the individual wire (Figure 3.4 (g)). Once the connection between the array of the contacts is secured to the wire lead, this assembly is then put into a mould and the array is over-moulded with silicone (Figure 3.4 (h)) to form a final assembly of electrode array, the part of which is as shown in Figure 3.4 (i).

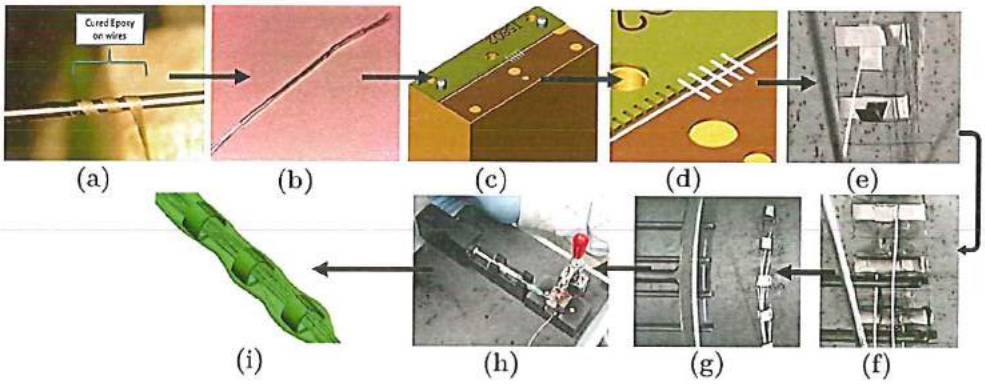

Figure 3.4 Assembly overview of the electrode arrays from Advanced Bionics. (*Adapted and printed with permission from Advanced Bionics Corporation® ERC GmbH, Germany).*

These electrode arrays are used for auditory nerve stimulation process to transmit the acoustical signals into an electrical impulse. The auditory nerve can be stimulated in several ways. These are; Monopolar, Bipolar, and Tripolar.

Monopolar type of stimulation is based on the fact that the body serves as anodal conductor. The electrode is placed in the cochlea and serves as the cathode. A reference electrode is located at a place at the beginning of the cochlea. When a stimulus is applied, a biphasic pulse is generated at the electrode which serves as cathode. The pulse is represented in Figure 3.5 (1). The spread of this type of stimulation is normally over a relative big part of the cochlea. This makes the monopolar stimulation rather non-selective.

In **Bipolar** type of stimulation uses two electrodes which are located very close to each other inside the cochlea. One acts as anode and the other as cathode. Both electrodes will give a biphasic pulse. These biphasic pulses are opposite to each other. Because of the bipolar stimulation, it is possible to stimulate the nerves more accurately in comparison to monopolar stimulation. The principle of bipolar

stimulation is as shown in Figure 3.5 (2) along with a sketch of an unrolled cochlear duct with the electrodes inside it. The location of the anodic and cathodic electrode can be chosen freely, as long as they are close to each other. At the left, the biphasic pulses of the cathodic and anodic electrodes are depicted as function of time. Both the electrodes are stimulating at the same time

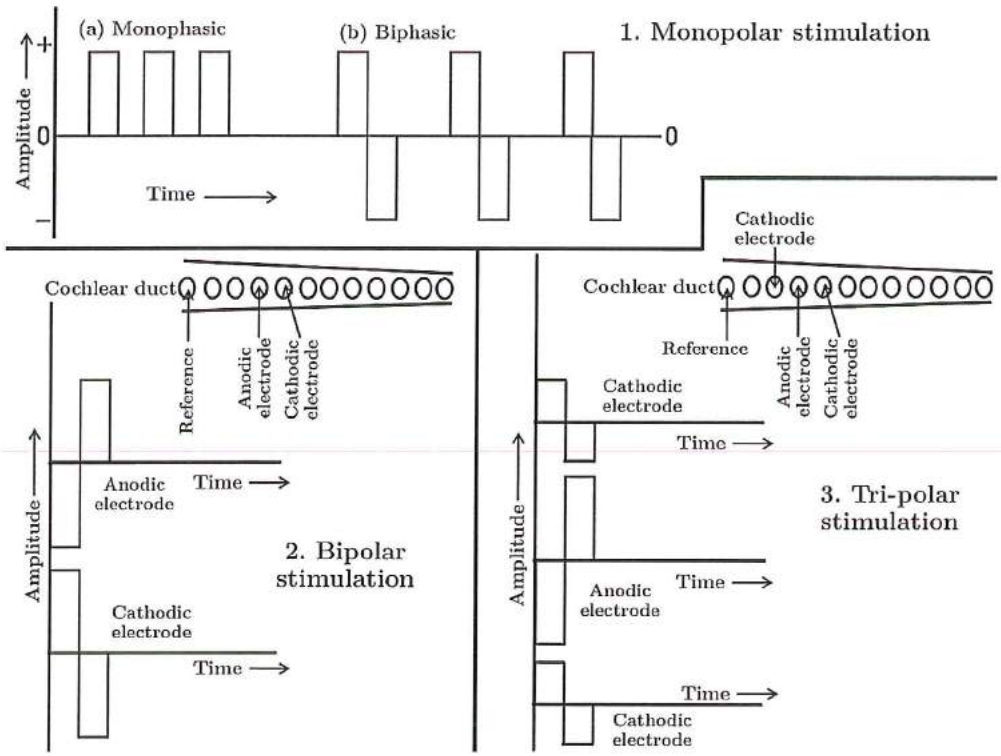

Figure 3.5 Different types of neural stimulation processes.

Tri-polar electrode type of stimulation uses three electrodes consisting of one anodic electrode and two cathodic electrodes. All three electrodes stimulate the nerves with a biphasic pulse (Figure 3.5 (3)). The cathodic and anodic electrodes are placed very close to each other. The location of these electrodes inside the cochlea can be random, provided that they are close to each other. The anodic electrode is the electrode in the middle. This electrode gets a normal biphasic stimulus. The cathodic electrodes each get half of the biphasic stimulus the anodic electrode gets. These stimuli are all generated simultaneously. Tri-polar type of stimulation enables the ability to stimulate more accurately than the bipolar stimulation. This method can be too selective which might result in an inappropriate charge transfer.

3.3 Micro-fabricated microelectrode arrays (MEAs)

The CI electrode array manufactured with the current technology are limited in electrode count, due to their large size relative to the dimensions of the scala tympani (ST). Also the electrode array has design restrictions for deeper insertion in the ST thus depriving the access to the low frequency auditory neurons. To stimulate the speech regions of the cochlea having a tonotopic organisation it's necessary that the array should be inserted to a length of 14-25 mm from the stapes to achieve stimulation frequencies ranging from 500 to 3000 Hz [11]. The CI electrode array; an important component of the CI which sits in close proximity of the auditory neurons inside the cochlea is been evolved from the past decades from simple single channel devices to multiple electrode contact sites arrays of 12 to 22 hand manufactured in the traditional way as explained in earlier sections. Microfabrication using photolithographic and silicon micromachining techniques in addition with micro-electro-mechanical systems (MEMS) permits high volume, batch production to fabricate arrays with microscale dimensions. Such arrays can be used for highly localized stimulation and recording of neural tissue. These arrays often referred to as Microelectrode arrays (MEAs) are mainly intended to restore body functionality by electrical stimulation or to collect bioelectrical activities from the nervous system. MEAs can be roughly divided into two types: stiff and flexible.

The stiff ones are mostly silicon or ceramics base substrates which are fabricated using common methods of MEMS like photolithography, physical vapour deposition (PVD) techniques of metals and inorganic layers, dry reactive ion etching or wet etching processes. These stiff MEAs are mostly used for neuro-cortical stimulation for short term (<1 year) studies. The flexible MEAs for medical field can be divided into two groups; a) Flexible MEAs fabricated with known machining methods such as drilling, milling and laser cutting etc. b) Electrodes fabricated using micromachining techniques such as photolithography, PVD methods, etching etc. Silicone rubber which is used for making flexible arrays have limited process integration capabilities but are easily been approved for medical use. On the other hand parylene or PI are nowadays more favourable due to their thin-film processing competences in the MEMS fabrication areas. Although the second option requires large investment in complex machinery and tools with longer processing periods it has the advantage of heterogeneous process integration with miniature size devices. Human diseases related to hearing, eyesight and other areas where biological complexity and small devices are required to restore deafness, then these MEMS related devices play a major role in meeting the requirements.

3.3.1 Current and future requirements of MEAs

MEAs which are intended to be implanted inside the human body has to satisfy various requirements when comes in direct contact with nerve tissue which is intended to be an bidirectional interface to transfer the required sensory neural information. The initial requirement is regarding the exposed materials to the human body which must be biostable (functionally stable witout affecting itself and the intended environment) in the specific and biocompatible during the use of the medial device [12] and should not form any harmful reaction in the biological environment. Also the material should not be disintegrated or precluded by the human body. Moreover, by foreign body insertion will create a mechanical loading scenario on the nerves and their surrounding tissues will initiate a counter reaction in response to this load. The extent of this reaction may lead to a non-reversible wear of the tissue [13]. The implant device therefore has to meet the physical biocompatibility and the electrochemical stability of the stimulation materials (especially metals) used in the implants. These materials should be stable over a wide range of electrical impulses to deliver the required charge to produce a biological response. This charge is nothing but an action potential in the nerves without delivering an irreversible electrical corrosion reactions [14]. For a specific intended application a particular MEA have to be chosen from different MEAs which varies in geometrical specifications such as length, width, thickness and number of electrodes. Other properties such as electrical range of the stimulation sites, flexibility (or stiffness), the type of manufacturing process used etc. are to be considered. The most common applications for MEAs (cortical electrodes) is in the central nervous system (CNS). For this there is an requirement for large brain arrays which need to adapt globally to the spherical shape of the brain and their irregularities on the surface to stimulate/record the neural activity for which superficial cortical arrays [15–17] as shown in Figure 3.6 (a–c). In these electrodes polymers are used for their better mechanical and biological properties, but still they do not provide the required stiffness to penetrate the neural environment of the brain. So accordingly stiff silicon-based probes are been used for this purpose. The first one of its kind 3D penetrating Utah arrays [18] as shown in Figure 3.6 (f) and the commercially available neural electrodes from NeuroNexus® [19] are the examples of such stiff probes. Retinal implants [20–22] which restore partial vision needs to have a planar flexible surface as seen in Figure 3.6 (g–i) well equipped to adapt the eye curvature in order to provide an close contact between the array and the tissue. To restore hearing for hearing impaired people CI's are required to fit to the smaller dimensions of the cochlea and mechanically flexible enough to curl around. The WIMS^2 group in Michigan, USA has demonstrated a prototype [8] fabricated by

silicon bulk micromachining techniques. A complete overview of some similar devices in the human nervous system is shown in Figure 3.6. Stiff and flexible polymer-based devices are the current neural prosthesis devices used for addressing the problems related to the human CNS. Stiff silicon devices based on silicon micromachining mostly fall under the neuroscience research which another area of research. Moreover, the process and considerations for making stiff probe type electrodes will be described in further chapters. Types of flexible MEAs and their subsequent approach will be the point of discussion in the following sections.

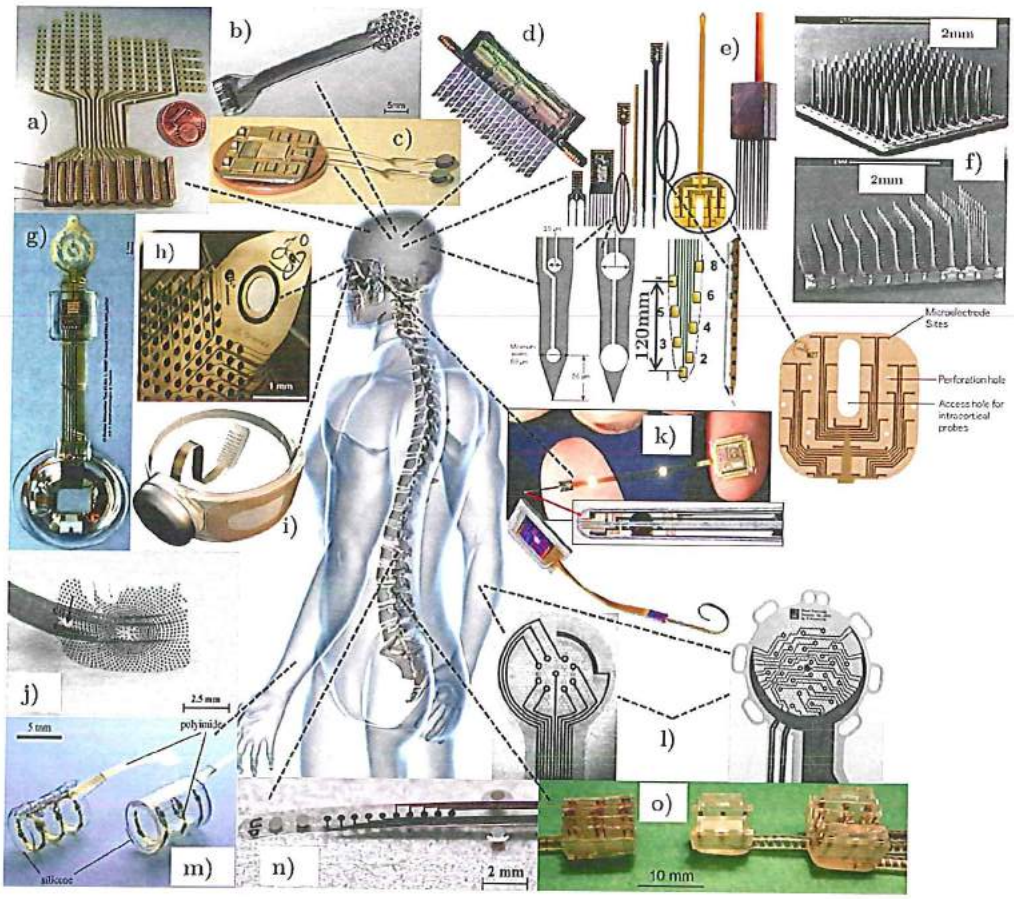

Figure 3.6 An outline of MEAs with its application to different parts of the human nervous system. Human central nervous system can be stimulated/recorded by cortical electrodes (a – d) [15–17,55], 2D penetrating MEAs from NeuroNexus® (e) and typical Utah MEAs (f) [18,19] or for the human eye by flat MEAs (g, h, j) [20–22] and the commercial available Argus®II Retinal prosthesis from second sight (i) (*Image courtesy from http://www.2-sight.eu/ee/*) [56]. Cochlear nerve endings been stimulated by an research MEA been developed at WIMS^2, Michigan, USA (k) [8]. The exterior nerves can be in connection for stimulation and recording by cuff (m) [57], sieve [18] type of MEAs. A parylene MEA (n) [22] and an active book (o) [58] MEA for spinal cord stimulation and recording.

3.3.2 Stiff and penetrating Silicon-based MEAs

Silicon (Si) micromachining combined with MEMS techniques opens the door to micro-fabricate silicon MEAs in voluminous batches and have satisfactory uniformity and high yield at low cost. In terms of mechanical strength and flexibility, silicon microelectrodes are good in comparison to silicon/silicon dioxide probes [23,24]. Also the biocompatibility of the microelectrodes made out of silicon (Si), silicon dioxide (SiO_2), and silicon nitride (Si_3N_4) with the surrounding biological tissue have shown an acceptable performance [25]. This created an interest for the researchers to investigate the manufacturing and application capability in this direction. Researchers from Michigan and Utah successfully demonstrated the fabrication process of two or three dimensional silicon microelectrodes [25–27]. These silicon microelectrodes often referred as silicon microprobes can be fabricated using a single-crystalline silicon or silicon-on-insulator (SOI) based substrate wafer. Considering a single-crystalline silicon based fabrication process which involves a deep p^{++} boron diffusion process in order to determine the outer dimensions of the silicon microelectrode with higher concentration grades between the p^{++} layer and the silicon substrate. This process requires some rigid process requirements which puts some limitations in improving the process. On the other hand in the SOI based fabrication process, the top silicon layer determines the thickness of the silicon microelectrode with precise uniformity. Also, the buried SiO_2 layer acts as an etch stop layer during the device release.

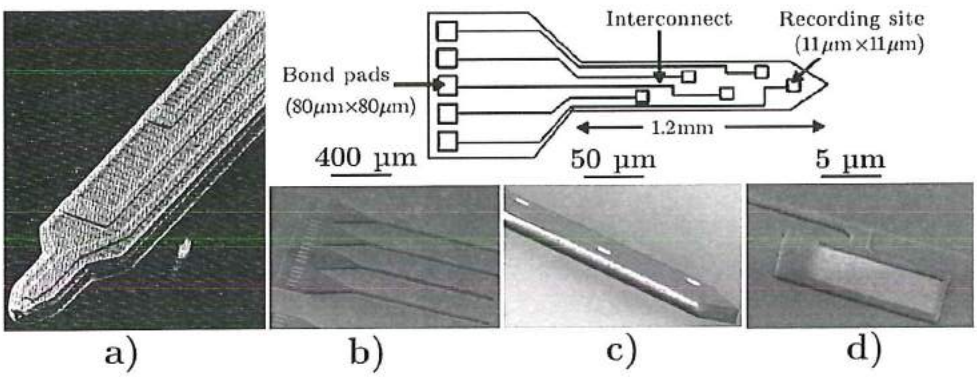

Figure 3.7 Overview of Si microelectrodes: a) SEM view of MEA tip with 8 µm interconnect line width [26]; b) – d) SEM images of a micro-machined probe as per shown in the schematics above; b) MEA including four probe shanks; c) a single probe shank; c) Recording site (contact hole) [23].

3.3.3 Flexible PDMS or Silicone-based MEAs

The current devices which have been approved for clinical practice as medical prostheses such as cardiac pacemakers, cochlear implants, bladder control implants use thick metal foils (10–25 µm) which are either machined or stamped out of the bulk substrate material and further entrenched through fabrication inside a thick (50–500 µm) bulk silicone rubber (PDMS: polydimethylsiloxane). This ensures the isolation of the metallic contacts from the external surroundings [28]. The manufacturing process adapted for producing silicone based MEAs are limited by the resolution of the processing methods resulting in fewer contacts on the device. In the early 1990's Naples *et al.* demonstrated a spiral nerve cuff electrode manufactured by bonding together two pieces of silicone rubber with different natural resting lengths [29], similarly Schuettler *et al.* in 2005 presented a new method of fabricating implantable MEAs by laser cutting the metal foil on the spun-on medical grade silicone rubber [30]. This unique fabrication process is suitable for planar, flexible electrodes which are customized to serve certain requirements for neural stimulation. Devices such as the cuff electrodes [31] for nerve stimulation with microfluidic channels and retinal stimulation electrodes [32] have demonstrated the capabilities of multilayer device fabrication. Due to technology limitations the traditional materials used during manufacturing these devices are silicone rubber (medical grade) and metal foils. Normally a metal foil of 5 µm to 25 µm is chosen The choice of these materials also depends on the final device application. Cogan *et al.* [33] validated by experiments the higher charge injection capacities for platinum and sputtered iridium oxide (SIROF) with minimum influence of oxygen reduction reaction at the electrode surface been used for electrical stimulation process.

3.3.4 Flexible Parylene and Polyimide based MEAs

Polymer materials such as parylene and polyimide are attracting attention due to their excellent processing and conformal coating capabilities with strong electrically insulation properties for conductors and medical devices to survive in harsh corrosive environments. The usage of such polymers into the microfabrication of flexible MEAs has led to more functional and high density electrode sites however reducing overall dimensions of MEAs. Parylene (a trade name) which belongs to a family of linear, noncross-linked semi-crystalline thermoplastic polymer commonly known as polyparaxylylene (PPX). Parylene C poly(dichloro-*p*-xylylene) (Figure 3.8), the mostly used parylene is used as a substrate or encapsulation material for biomedical micro-devices and exhibits a good combination of electrical and barrier properties. Its excellent biocompatibility (FDA approved, USP class VI), chemically and biologically inertness, smooth surface and its function as an electrical insulator makes

it the favourable substrate or encapsulation material for implanted medical devices [12]. Parylene HT which is similar in properties with Parylene C with additional high temperature stability is been successfully been used as a substrate material to fabricate flexible MEA [22]. Despite of Parylene C been broadly used due to its above-mentioned properties, handling is crucial in comparison with polyimide of the same thickness. Parylene is more fragile and is not as strong and robust during substrate integrated MEA [12]. Moreover Parylene-C forms a flexible but non-stretchable carrier for embedded metal micro-tracks and contact sites. Parylene-C in addition to its similar mechanical and insulation properties to polyimide has an added advantage of being a US Food and Drug Administration (FDA, USP class VI) approved material.

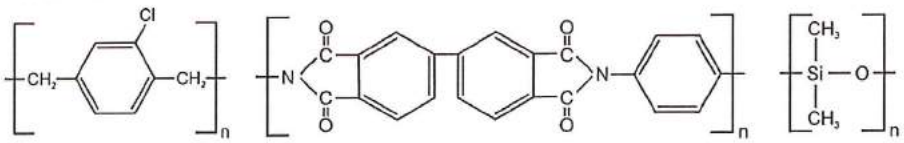

Figure 3.8 Chemical structure of Polymers (a) Parylene C; (b) Polyimide, type BPDA-PPD; (c) Polydimethylsiloxane (PDMS).

Polyimide; a branch of commercial polymers with an application to the field of biomedical and microelectronics is mainly used as insulation or passivation layer in order to provide safeguard the electronics and metal tracks from effects such as moisture absorption, chemical ion transport, corrosion and physical damage. Additionally, it acts as an effective absorber for alpha particles that can be emitted by ceramics, and as a mechanical stress buffer [34]. The BPDA/PPD type polyimide (Figure 3.8) which nowadays mostly been used as a biomaterial and commercially available under the trademark name of DuPont's PI2611 or UBE's U-varnish-S is not a certified biomaterial according to ISO 10993 standards. On the other hand some researchers have proven its biocompatibility, low cytotoxicity and low haemolytic capacity, both bulk materials [35] and for long-term implanted electrodes [36]. MEAs fabricated from polyimides have varied applications which include peripheral nervous system (PNS) and central nervous system: "ECoG arrays" for cortical recordings [15], electrodes for retinal stimulation [20], cuff electrodes for peripheral nerve stimulation [29], intrafascicular MEAs [37]. These devices made out of polyimide caused mild foreign body reactions in applications like the PNS and CNS exhibiting good surface and structural biocompatibility. They also show good functional stability in chronic *in vitro* [38] and *in vivo* studies [39]. All these thin-film polymer-based devices exhibit exceptional short-term application stability but due to poor

polymer metal adhesion do not withstand longer duration stability in harsh human body environment. Due to involvement and originating mechanical forces of different type under physical movements of patient leads to quick failure of the MEAs [40]. Improvement in process fabrication steps in combination with different materials are some steps which is essential to demonstrate the long-term stability of such MEAs.

3.4 MEMS based micro-fabrication technologies

MEMS is a manufacturing technique that contains both electrical and mechanical components. The traditional technologies used to create microelectronic components forms an inspirational platform for the MEMS devices which serve to bridge the gap between the integrated circuits (IC) world with the analog physical world. Although most of the technology is largely based on semiconductor IC technology, MEMS technology apart from the silicon-based devices used in semiconductor fabrication are motivated to use different substrates such as glass/quartz, ceramics and polymer materials leading to the devices that are smaller, better and cheaper. MEMS devices usually leave smaller footprints than their conventional counterparts thus are superior or faster in performance, consume less power and are more selective and sensitive. Basic MEMS processing methods such as photolithography, oxidation, diffusion, ion implantation, physical vapour deposition techniques (evaporation and sputtering), chemical vapour deposition, wet chemical and dry plasma etching etc., are borrowed from the semiconductor IC technology [41].

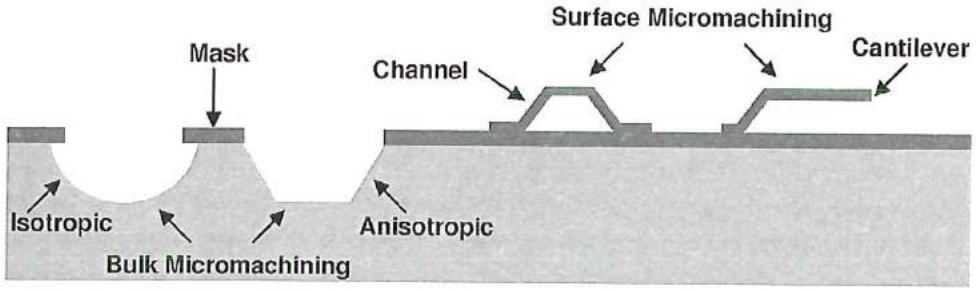

Figure 3.9 Illustration showing difference between bulk micromachining and surface micromachining.

Over the years MEMS has also developed some microfabrication techniques such as Deep Reactive-Ion-Etching (DRIE), bulk chemical etching, LIGA (German acronym for x-ray lithography, electroforming and moulding), wafer bonding, electroplating and stereo lithography [42]. In the recent year, polymer-based MEMS devices have gained popularity, resulting to many new methods suitable for polymers, like soft lithography [43–45]. In order to fabricate a complete MEMS

device several basic fabrication steps are combined and performed sequentially which are classified as bulk micromachining [46] and surface micromachining [47]. As shown in Figure 3.9 the bulk micromachining process uses a wet chemical or a dry plasma etching process to remove selectively the substrate material with the help of masking films to form the required structures. This etching process can be of two types: (a) isotropic (etching from all sides) using chemicals such as HNA (hydrofluoric acid + nitric acid + acetic acid) or etching gas like Xenon difluoride (XeF_2); (b) anisotropic (etching as per Silicon crystal structure orientation) using potassium hydroxide (KOH) or tetra-methyl-ammonium-hydroxide (TMAH) wet chemicals or using a combination of SF_6 + C_4F_8 gases by the DRIE process. Surface micromachining on the other hand is a process which shapes the required devices on the top surface of the substrate, usually with the help of sacrificial materials (photoresist, polyimide, metals, polysilicon) to form free standing membranes or even completely released thin-film microstructures for e.g. micro-cantilevers or micro-channels (Figure 3.9).

3.4.1 Photolithography

Photolithography is one of the basic technology in the semiconductor IC and MEMS or microsystem technology which enables structuring techniques for the deposited thin-films down to feature sizes of some hundred nanometer. With the help of photoresist to create patterns on the substrate (e.g. silicon, glass etc.), selective regions are then subjected to etching or deposition process steps, thus transmitting the required pattern to the substrate [41,42]. Repetition of this procedure of pattern definition followed by deposition and etching with different Photomask patterns facilitates creation of complex IC structures and MEMS devices. A traditional photolithography process consists of 3 basic steps: photoresist application, exposure and development (Figure 3.10). Photoresist is an light sensitive chemical that undergoes an chemical change when exposed to certain wavelength of Ultraviolet (UV) light. A conventional photoresist consist of 3 materials: solvent, matrix resin, and photoactive compound (PAC). The liquid state of the photoresist is maintained by the solvent until application and processing on the substrate wafer.

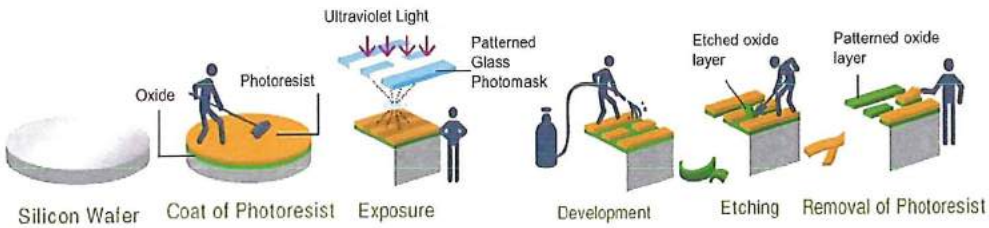

Figure 3.10 Illustration of the basic photolithography process.

The photoresist after spinning onto the substrate is soft-baked, during which most of the solvent (approximately 80–90%) is baked out of the photoresist. The matrix resin and the PAC stays behind after the solvent removal. The photoresist film with the help of matrix resin provides the necessary adhesion and etch resistance properties even in the absence of the solvent. In other words, the matrix resin confirms that the photoresist adheres to the substrate during the subsequent exposure and development steps. In addition, the matrix resin determines the thickness of the photoresist and resists the chemical or plasma etching that follows photoresist development. The last component, PAC undergoes a chemical reaction when exposed to UV light, which then determines the etch rate of the photoresist in developer. In positive photoresists, the PAC, once exposed to UV light, acts as a catalyst, increasing the rate at which the resist will dissolve when placed in the developing solution. In contrast, the PAC in negative photoresists, after exposure to UV light becomes cross-linked and acts as an inhibitor, decreasing the rate at which the resist dissolves when placed in the developing solution. Once the photoresist is spun on and soft-baked, it is then exposed to UV light through a glass photomask (Figure 3.10). This mask contains the transparent and opaque features that define the pattern to be transferred to the photoresist. The exposure to the UV light triggers the PAC, rendering the areas of the photoresist either soluble or insoluble to developing. After exposure, the developer dissolves either the exposed regions of the photoresist (in the case of positive photoresist) or the unexposed regions of the photoresist (in the case of negative photoresist). In both cases, once developing is complete, the features in the mask will have been realistically replicated in the photoresist. At this point, the exposed substrate then can be subjected to a variety of wet etchants or to a reactive ionized gas (e.g. O_2 or CF_4) to remove the exposed areas or also follow other deposition processes explained in the later sections. The presence of the photoresist protects the substrate in those regions from other processes. Thus, the features in the masks can be successfully replicated on the substrate. Depending on application various photoresists are available for very thick and thin depositions, of which some are suitable for fabricating structures with large aspect-ratios while others are more resilient to wet or dry etchants. Most of the resists are stable until 120 ^{o}C before reaching the softening point to start oxygen reactions. There's also a small group of negative resists exhibiting a thermal stability at 250 ^{o}C which are suitable for wet chemical etching.

3.4.2 Spin Coating

Spin coating is generally a starting step in the microfabrication process for producing thin polymeric layers ranging between 1µm to 500 µm. The material to be deposited is normally deposited in liquid form onto the substrate (e.g. silicon, glass

etc.) which is fixed by vacuum to a rotating chuck. A viscous fluid deposition on a horizontal rotating substrate (disc) produces a uniform liquid film. In the deposition process the substrate should either be static or rotating with a low angular velocity, where after the substrate is accelerated to a high angular velocity (spin speed). The adhesive forces at the liquid/substrate interface and the centrifugal forces generated due rotation act on the polymeric fluid (e.g. photoresist, polymers etc.) results in a strong sheering force of the liquid allowing it to spread in the radial direction over the substrate till the peripheral end with some excess material to accumulate or even rejected over the substrate edges (Figure 3.11). Depending on fluid viscosity and the flow behavior on different surfaces the coating thickness can be adjusted by defining a particular angular speed in combination with the spinning time.

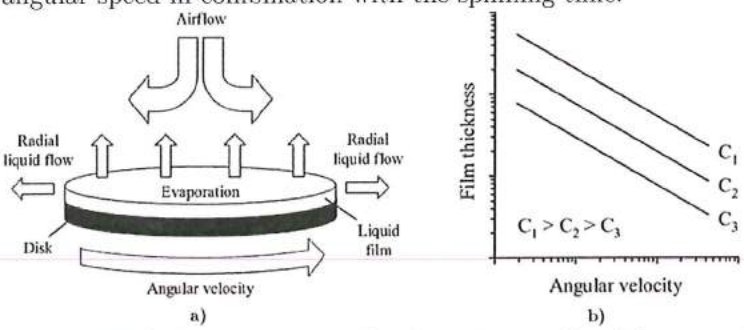

Figure 3.11 Spin coating: a) Process schematics. b) Relation between film thickness, angular velocity and concentration (Cn) in a spin-coating process [48].

An organic coating layer of equal thickness on the substrate can be achieved by heating up the substrate to specific temperatures thus removing the solvents, if any and polymerizing the coating. This combined rotation and evaporation reduces the thickness of the remaining liquid film causing the polymer concentration to increase (and thus the viscosity) at the liquid/vapour interface, i.e. a concentration gradient is formed through the liquid film, which, after evaporation of most of the remaining solvent, consequently results in the formation of a uniform practically solid polymer film [48]. In such polymer solutions the concentration is directly proportional to viscosity, *i.e.*, viscosity increases for higher concentrations (typically not linearly). A generalized relationship between angular velocity and concentration (or viscosity) can be shown schematically in Figure 3.11. Generally accepted mathematical relationship is as follows:

$$h = k_1 \omega^{\alpha} \qquad (1)$$

where h is the film thickness, ω is the angular velocity, while k_1 and α are empirically determined constants. Figure 3.11 shows that for higher angular velocities

the film thickness will decrease, and that for lower concentrations (at a given angular velocity) the film thickness will also decrease. The constants, k_l and α, are dependent on various parameters, such as physical properties of the polymer, the solvent, and the substrate, polymer/solvent interactions and solution/substrate interactions, and thus also rheological properties [48]. Spin coating is one of the important deposition processes been widely used for organic materials since most of the resists are applied through this method to structure thin films. Spin coating does not exhibit high binding energies, the only combined energy seen in the layers comes from the thermal energy during the curing step (e.g. Polyimide being cured at 400 ^{o}C).

3.4.3 Growth, deposition and structuring of thin films

In comparison to the known common machining methods where the final device is structured out of one or many pieces of bulk material, thin film fabrication methods involves the growth of metallic or non-metallic inorganic layers layer by layer until desired thickness to be achieved. These layers can be deposited by various techniques by physical or chemical means of the matter which at the end condenses on the substrate forming the desired layers. Physical vapour deposition (PVD) processes such as sputtering and evaporation allows metals like Titanium (Ti), Platinum (Pt), Aluminium (Al), Chromium (Cr), Copper (Cu) etc., to obtain metallic layers ranging from few nanometres to hundreds of microns. Other non-metal covalent ceramics like silicon di-oxide (SiO_2), silicon nitride (SiN), silicon carbide (SiC) are fabricated by plasma enhanced chemical vapour deposition (PECVD) process in which the required gases (reactants) are injected into the deposition chamber as a gas. The polymer deposition can also be done by CVD or though the spin coating described earlier. PVD and CVD methods will be dealt shortly in the following sections to gain more insight into it [49,50].

3.4.3.1 Physical vapour deposition (Evaporation)

Evaporation is one of the oldest PVD deposition techniques used for depositing thin films (generally metals). As the name goes, evaporation is a process in which the material to be deposited is first vaporised by heating it above its melting temperature through resistive or inductive heating or electron beam vaporization from a source and then condensed onto the substrate. In resistive heating, the metal is contained in a highly resistive container (e.g., a tungsten boat) and a high current is passed through the container heating it and causing the metal to evaporate (Figure 3.12). In electron beam heating, an electron beam is magnetically focused onto the target metal causing it to locally melt and evaporate. The thermal energy allows the particles at the surface of the melt to evaporate, thus leaving the bulk

material. The particle travel from the melted metal surface to the substrate requires a high vacuum (1.3×10^{-3} Pa) chamber environment. This ensures no collisions with other particles and the mean free path of the evaporated atoms which are large enough to reach the desired position (substrate), resulting in adsorption at the substrate surface and initiating the film growth process. Some advantages of using evaporated metal are higher deposition rates, less substrate heating, and fewer impurities, due to the higher vacuum and the fact that in evaporation a new charge of metal is used for each deposition, as opposed to sputtering where the target is re-used for multiple depositions.

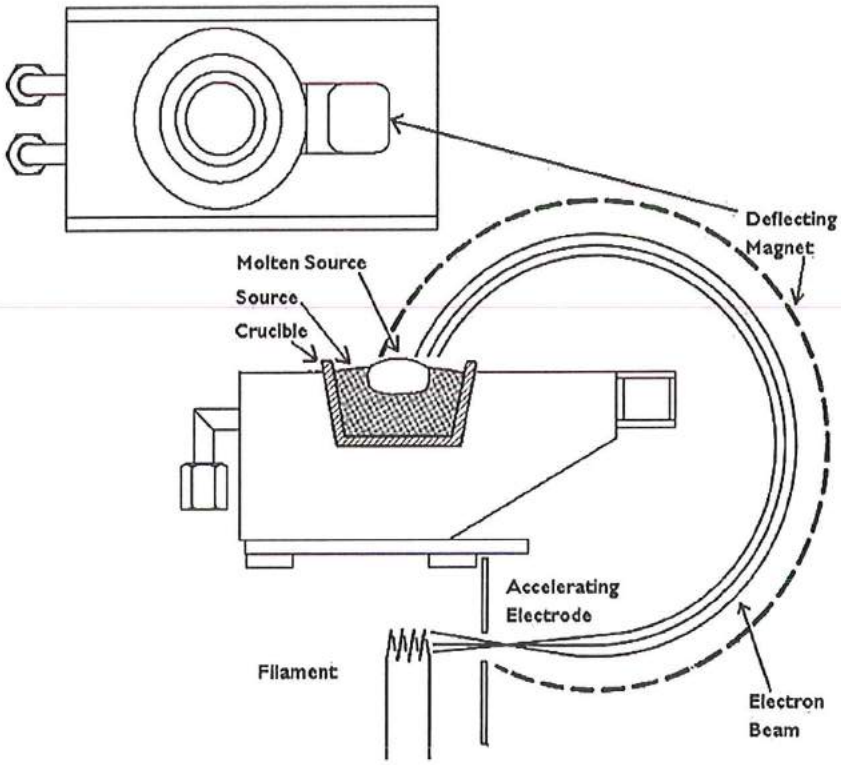

Figure 3.12 Illustration showing the basic principle of electron beam evaporation.

Advantages of e-beam evaporation:

1. Versatile method used for almost any material having very high melting point metal oxides that cannot be evaporated by resistive heating.
2. Deposited films are often purer in comparison to other PVD processes.
3. The e-gun sources can be configured to hold a great deal of material and can be purchased with continuous feed for large amount of depositions.

Disadvantages of e-beam evaporation:

1. More complicated and expensive to install and maintain.

2. Generation of X-rays during the e-beam evaporation method can penetrate the surface layers of the devices, causing damage such as the creation of oxide-trapped charges.
3. Bad step coverages when using complex shapes and structures.

3.4.3.2 Physical vapour deposition (Sputtering)

Sputtering is the most popular PVD technique not only used in deposition of metals but a wide variety of materials including oxide, silicon, silicon-nitride and polysilicon [41,42]. Similar to the evaporation process, the target (a disc of the material to be deposited) held at high negative potential and the substrate (positive anode) on which deposition is to be occurred are placed in an evacuated chamber separated at a distance of few centimetres Figure 3.13. The sputtering process requires positive ions of inert gases such as argon or xenon in a high energetic state (plasma) which are accelerated/bombarded by an electrical field towards the target were the neutral atoms of the target are released wit high kinetic energy. The bombardment, and subsequent sputtering, transfers the momentum of the positive ions to the neutral atoms allowing the neutral atoms to travel to and condense on the substrate to form the desired layer. In this deposition process, insertion of another reactive gas (e.g. O_2 or N_2) results in the growth of metal oxides or metal non-metal ionic ceramics (e.g. TiN, TiO_2, Al_2O_3, AlN).

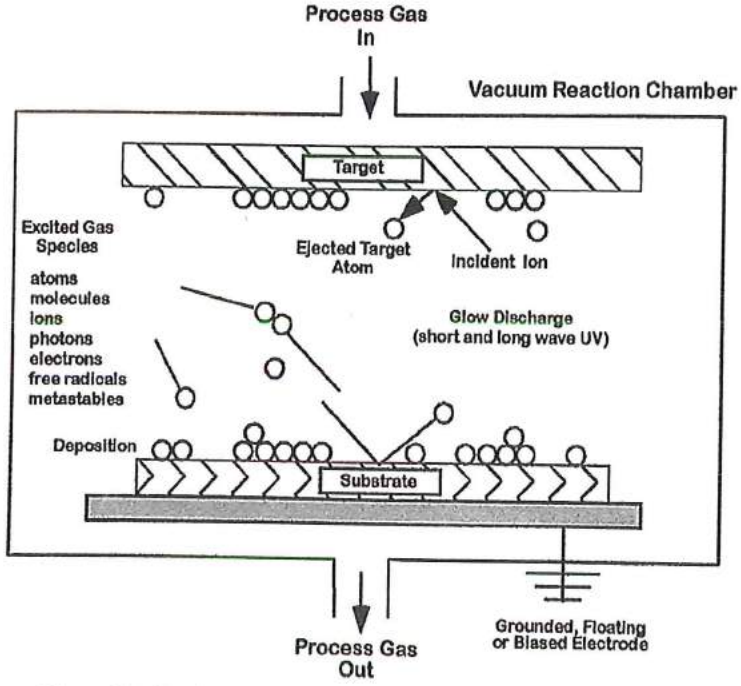

Figure 3.13 Graphic representation of a planar diode sputtering process.

The sputtered particles lose some kinetic energy in their path towards the substrate by colliding with the process gas. Additionally, collisions lead to a rather strong scattering of the particles, making them to impact the substrate from different directions. Even though collisions reduce the energy of the atoms when approaching the substrate, the average kinetic energy of sputtered atoms is around 20 times higher of that of evaporated materials [49]. Sputtering to deposit oxide layers does not limit the choice of substrate and sputtered oxide can be deposited on silicon, metal, and polymers. Similar thicknesses are achievable with both sputtered and thermal oxide, although sputtered oxide does not require high temperatures for deposition. Thus, sputtered oxide is ideal for use as a sacrificial material. However, as it often contains impurities, its less ideal as an insulating material.

Advantages of sputtering:

1. Faster deposition rates with better control of the film thickness.
2. Film obtained at low temperatures, avoiding damaging the substrate.
3. Better surface morphological conditions due to vacuum environment.
4. Better surface morphology of the films due to less target heating.
5. Homogenous and defect free membranes are obtained.
6. Alloy deposition is easier as compared to other techniques.

Disadvantages of sputtering:

1. Materials like organic solids are degraded by ionic bombardment.
2. Greater tendency to introduce impurities in the substrate.
3. Non-directional deposition method.

3.4.3.3 Chemical vapour deposition (CVD)

Chemical vapour deposition can be defined as the condensation of a compound or compounds from the gas phase on to a substrate where reaction occurs to produce a solid deposit. The process can be summarized by the following Figure 3.14 [51]. The basic mechanism of the CVD is that the starting material is vaporised and then chemically reacts with the molecules on the substrate surface to create the desired deposited material. This deposition process is normally done in a reaction chamber at a low pressure of 50 mbar (LPCVD) up to atmospheric pressure (APCVD). The process starts by moving the reactant gases (normally diluted with an inert gas) inside the deposition chamber. As the gases flow though the chamber, the reactant gaseous compounds which contain the deposit material which must be in vapour state if not, then is formed by volatilization from either a liquid or a solid feed and causes flow by a pressure differential or the action of the carrier gas to the substrate, further transporting it to the surface where the dissociation of molecules occur at the substrate surface. The desired coating is deposited by the thermal decomposition or

chemical reduction of the gaseous compound on the substrate. All the parts of the system are kept hot as the temperature of the vapour source. The reaction part of the system has higher temperature than the vapour source but lower than the melting temperature of the deposit [51]. The gases and desired metal can require up to ~1400 °C so some of the materials (metals and polymers) with low melting temperatures cannot withstand such temperatures. So in order to bring down the process temperature but still achieving the molecular dissociation at the surface often a Ar^+ plasma is coupled to the chamber. This process is called as plasma-enhanced chemical vapour deposition process (PECVD) in which the plasma can vary from low frequency (187 kHz) to high-frequency (13.56 MHz) depending upon the generator type. The PECVD process brings down the temperature normally 200 to 500 °C. The reaction chamber for PECVD consists of a parallel plate capacitor in which the plasma is generated. The plasma couples energy into the reactant gases which dissociate into ions or radicals and react forming the desired species. The reactive species can undergo reactions with other gaseous reactants or with the substrate itself directly. Gaseous matter reacting in the chamber can condense on the surface of the substrate and yield the desired layer. Even though the layer growth of CVD or PECVD is similar to that of PVD the process is different in terms of the chemical kinetics of the reactants present in the chamber which are in the form of free radicals or ionized matter. At low deposition pressures (100–600 mbar), these ions and radicals reach the surfaces faster than they are consumed in the chemical reaction in the gas, so the layer growth is limited to surface reactions, improving covalent bond creation in the substrate, if the material combinations allow it [49].

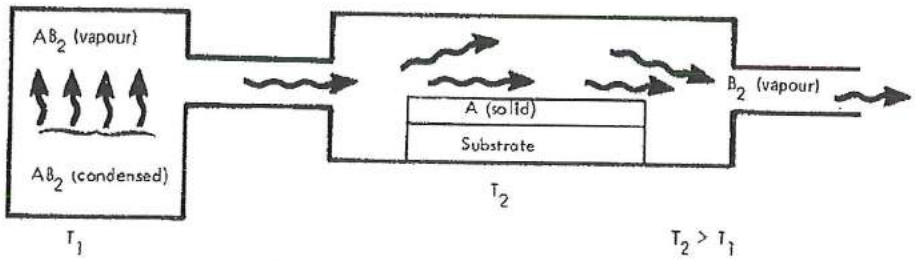

Figure 3.14 Schematic representation of a CVD process [51].

Advantages:

1. Capable of depositing high melting temperature elements such as tungsten, tantalum, or carbon.
2. It can also deposit many alloys, as well as compounds including oxides, nitrides, and carbides.

3. The CVD process is easy to scale up and flexibility to coat metal film on the support of different geometry thus having good step coverages.
4. A unique technique which promotes the transport of the depositing metal directly into the pores of the substrate for the deposition process.

Disadvantages:

1. It is difficult to control during the deposition process the composition of the metal alloy deposited on the surface.
2. It's being costly because of the high temperatures that are required to produce certain coatings and the reactor design is very critical to achieve the uniform coating on the complex shaped structure.

3.4.3.4 Thermal Oxidation

Silicon dioxide (SiO_2 or oxide) is mainly used in a variety of MEMS applications, including as an insulator for electrodes, masking material for etching processes, and sacrificial material for surface micromachining [41]. Thermal oxidation is the process involving heating of a silicon substrate in an oxygen atmosphere [41,42]. Although the silicon oxidizes readily in ambient air, even at room temperature, creating native oxide layers of approximate 20 Å thick, the elevated temperatures allow thicker layers of oxide to be grown. The high temperature, generally between 600 ^{o}C and 1250 ^{o}C, aids in the diffusion of the oxidizing material through the oxide present on the surface to the silicon interface, where it then converts the silicon to oxide. The oxidizing material is either water vapour (wet oxidation) or oxygen gas (dry oxidation). The chemical reactions involved in this oxidation process are:

$$Si_{(Solid)} + 2H_2O \xrightarrow[WetOxidation]{} SiO_{2(Solid)} + H_{2(Gas)} \quad (2)$$

$$Si_{(Solid)} + O_{2(Gas)} \xrightarrow[DryOxidation]{900-1200^0\,C} SiO_{2(Solid)} \quad (3)$$

Thermal oxidation is usually used for most of the insulation and masking applications where the growth of thin layer of oxide is restricted to <1 µm. The only disadvantage of this oxidation process is that the silicon substrate must be free from all metal or polymers as these materials cannot survive such high temperatures and will also hinder the oxidation reaction process. Therefore the thermal oxide cannot be used as a sacrificial layer in many microfabrication processes.

3.4.4 Etching

Etching is an essential process step for device fabrication in the MEMS systems. The purpose of the etch process is to remove material from the areas identified by the lithography process, to create structures for functional use and to remove oxide layers below features to allow for any desired motion. There are two main types of etching; wet and dry (including plasma) etching processes. Even though the wet etching is faster and can provide better selectivity than dry etching, it also requires the use of potentially dangerous acids and solvents. As such, dry etching, requires only small amounts of chemicals. Some other advantages obtained by dry etching are both isotropic and anisotropic etch profiles, directional etching (independent of the crystal orientation of the underlying silicon), high-resolution patterns, and better process control [41,42].

3.4.4.1 Wet Etching and wet etchants

By definition, wet etching method is a material removal process which uses liquid chemicals or etchants to remove the desired material from the substrate wafer. The required patterns are been created by standard lithography process using photoresist masks. A typical wet etching process involves multiple reactions which consume the original reactants and produce new reactants. The basic wet etching process involves three fundamental steps; (1) the diffusion process of the reactants (liquid etchant) transported to surface where materials is to be removed, (2) the surface reaction occurs between the reactants and the material to be etched away. A reduction-oxidation reaction usually occurs. This reaction involves the oxidation of the material and then dissolving of the oxidized material, and finally (3) the diffusion of the by-products of the surface reaction must be transported away from the reacted surface. In general, wet etchants contains three key elements: an oxidizer, an acid or base to dissolve the oxidized surface, and a diluent in which the reactants and by-products are transported [52].

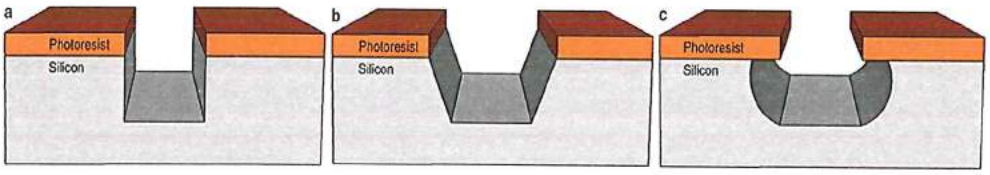

Figure 3.15 Wet etching, (a) Totally anisotropic, (b) Partially anisotropic, (c) Isotropic etching [52].

Wet etchants can be classified by the etching profile they create (Figure 3.15). Isotropic etchants are the etchants which attack the material isotropically (uniform in all directions), in other words, the lateral etch rate is the same as the vertical etch

rate, and these are independent of the mask or substrate orientation. These etchants will undercut the mask layer if etching continues more than the prescribed time duration (Figure 3.15). Anisotropic etchants etch material by anisotropic etching (uniform in vertical direction), the etch rate depends on the crystal orientation of the material to be etched. Thus the lateral etch rate can be significantly larger or smaller depending upon the orientation of the mask to the crystalline axes of the substrate. The material etch rate in wet etching is usually faster than the dry etching process and can be easily altered by varying the temperature and active species concentration [52].

3.4.4.2 Dry etching and dry etchants

Dry etching is similar to wet etching which is an material removing process, the only difference is that in dry etching, plasmas or etchant gasses remove the material. The reaction that takes place can be done by utilizing high kinetic energy of particle beams, chemical reaction, or a combination of both. Two main type of dry etching are: non-plasma (Chemical dry etching) and plasma (Physical dry etching and Reactive-Ion etching [RIE] and Deep Reactive-Ion etching [DRIE]) based etching. Non-plasma based dry etchants are isotropic and generally limited to etching silicon. These etchants typically are fluorine-containing gases, such as xenon difluoride or bromine trifluoride, that readily etch silicon. The etch rate is easily controlled by the temperature and pressure of the reactants. *Chemical dry etching* (or *vapour phase etching*) is a process which does not use liquid chemicals or etchants but uses an etchant gas to attack the silicon surface by a chemical reaction between the two. This etching is usually an isotropic process with high selectivity which is opposite to anisotropic which etches finer resolution and high aspect ratio.

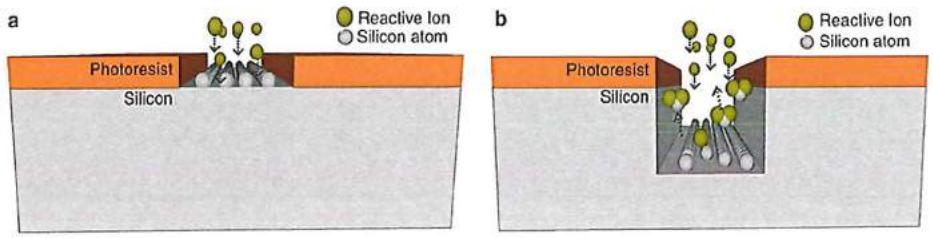

Figure 3.16 Process of chemical dry etching, (a) Interactions between reactive ion and silicon atom, (b) Bond between reactive ion and silicon atom chemically removes silicon atoms form the surface [52].

Undercutting can be avoided due to directional nature of dry etching. Commonly used ions in this etching are tetrafluoromethane (CH_4), sulfur hexafluoride (SF_6), nitrogen trifluoride (NF_3), chlorine gas (Cl_2), or fluorine (F_2). *Physical dry etching* is

an etching process which requires high kinetic energy (ions, electrons or photons) beams to etch the substrate atoms.

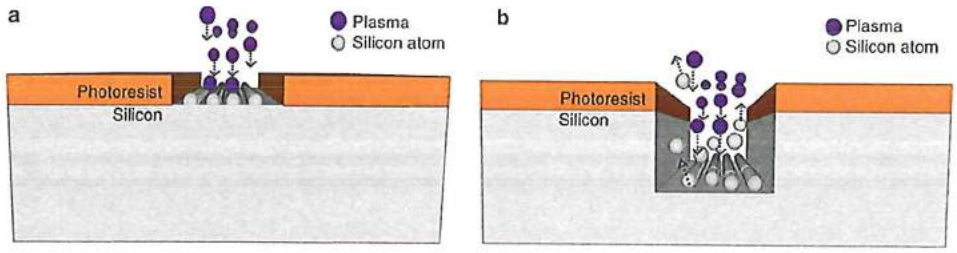

Figure 3.17 Physical etching in which high energy plasma hits Si surface to knock atoms from the surface (a) plasma atoms hitting the surface, (b) the silicon atoms being evaporated off from the surface [52].

When high energy particles bombard at the substrate surface they knock off the atoms from the surface, thus evaporating the material after leaving the substrate surface. There is no chemical reaction taking place in this process but rather a physical knocking process of the material that is unmasked in the process. The physical reaction is illustrated in Figure 3.17. *Reactive-Ion etching* (RIE) or *Deep Reactive-Ion etching* (DRIE) makes use of both the physical and chemical interaction means to achieve the required resolution at a faster pace. High energy collision from the ionization helps to dissociate the etchant molecules into more reactive species. In a typical RIE process which usually contains CF_4, SF_6 and $BCl_2 + Cl_2$ reactive gases to etch Silicon are accelerated towards the substrate with high energy in an plasma environment to etch the material (mostly Silicon) by chemical reaction of the reactive gases with the etching material.

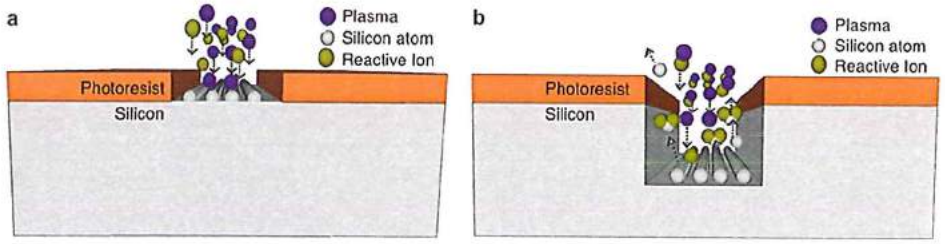

Figure 3.18 The RIE process combining physical and chemical means to etch the silicon [52].

3.5 Conclusions

This chapter gives the reader a brief overview of the state-of-the-art of the CI electrode array and its assembly procedure with standard different types of neural stimulation processes (monopolar, bipolar and tri-polar) been used nowadays. Then a detailed discussion about the different microfabricated MEAs (stiff silicon based,

flexible PDMS, parylene and polyimide based) is done mentioning the associated current and future requirements of MEAs. The later section of the chapter deals with the overview of the different microfabrication technologies such as photolithography, growth, deposition and structuring of thin films, etching etc. which were used in the microfabrication of the micromachined electrode array demonstrators which will be described in detail in the later chapters.

3.6 References

1. Clark, G. *Cochlear implants: fundamentals and applications*; springer, 2003.

2. Mercer, H. D.; White, R. L. Photolithographic fabrication and physiological performance of microelectrode arrays for neural stimulation. *IEEE Trans. Biomed. Eng.* **1978**, *25*, 494–500.

3. Shamma-Donoghue, S. a.; May, G. A.; Cotter, N. E.; White, R. L.; Simmons, F. B. Thin-film multielectrode arrays for a cochlear prosthesis. *IEEE Trans. Electron Devices* **1982**, *29*, 136–144.

4. van der Puije, P. D.; Pon, C. R.; Robillard, H. Cylindrical cochlear electrode array for use in humans. *Ann. Otol. Rhinol. Laryngol.* **1989**, *98*, 466–71.

5. Clark, G. M.; Shepherd, R. K.; Patrick, J. F.; Black, R. C.; Tong, Y. C. Design and fabrication of the banded electrode array. *Ann. N. Y. Acad. Sci.* **1983**, *405*, 191–201.

6. Berrang, P.; Bluger, H. Modiolar hugging electrode array. *US Pat. 6,374,143* **2002**.

7. Berrang, P.; Bluger, H.; Jarvin, S.; Lupin, A. Totally implantable cochlear prosthesis. *US Pat. 6,358,281* **2002**.

8. Bhatti, P. T.; Wise, K. D. A 32-Site 4-Channel High-Density Electrode Array for a Cochlear Prosthesis. *IEEE J. Solid-State Circuits* **2006**, *41*, 2965–2973.

9. Jolly, C. N.; Gstöttner, W.; Hochmair-Desoyer, I.; Baumgartner, W. D.; Hamzavi, J. Principles and outcome in perimodiolar positioning. *Ann. Otol. Rhinol. Laryngol. Suppl.* **2000**, *185*, 20–3.

10. Roland, J. T. A model for cochlear implant electrode insertion and force evaluation: results with a new electrode design and insertion technique. *Laryngoscope* **2005**, *115*, 1325–39.

11. Greenwood, D. D. A cochlear frequency-position function for several species--29 years later. *J. Acoust. Soc. Am.* **1990**, *87*, 2592–605.

12. Hassler, C.; Boretius, T.; Stieglitz, T. Polymers for neural implants. *J. Polym. Sci. Part B*

Polym. Phys. **2011**, *49*, 18–33.

13. Williams, D. F. On the mechanisms of biocompatibility. *Biomaterials* **2008**, *29*, 2941–53.

14. Rose, T. L.; Robblee, L. S. Electrical stimulation with Pt electrodes. VIII. Electrochemically safe charge injection limits with 0.2 ms pulses. *IEEE Trans. Biomed. Eng.* **1990**, *37*, 1118–20.

15. Rubehn, B.; Bosman, C.; Oostenveld, R.; Fries, P.; Stieglitz, T. A MEMS-based flexible multichannel ECoG-electrode array. *J. Neural Eng.* **2009**, *6*, 036003.

16. Green, R. a; Ordonez, J. S.; Schuettler, M.; Poole-Warren, L. a; Lovell, N. H.; Suaning, G. J. Cytotoxicity of implantable microelectrode arrays produced by laser micromachining. *Biomaterials* **2010**, *31*, 886–93.

17. Wise, K. D. Integrated sensors, MEMS, and microsystems: Reflections on a fantastic voyage. *Sensors Actuators A Phys.* **2007**, *136*, 39–50.

18. Navarro, X.; Krueger, T. B.; Lago, N.; Micera, S.; Stieglitz, T.; Dario, P. A critical review of interfaces with the peripheral nervous system for the control of neuroprostheses and hybrid bionic systems. *J. Peripher. Nerv. Syst.* **2005**, *10*, 229–58.

19. Technologies, N. *Neuronexus*. NeuroNexus Technologies 2011, pp. 1 – 146.

20. Stieglitz, T. Development of a micromachined epiretinal vision prosthesis. *J. Neural Eng.* **2009**, *6*, 065005.

21. Ordonez, J. S.; Schuettler, M.; Ortmanns, M.; Stieglitz, T. A 232-channel retinal vision prosthesis with a miniaturized hermetic package. *Conf. Proc. Annu. Int. Conf. IEEE Eng. Med. Biol. Soc. IEEE Eng. Med. Biol. Soc. Annu. Conf.* **2012**, *2012*, 2796–9.

22. Rodger, D.; Fong, a; Li, W.; Ameri, H.; Ahuja, a; Gutierrez, C.; Lavrov, I.; Zhong, H.; Menon, P.; Meng, E. Flexible parylene-based multielectrode array technology for high-density neural stimulation and recording. *Sensors Actuators B Chem.* **2008**, *132*, 449–460.

23. Xiao-Hong, S.; Wei-Hua, P.; Ruo-Xin, Z.; Lin, L.; Hong-Da, C. A Micromachined SiO 2 /Silicon Probe for Neural Signal Recordings. *Chinese Phys. Lett.* **2006**, *23*, 1932–1934.

24. Xiao-Hong, S.; Ruo-Xin, Z.; Wei-Hua, P.; Hong-Da, C. A novel implantable multichannel silicon-based microelectrode. *Chinese Phys.* **2007**, *16*, 2116–2119.

25. Normann, R. A.; Maynard, E. M.; Rousche, P. J.; Warren, D. J. A neural interface for a cortical vision prosthesis. *Vision Res.* **1999**, *39*, 2577–2587.

26. Najafi, K.; Wise, K. D.; Mochizuki, T. A high-yield IC-compatible multichannel recording array. *IEEE Trans. Electron Devices* **1985**, *32*, 1206–1211.

27. Najafi, K.; Hetke, J. F. Strength characterization of silicon microprobes in neurophysiological tissues. *IEEE Trans. Biomed. Eng.* **1990**, *37*, 474–81.

28. Zhou, D.; Greenbaum, E. *Implantable Neural Prostheses 1*; Greenbaum, E.; Zhou, D., Eds.; Biological and Medical Physics, Biomedical Engineering; Springer US: New York, NY, 2009.

29. Naples, G. G.; Mortimer, J. T.; Scheiner, A.; Sweeney, J. D. A spiral nerve cuff electrode for peripheral nerve stimulation. *IEEE Trans. Biomed. Eng.* **1988**, *35*, 905–16.

30. Schuettler, M.; Stiess, S.; King, B. V; Suaning, G. J. Fabrication of implantable microelectrode arrays by laser cutting of silicone rubber and platinum foil. *J. Neural Eng.* **2005**, *2*, S121–8.

31. Schuettler, M.; Schroeer, S.; Ordonez, J. S.; Stieglitz, T. Laser-fabrication of peripheral nerve cuff electrodes with integrated microfluidic channels. In *2011 5th International IEEE/EMBS Conference on Neural Engineering*; IEEE, 2011; pp. 245–248.

32. Suaning, G. J.; Schuettler, M.; Ordonez, J. S.; Lovell, N. H. Fabrication of multi-layer, high-density micro-electrode arrays for neural stimulation and bio-signal recording. In *2007 3rd International IEEE/EMBS Conference on Neural Engineering*; IEEE, 2007; pp. 5–8.

33. Cogan, S. F.; Ehrlich, J.; Plante, T. D.; Gingerich, M. D.; Shire, D. B. Contribution of oxygen reduction to charge injection on platinum and sputtered iridium oxide neural stimulation electrodes. *IEEE Trans. Biomed. Eng.* **2010**, *57*, 2313–21.

34. Frazier, a. B. Recent applications of polyimide to micromachining technology. *IEEE Trans. Ind. Electron.* **1995**, *42*, 442–448.

35. Richardson, R. R.; Miller, J. A.; Reichert, W. M. Polyimides as biomaterials: preliminary biocompatibility testing. *Biomaterials* **1993**, *14*, 627–635.

36. Lago, N.; Ceballos, D.; Rodríguez, F. J.; Stieglitz, T.; Navarro, X. Long term assessment of axonal regeneration through polyimide regenerative electrodes to interface the peripheral nerve. *Biomaterials* **2005**, *26*, 2021–31.

37. Boretius, T.; Badia, J.; Pascual-Font, A.; Schuettler, M.; Navarro, X.; Yoshida, K.; Stieglitz, T. A transverse intrafascicular multichannel electrode (TIME) to interface with the peripheral nerve. *Biosens. Bioelectron.* **2010**, *26*, 62–9.

38. Rubehn, B.; Stieglitz, T. In vitro evaluation of the long-term stability of polyimide as a material for neural implants. *Biomaterials* **2010**, *31*, 3449–58.

39. Merrill, D. R.; Bikson, M.; Jefferys, J. G. R. Electrical stimulation of excitable tissue: design of efficacious and safe protocols. *J. Neurosci. Methods* **2005**, *141*, 171–98.

40. Murray, S.; Hillman, C.; Pecht, M. Environmental Aging and Deadhesion of Polyimide Dielectric Films. *J. Electron. Packag.* **2004**, *126*, 390.

41. Wolf, S.; Tauber, R. N. *Silicon processing for the VLSI era*; Lattice Press: California, USA, 2000.

42. Madou, M. J. *Fundamentals of Microfabrication: the science of Miniaturization, Second Edition*; 2nd ed.; CRC Press: Boca Raton, Fla, 2002.

43. Xia, Y.; Whitesides, G. M. SOFT LITHOGRAPHY. *Annu. Rev. Mater. Sci.* **1998**, *28*, 153–184.

44. Whitesides, G. M.; Ostuni, E.; Takayama, S.; Jiang, X.; Ingber, D. E. Soft lithography in biology and biochemistry. *Annu. Rev. Biomed. Eng.* **2001**, *3*, 335–73.

45. McDonald, J. C.; Duffy, D. C.; Anderson, J. R.; Chiu, D. T.; Wu, H.; Schueller, O. J.; Whitesides, G. M. Fabrication of microfluidic systems in poly(dimethylsiloxane). *Electrophoresis* **2000**, *21*, 27–40.

46. Kovacs, G. T. a.; Maluf, N. I.; Petersen, K. E. Bulk micromachining of silicon. *Proc. IEEE* **1998**, *86*, 1536–1551.

47. Bustillo, J. M.; Howe, R. T.; Muller, R. S. Surface micromachining for microelectromechanical systems. *Proc. IEEE* **1998**, *86*, 1552–1574.

48. Norrman, K.; Ghanbari-Siahkali, A.; Larsen, N. B. 6 Studies of spin-coated polymer films. *Annu. Reports Sect. "C" (Physical Chem.* **2005**, *101*, 174.

49. Menz, W.; Mohr, J.; Paul, O. *Microsystem Technology*; John Wiley & Sons, 2008.

50. Ohring, M. *Materials Science of Thin Films*; 2001.

51. Bryant, W. A. The fundamentals of chemical vapour deposition. *J. Mater. Sci.* **1977**, *12*, 1285–1306.

52. Bhusan, B. *Encyclopedia of Nanotechnology*; Bhushan, B., Ed.; Springer Netherlands: Dordrecht, 2012.

53. Cochlear Nucleus 5 Cochlear Implant CI512 (Technical specifications) www.cochlear.com.

54. HiFocus electrode
http://www.advancedbionics.com/com/en/products/hifocus_electrodefamily.html.

55. Wise, K. Silicon microsystems for neuroscience and neural prostheses. *IEEE Eng. Med. Biol. Mag.* **2005**, *24*, 22–29.

56. Sight, S. TheArgus® II Retinal Prosthesis System http://www.2-sight.eu/ee/system-overview.

57. Schuettler, M.; Stieglitz, T.; Gross, M.; Altpeter, D.; Staiger, A.; Doerge, T.; Katzenberg, F. Reducing stiffness and electrical losses of high channel hybrid nerve cuff electrodes. In *2001 Conference Proceedings of the 23rd Annual International Conference of the IEEE Engineering in Medicine and Biology Society*; IEEE, 2001; Vol. 1, pp. 769–772.

58. Schuettler, M.; Vanhoestenberghe, A.; Saeidi, N.; Liu, X.; Evans, J.; Colinge, C.; Demosthenous, A.; Donaldson, N. Realization of an active book for multichannel intrathecal root stimulation in spinal cord injury--preliminary results. *Conf. Proc. Annu. Int. Conf. IEEE Eng. Med. Biol. Soc. IEEE Eng. Med. Biol. Soc. Annu. Conf.* **2011**, *2011*, 2965–8.

Section II

Materials and Design

Chapter 4
Material selection and validation

In order to govern, the question is not to follow out a more or less valid theory but to build with whatever materials are at hand. The inevitable must be accepted and turned to advantage.

Napoleon Bonaparte (French military and political leader)

Electrode array, an important component of the Cochlear Implant (CI) design holds a key position in restoring the hearing process to the people with hearing loss. It represents a direct interface between the auditory nerve (biological tissue) and the electronic system of the CI. Electrode arrays from various manufacturers' are available in different designs, material, shape and size. The electrode arrays used nowadays are made of noble metals such as Platinum (Pt), Iridium (Ir) or combination of both. These FDA approved materials are used with proven technology for these medical devices (CI). In this chapter we mention about different electrode array materials used for stimulation purposes in CI electrode array. Here we discuss the CMOS compatible electrode material Titanium Nitride (TiN) as one of the possible candidate for electrical neural stimulation. A stimulation material should comply to certain requirements like the ability to deliver enough charge to the nerve ending in the harsh environment inside the cochlea. TiN sputtered thin films developed at the Else Kooi Laboratory (formerly referred as DIMES) followed by electrical characterisation in terms of the current density, Electromigration, Impedance, and Temperature Coefficient of resistance (TCR) were performed to demonstrate the capabilities required for our application. In our experiments performed TiN was able to withstand high current densities without any electromigration effect in comparison to known conductor (aluminium) which is normally preferred material in CMOS fabrication labs.

The research presented in this Chapter was a part of the Master's Thesis work from Joost van Driel entitled: *"Characterization of metals for Cochlear Implants"*.

4

4.1 Introduction

CI's today has provided a functional hearing to more than 400000 hearing impaired people and also is an industry lucrative for the researchers. CI electrode array is one of the important components of the implant which is in close proximity with the auditory neurons passing the external auditory information in terms of electrical signal through the auditory nerve to the auditory cortex. The electrode array available in the pre-curled options is placed inside the curled cochlea with the help of an straight insertion tool. During the placement, the array is pushed off the insertion tool, curling itself into the scala tympani (ST). Contact with the walls should be avoided to minimize trauma. However, 10–20% of the patients receiving a CI lose their residual hearing during the surgery due to unwanted physical contact [1]. The placement of an electrode array inside the ST in the basal turn of the cochlea is as seen in Figure 4.1.

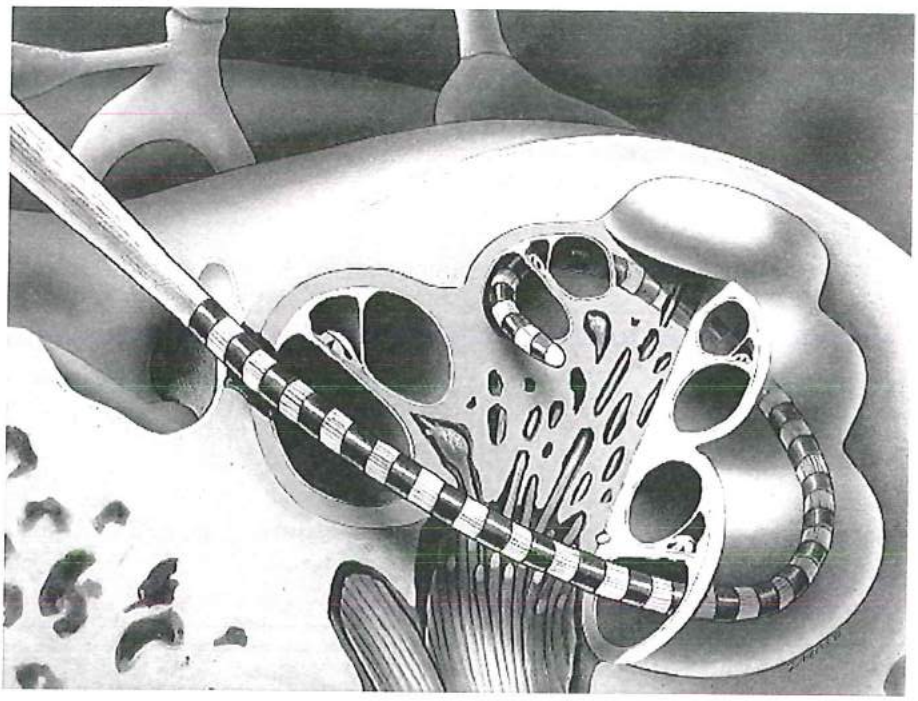

Figure 4.1 Banded electrode array placement inside the cochlea [68].

For proper insertion, the array needs to have a proper balance between flexibility and stiffness where it should neither be too stiff causing tissue damage nor should be too flexible to curl around itself during the insertion process.

4.2 CI Microelectrode array (material and methods)

Over the past decades, the design of MEA has developed from simple single channel devices to multiple site arrays consisting of 12–22 stimulation sites. The principal goal while designing these electrodes includes deeper insertion into ST to match the tonotopic place of stimulation to the frequency band assigned to each electrode channel, greater operating efficiency and reducing the intra-cochlear damage [2]. The present electrodes arrays are a bundle of Pt 90% – Ir 10% wires welded to platinum strips acting as stimulation sites. The amount of electrodes and choice of material is dependent on the model and the manufacturer. Some of them have implants made of titanium wires, attached to approx. 20 titanium electrodes, which are coated with a soft bio-compatible polymer. There are three major CI manufacturers namely Advanced Bionics Corp, Cochlear Ltd. and MED-EL GmbH. An electrode array from MED-EL GmbH is shown Figure 4.2 in which rectangular platinum stimulation sites are attached to the flexible wave-shaped Pt-Ir wires.

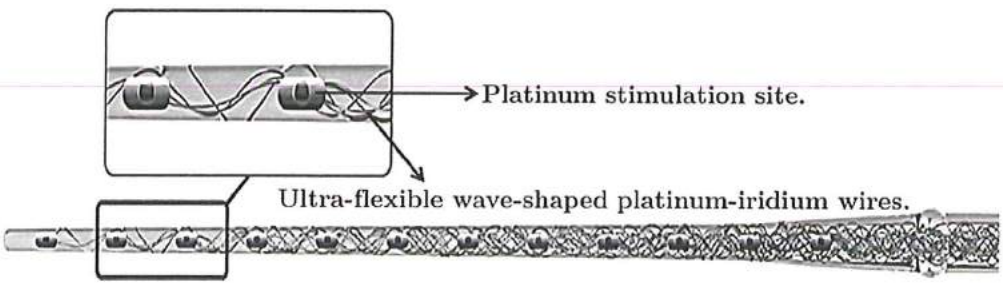

Figure 4.2. An uncurled soft, flexible electrode array from MED-EL, (*Image courtesy MED-EL* [69]).

The electrode arrays manufactured with the current technology are limited in electrode count, due to their large size in relative to the size of the ST. Also the design has restrictions for deeper insertion in ST thus depriving the access to the low frequency auditory neurons. To stimulate the speech regions of the cochlea having a tonotopic organisation it's necessary that the array should be inserted to a length of 14–25 mm from the stapes to achieve stimulation frequencies ranging from 500 to 3000 Hz [3]. Figure 4.3 shows the existing intracochlear electrode arrays. Even though they are similar, each one of them represents certain features that attempt to achieve the goal of auditory nerve stimulation inside the cochlea in different ways. The current straight Med El Combi 40+^{TM} intracochlear array (Figure 4.3 A), the longest in the market (31.5 mm in length) has a pair of foil-stimulating contacts at each stimulation site to ensure the sites facing directly the neuronal target within the modiolus and allowing ease of insertion into the ST of the cochlea. Even though Combi 40+^{TM} inserts to a depth greater than two cochlear turns, temporal bone

insertion depth studies of one full cochlear turn or greater resulted in increased trauma in 50% or more of the trial insertions [4]. The Advanced Bionics Helix™ (Figure 4.3 B,C) and the Cochlear Contour™ electrodes (Figure 4.3 D) which are specially designed pre-spiral shaped to be positioned near the modiolus and so called as perimodiolar electrodes.

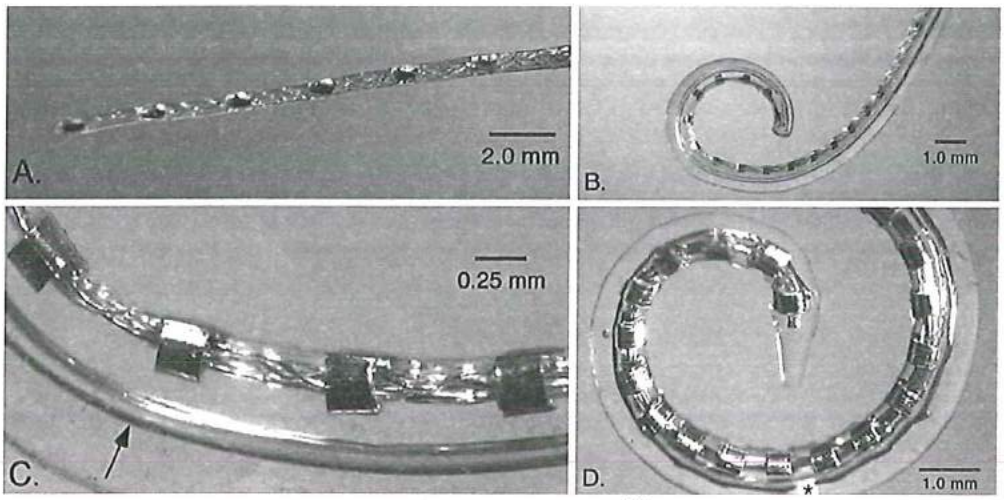

Figure 4.3. CI electrode manufacturers A) Med-El Combi 40+™ straight electrode with 12 paired contacts. B) Advanced Bionics Helix™ with closer view in C) using lead wires to increase flexibility. D) Cochlear Contour Advance™ and C) are pre-molded spirals designed to be located near the modiolus of the ear canal after insertion (*Image courtesy: Adapted and reprinted from* [70])

Both these types have flattened foil shape contacts orienting the face towards the modiolus when electrodes are fully inserted. Various temporal bone studies along with clinical threshold data confirm that the perimodiolar electrode arrays when inserted in the desired position inside the spiral ganglion to perform the stimulation results in more efficient overall activation process of these neurons [5–9]. Due to cochlea anatomical limitations it would be difficult to insert the pre-curled electrodes without straightening the array. So in order to do this a micro-channel is moulded into each spiral array (refer the arrow in Figure 4.3 C) which facilitates the use of a straight wire stylet. The function of the stylet is to hold the electrode array in a straight position at the primary stage of insertion. As the tip of the array is been inserted ahead to a position just beyond the first cochlear turn then the stylet holding is held in place and the electrode array is advanced-off of the stylet to its full insertion depth. Therefore, this procedure is often referred to as the Advance-Off Stylet (AOS) technique. Even though the AOS technique, in theory should result in less trauma if any contact occurs with the lateral wall of the scala tympani [10], recent temporal bone studies performed with Contour™ design shows that damage may result to the tissue with this electrode. This damage occurs if the straightened

Cochlear Contour™ electrode with the stylet is placed deeply inside the scala tympani. As seen from Figure 4.3D, the asterisk marker indication is the location of approximate 9 mm distance from the electrode tip. However, as reported by Rebscher S, [11] the distance from the anterior edge of the round window to the cochlea's first turn varies between 4.6 mm to 8.2 mm (mean = 6.7 mm, n = 62). Unfortunately, the current manufacturing methods leading to the sizes and the anatomical restrictions do not allow the electrode array to go deeper inside the scala tympani. To reduce insertion trauma the Contour™ and the Helix™ electrodes shown above (Figure 4.3 B, C) comprise of extra mechanical features especially the latest version of Contour™ electrode which is the Contour Advance or Softip™, has an elongated tip with soft silicone elastomer. This advancement in the tip design appeared to reduce the trauma as mentioned in a temporal bone comparison study with the standard Contour™ design [6]. Advanced Bionics Helix™ and 1J electrode array which is a slightly pre-curled version has an increased mechanical stiffness allowing minimized electrode deviation in the vertical plane through the basilar portion into the scala vestibuli. This approach adapted by Advanced Bionics for their electrode designs is effective to reduce intracochlear trauma [7,11–13].

4.2.1 Requirements for electrode arrays

The requirements for microelectrode materials used in CI's and neural implants is increasing nowadays for achieving high performance and stability in their dedicated applications. The microelectrode material selection is a key factor for the success of such implants. The technological challenges involved in the CI's led the major companies to get involved in this business and to take steps for building the future CI's. In line with the other CI components the improvement of the wired electrode array plays a key role in the overall development process. In this chapter we will restrict our discussion to the microelectrode material requirements with the charge transfer techniques between the electrode material and the electrolyte.

Electrodes are the direct interface between the biological structures (auditory neurons) and the electronic system in the CI's. Stimulation electrodes inject charge into the tissue to functionally excite the nerves by electrical stimulation. In other words, electrodes measure the electric potential for charge transfer between solid metal state and electrolyte solution in liquid state inside the cochlea. For better stability, implant electrode properties must be evaluated with respect to a biocompatible application for optimum stability, efficacy and life time with a minimum toxicity. From the material point of view the requirements of an "ideal" electrode [14–16] might be summarized as follows:

- Effective charge injection from the geometrically small available electrode surface area with minimum energy consumption for stimulation.

- Low material impedance along with low frequency dependence.
- Low tendency to create irreversible reaction products caused due to high reversible charge injection limits which avoids corrosive and inflammatory products.
- Low after-potentials and low separation at the phase boundary of electrode and the electrolyte.
- Delivery of safe stimulation charge at the functional interface with stable and low electrode impedance.
- Biocompatible material coatings accepted by the body with minimum contact tissue or electrolyte reactions and its low impedance.
- Extensive performance and material stability for years in chronic implants, i.e., negligible or no deterioration with excellent bio-stability.
- Preparation for more available electrochemical surface area by surface reconditioning methods to achieve optimum charge transfer.
- Radiographic visibility of the electrode material.

From the functioning and the biological point of view for an ideal electrode more crucial points are to be considered, however the above properties can assist us for a general selection of the electrode for a particular application.

4.2.2 Electrode materials and charge transfer methods

The most common noble metals used for stimulation are Platinum (Pt) [17], Platinum – Iridium (Pt-Ir) [18,19], Titanium Nitride (TiN) [20], Iridium (Ir) [21], Iridium oxide (IrO) [22,23]. When a metal electrode is placed inside a biological medium for. e.g. Perilymph (equivalent to saline solution) inside the cochlea then an interface is formed between the two segments. In the first electrode metal segment which is connected to electrical circuits the electrons carry the charge. While in the second biological medium (electrolyte) charge is carried by sodium, potassium and chloride ions present in the electrolyte medium. There are two basic mechanisms of charge transfer which takes place at the electrode-electrolyte phase boundary as illustrated in Figure 4.4 [24,25] as follows:

- Non-Faradaic reactions or Capacitive type charge injection in which no electrons are transferred between the electrode surface and the electrolyte medium. The reaction includes the redistribution of charged chemical species in the conductive electrolyte medium, for e.g. such reactions are observed in TiN.
- Faradaic reaction mechanism in which there is transfer of electrons between the electrode and electrolyte, which results in oxidation reduction reactions of the chemical species in the electrolyte. Faradaic reactions are further subdivided into electrochemical reversible faradaic reactions and Surface redox non-reversible faradaic reactions. In reversible process the products do not diffuse far

away from the electrode or they remain attached to the electrode surface, for e.g. Pt, Ir and with the combination of Pt-Ir metals.

- In the non-reversible case the products tend to diffuse away from the electrode surface by surface redox reactions resulting in hydrated oxide film with a high charge injection capacity, for e.g. these reactions occur in IrO.

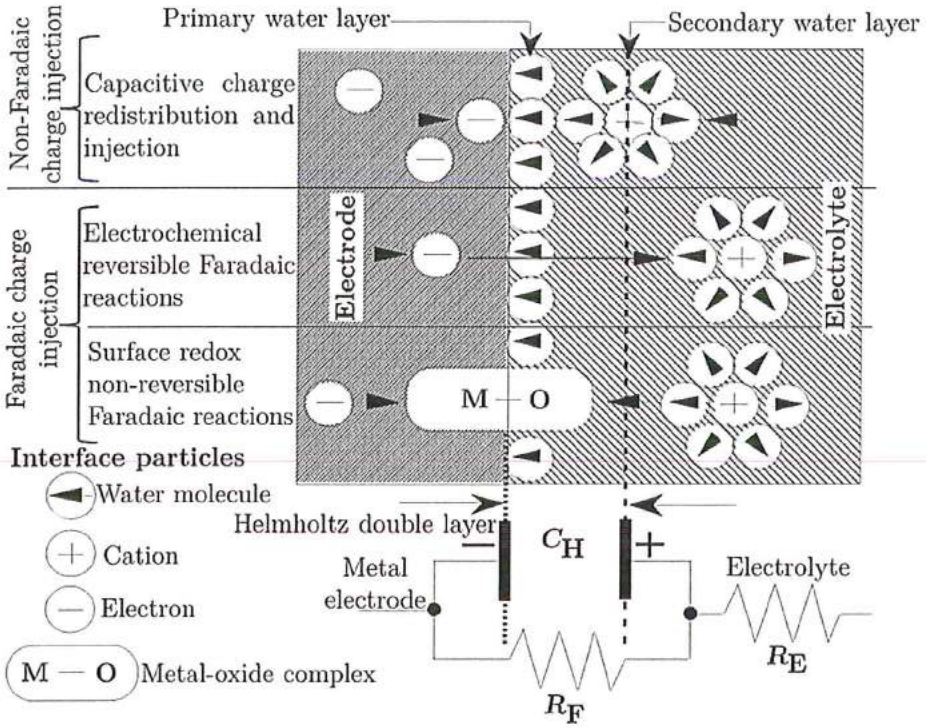

Figure 4.4. Electrochemical reactions at the electrode-electrolyte interface (*Image: Adapted and redrawn from* [24]).

In case of CI's the auditory nerve is stimulated by Pt used in the stimulation site. Electric charge is transferred from the stimulation site to nerve via a series of reversible electrochemical reactions at the electrode – tissue interface. This faradaic charge injection is usually capable of delivering more charge to the nerve ending than capacitive charge injection. The latter does not work with the electrochemical reactions, because it works in an electrostatic (charge separation or dipole orientation) or electrolytic (charge storage) manner. It depends on the material of the electrode and the charge injection phenomenon occurring at the interface. Pt utilizes faradaic charge injection, because it makes the use of electrochemical reactions to transfer this charge. If the charge density is not too high, the reactions are reversible, and are usually oxidation and reduction, or H–atom plating, which is normally the case for Pt electrode [17]. At the positive anode, OH^{1-} ions are attracted

to the platinum to form PtO leaving H^{1+} in the solution resulting in the electron(s) (e) release.

$$Pt + H_2O \leftrightarrow PtO + 2H^{1+} + 2e^- \quad (1)$$

The positive hydrogen ions are attracted towards the negative cathode to generate the H atoms for the plating process with the absorption of electrons and (OH^{1-}) ions in the solution.

$$Pt + H_2O + e^- \leftrightarrow PtH + OH^{1-} \quad (2)$$

Improved charge transfer capacity is commonly estimated by using a reversible charge injection process through double layer capacitive reactions and reversible faradaic charge transfer reactions at the electrode/electrolyte interface as shown in Figure 4.4. Primary and secondary water layers consist of a simple interface model known as the Helmholtz double layer. More complex models may be modelled if many primary layers are considered. From the metal electrode side electrons are forced towards interface surface by their attraction to positive ions present in the electrolyte solution for e.g., Na+ and H+. On the other hand electrolyte cations are also drawn to the interface surface by their attraction for electrode's electrons. An electrical filed is thus established by equal and opposite charge concentrations on each side of the electrode-electrolyte interface. In electrical analogy the Helmholtz double layer is commonly modelled as parallel RC network with plate or Helmholtz capacitance (CH) due to surface area of interface, with Faradaic resistance (RF) and electrolyte resistance (RE). More details of electrochemistry and other charge transfer models at electrode-electrolyte can be found at [26]. Normally for electrically stimulating electrodes a faradaic process is reported due to charge availability to reach a certain activation threshold for metal electrodes exceeds from the ideal capacitive transfer [26]. If these reactions are chemically neutral and reversible they are accounted in a safe zone. But once the charge density increases, then the reactions are irreversible with hydrogen and oxygen gas evolutions.

$$2H_2O + 2e^- \rightarrow H_2 \uparrow + 2OH^{1-} \quad (3)$$

$$2H_2O \rightarrow O_2 \uparrow + 4H^{1+} + 4e^- \quad (4)$$

The extent of these irreversible can lead to undesirable pH changes, metal deterioration and dissolving or formation of metal complexes [27]. These toxic products formed could also be build up in the perilymph [28]. These toxic products causes damage to the neural tissue so in order to avoid this the charge density has to

be kept below the level at which the irreversible reactions occur. These reactions can be avoided if a biphasic stimulus pulse is used so that the double layer capacitors can be charged and discharged. Most of the CI manufacturers use a biphasic charge-balanced current pulse for the neural stimulation process. By using a charge-balanced biphasic stimulus pulse the possibility of the irreversible electrochemical reactions emitting toxic products is reduced as a safe charge transfer process is ensured from the electrode to the electrolyte.

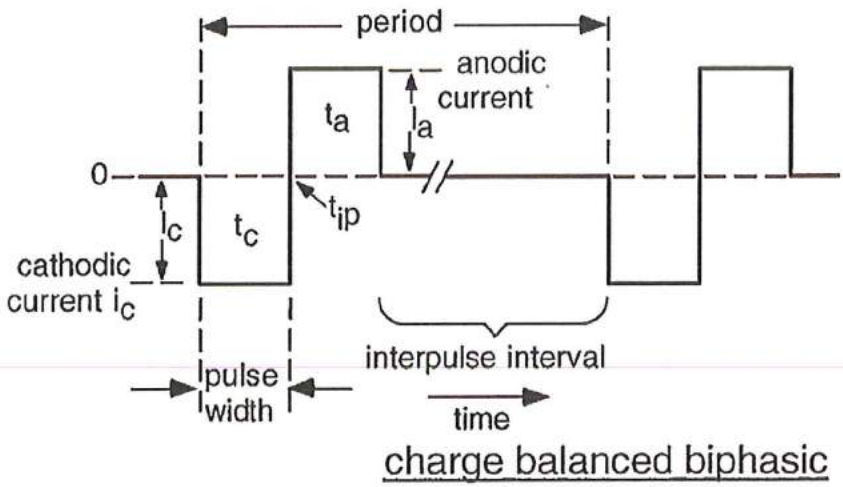

Figure 4.5. A charge-balanced biphasic current pulse [25].

A typical charge-balanced biphasic current pulse consists of an anodic and a cathodic pulse which can be symmetric, like shown here (Figure 4.5) or can be asymmetric with current amplitudes and durations that result in an overall zero net charge for the pulse (charge-balance). A cathodal current reduces at the stimulation electrode, with the direction of electron flow from electrode to the tissue. On the other hand the anodal oxidising current with electrons flows in the opposite direction. The charge delivered is simply the time integral of the current, which is $i_c \times t_c$, for a cathodal constant-current pulse of magnitude i_c and pulse width t_c [29]. The charge per phase is defined as: $q_C = I_C \times t_C$ where I_C is the absolute current level of the cathodic pulse and t_C is the duration of the cathodic pulse (pulse width). Furthermore, a charge per density can be defined as (q_C/GSA) where GSA is the geometric surface area of the electrode which is used to define the charge and current densities. This GSA is different from the electrochemical surface area (ESA) which also takes into account the surface roughness of the electrode site and which varies by greatly depending on the method and the conditions used in the measurement

process, and is difficult to predict for porous electrodes and electrodes with electroactive coatings [29].

The reactions taking at the electrode-electrolyte interface can change the pH, create hydrogen and oxygen, dissolve metal or can lead to complex combinations of metal with proteins. This happens when the charge at the electrode interface is too high, either due to the build-up of residual charge or due to a too high stimulus voltage. Møller, A. R. *et al.* [1] stated that the required charge needs to be delivered at the electrodes ranges from less than 10 nC/phase up to more than 200 nC/phase using a charge-balanced pulses of 300 µs in duration. This value is calibrated during the first turn-on of the CI and will remain the same for a long time. No large variations will occur after the surgery. This minimal charge per phase to trigger an action potential is called the threshold charge/phase. This also introduces the term threshold charge density which is defined as the minimum charge per surface area per phase that triggers an action potential. Another parameter that needs to be introduced is the stimulus rate, which is defined as the amount of pulses per second. This ranges from 100 pulses/sec up to 200 pulses/sec [30].

For any type of stimulation there is a requirement of at least a pair of electrodes, a positive and a negative cathode, as well as a stimulus generator. The excitable tissue in our case the auditory nerve closes the current loop between the two electrodes, and the neurons that are close enough to activate electrodes to pass their stimulation threshold level get activated by initiating an electrophysiological response called an action potential [31]. In maximum cases, the active or the working electrode with small surface area, is located within the neural tissue which is to be excited. The other electrode also called the counter electrode which is larger than the active electrode generally forms the body of the implanted device package [32]. There are three types of stimulation modes: monopolar, bipolar and common ground.

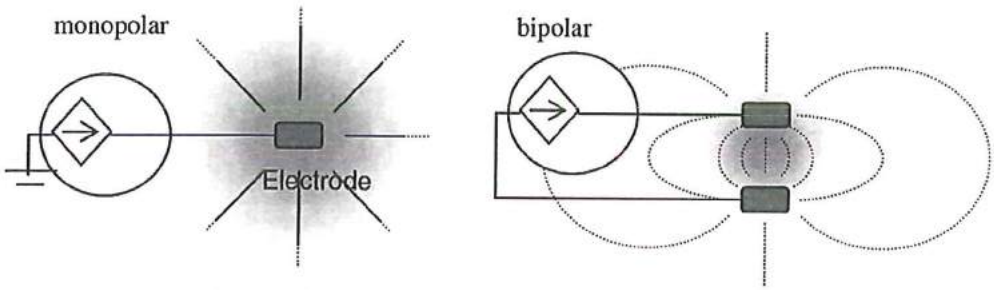

Figure 4.6. Monopolar and bipolar electrode configurations [33].

In monopolar electrode (a single current carrying electrode) excitation, the tissue excitation is only around the working electrode which is much smaller and therefore creates a larger stimulus current density as compared to counter electrode as in bipolar electrode stimulus. Monopolar electrode stimulation is omnidirectional and

less spatially specific as the propagation of the stimulus current is on a larger volume of the tissue as compared to bipolar in which the stimulation is more precise since the counter electrode is located very close to the working electrode as seen from Figure 4.6 [33]. With common ground, every electrode is kept as ground, only the stimulated electrode is put on a certain voltage. Monopolar stimulation means that there are one or more fixed ground electrodes and a potential difference is created between the stimulated electrode and the ground electrode(s).

4.3 Electrode material failures

Neural prosthesis devices used for neural stimulation demands high performance, high resolution microelectrodes for their application. Increasing demand leads to more developed devices fabricated with micro dimensions for spatial resolution along with adequate charge delivery without the generation of irreversible electrochemical reactions. In these devices the choice of the electrode material is a key factor for their success. For a typical neuronal cell bodies which are at the order of 10 to 30 µm in diameter, the microelectrode material selectivity scales inversely with the type of microelectrode material used, its dimensions, working environment and the microfabrication technique used for fabricating the devices. These microelectrode materials may have to inject considerable amount of charge, withstand extreme local pH changes at the electrode-electrolyte interface, and at the end remain functioning for a longer duration time. For long term stability these devices must be thoroughly tested before using it for a particular application. A microelectrode material used for neural stimulation purposes should have low impedances, greater corrosion resistance especially against the harsh and saline working environment and high reversible charge injection limit. This limit is nothing but the charge accumulation capacity at the electrode material which can be exchanged at the electrode tissue or electrolyte interface. The choice of the neural stimulation materials as mentioned in section 4.2.2 are chosen due to their ability to inject a considerable amount of charge with negligible electrode degradation. Apart from the noble metals mentioned above, gold (Au), palladium (Pd) and rhodium (Rh) are also preferred for electrical stimulation [34]. However, even the working of these noble metals for electrical stimulation under saline environmental conditions cause corrosion. The corrosion is observed in terms of weight loss, metal ion dissolution, scattering of these ions in the electrolyte solution and unstable tissue layer formation. Even though the corrosion rates are minimal but considering the long term functioning of the electrode which affects not only its own deterioration but also toxicity of the electrolyte. In case of Pt metal there is a continuous deterioration /dissolution during cathodic phase and deposition during the anodic phase when a charged biphasic stimulus pulse is applied to the stimulation site. David Zhou *et al.* found that a thick oxide layer is normally formed

on Pt electrode surface due to pulse stimulation conditions for DC experiments in diluted sulphuric acid. This oxide layer shows a high impedance during working which causes surface expansion, cracking of metal surface and finally leads to delamination as seen Figure 4.7 [35]. Further research and investigation is to be carried out for better understanding of the electrode surface when subjected to pulse stimulation under saline electrolyte environmental conditions [36,37]. Taking into account these material failures a need of an alternative biocompatible material with relevant microfabrication capabilities is necessary for future microelectrodes.

4.4 Why Titanium Nitride ?

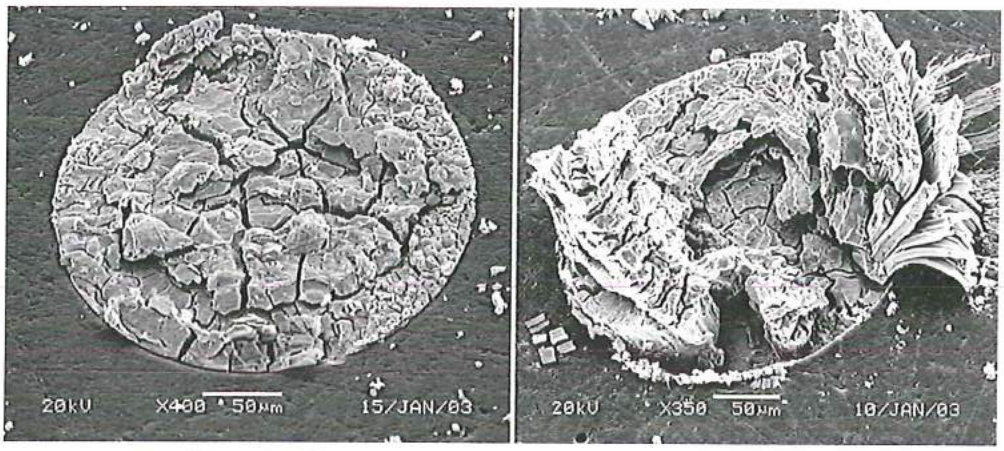

Figure 4.7. Platinum Oxide surface layer expansion and cracks [35].

Thin TiN films due to their high temperature stability, low coefficient of friction, high hardness and wear resistance not only find its applications into machine industry as an refractory material [38–40] but also due to its biocompatibility [41] and good corrosion resistance [42] makes them ideal for medical industry especially when coming in contact with the biological fluids. In the medical field TiN is used as thin film coatings on medical devices [43,44] like orthopaedic implants as well as screws and joints used in hip and knee implants. TiN is a compound of titanium (Ti) and nitrogen (N_2) in which the content of nitrogen may vary as per requirement. It is expressed by the chemical formula TiN_x (x can vary between 0.4 and 1). TiN when produced in large scales with high purity is commonly referred to as a technical TiN containing small amount of oxygen which can be removed at high temperatures. At room temperature TiN is solid and has a density of 5.2 g/cm^3, that is about double the density of glass but lower than most metals [45]. The melting point is high (@ 3000 ^{0}C), but at temperatures above 500 ^{0}C it starts to form titanium oxides in air. TiN is very hard, comparable to Corundum (a form of aluminium oxide), a material that is used in abrasives, e.g. sandpaper (Vickers hardness of TiN is 2400) [45]. The

electrical conductivity (30-70 μΩ.cm [46]) is in a similar range of steel. All physical properties depend on the nitrogen content and, partly, on the microstructure (grain size) of the material. Titanium nitride is insoluble in water and stable against cold acids but can be attacked by hot bases [45]. In semiconductor IC industry TiN is generally used as diffusion barrier layer [47–50], in glass and solar industries as reflecting materials and also as protective coatings in the ornament industry. It's use in modern microelectronics is because of its excellent electrical and mechanical properties, low electrical resistivity and metallurgical stability at high temperatures [51,52]. TiN thin films have been fabricated by many different deposition techniques (sputtering, evaporation, electroplating etc.) and have also been studied extensively for their microstructural surface properties, surface chemical composition, mechanical and electrical properties. DC magnetron sputtering has been investigated intensively and has been proved and promoted to an industrial scale for many years [53].

4.5 TiN investigation parameters

Owing to the favourable properties of TiN for manufacturing and application TiN was our favourable candidate. During investigation of TiN, properties for device microfabrication and its application were engineered which are described further.

4.5.1 Sputtered TiN films and its characterisation

There are several techniques for depositing thin film TiN films such as thermal evaporation, Physical Vapour Deposition (PVD) or magnetron plasma sputtering, ion beam coating, electroplating and chemical vapour deposition (CVD). In PVD methods a Ti target is heated in a nitrogen atmosphere in a crucible or locally by plasma or an electron beam. Ti vaporises, reacts in the gas phase with Nitrogen to TiN and is deposited on the substrate. In chemical methods mainly titanium tetrachloride is used as titanium source. Among these sputtering techniques (dc and rf) are considered the most suitable methods which are being extensively used for deposition. TiN thin layers are generally deposited by PVD techniques which results in a micro-columnar structure rendering an increased effective available surface area which is ideal for nerve stimulation purposes. The growth rate may vary from few nm/min up to several microns per hour depending upon deposition parameters and substrate surface conditions.

In the fabrication path of developing a thin film sputtering recipe for TiN separate Ti and TiN films (200 nm thick) are deposited by DC magnetron sputtering process. TiN metal layers are selectively patterned by lithographic techniques on silicon substrates. These films are sputter deposited on a p-type Si(100) wafers by DC reactive magnetron sputtering from a Ti target of 332 mm diameter with 99.999% purity, using Sigma 204 SPTS deposition system. This deposition system is

fitted with a high vacuum assembly with an diffusion pump system yielding a base pressure of about 1.332×10^{-12} mbar. By roughening and cryo-pump, fitted to deposition chamber, a base pressure of 2.106×10^{-8} mbar is achieved. At this pressure the chamber is purged with pure Argon (99.9% pure at 100 sccm) and Nitrogen (99.9% pure at 300 sccm). The working pressure during deposition is between 0.0066 mbar to 0.0133 mbar. The distance between the Ti target and the substrate is kept 275 mm. Prior to sputtering, Ti was cleaned at 5 kW by a pre-sputtering step for 2 minutes in argon atmosphere to avoid oxidation and nitriding of the target surface. Before deposition the wafers are cleaned by standard nitric acid cleaning. As the substrate temperature between 27 and 400 ^{o}C has insignificant effect on mechanical properties, sputtering is carried at 300 ^{o}C. To study the RF power effects on the crystallography, stress and surface roughness we deposited TiN at 0.5, 2.5 and 5 kW with different sputtering time to achieve 200 nm thickness. The substrate bias voltage is kept to 0 V for optimum sputtering conditions.

4.5.1.1 Stress measurements of thin films

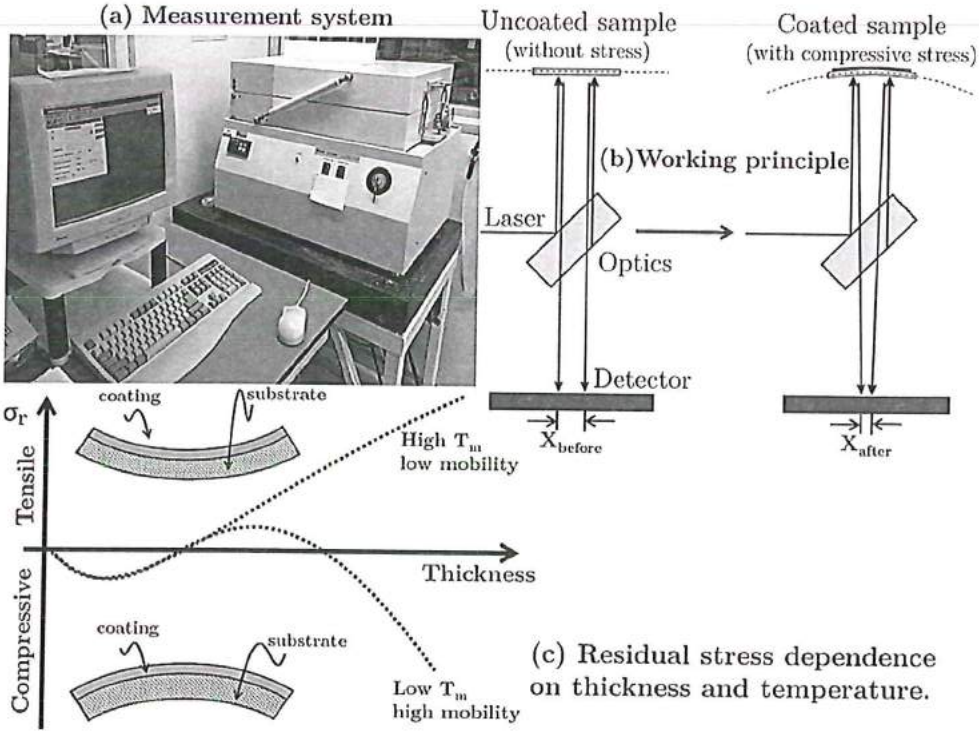

Figure 4.8. Thin film stress measurement system (a) with working principle (b) and schematized graph of residual stress dependence on thickness for low and high temperature melting materials. (*Image (c) adapted and redrawn from Abermann et al.* [55–57]).

Stress (σ) in its classical definition is a force F on a unit area A of a body. It is an important measure in continuum mechanics, as its square is directly proportional to the elastic deformation energy G_ε of a body:

$$G_\varepsilon = \frac{\sigma^2}{2E} \tag{5}$$

where E is the biaxial modulus expressed through the Young's modulus E_y and the Poisson's ration υ of the material.

$$E = \frac{E_y}{(1-\upsilon)} \tag{6}$$

Residual stress (σ_r) also referred to as the internal stress of the film which is the force left over from the deposition process which acts on the thin-film and is the sum of the two components as follows [54]:

$$\sigma_r = \frac{E_y t_s^2}{6(1-\upsilon t_f)}\left(\frac{1}{R_a} - \frac{1}{R_b}\right) \tag{7}$$

where R_a and R_b are the radii of the substrate curvature before and after the film deposition process, t_f and t_s are the thicknesses of the film substrate, respectively. Residual stress in thin films is important and has to be taken into account since high residual stress results in deformation or breakage of devices. The internal residual stress was measured on the deposited films with the help of a KLA Tencor FLX-2908 thin film measurement system using laser scanning technique (Figure 4.8 (a), (b)) which uses an simple optical principle where the difference between the two conditions (before and after layer depositions) is showed to indicate the stress in the deposited layers. The computer connected to the measurement system as shown in Figure 4.8 (a) collects and controls the data measured by the measurement system. The value of the stress is been calculated automatically by the software using the equation 7. The results are been generated in the graphical form as shown in Figure 4.9, individually for sputter deposited Titanium and TiN (200 nm thick) layers deposited at 300 ^{o}C. They were deposited with similar conditions at 0.5 Kw power. From results it is seen that TiN layers exhibits compressive stress for layers deposited at low power and tensile stress for layers deposited at high power which is shown in section 4.5.1.2.

There are many analysis performed by researchers worldwide to explain and quantify the exact mechanisms causing the stress which results in tensile or compressive stress. Normally a negative sign is assigned for compressive stress and a positive value for a tensile stress. Abermann *et al.* [55–57] investigated and demonstrated the variance of the internal stress dependability on thickness and the melting temperature of the deposited thin film material. This behavior is reproduced from his findings as shown in Figure 4.8 (c). Increase in temperature causes the mobility of the atoms in the material. If this mobility change is somehow not adjusted in the lattice structure of the material then it may result in increased internal stress levels which sometimes might go beyond the yield strength of the material itself. As per the minimum energy theory, the elastic deformation energy G_e or the strain energy caused due to the residual stress σ_r can be reduced by film delamination or cracking until an equilibrium state is reached. This type of film delamination or cracking is nothing but the stress relaxation occurring at a molecular level in these thin films at the end resulting to the area of fracture mechanics.

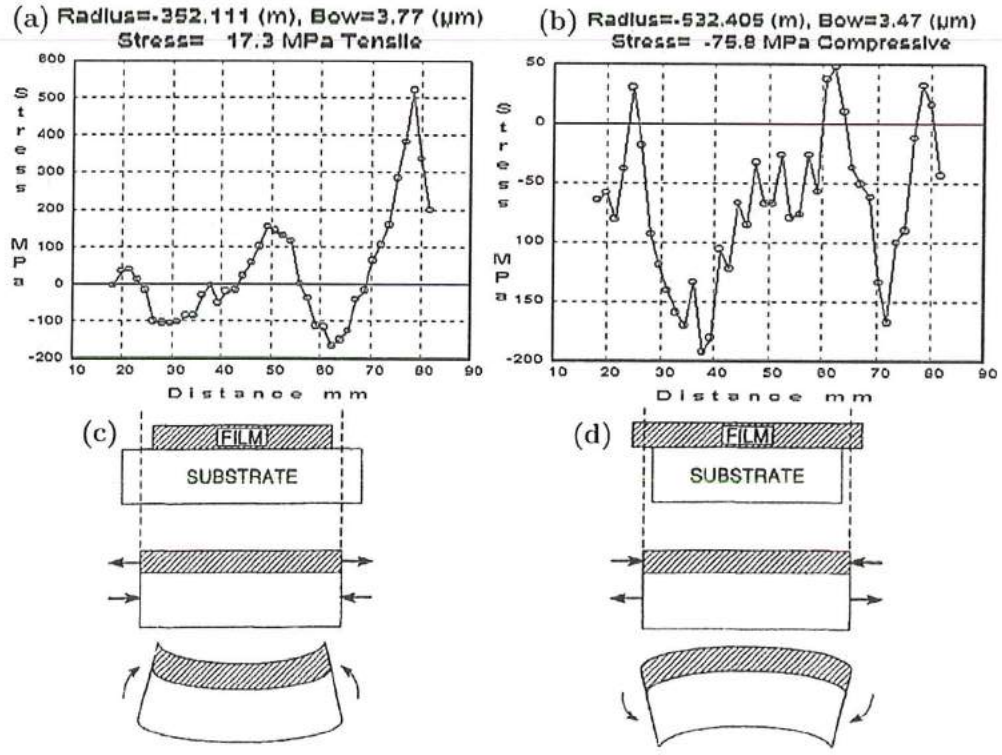

Figure 4.9. Graphical illustration of film under (a) tensile stress and (b) compressive stress at 0.5 KW power; (c) tensile stress and (d) compressive stress schematic representation (*Image (c) and (d) adapted from Ohring et al.* [71]).

4.5.1.2 XRD and AFM characterisation

X-ray diffraction (XRD) is an non-destructive method which is used to determine the lattice parameters, strain, composition and the thickness of thin films. In this technique, the crystal lattice of the layers is explored by an X-ray radiation with a wavelength (λ) in the same order of the lattice spacing.

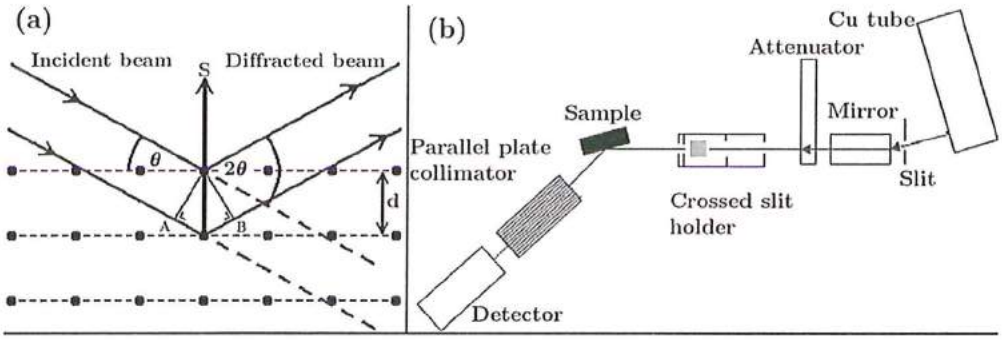

Figure 4.10 (a) Schematics of x-ray diffraction. *(Image adapted and redrawn from Moram et al.* [58]; b) Internal setup of the XRD machine used for our analysis *(Image courtesy: Ruud Hendrikx, 3ME).*

A monochromatic ray is normally filtered from a broad spectrum of X-rays generated by electron bombardment of a copper (Cu) electrode placed inside a vacuum tube. The scattering of the X-ray beam takes place due to the interaction between the surrounding cloud of atoms/ions and the X-ray photons. When the path length differs from the scattered rays by an angle $2d\,sin\theta$ as shown in Figure 4.10 (a) an constructive interference occurs. The lattice spacing can be calculated by Bragg's law:

$$n\lambda = 2d\,sin\,\theta \tag{8}$$

where n is an integer, λ is the wavelength of incident X-ray, d is the spacing between two lattice planes, S is the symbol for crystal planes, and θ is the angle between the incident rays and the lattice planes. The angle 2θ is the angle achieved by rotating the sample or the X-ray detector. Generally the samples are 3 dimensional for these X-ray diffraction process, but the approach shown by Moram *et al.* indicates that the 2D investigation is possible. Each diffracted spot corresponds to each plane in the crystal. The spacing of the plane and the size of the crystal are related to the location and the size of the diffracted spots [58]. Figure 4.11 shows the measured XRD pattern. These XRD patterns are a result of measurements performed by a D8-Discover Diffractometer system (BRUKER, XRD system) on thin Ti and TiN films. These thin films were deposited by DC magnetron PVD sputtering process at 300 ^{o}C at 5 KW power to achieve a thickness of 200 nm. These XRD measurements were done at the Department of Materials Science and Engineering of

3ME faculty. The crystal structure of the films was examined and the θ-2θ scan angles were recorded using the system setup as in Figure 4.10 (b).

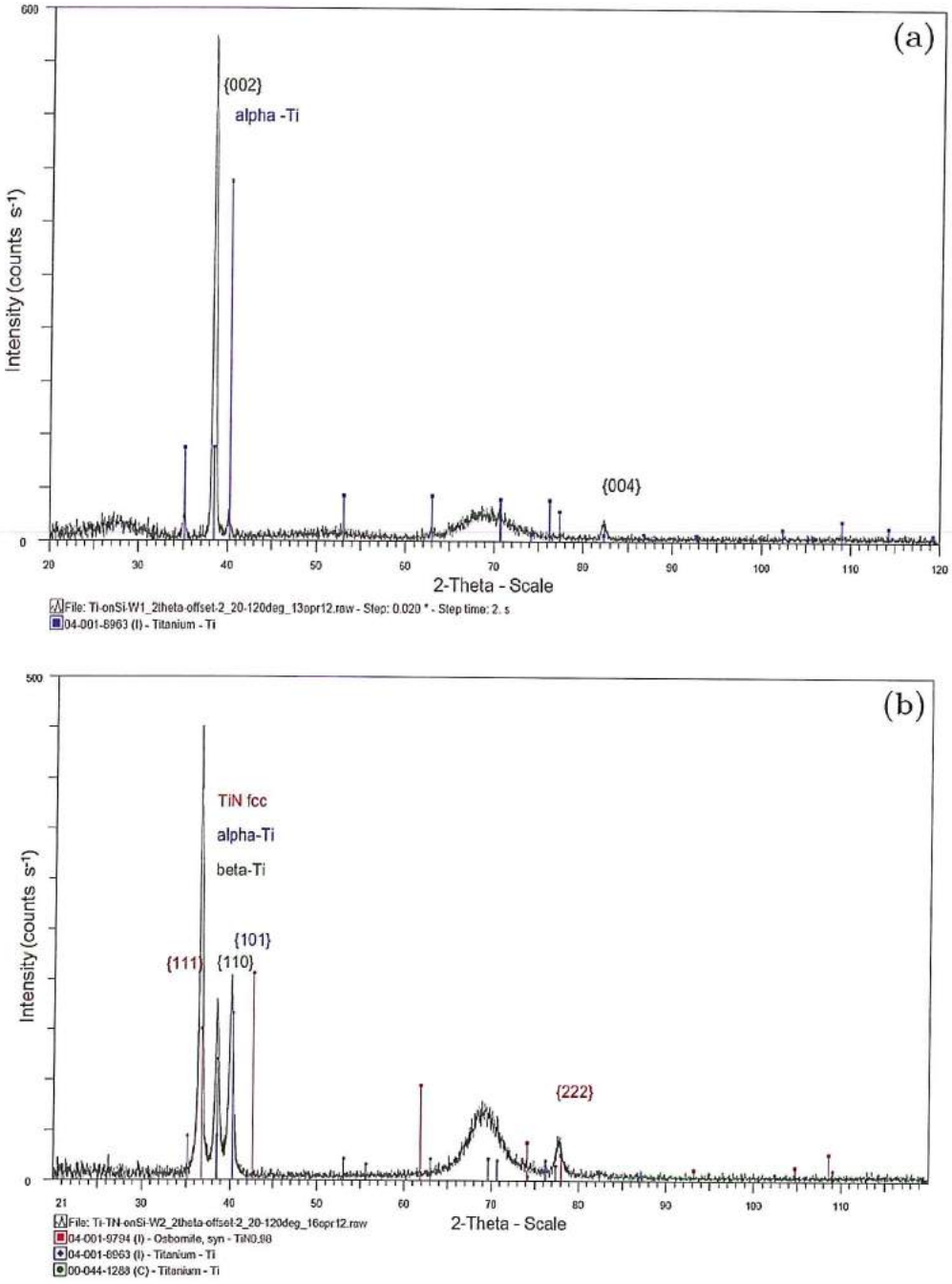

Figure 4.11 (a) XRD pattern for Titanium and ; b) TiN 200 nm thick each.

The geometry is a parallel beam of CuK_a radiation operating at 40 kV and 40 mA. After sample alignment, two diffraction patterns were recorded between 20 and $120^{O}\,2\theta$ with a fixed omega offset of 2^{O}, step size 0.02^{O} and step time of 0.5 sec. The coloured sticks of Figure 4.11 gives the peak positions and intensities of the identified phases of Ti and TiN. The blue sticks gives the peak positions and relative intensities of Ti with random orientation of all hkl planes. The alpha-Titanium (α-Ti) {001} is highly textured. For another sample with a combination of Ti (40 nm) and TiN (200 nm) layers, the cubic fcc TiN {111} phase is textured. The titanium is multiphase with presence of alpha (α) and beta (β)phases. The "bump" seen in both XRD patterns at $69^{O}\,2\theta$ is due to the silicon single crystalline substrate.

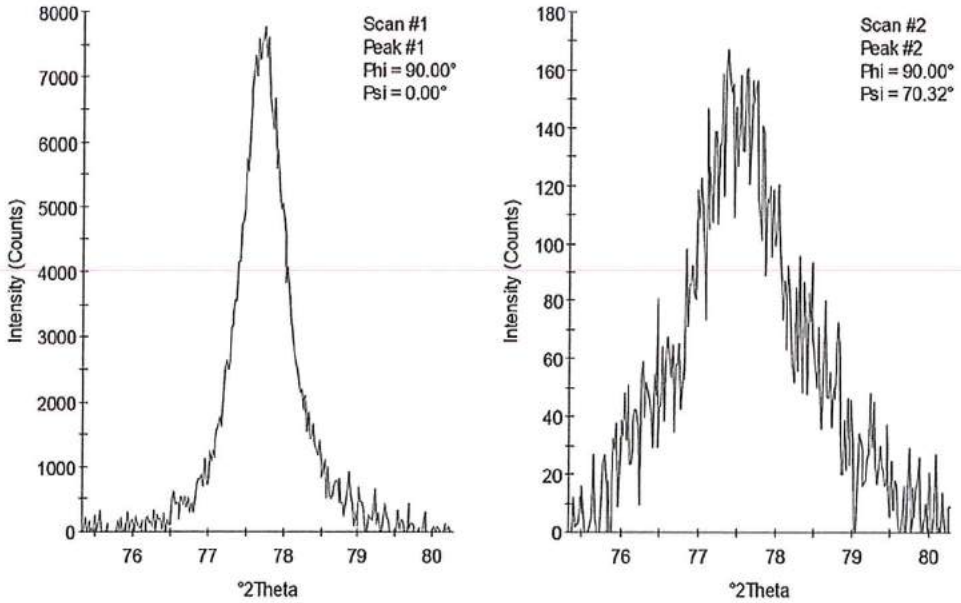

Figure 4.12 $\theta-2\theta$ scans of the TiN {222} reflections *(Image courtesy: Ruud Hendrikx, 3ME).*

XRD technique was also used to determine the residual stress in the thin films which are the stresses that remain in the material in the absence of any external forces. This XRD feature is generally termed as X-ray stress analysis (XRS). XRS uses the distance between crystallographic planes as strain gauge to calculate the internal residual stress. The deformations or imperfections in the layers causes changes in the lattice plane spacing from the stress free value to new stress value which is equal to the magnitude of the residual stress. Due to the effect Poisson's ratio, if a tensile stress is applied, the lattice spacing increases in the planes perpendicular to the stress applied, and decreases for planes parallel to the stress direction. This changed spacing distance will be same in any similarly oriented

planes, with respect to the applied stress, because of this reason this method can only be applied to crystalline, polycrystalline and semi-crystalline materials. The diffraction angle (2θ) is measured experimentally by the XRD technique and then the lattice spacing (d) is calculated from the diffraction angle, and the known x-ray wavelength by using the Bragg's law (Equation 8). Once the d-spacing values are found out then they are plotted versus $sin^2\psi$ (psi) where psi is the tilt angle. More details and equations considered for residual stress measurement can be found in the book "Thin Film analysis by X-ray scattering" (chapter 6: Residual Stress Analysis) from M. Birkholz *et al.* [59] and N. B. Thomsen *et al.* [60]. XRS experiments were performed on TiN thin films with the setup as shown in Figure 4.10 (b). The residual stress data analysis was performed with the Panalytical software Xpert Stress Plus 2.0. As mentioned earlier that TiN layer is highly textured no normal d Vs $sin^2\psi$ plot can be obtained. In a psi scan with $2\theta = 77.8^{\circ}$, the {222} reflection intensity shows maxima at psi = 0 and psi = 70.32 $^{\circ}$ (Figure 4.12). further the subsequent d spacing values of the peak maxima in the $(\theta-2\theta)$ scans at $\psi = 0^{\circ}$ and $\psi = 70.32^{\circ}$ are plotted Vs $sin^2\psi$ (psi). From the slope of the line in Figure 4.13 (a) and the elastic constants s1 and s2 (for TiN s1 = -0.49, s2 = 2.89; ref. from W.G. Sloof *et al.* [59]) the estimation of the residual stress can be made, 670 MPa. The slope is positive meaning the stress is tensile. This absolute stress value is an indication with an assumption that the layer is of single phase only for simplification purpose.

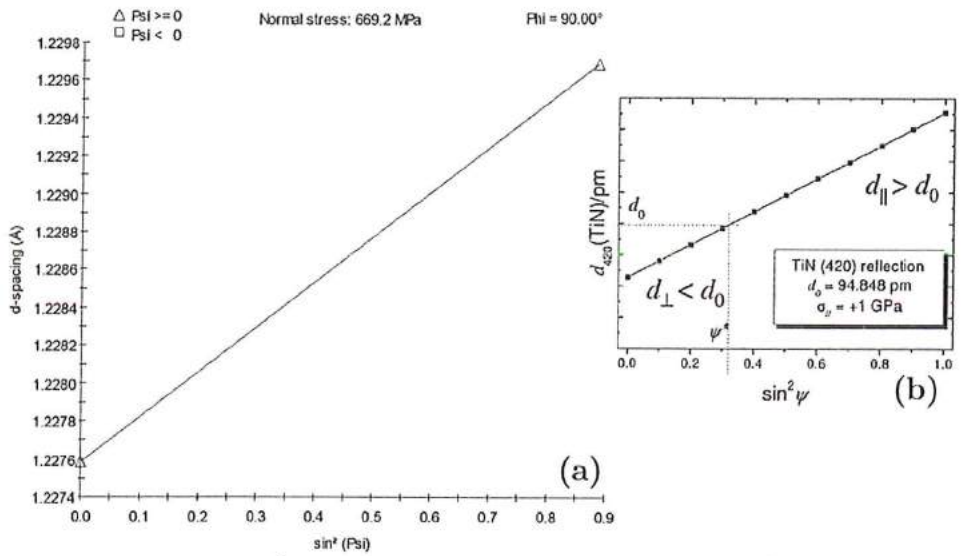

Figure 4.13 (a) d Vs $sin^2\psi$ plot of measured TiN layer and b) similar $d(\psi)$ of thin TiN film under tensile strength. (*Image: adopted from M. Birkholz et al.* [72]).

Surface topographical characterisation was done by Atomic Force Microscopy (AFM). The AFM scan was carried with semi-contact mode on both sputtered Ti and TiN layers on the surface (scan area of 5 µm×5 µm). From AFM images (Figure 4.14) Ti surface shows more hillocks type structure with less porous surface, on the other hand TiN surfaces show porous structure consisting of tapered crystallites with less hillocks than Ti surface. This textured surface of TiN is beneficial for our stimulation process adding more surface area with increased grain boundaries.

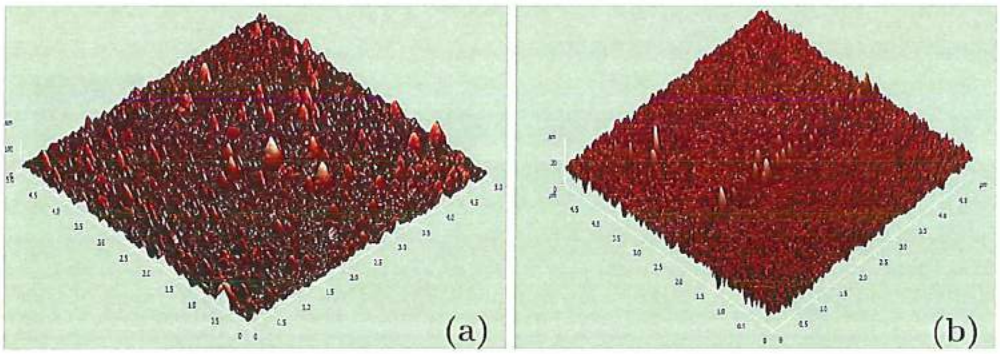

Figure 4.14 AFM topographical characterization of (a) Ti and (b) TiN films.

After the surface related topographical characterisation with internal residual stress estimation was done then the next characterisation step for TiN was to investigate for its electrical properties such as impedance, temperature coefficient of resistance, electromigration etc. which will be explained in the following sections.

4.6 Test measurement die for material characterisation.

In the next step of electrical property characterisation of the materials a test die (Figure 4.15) was designed and manufactured. The test die is a square shape (20 mm × 20 mm) silicon substrate glued and bonded at the centre of the PCB.

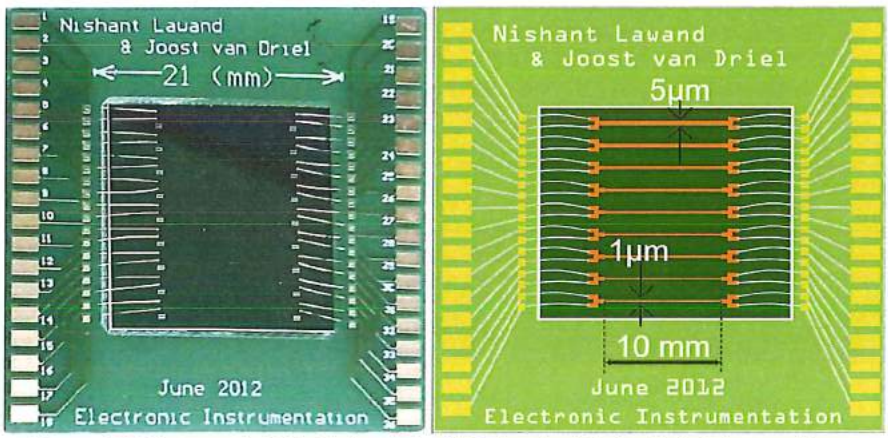

Figure 4.15 Photograph (Left side) and the CAD drawing (Right side) of the test die.

This test die contains nine parallel tracks of the material that needs to be characterized. These tracks have different widths, the smallest is 1µm and the largest is 5 µm. The other seven tracks are increments of 0.5 µm on the 1 µm track. They are all 10 mm in length and the thickness of the material (metal) that needs to be characterized differs as per different configurations shown in Figure 4.16. The TiN needs an additional Ti layer of 40 nm under it for adhesion purposes. The track ends with two Aluminium (Al) covered bonding pads at each side. Al bond wires are used to connect the die to the printed circuit board (pcb). The pcb is only used as an adapter for the measurement equipment.

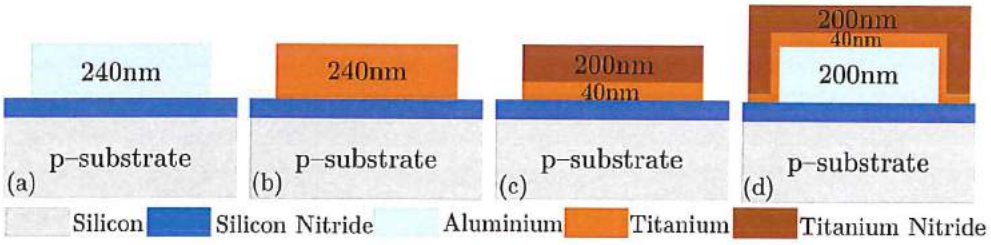

Figure 4.16 Cross-sections of different metal configurations on Si substrate.

Silicon nitride (Si_3N_4) was used as a starting base layer as an isolation of the sputter deposited and lithographically patterned metal layers from the underneath p-type Silicon substrate. The details of the fabrication process is similar to sputtering and patterning steps mentioned in the fabrication flow chart for stiff probes in Chapter 5 and also in the publication [60]. The SEM results of the fabricated dies is shown in Figure 4.17.

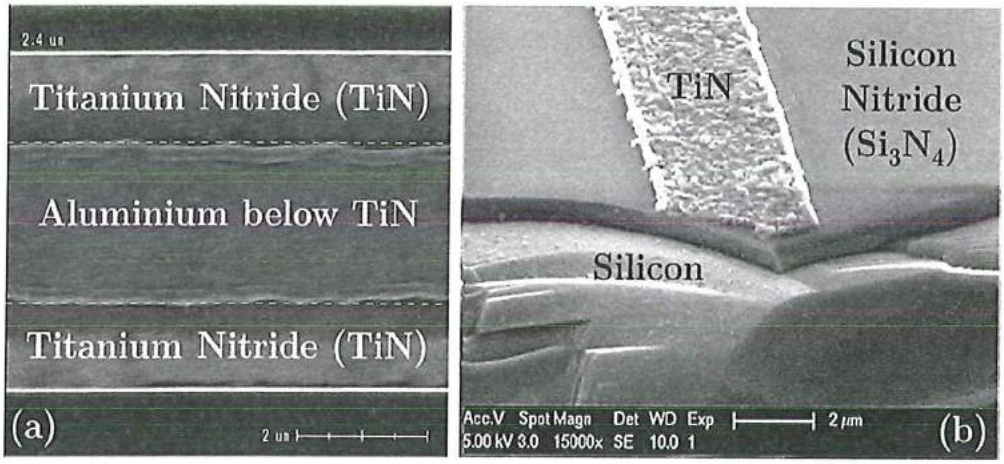

Figure 4.17 SEM images (a) and (b) of the microfabricated test die.

4.6.1 Impedance

Electrode impedance is an important parameter while fabricating the microelectrode array. An impedance measurement can be used as a standardized test for quickly estimating the roughness and porosity of a surface. It is performed by applying a small ac voltage signal (10 mV) at various frequencies (typically 10 kHz–0.1 Hz) and using the measured electrode current to calculate its impedance [61,62]. Lower impedance is generally favoured for the stimulation material which enables high charge transfer capabilities. Looking closer at the electrode–electrolyte interface, the electrode impedance is dominated by the double-layer capacitance (C_d) as explained in section 4.2.2, which is in series with the resistance of the electrolyte (R_e) [26]. This acts like a high–pass filter with a cut-off frequency at:

$$f = \frac{1}{2.\pi.R_e.C_d} \tag{9}$$

At high frequencies (>10 kHz), the capacitor C_d blocks all the current, and the resulting electrode impedance is approximately equal to the electrolyte resistance R_e. At low frequencies (~0.1 Hz), C_d acts as an open circuit, resulting in a total electrode impedance of $R_e + R_i$, where R_i is typically the irreversible reaction pathway resistor. At intermediate frequencies, the impedance is governed by the capacitance:

$$Z = \frac{1}{j.w.C}, with C \infty A \tag{10}$$

Therefore, an electrode with rougher surface would exhibit a larger surface area, and thus resulting in higher capacitance. Moreover there is a reduction in the pacing voltage loss using a porous electrode tip surface in comparison to a relatively smooth surface as shown in Figure 4.18. The decrease in voltage is mainly contributed to by decreased electrode polarization associated with increased active surface area. This would not be the case for the smoother Pt strips which are used as stimulation sites in the cochlear implant electrode arrays. Impedance measurements were performed on various test measurement dies with different metal configurations as represented in Figure 4.16. These measurements are done in order to see if the metal under test is purely resistive. If this is not the case, then it could indicate that signals (especially the square waves) are distorted due to capacitive or inductive behaviour. It is useful to know that the sheet resistance of the material can be used in further calculations. The impedance characteristics are shown as a Bode plot, including both

the impedance and the respective phase angles. The measurements were done with a *HP 4194A Impedance/Gain Phase Analyzer* at room temperature, using a short integration time (500 µs) with no averaging been done and a sweep from 100 to 40 MHz. This covers the complete range of the device. A GPIB link from the device to PC with Labview® has been used to transfer the data.

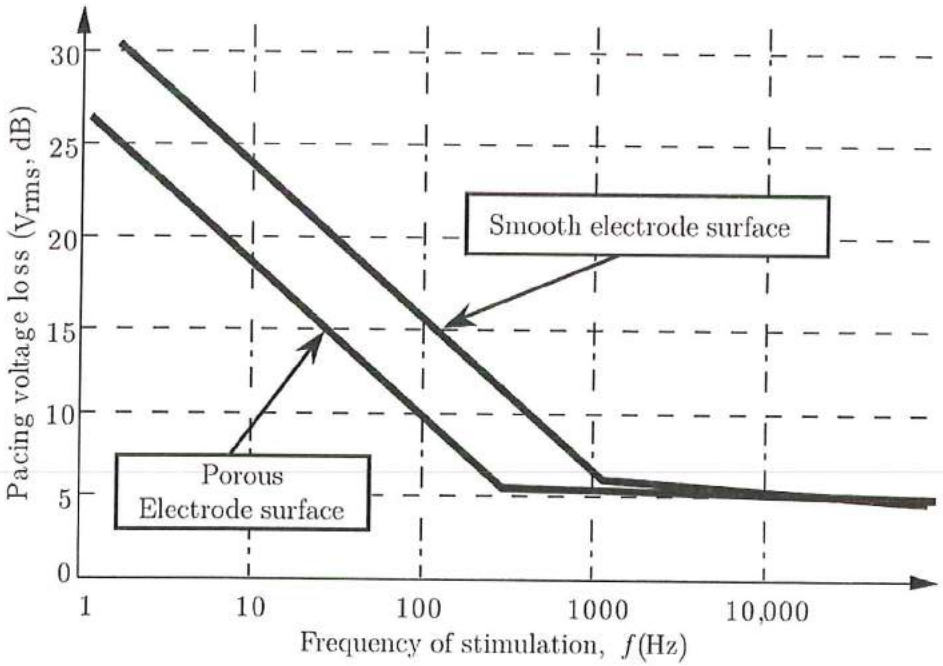

Figure 4.18 Reduced pacing voltage loss at tissue-electrode interface due to porous surface in relation to smooth electrode [24].

A typical representation of the Bode plots of the four different test dies with respective 4 different metal configurations (Figure 4.16) are shown in Figure 4.19 (a) Al (refer to Figure 4.16 (a)), (b) Ti (refer to Figure 4.16 (b)), (c) TiN (refer to Figure 4.16 (c)), and (d) Al under TiN (refer to Figure 4.16 (d)). The characteristics can be modelled as a resistor with a capacitor in parallel. The value of the resistor is the horizontal part of the impedance magnitude in the Bode plot and the capacitor defines the cut-off frequency. The capacitor acts as an open circuit at lower frequencies, but its impedance magnitude decreases with higher frequencies. The cut-off frequency is taken at the point where the phase is at -45°. There was a problem when determining the cut-off frequency for some of the aluminium tracks, because the phase did not get to -45°. The downwards slope was extrapolated at its linear piece to obtain a 'virtual cut-off frequency'. This gives an indication, but it is not as reliable as a real measurement. The modelled resistor and the capacitor values of Al, Ti and TiN are tabulated in the Table 1.

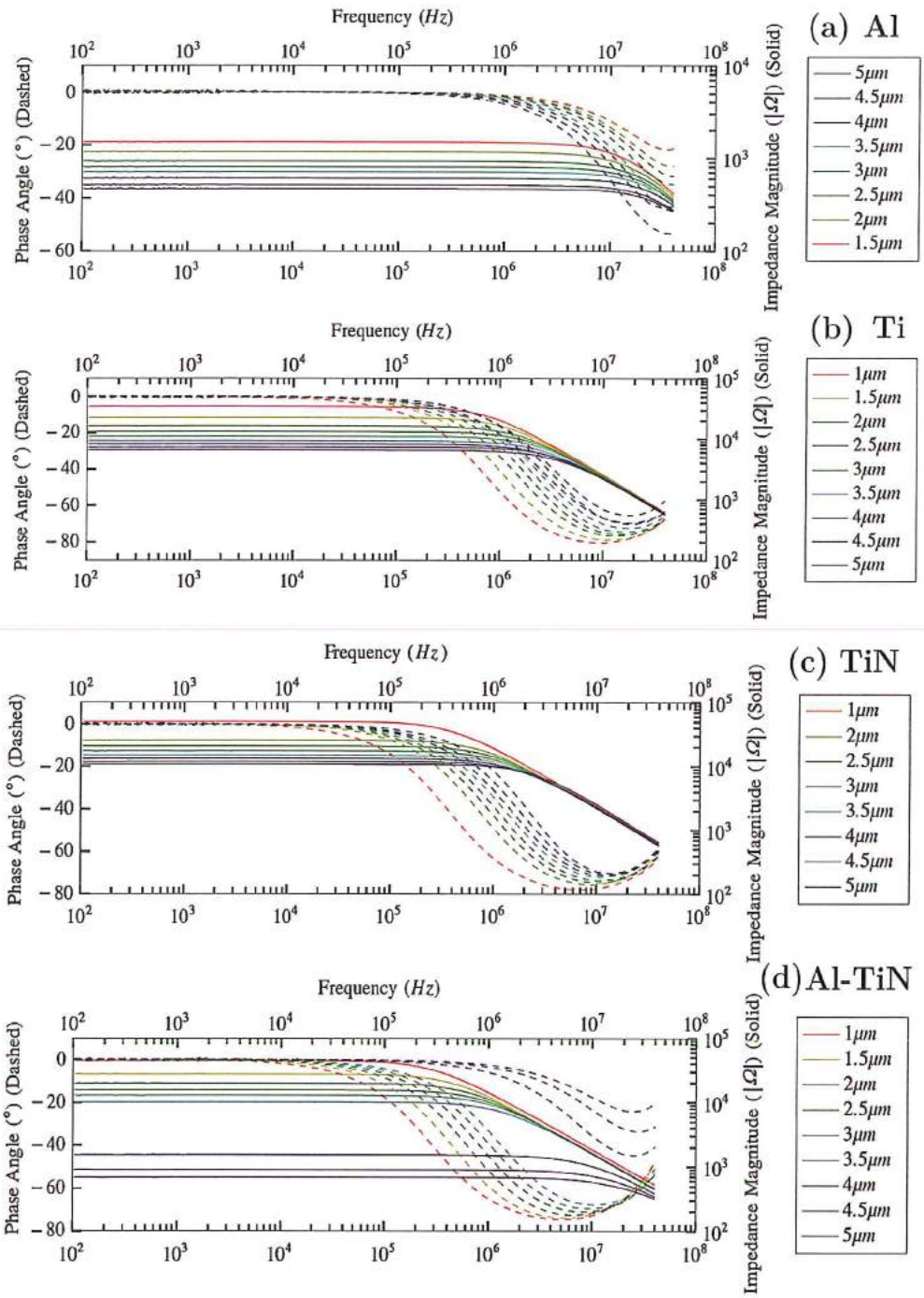

Figure 4.19 Bode plots of the measured test dies for the respective metal track width configurations; (a) Al (240 nm), (b) Ti (240 nm), (c) Ti (40 nm) + TiN (200 nm), (d) Al (200 nm) underneath Ti (40 nm) + TiN (200 nm).

The Bode plot of the Al-TiN test die (Figure 4.19 (d)) shows that 3 of the nine tracks (between –60 to –40° phase angle) have a combination of Al and TiN. This can be concluded from the fact that 3 of the tracks have lower resistance than the regular TiN test die. The (parasitic) capacitance is mostly from the track to substrate with Si_3N_4 in between. The change in impedance will not affect the working of CI, because the cut-off frequency is much higher than the spectrum that CI's use.

	Al		Ti		TiN	
Track width	R (Ω)	C (F)	R (Ω)	C (F)	R (Ω)	C (F)
1.0 µm			34300	3.85×10^{-11}	50400	4.53×10^{-11}
1.5 µm	1488	3.89×10^{-11}	22200	3.90×10^{-11}		
2.0 µm	1165	2.25×10^{-11}	16400	3.84×10^{-11}	25800	4.50×10^{-11}
2.5 µm	923	3.62×10^{-11}	13200	3.94×10^{-11}	20600	4.50×10^{-11}
3.0 µm	811	3.48×10^{-11}	10900	3.92×10^{-11}	17400	4.53×10^{-11}
3.5 µm	705	2.55×10^{-11}	9320	3.90×10^{-11}	14900	4.36×10^{-11}
4.0 µm	610	2.46×10^{-11}	8110	4.07×10^{-11}	13300	4.28×10^{-11}
4.5 µm	518	2.32×10^{-11}	7350	4.06×10^{-11}	12000	3.91×10^{-11}
5.0 µm	470	1.14×10^{-11}	6530	3.78×10^{-11}	10800	3.59×10^{-11}

Table 1 Calculated resistance and capacitances values for different metal tracks.

4.6.2 Electromigration

The current carrying capability of a conductor is mainly determined by the electrical resistance of the chosen metal and physical dimensions. Resistance of a uniform conductor can be calculated as follows:

$$R = \rho \frac{l}{A} \tag{11}$$

where, ρ is the electrical resistivity, l is the length and A the cross-sectional area of the current carrying conductor. The materials examined here are also the probable candidates for interconnects which were designed to withstand possible failures due to electromigration (EM) during its intended lifetime usage of the devices in the saline environment (bodily fluids). Electromigration is the phenomenon normally observed in the interconnects used in integrated circuits which damages the metal when the current density exceeds the safe operating limits. In cochlear implants (CI's) this parameter is important while designing the metal interconnects which connects the bond pads with the stimulation sites in the micro electrode arrays

(MEA's). Electromigration occurs when the dimensions shrink, but the amount of current that needs to be transported stays the same. Earlier this was only a problem in integrated circuits, but cannot be neglected for the metal tracks in CI's. Instead of the Pt wires used in CI's that has a diameter of 0.025 mm now tracks of almost 10 µm wide and 240 nm thick are been used in our MEA design and generally observed in the same range as the modern MEA's. This leads to a current density increase by a factor of at least 100. It is possible to use multiple electrodes, decreasing the amount of current per channel, but there will be an increase in the current density of a single track. Electromigration is the phenomenon which follows a forced atomic diffusion that occurs due to a large electric field [63]. When DC current flows through the conductor some of the free electron momentum is transferred to the metal ions, causing transfer of material in the direction of current flow. These metal ions are physically transported from one place to another, it will cascade until there is no metal left at the spot where it happened, because there is a local increase of current density. This effect causes build-up of the metal atoms that form hillocks as well as voids at the grain boundaries of the metals [64]. Hillocks can result in short circuits between densely spaced lines, whereas voids cause local resistance increases leading to complete line failure (refer Figure 4.20).

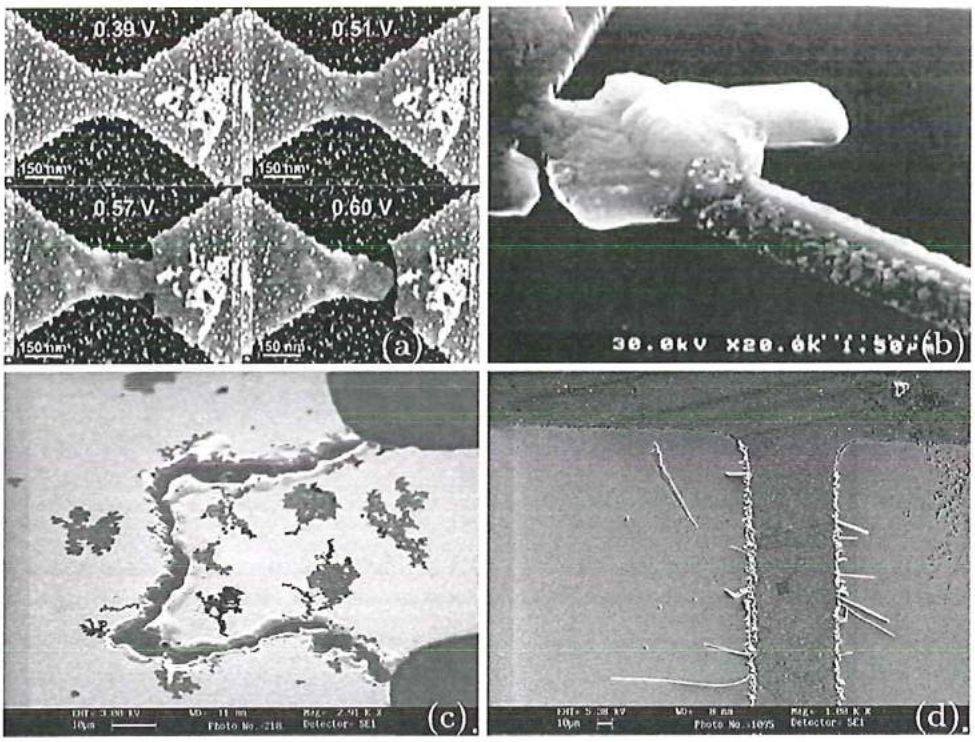

Figure 4.20 (a) Electromigration in gold at different voltages [73], (b) Hillocks [64], (c) Voids in interconnects and Whisker growth due to electromigration [74].

The most widely used equation (Black's equation) developed by J. R. Black to estimate the Mean-Time-To-Failure (MTTF) for interconnects in IC industry is as below:

$$MTTF = \frac{A}{J^n} exp\left(\frac{E_a}{kT}\right) \tag{12}$$

where, A is a constant which contains a factor involving the cross-section area of the film, J is the electric current density (A/cm^2), n is the scaling factor, E_a is the activation energy in electron volts which mainly depends on the structure of the film material {(0.7 eV for Al) (8.0406 eV or 775.8 ± 29.8 kJ/mol for TiN [65])}, k is the Boltzman's constant (1.38×10^{-23} J/K) and T is the film temperature [66]. Normally interconnects on Silicon (Si) or integrated to Si structures can withstand higher current densities without melting the electrical wires, since the thermal conductivity of Si is high. For increased lifetime of the interconnects the operating current densities has to lower than the critical values. Also elevated temperature operating conditions can lead to reduced MTTF. In our MEA designs (for detailed MEA designs refer to Chapters 5 and 6) the interconnects will be "sandwiched" between two polyimide layers and moreover the operating temperatures of devices would not exceed 50 ^{o}C. Stress due to constant electric field and operating temperature fluctuations can also lead to the phenomenon of EM. To validate our materials (Al, Ti and TiN) for potential EM effect a setup was designed where similar test measurement dies containing tracks for different width where used. The EM phenomenon was tested by passing current through the smallest (1 µm) track. The smallest track was chosen because of the high current density even though the heat dissipation stays low. This is relevant, because a failure due to a too high temperature was not the goal of this test. The test was done with the three materials (Al, Ti and TiN) using the *Yokogawa GS200 DC voltage/current source* and *Binder FD53 Drying/heating oven*. The GS200 is controlled and monitored using Labview® through a GPIB connection. The test die is put in the oven at a constant current (1.1mA) temperature (37 ^{o}C). The measurement stops when the voltage hits 30V, the maximum of the *GS200*. At this point the track will be interrupted. Both Ti and TiN did not show any problems after one week of applying approximately 28 V (due to constant current) at 37 ^{o}C. The TiN was also exposed to higher temperatures, but apart from the higher potentials due to the temperature coefficient of resistance (TCR), there was no effect. Al did break down after 3.5 days of passing 1.1mA (current density of 5.5 mA/µm^2) and the last 30 minutes are as shown in Figure 4.21. The first damage (invisible) to the metal track was done at 500 seconds, a slight

increase in the potential was the result of that. A part of the track was missing, but there was still a direct electrical connection. However, the current density at the location of the damage was higher than before, so a fatal damage will occur faster. This can be observed between 1600 and 1900 sec (refer graph in Figure 4.21), the line breaks down after some spikes. These spikes show the physical movement of the track due to the applied electrical field, but the first two movements did not result in a fatal breakdown. A image using a regular light microscope was done to verify the breakdown (refer image in Figure 4.21). Ti and TiN metals apparently did not encounter any EM failures in this test.

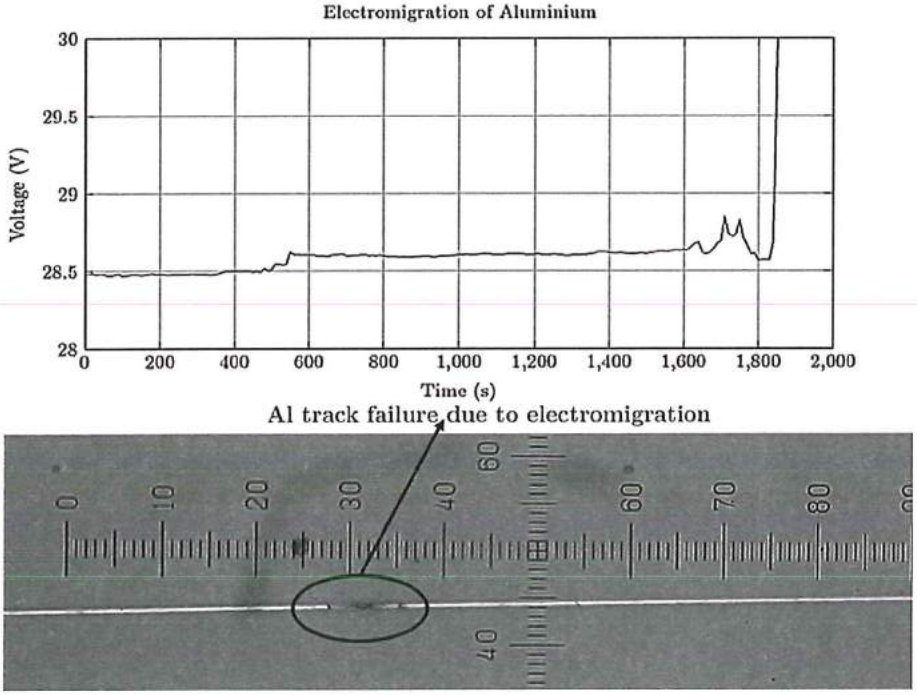

Figure 4.21 Graph of the last 30 min. of the electromigration test on Al (Note: Offset of 3×10^5 sec is present as the test was running for 3.5 days) and the microscopic image showing a visible damage to the 1 µm Al track during the test.

4.6.3 Temperature Coefficient of Resistance (TCR)

TCR is a material dependent parameter that describes the change in the impedance with respect to temperature. It determines the relation between the resistance and the temperature of the material. For most materials the resistance increases with increasing temperature, some materials exhibit an opposite behaviour. These materials have a Positive Temperature Coefficient (PTC) or a Negative Temperature Coefficient (NTC). In rare occasions it is possible that the resistance is

close to 0 Ω when it reaches to a very low temperature. It depends on the material temperature, but the highest temperatures reported are around 125 °K. The TCR of a metal can be described by a simple equation 13, where $\rho(T)$ is the resistivity of the material at temperature T given in (Ω.m), ρ_0 is the resistivity at reference temperature T_0 and α is the TCR [67].

$$\rho(T) = \rho_0 \left\{1 + \alpha\left(T - T_0\right)\right\} \tag{13}$$

$$\alpha = \frac{1}{\rho_0}\left[\frac{\partial \rho}{\partial T}\right]_{T=T_0} \tag{14}$$

The resistivity ρ can be replaced with the resistance R in equations 13 and 14, the α stays the same, because its unit is $(^{\circ}C)^{-1}$. These (linear) equations apply to simple materials like the metals, but semiconductor materials comply to non-linear equations. Although the human body temperature remains fairly constant (except in unusual situations for e.g. illness, disease etc.), a minimal temperature range of the human body is something to be kept in mind when designing and calibrating the CI electrode arrays. The method that we have adapted to determine the TCR is to measure the resistance at different temperatures. The results are then combined with equation 13 to obtain the TCR. The resistance should not be very susceptible to temperature changes, thus the TCR must be relatively low.

Three measurement test dies with Al, Ti and TiN were investigated were investigated to determine the coefficient for each material. A *Yokogawa GS200 DC voltage/current source* with a GPIB link to Labview® and a *Binder FD53 Drying/heating oven* have been used to obtain reliable results. A current sweep from zero to 30 V is done at different temperatures. The current step size can be adjusted in Labview® front panel. Materials with a higher resistance have a smaller step size to achieve the same amount of steps per material. The current is applied through two of the four connections of a track at the test die. The voltage is measured at the other two connections of the track. This four point measurement makes sure that the measured voltage is only the potential difference over the track. The measurements were done for each test die with a possibility to switch between tracks. The applied current is plotted against the measured voltage. Ohm's Law tells us that: V = I × R, so the slope of the (linear) graph is the resistance. The slope is obtained using the fit function of Matlab. The TCR is then calculated using equation 13 by plotting the calculated resistances against the temperatures. The results from the plotted graphs can tabulated as in Table 2.

Track width (µm)	Al	Ti	TiN
1.0	3.845×10^{-3}	4.651×10^{-3}	5.826×10^{-4}
1.5	3.656×10^{-3}	4.559×10^{-3}	5.818×10^{-4}
2.0	3.572×10^{-3}	4.504×10^{-3}	5.840×10^{-4}
2.5	3.588×10^{-3}	4.457×10^{-3}	5.852×10^{-4}
3.0	3.493×10^{-3}	4.417×10^{-3}	5.867×10^{-4}
3.5	3.311×10^{-3}	4.385×10^{-3}	5.871×10^{-4}
4.0	3.3×10^{-3}	4.352×10^{-3}	5.915×10^{-4}
4.5	3.223×10^{-3}	4.321×10^{-3}	5.967×10^{-4}
5.0	3.333×10^{-3}	4.302×10^{-3}	6.050×10^{-4}
Average →	3.5×10^{-3}	4.4×10^{-3}	5.9×10^{-4}

Table 2. The TCR's of the respective materials on test dies ($^{o}C^{-1}$).

The results obtained should be similar for each material, but for Al and Ti it shows a difference between the different track widths. TiN shows linear results and has a relatively low TCR, which is favourable for a different applications. Al changes its resistance with an increase of the current, probably due to self-heating as shown in Figure 4.22. The notable increase in resistance of Al is probably due to self-

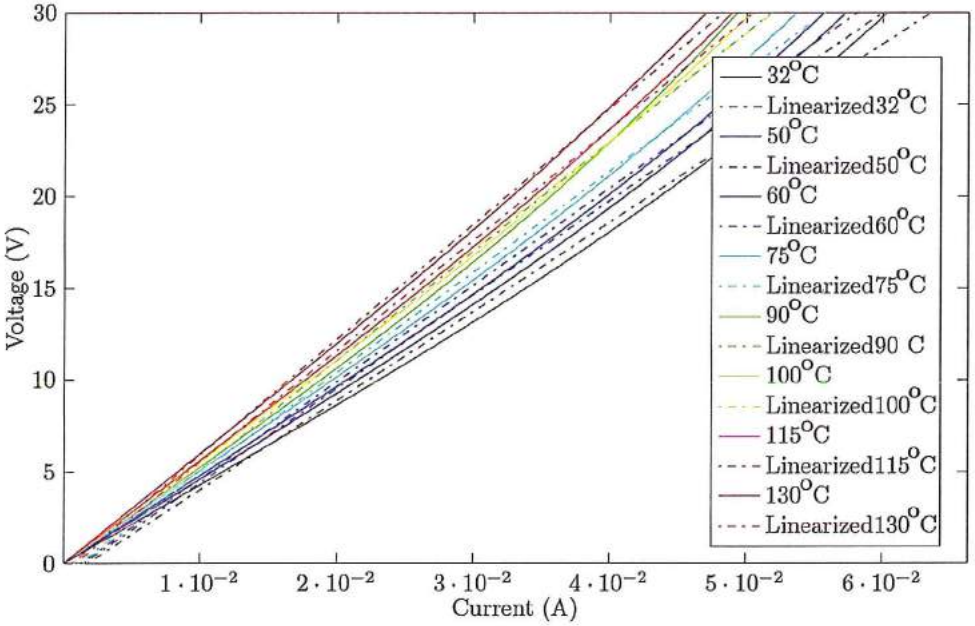

Figure 4.22 Non-linear current-voltage relationship of the 5 µm Al track on the test die due to the differences in the TCR values listed in Table 2.

heating, because the current is much higher than supplied to Ti and TiN and each measurement took more time.

4.6.4 Physiological saline solution immersion test

The current CI manufacturers when develop the future CI's are focusing on using the long term stable materials for the intended usage period of the device. Polymer delamination from metal, surface rupture, cracks, material degradation are some of the common problems associated with the materials been used for the electrode arrays when used in the harsh electrochemical environment of cochlea.

In order to test the stability of the material (TiN) in saline environment an accelerated test is proposed with a continuous stimulation with different stimulus waveforms, for example: a sine, square or saw tooth wave. During the test, the current through the metal track is measured. A change in the amount of current indicates an alteration in the circuit, which could be material damage. This can be verified by an extended impedance measurement and an microscopic inspection. If the impedance does not change over time during the testing period, then this measured parameter gives an initial indication towards material stability in the saline environment. Below are the tests performed in this physiological saline solution immersion test on the measurement dies which consists of metal tracks (TiN) which are been exposed to the saline environment by mounting a glass container filled with saline solution as shown within the second graph of Figure 4.23:

1) The impedance of a track of the test die is analysed while being exposed to the saline solution.
2) The impedance of the saline solution is measured while different potential waveforms are applied to a track.

The above mentioned impedance tests also indicates for any fatal damage in the track. An intact track can be modelled as a resistor in parallel with a capacitor, but a damaged track is a full capacitor, due to the lack of a conducting path. The impedance of the saline solution might give an indication of a change in dissolved products like the metal of the track. Saline solution is created by mixing 9 grams of kitchen salt (NaCl) with 1liter of demineralized water. This mimics the amount of sodium ions in perilymph. The glass container on top of the test die holds 1ml of a fluid. The saline solution does not cover all of the tracks on the test die, the glass container and its glue cover the four outer lines. The 1 µm, 1.5 µm, 4.5 µm and 5 µm tracks are not exposed to the saline solution. These are not considered during measurements, the 3 µm track is mostly used. The first two tests have been performed using the *HP 4194A Impedance/Gain Phase Analyzer* at room temperature, using a short integration time (500 s), no averaging and a sweep from 100 Hz to 40 MHz. Furthermore, a *HP 33120A Function/Arbitrary Waveform*

Generator and an *Agilent 34401A 4 1/2 Digit Multimeter* is used for the second and the third test. All of the instruments are controlled using GPIB and Labview. The first test, measuring the impedance of a track over time, results in a Bode plot as shown in Figure 4.23. It shows the difference between a TiN track in air and in saline solution. The interface between the saline solution and the track introduces an extra parallel capacitor with resistance. This particular test consists of 664 measurements which were taken for 8 consecutive days. The details of these measurements are plotted in a Bode plot in the Appendix region which exhibits similar curve profile as shown in Figure 4.23. During the experimentation, the saline solution was completely evaporated in 3 days leaving back some salt sediments. To compensate this addition of demineralized water was done when necessary. Due to salt deposition damaging of the bond wires was an visible effect which resulted in total breakdown. Glob-Top (a glue mostly used in IC industry to isolate the wire bonds) was used to seal the glass container edges touching the PCB. Its low surface tension makes sure that the bond wires do not break when it cures.

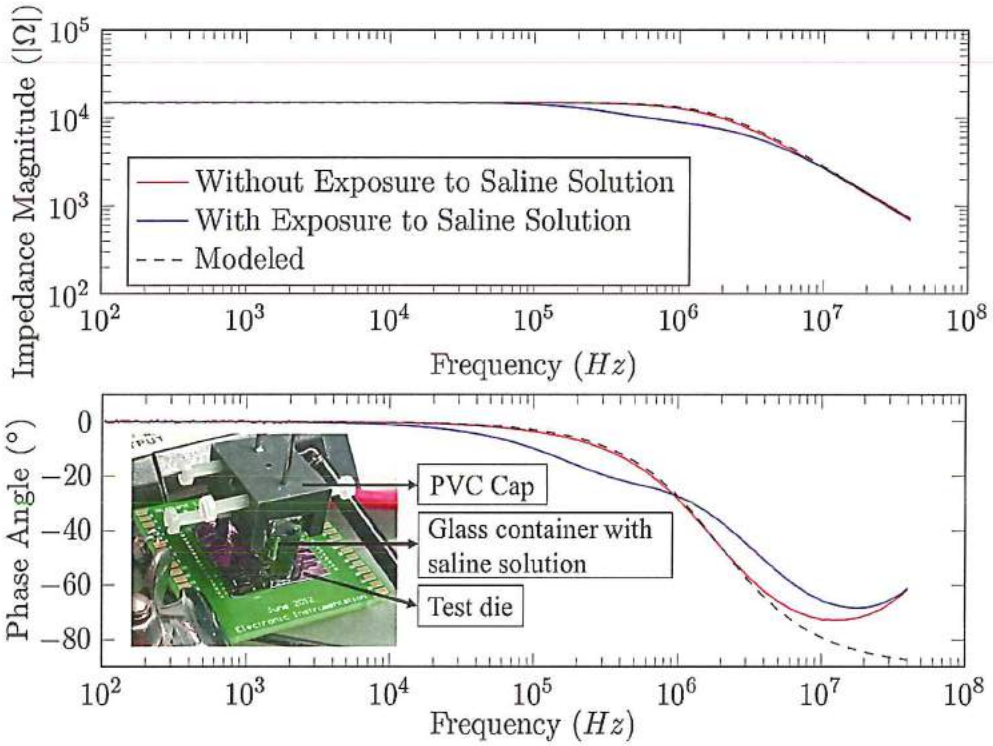

Figure 4.23 Bode plot of 3.5 µm TiN track with and without saline exposure along with modelled resistor and capacitor in parallel of the unexposed track.

The impedance of the saline solution was observed and noted down for a week before the salt deposition destroyed uncovered Al bond wires resulting in the setup failure. The addition of another material in the saline solution could introduce a shift in the impedance spectrum. Various measurements (1014 in total) were done until the test setup broke down. The bode plot of these measurement is shown in Figure 4.24. The figure does show a difference in impedance over time, this indicates the evaporation of the water until no fluid left. This was observed after 4 days (marked by the light blue lines), the duration of the test was eight days. Demineralized water was supplied a day after, resulting in a small decrease of the absolute value of the impedance. The peak to peak voltage was set to 5 V with an resulting RMS current plot as seen in Figure 4.25. All tests were performed at room temperature (25 °C).

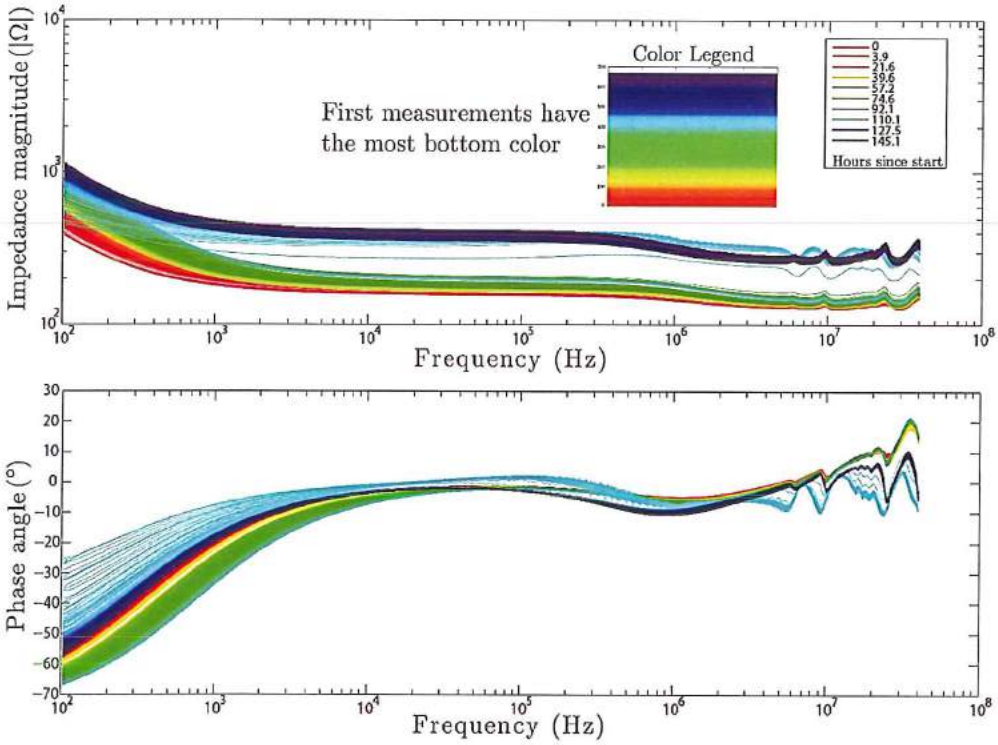

Figure 4.24 Impedance spectrum of the saline solution when using TiN tracks.

In Figure 4.25 the readings beyond 130 hours shows the complete evaporation of the saline solution. The current was still some current consumption during the measurements, indicating the survival of the metal track. Due to evaporation useful conclusion was hard to judge from the impedance spectrum. As an improvement another setup with commercial saline solution is recommended to avoid evaporation

resulting salt depositions. Another suggestion would be to perform similar experiments for longer durations to validate the material for long term stability.

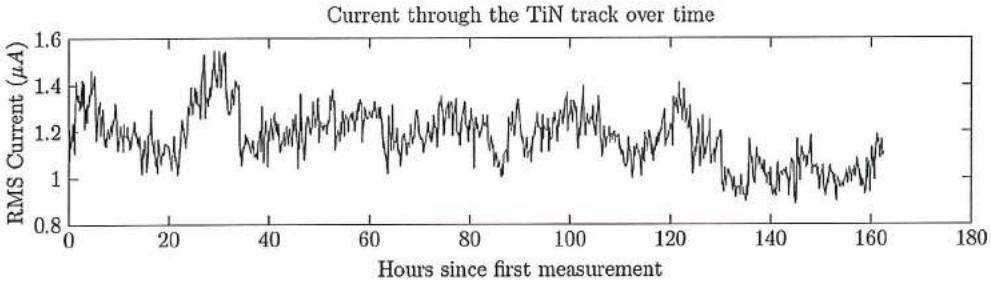

Figure 4.25 Current measurement trough 4 μm TiN track during saline solution impedance measurement.

4.7 Conclusions

This chapter exhibits the material problems associated with the current microelectrode materials been used in the CI devices. Requirements for an ideal electrode array with the related charge transfer methods occurring at the electrode electrolyte interface were explained with the normal failures encountered with MEA material when operating in the harsh cochlear environment. In our material investigation for MEA we demonstrated the characterisation of the fabricated test measurement dies where TiN as a CMOS compatible metal was used. Mechanical characterisations which included residual stress, XRD and AFM measurements proving a potential MEA material for our application. In our electrical tests performed it was concluded that TiN was able to withstand a high current density 2.8 mA/μm^2, while aluminium failed due to electromigration; even when coated with TiN. The resistance of a 10 mm long and 5 μm wide track decreases from 1.08×10^{1} Ω to 6.9×10^{2} Ω when a combination of Al and TiN is made. This reasonably solves the high resistance issue of TiN. The self-heating and the change in resistance due to temperature changes are measured, because the amount of dissipated heat should stay as low as possible. TiN which has a low TCR (5.9×10^{-4}) was able to withstand the harsh current acceleration tests at high temperatures between 60 to 70 ^{o}C. Short duration physiological saline solution immersion tests gave us initial impedance indications and the failures which helped to learn the short comings which can be used to build a more extensive long term material stability experimentation. For long term material stability a possibility of coating the devices with bio-compatible insulation (for e.g. Parylene) is another important research area where the leading CI manufacturers can focus on. Surface enhancement and coating with

bioactive conducting polymers can improve the life time of the implants where still a potential exists for in-vivo and in-vitro capabilities to be proven.

4.8 References

1. Møller, A. R. *Cochlear and Brainstem Implants*; Møller, A. R., Ed.; Karger Medical and Scientific Publishers, 2006.

2. Greenwood, D. D. A cochlear frequency-position function for several species--29 years later. *J. Acoust. Soc. Am.* **1990**, *87*, 2592–605.

3. Zhou, D.; Greenbaum, E. *Implantable Neural Prostheses 1: Devices and Applications*; Springer Science & Business Media, 2009.

4. Adunka, O.; Kiefer, J. Impact of electrode insertion depth on intracochlear trauma. *Otolaryngol. Head. Neck Surg.* **2006**, *135*, 374–82.

5. Cords, S. M.; Reuter, G.; Issing, P. R.; Sommer, A.; Kuzma, J.; Lenarz, T. A silastic positioner for a modiolus-hugging position of intracochlear electrodes: electrophysiologic effects. *Am. J. Otol.* **2000**, *21*, 212–7.

6. Stöver, T.; Issing, P.; Graurock, G.; Erfurt, P.; ElBeltagy, Y.; Paasche, G.; Lenarz, T. Evaluation of the advance off-stylet insertion technique and the cochlear insertion tool in temporal bones. *Otol. Neurotol.* **2005**, *26*, 1161–70.

7. Wright, C. G.; Roland, P. S.; Kuzma, J. Advanced bionics thin lateral and Helix II electrodes: a temporal bone study. *Laryngoscope* **2005**, *115*, 2041–5.

8. Gstoettner, W.; Franz, P.; Hamzavi, J.; Plenk, H.; Baumgartner, W.; Czerny, C. Intracochlear position of cochlear implant electrodes. *Acta Otolaryngol.* **1999**, *119*, 229–33.

9. Tykocinski, M.; Cohen, L. T.; Pyman, B. C.; Roland, T.; Treaba, C.; Palamara, J.; Dahm, M. C.; Shepherd, R. K.; Xu, J.; Cowan, R. S.; Cohen, N. L.; Clark, G. M. Comparison of electrode position in the human cochlea using various perimodiolar electrode arrays. *Am. J. Otol.* **2000**, *21*, 205–11.

10. Roland, J. T. A model for cochlear implant electrode insertion and force evaluation: results with a new electrode design and insertion technique. *Laryngoscope* **2005**, *115*, 1325–39.

11. Rebscher, S. J.; Hetherington, A.; Bonham, B.; Wardrop, P.; Whinney, D.; Leake, P. A. Considerations for design of future cochlear implant electrode arrays: electrode array stiffness, size, and depth of insertion. *J. Rehabil. Res. Dev.* **2008**, *45*, 731–47.

12. Wardrop, P.; Whinney, D.; Rebscher, S. J.; Luxford, W.; Leake, P. A temporal bone study of insertion trauma and intracochlear position of cochlear implant electrodes. II: Comparison of Spiral Clarion and HiFocus II electrodes. *Hear. Res.* **2005**, *203*, 68–79.

13. Rebscher, S. J.; Heilmann, M.; Bruszewski, W.; Talbot, N. H.; Snyder, R. L.; Merzenich, M. M. Strategies to improve electrode positioning and safety in cochlear implants. *IEEE Trans. Biomed. Eng.* **1999**, *46*, 340–52.

14. Bolz, A. Die Bedeutung der Phasengrenze zwischen alloplastischen Festkörpern und biologischen Geweben für die Elektrostimulation. *Fachverlag Schiele und Schoen, Berlin, Ger.* **1995**.

15. Loeb, G. E.; Peck, R. A.; Martyniuk, J. Toward the ultimate metal microelectrode. *J. Neurosci. Methods* **1995**, *63*, 175–183.

16. Stieglitz, T.; Meyer, J. U. Microtechnical interfaces to neurons. *Microsyst. Technol. Chem. Life Sci.* **1998**, *194*, 131–162.

17. Rose, T. L.; Robblee, L. S. Electrical stimulation with Pt electrodes. VIII. Electrochemically safe charge injection limits with 0.2 ms pulses. *IEEE Trans. Biomed. Eng.* **1990**, *37*, 1118–20.

18. Cogan, S. F.; Troyk, P. R.; Ehrlich, J.; Plante, T. D. In vitro comparison of the charge-injection limits of activated iridium oxide (AIROF) and platinum-iridium microelectrodes. *IEEE Trans. Biomed. Eng.* **2005**, *52*, 1612–4.

19. Yoshida, K.; Horch, K. Selective stimulation of peripheral nerve fibers using dual intrafascicular electrodes. *IEEE Trans. Biomed. Eng.* **1993**, *40*, 492–4.

20. Yuan, F.; Wiler, J.; Wise, K.; Anderson, D. Micromachined multi-channel microelectrodes with titanium nitride sites. In *Proceedings of the First Joint BMES/EMBS Conference. 1999 IEEE Engineering in Medicine and Biology 21st Annual Conference and the 1999 Annual Fall Meeting of the Biomedical Engineering Society (Cat. No.99CH37015)*; IEEE, 1999; Vol. 1, p. 379.

21. Wessling, B.; Mokwa, W.; Schnakenberg, U. Sputtered Ir Films Evaluated for Electrochemical Performance I. Experimental Results. *J. Electrochem. Soc.* **2008**, *155*, F61.

22. Cogan, S. F.; Plante, T. D.; Ehrlich, J. Sputtered iridium oxide films (SIROFs) for low-impedance neural stimulation and recording electrodes. *Conf. Proc. IEEE Eng. Med. Biol. Soc.* **2004**, *6*, 4153–6.

23. Dias, N. S.; Carmo, J. P.; da Silva, A. F.; Mendes, P. M.; Correia, J. H. New dry electrodes based on iridium oxide (IrO) for non-invasive biopotential recordings and stimulation. *Sensors Actuators A Phys.* **2010**, *164*, 28–34.

24. Schaldach, M. *Electrotherapy of the Heart*; Springer Berlin Heidelberg: Berlin, Heidelberg, 1992.

25. Cogan, S. F. Neural stimulation and recording electrodes. *Annu. Rev. Biomed. Eng.* **2008**, *10*, 275–309.

26. Zhou, D.; Greenbaum, E.; Merrill, D. *Implantable Neural Prostheses 2*; Zhou, D.; Greenbaum, E., Eds.; Biological and Medical Physics, Biomedical Engineering; Springer New York: New York, NY, 2010.

27. Brummer, S. B.; Turner, M. J. Electrochemical considerations for safe electrical stimulation of the nervous system with platinum electrodes. *IEEE Trans. Biomed. Eng.* **1977**, *24*, 59–63.

28. Clark, G. M.; Tong, Y. C.; Black, R.; Forster, I. C.; Patrick, J. F.; Dewhurst, D. J. A multiple electrode cochlear implant. *J. Laryngol. Otol.* **2007**, *91*, 935–945.

29. Cogan, S. F. Neural stimulation and recording electrodes. *Annu. Rev. Biomed. Eng.* **2008**, *10*, 275–309.

30. Lithgow, B. Cochlear implant threshold changes at high electric stimulus pulse rates. In *Proceedings of the 2nd International Conference on Bioelectromagnetism (Cat. No.98TH8269)*; IEEE, 1998; pp. 117–118.

31. Kuncel, A. M.; Grill, W. M. Selection of stimulus parameters for deep brain stimulation. *Clin. Neurophysiol.* **2004**, *115*, 2431–41.

32. Merrill, D. R.; Bikson, M.; Jefferys, J. G. R. Electrical stimulation of excitable tissue: design of efficacious and safe protocols. *J. Neurosci. Methods* **2005**, *141*, 171–98.

33. Zhou, D.; Greenbaum, E. *Implantable Neural Prostheses 2: Techniques and Engineering Approaches*; 2010.

34. Johnson, P. F.; Hench, L. L. An in vitro Analysis of Metal Electrodes for Use in the Neural Environment. *Brain. Behav. Evol.* **1977**, *14*, 23–45.

35. Zhou, D.; Greenberg, R. Electrochemistry in Neural Stimulation by Biomedical Implants. *Electrochemistry* **2011**, *17*, 249–262.

36. Hudak, E. M.; Mortimer, J. T.; Martin, H. B. Platinum for neural stimulation: voltammetry considerations. *J. Neural Eng.* **2010**, *7*, 26005.

37. Hung, A.; Zhou, D.; Greenberg, R.; Goldberg, I. B.; Judy, J. W. Pulse-Clamp Technique for Characterizing Neural-Stimulating Electrodes. *J. Electrochem. Soc.* **2007**, *154*, C479.

38. Glocker, D. A.; Shah, S. . *Handbook of Thin Film Process Technology, Volume 2*; 1995.

39. Rickerby, D.; Mathews, A. *Advanced surface coatings : a handbook of surface engineering*; Blackie: Glasgow [u.a.], 1991.

40. Schulz, A.; Stock, H.-R.; Mayr, P.; Staeves, J.; Schmoeckel, D. Deposition and investigation of TiN PVD coatings on cast steel forming tools. *Surf. Coatings Technol.* **1997**, *94-95*, 446–450.

41. Williams, D. F. Biomaterials and biocompatibility. *Med. Prog. Technol.* **1976**, *4*, 31–42.

42. Kruger, J. Fundamental Aspects of the Corrosion of Metallic Implants. In *Corrosion and Degradation of Implant Materials, ASTM STP 684*; Syrett, B. C.; Acharya, A.; Eds., Eds.; ASTM International, West Conshohocken, PA, 1979; pp. 107–127.

43. Gotman, I.; Gutmanas, E. Y. Titanium nitride-based coatings on implantable medical devices. **2014**.

44. Narayan, J.; Fan, W. D.; Narayan, R. J.; Tiwari, P.; Stadelmaier, H. H. Diamond, diamond-like and titanium nitride biocompatible coatings for human body parts. *Mater. Sci. Eng. B* **1994**, *25*, 5–10.

45. Steinbach, C. Titanium nitride - Material Information http://nanopartikel.info/en/nanoinfo/materials/titanium-nitride (accessed Mar 1, 2015).

46. Wikipedia Titanium nitride http://en.wikipedia.org/wiki/Titanium_nitride (accessed Mar 1, 2015).

47. Dixit, G. A.; Wei, C. C.; Liou, F. T.; Zhang, H. Reactively sputtered titanium nitride films for submicron contact barrier metallization. *Appl. Phys. Lett.* **1993**, *62*, 357.

48. Grigorov, K. G.; Grigorov, G. I.; Stoyanova, M.; Vignes, J. L.; Langeron, J. P.; Denjean, P.; Perriere, J. Diffusion of silicon in titanium nitride films. Efficiency of TiN barrier layers. *Appl. Phys. A Solids Surfaces* **1992**, *55*, 502–504.

49. Suni, I. Performance of titanium nitride diffusion barriers in aluminum–titanium metallization schemes for integrated circuits. *J. Vac. Sci. Technol. A Vacuum, Surfaces, Film.*

1985, *3*, 2233.

50. Hara, T.; Yamanoue, A.; Iio, H.; Inoue, K.; Washidzu, G.; Nakamura, S. Properties of Titanium Nitride Films for Barrier Metal in Aluminum Ohmic Contact Systems. *Jpn. J. Appl. Phys.* **1991**, *30*, 1447–1451.

51. Wittmer, M. Electrical characteristics of TiN contacts to N silicon. *J. Appl. Phys.* **1981**, *52*, 5722–5726.

52. Ting, C. Y.; Wittmer, M. The use of titanium-based contact barrier layers in silicon technology. *Thin Solid Films* **1982**, *96*, 327–345.

53. Arnell, R. .; Kelly, P. . Recent advances in magnetron sputtering. *Surf. Coatings Technol.* **1999**, *112*, 170–176.

54. Janssen, G. C. A. M.; Abdalla, M. M.; van Keulen, F.; Pujada, B. R.; van Venrooy, B. Celebrating the 100th anniversary of the Stoney equation for film stress: Developments from polycrystalline steel strips to single crystal silicon wafers. *Thin Solid Films* **2009**, *517*, 1858–1867.

55. Abermann, R.; Kramer, R.; Mäser, J. Structure and internal stress in ultra-thin silver films deposited on MgF2 and SiO substrates. *Thin Solid Films* **1978**, *52*, 215–229.

56. Koch, R.; Abermann, R. Microstructural changes in vapour-deposited silver, copper and gold films investigated by internal stress measurements. *Thin Solid Films* **1986**, *140*, 217–226.

57. Abermann, R. Internal stress of vapour-deposited aluminium on aluminium substrate films: Effect of O2 and water incorporated in the substrate. *Thin Solid Films* **1990**, *188*, 385–394.

58. Moram, M. A.; Vickers, M. E. X-ray diffraction of III-nitrides. *Reports Prog. Phys.* **2009**, *72*, 036502.

59. Sloof, W. G.; Kooi, B. J.; Delhez, R.; de Keijser, T. H.; Mittemeijer, E. J. Diffraction analysis of nonuniform stresses in surface layers: Application to cracked TiN coatings chemically vapor deposited on Mo. *J. Mater. Res.* **2011**, *11*, 1440–1457.

60. Lawand, N. S.; French, P. J.; Briaire, J. J.; Frijns, J. H. M. Thin Titanium Nitride Films Deposited using DC Magnetron Sputtering used for Neural Stimulation and Sensing Purposes. *Procedia Eng. Eurosensors* **2012**, *47*, 726–729.

61. Macdonald, J. R. Impedance spectroscopy. *Ann. Biomed. Eng.* **1992**, *20*, 289–305.

62. Norlin, A.; Pan, J.; Leygraf, C. Investigation of Electrochemical Behavior of

Stimulation/Sensing Materials for Pacemaker Electrode Applications. *J. Electrochem. Soc.* **2005**, *152*, J7.

63. Pierce, D. G.; Brusius, P. G. Electromigration: A review. *Microelectron. Reliab.* **1997**, *37*, 1053–1072.

64. Lienig, J. Introduction to electromigration-aware physical design. In *Proceedings of the 2006 international symposium on Physical design - ISPD '06*; ACM Press: New York, New York, USA, 2006; p. 39.

65. Du, L.; Edgar, J. H.; Kenik, E. A.; Meyer, H. Sublimation growth of titanium nitride crystals. *J. Mater. Sci. Mater. Electron.* **2009**, *21*, 78–87.

66. Black, J. R. Electromigration;A brief survey and some recent results. *IEEE Trans. Electron Devices* **1969**, *16*, 338–347.

67. Kusy, A. An equivalent network for resistance and temperature coefficient of resistance versus temperature and composition of thick resistive films. *J. Appl. Phys.* **1987**, *62*, 1324.

68. Clark, G. *Cochlear implants: fundamentals and applications*; springer, 2003.

69. MED-EL Cochlear Implants for Hearing Loss http://www.medel.com/int/cochlear-implants (accessed Mar 1, 2014).

70. Zhou, D.; Greenbaum, E. *Implantable Neural Prostheses 1*; Greenbaum, E.; Zhou, D., Eds.; Biological and Medical Physics, Biomedical Engineering; Springer US: New York, NY, 2009.

71. Ohring, M. *The Materials Science of Thin Films*; Elsevier, 1992.

72. Birkholz, M. *Thin Film Analysis by X-Ray Scattering*; John Wiley & Sons, 2006.

73. Taychatanapat, T. (CMMR) Electromigration in gold http://www.ccmr.cornell.edu/.

74. Gutmann, P. Data Remanence in Semiconductor Devices. In *Proceedings of the 10th USENIX Security Symposium*; Washington, D.C., USA, 2001; pp. 39–54.

Chapter 5

Design of Microelectrode Arrays and Electric Field Density analysis

What is design? It's where you stand with a foot in two worlds – the world of technology and the world of people and human purposes – and you try to bring the two together.

Mitchell Kapor (Entrepreneur, Software designer, and Investor).

Until now the background knowledge for the different microfabrication technologies was build up in the earlier chapter. We now move ahead in describing the various design options considered for the stiff probes, 1st generation completely flexible and the 2nd generation "Flexi-Stiff" microelectrode array (MEA). The various dimensional aspects in the designs are discussed with the subsequent CAD data. The later section of the chapter deals with the simulation study and analysis of the electric field density distribution due to electric stimulation. The goal of this study was to answer fundamental questions related to the electrical stimulation caused to these metal electrodes. What is the spatial distribution of the current density distribution at the electrode surface? How will the finite element analysis help us to determine the geometrical influence of the electrode on the current density distribution? These are the main questions to which this chapter will be answered to. This is important for determining the appropriate design configuration of the metal stimulation site of the MEA.

This chapter's work is the part of MSc theis (Characterization of metals for Cochlear Implants, Joost van Driel and the published artciles: N. S. Lawand, *et al.*: "Silicone probes for cochlear auditory nerve stimulation & measurement", *Proc. ICMAT, Adv. Mat. Research,* 2011, Vol. 254, pp. 82-85; N. S. Lawand, *et al.*: "Development of probes for cochlear implants", *IEEE Sensors,* 2011, pp. 1827-1830; N. S. Lawand, *et al.*: "Design & fabrication of silicon of stiff probes: A step towards developed cochlear implatn electrodes", *Proc. Eurosensors XXV,* 2011, pp. 1012-1015.

5 5.1 Introduction

In a development cycle of MEAs the preliminary design considerations is a combination of design guidelines defined in literature research and its intended application area. In this process combined knowledge from the people associated to neural engineering, audiologists, process engineers, and the up-to-date information adapted from the field of microfabrication technology is necessary. Apart from these aspects the limitations and the lessons learned from the state-of-the-art CI electrode array forms an important base in designing the future illustrators of the "Flexi-Stiff" MEA which is intended to be used as a concept demonstrator for animal experimentation. In this thesis, all such design paradigms were realised in a step wise approach of the stiff probes and the completely flexible MEA, allowing the proof-of-concept which was solely intended to study and understand the fabrication technology and material related boundaries. The insights gained in this "knowledge segment" motivated further to implement the lessons learned for the second generation "Flexi-Stiff" MEA. This was aimed to develop a demonstrator which will lay the foundation for the future developmental path for the Cochlear Implant.

The electrode design is the key aspect of the MEA used for the intended application as they form an interface between the nervous system and the technical system to record the bioelectric nerve signals or to excite the nerve by means of an electrical stimulation [1]. The design requirements must fulfil certain criteria necessary for an MEA. Firstly, the materials been used in the microfabrication process for e.g. for the device substrate, stimulation electrode metals, and insulation used must be biocompatible. Secondly, the device dimensions should be defined in such a manner that it should withstand the mechanical stability during insertion with minimal tissue damage and adaptation to the complex structure of the biological organ (for e.g. cochlea) which limits the minimal thickness and the width of the device. Due to new micromachining techniques used to fabricate these miniature MEAs the electrodes need to geometrically characterize for further development in terms of size, space and exposed stimulation surface. The already known electrical and material characterization methods such as Electrochemical Impedance Spectroscopy (EIS) are not sufficient enough to characterize such geometrical features. Finite Element Analysis (FEA) simulation is normally adapted by researchers to approach and characterize such geometrical related features [2–4]. In the later sections of this chapter when the various designs will be explained then the topic of geometrical influence on the electric density field density distribution will be demonstrated by means of COMSOL 4.2a.

5.2 Stiff probes (design and fabrication)

There were two goals in designing the stiff probe design; the first stiff probe was designed to perform simulation studies to understand the stimulation pattern when the stiff probe is "punctured" perpendicularly inside the auditory nerve. The second goal was to realise the production capabilities and design a preliminary process flow chart. This helped to realise the microfabrication boundaries by considering the equipment's available at Else Kooi Laboratory, formerly referred as The Delft Institute of Microsystems and Nanoelectronics (DIMES).

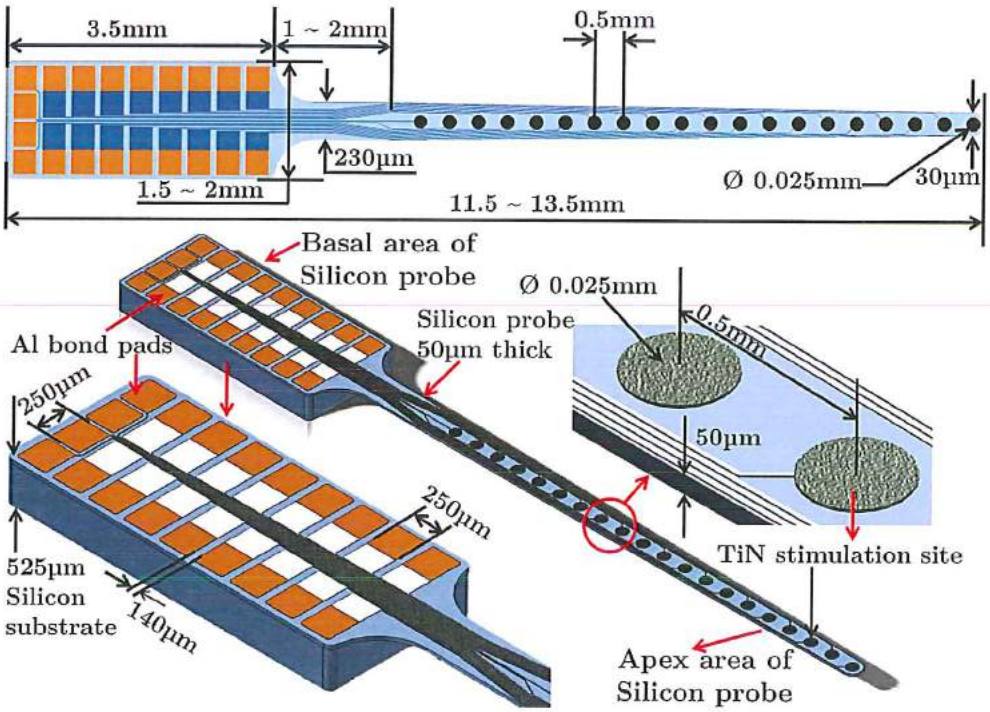

Figure 5.1 CAD illustration of the stiff probe showing the major dimensions.

Figure 5.1 shows the preliminary design for the stiff probe which consists two sections the silicon probe base section and the apex section, each one of different thicknesses. The base silicon area is of 525 µm full wafer thickness with an probe area thinning down to 50 µm by standard deep reactive ion etching (DRIE) process for silicon etching. The major dimensions are as shown in Figure 5.1. Some of the dimensions such as the length and the basal width is kept variable in order to accommodate different combinations of stimulation sites corresponding to the subsequent bond-pad areas.

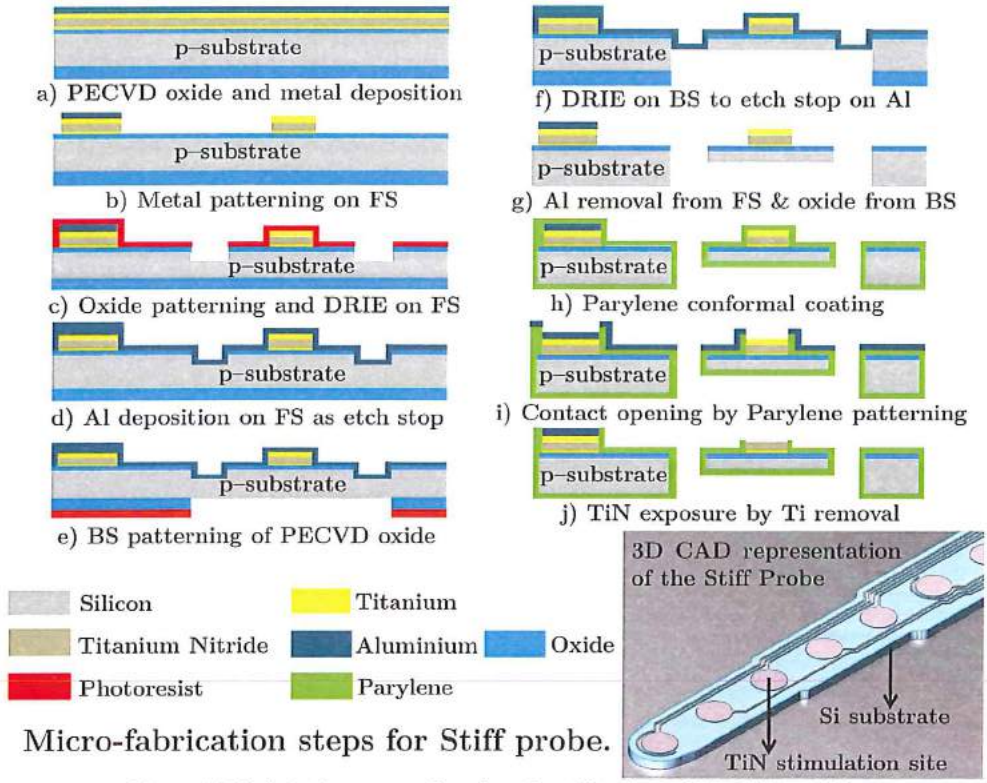

Figure 5.2. Fabrication process flow chart for stiff probe and 3D CAD model.

The stiff probe was fabricated to investigate the photolithographic limits and the problems encountered in the fabrication procedure. The process begins with a single crystalline p-type (100) wafer with the specifications: thickness: -525 ± 15 µm, diameter:- 100.0 ± 0.2 mm and resistivity:- 2 to 5 Ωcm. PECVD oxide deposition of different thicknesses (1 µm on fronts side {FS} and 6 µm on back side {BS}) was the first process done with standard PECVD deposition techniques. After PECVD deposition the metal stack, Titanium (Ti: 40 nm) + Titanium Nitride (TiN: 200 nm) + Titanium (Ti: 40 nm) + Aluminium (Al: 3µm) was deposited by standard sputter deposition techniques (Sigma 204). The Al top layer was patterned by a wet PES etching process. The wet etching bath used for PES is a combination of phosphorus acid (H_3PO_4; 85%), nitric acid (HNO_3; 65%), concentrated acetic acid (CH_3COOH; 100%) and deionized demi water (Mixing ratio: 4:4:1:1). After wet etching and standard cleaning procedure the metal stack was patterned by dry etching techniques where an combined reactive ion etching (RIE) process was used to etch the complete metal stack and land on the underneath PECVD oxide layer. After the metal patterning and cleaning step a photoresist (3 µm thick) layer was deposited and patterned on the FS of the wafer by standard lithographic techniques. Using this

resit as a mask deep reactive ion etching (DRIE) process was done on the FS of the wafer to approximately timely etch 50 to 60 µm in silicon which defines the probe thickness. The wafer went through the standard cleaning procedure which includes stripping of photoresist in oxygen plasma, residual removal in alternate fuming nitric acid bath and 65% nitric acid bath with intermediate cleaning in quick dump rinsing (QDR) bath. After defining the probe thickness another Al layer was sputter deposited on the wafer by 100% Al target at a room temperature (25 ^{o}C) with an argon flow of 100 sccm to achieve a thickness of 2 µm. Sputter deposited layer was uniform with better step coverage in the trenches of 50 µm on the front side. For the back side processing of the wafer 6 µm PECVD oxide was used. Window etching of this oxide was done in a plasma etcher to land on the silicon surface.

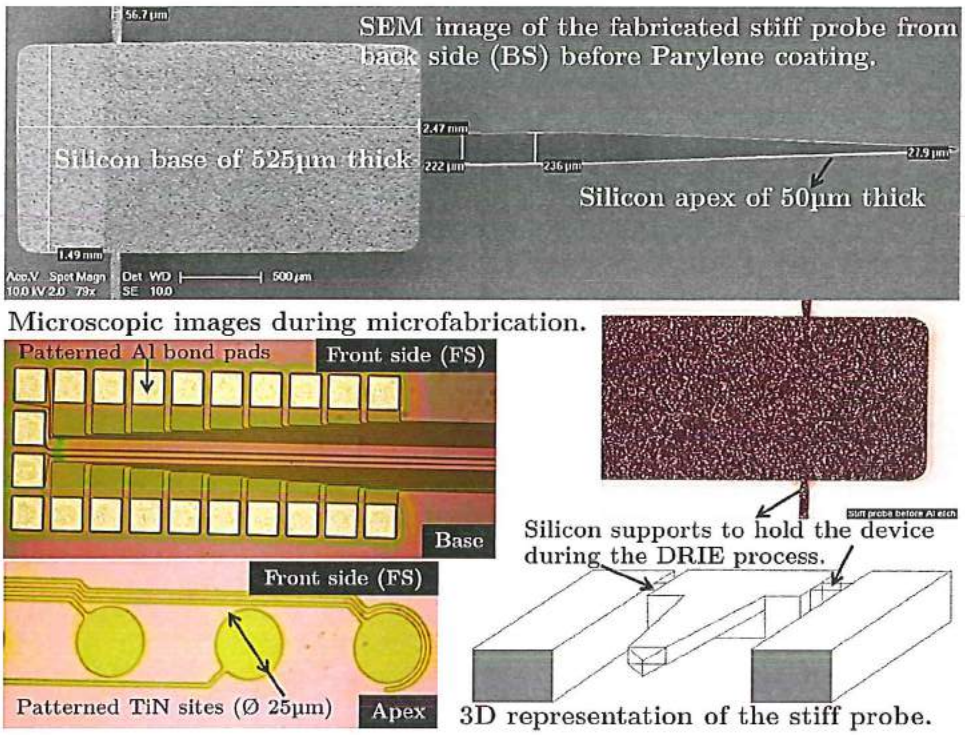

Figure 5.3 Fabrication results of the stiff probe fabricated in DIMES.

This etching process was performed by chloro-fluorocarbon gases: C_2F_6 and CHF_3. The etching was carried for approximate 18minutes with etching parameters: RF power:- 200 W, Helium gas pressure:- 12 Torr. Then the standard cleaning followed to remove traces of photoresist. In the next step by the standard DRIE process, through silicon wafer etching from the BS was performed to land on the aluminium

(FS) which acts as an etch stop layer. This was the crucial step in the complete fabrication process in which the machine parameters such as gas flow and temperature has to be maintained and tuned accordingly to obtain the required anisotropy of the trenches. After this the probes were released by aluminium wet PES etching process similar to step b) of Figure 5.2. The probes were in position due to the supports at the basal end of the device as seen in Figure 5.3. These supports are of full wafer thickness (525 µm) thick with a width of 50 µm each at the base end on the either side of the device. These supports are purposely given a tapered shape at the point of contact which permits the easy breakage/separation from the substrate wafer. After Al removal from the FS the devices were released individually by dicing from the supports. Before the dicing procedure the whole wafer is parylene (Parylene C) coated and patterned. This was done in order not only to increase the robustness of the device but also to make the device biocompatible since parylene is used as a well-known biocompatible coating material in many of the medical implants used nowadays [5].

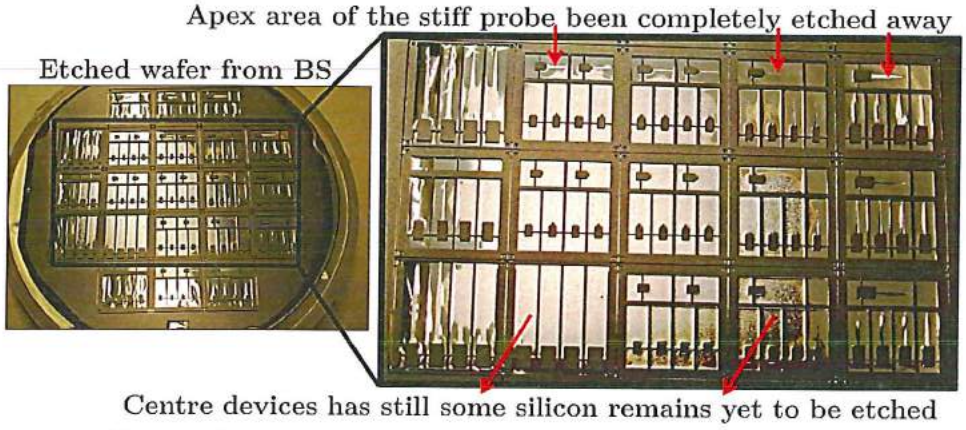

Figure 5.4 Image showing problems associated with the stiff probe fabrication.

Parylene was deposited by vapour deposition method from the vapour phase by a process which in some respects resembles vacuum metallising. This process consists of three distinct steps. The first step is vaporisation of the solid dimer at approximately 175 ^{o}C. The second step is the quantitative cleavage (pyrolysis) of the dimer at the two methylene-methylene bonds at about 650 ^{o}C to yield the stable monomeric compounds. Finally, the monomer enters the room temperature deposition chamber where it simultaneously adsorbs and polymerizes on the substrate wafer. No liquid phase has ever been isolated and the substrate temperature never raises more than a few degrees above the ambient. Other necessary components in this system are the mechanical vacuum pump and associated protective traps. By this deposition process

a thin-film, pinhole free parylene conformal coating is applied to the devices. Parylene provides excellent moisture, chemical and dielectric barrier protection [5]. The fabricated results of the stiff probe are as shown in Figure 5.3. As this fabrication was to understand the limits in response to the process flow steps undertaken in fabricating the stiff probes. Apart from the minor lithography patterning issues the important issue was the throughput of the device per wafer which was less than 30%. The reason to this was due to the uneven silicon etching process (DRIE) in which the peripheral devices were lost in other words the apex area of the stiff probes were completely etched away (Figure 5.4) while aiming for the middle devices. In some cases there were still some traces of Silicon left back after the DRIE process.

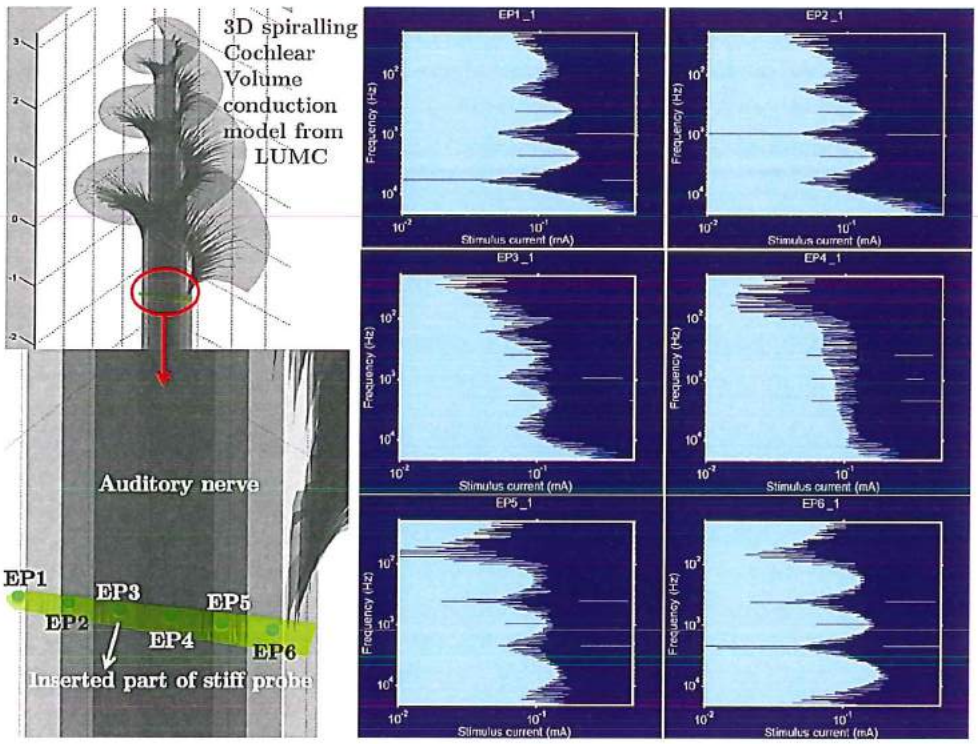

Figure 5.5 Stiff probe stimulation studies with generated stimulation pattern.

In addition to fabrication a simulation exercise to understand the stimulation pattern of the stiff probe design was performed on a cochlear volume conduction computational simulation model [6,7] developed at Leiden University of Medical Centre (LUMC). This model was developed to gain better understanding regarding the functionality of the CI's and as a tool in developing future generation CI's. This

computational model can predict the neural response to an arbitrary cochlear implant. This model at first computes the potential distribution set up in a three-dimensional, spiralling volume conduction model of the auditory part of the inner ear (cochlea) and then applies a nerve fibre model to construct input/output curves and excitation profiles of the auditory nerve [7]. The motivation to this simulation exercise was the result of an idea initiated at LUMC to see the possibility of puncturing the auditory nerve directly in a perpendicular direction with the help of the CAD generated stiff probe design enabling us to study the stimulation pattern obtained during this process. In this model the auditory nerve fibres are arranged as per frequency to match the actual tonotopic organization of the cochlea. High frequency fibres are at the base or entry and low frequency fibres are at the apex of the cochlear model. The stimulation threshold current to stimulate the stimulation contact site on the probe was in the range of 10^{-2} mA to 0.5 mA. From the excitation profiles as shown on the right side of the Figure 5.5 the light blue pattern indicates the absence of excitation and the dark blue pattern indicates the excitation for the respective stimulation sites. Stimulation site 1 (EP1) of the stiff probe being outside the bundle of fibres has higher threshold values than site 4 (EP4) with lower threshold value which is present in the centre of the auditory nerve bundle.

5.3 Cochlear geometry (Human and Guinea pig)

In the design process aiming towards making an MEA for in-vivo studies in guinea pig is an step which involves extensive verification of safety and performance in addition to in-vitro studies. In-vitro studies examines the charge delivery and electrode impedances normally performed in a phosphate buffered saline solution. In-vivo studies necessitate animal studies which investigates the MEA's in terms of charge delivery capabilities, mechanical insertion trauma and tissue interactions. Also, animal testing gives us the possibility of measuring neural responses as well as psychophysical testing in trained animal subjects. In order to develop the dimensions and features of the 1st and 2nd generation flexible MEA's a detailed knowledge of the cochlear geometry is required. Figure 5.6 (b) shows a cross-section of a guinea pig cochlea. In our studies the guinea pig animal model was selected because the guinea pig cochlea demonstrates a hearing range from 1000 Hz to 44 KHz that closely matches that of the humans and for in-vivo investigation purposes the peripheral auditory system and the inner ear are easily accessible. In Figure 5.6 a cross-section comparison of human cochlea with a guinea pig cochlea is shown. In the central part of the guinea pig cochlea a clearly visible bundle of nerve fibres (modiolus) is seen which enters the skull towards the brain in the lower right corner. The enlarged cross-section (shown in red rectangle) of the cochlea consists of three main fluid-filled compartments with relative good conductivity, separated by membranes with a much

lower conductivity. In most of the situations, the CI is inserted from the base of the cochlea to the apex into the lower of the three compartments, the scala tympani as shown in Figure 5.6d [6].

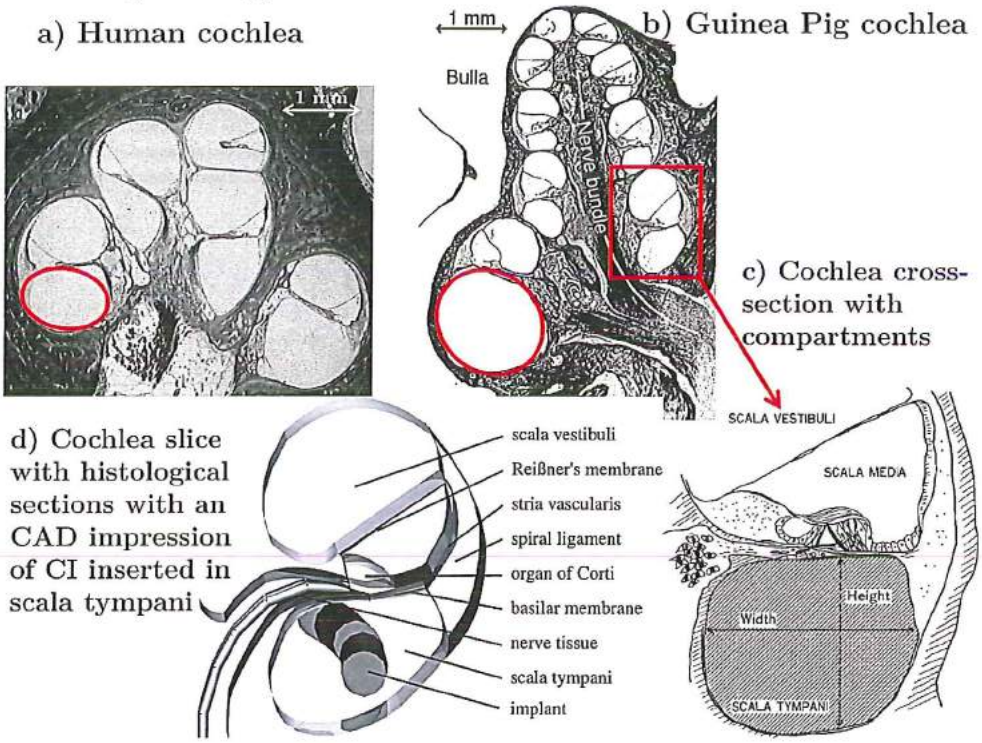

Figure 5.6 Human and Guinea pig cochlea. a) Human cochlea cross-section (*Image courtesy by Dr. F. Linthicum, House Ear Institute)*, b) Guinea Pig cochlea [6], c) Cochlea Sections, d) Cochlea slice with the histological details [6].

The guinea pig cochlea differs from the human one in many ways: It is approximately two times smaller (the length of the basilar membrane in the guinea pig is 18.8 mm which is smaller to human ones which is approximate 35 mm in length) with more turns, 3 ½ compared to 2 ¾ turns in the human cochlea situation. Moreover, the guinea pig cochlea with an air filled bulla protrudes as an human middle ear equivalent, whereas the human cochlea has an embedded solid petrous bone. This arrangement in the guinea pig cochlea thus makes it an good experimental candidate for auditory experiments with an addition to easy availability of large electrophysiological data [6]. Translating this information while designing the MEA posed challenges especially the rapid narrowing down of the scala tympani (ST) compartment. This compartment at first can be approximated (as shown in Figure 5.6 c) with a major axis as the width and the minor as the height of the ST.

In line with the MEA placement inside the cochlea the width of the MEA is limited by the minimum dimension which is the height ST compartment of the cochlea. The width of this compartment defines the MEA thickness with considering the placement of MEA facing the inner wall of the ST responsible for the auditory nerve stimulation process. In designing both generation MEA's (explained in further sections) our goal was to build an experimental guinea pig MEA for an shallow insertion up to 8 to 10 mm maximum, with an height of 150 to 200 µm. Other details regarding insertion and guinea pig cochlea will be dealt in more detail in later chapters (Chapter 7).

5.4 Design aspects of Flexible MEA (1st generation)

Referring to the anatomical features of the guinea pig cochlea and the microfabrication constraints the 1st generation completely flexible MEA was designed.

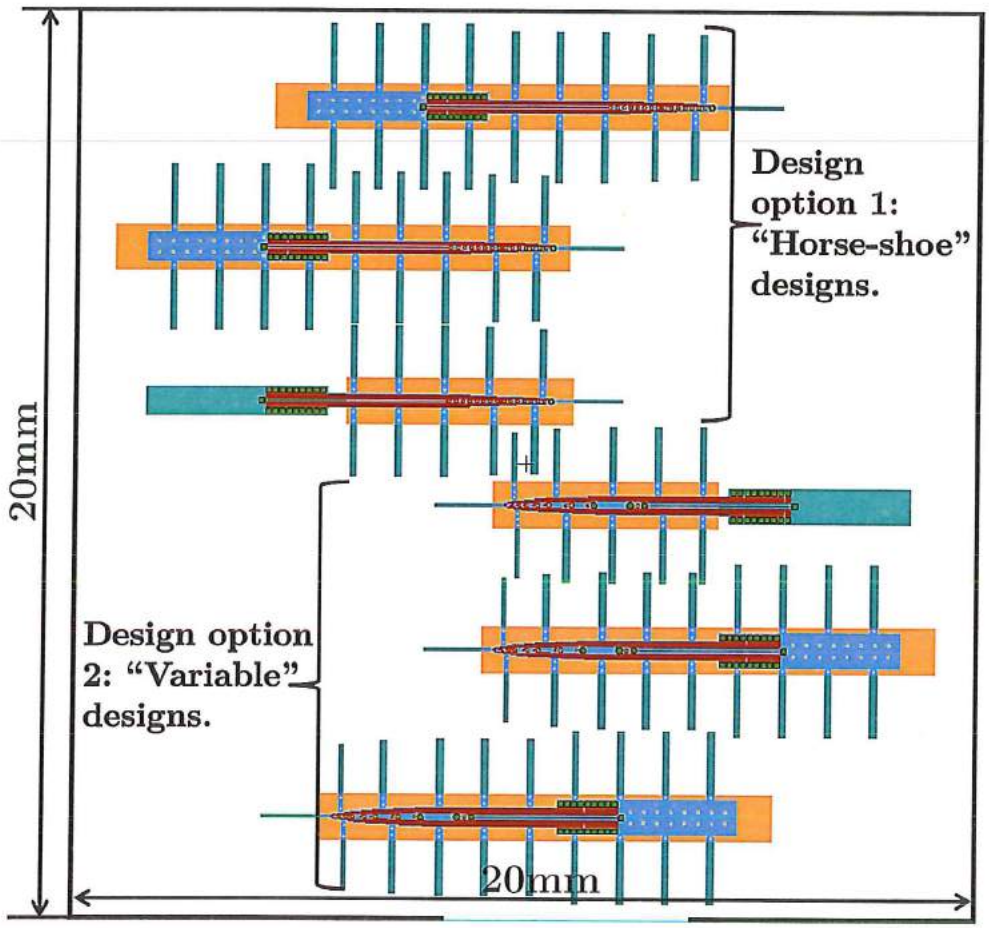

Figure 5.7 Single die CAD image including 2 different designs with 6 devices. [21]

In this section only the design aspects related to the completely flexible MEA will be dealt with, the microfabrication process and results will be discussed in the later chapters (Chapter 6). The first generation completely flexible MEA designs consists of two different design variants; a) "Horse-shoe" design: aiming to incorporate the recording site close to stimulation site of the MEA. b) "Variable" design where the stimulation and recording sites are varied over the length of the MEA. Both these designs (3 of each type) were placed in a single 20 mm × 20 mm (Figure 5.7) die which includes in all 12 dies over a single silicon wafer substrate of 100mm diameter. The major dimensions and the other geometrical features of the first design option ("Horse-shoe" design) variant is as shown in Figure 5.8. The completely flexible MEA consists of 16 TiN stimulation sites connected by individual metal tracks to the Al bond pads in turn connecting a compact 0.042 mm^2 programmable biphasic stimulator chip by W. Ngamkham(team member of SMAC-it project). In this chip, the stimulation current is set by scaling a reference current using a two stage binary-weighted transistor DAC (comprising a 3 bit high-voltage transistor DAC and a 4 bit low-voltage transistor DAC) [8].

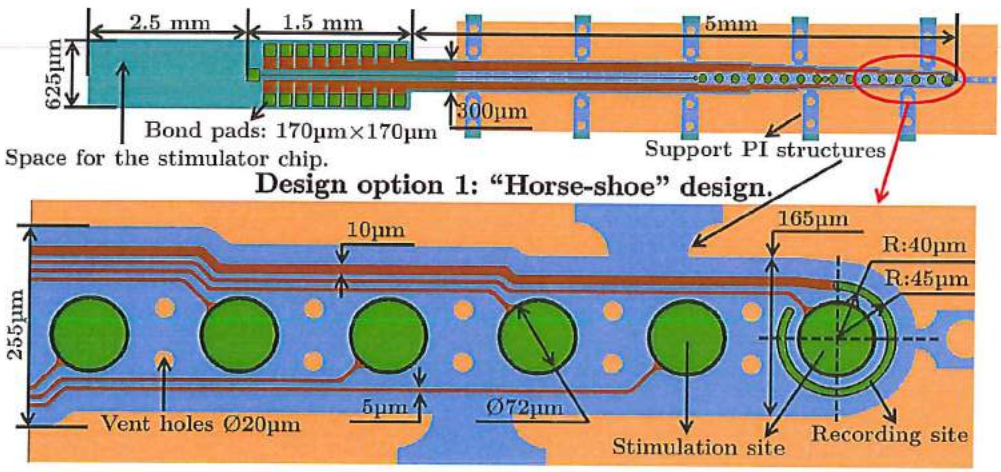

Figure 5.8 CAD illustration of the "Horse-shoe" design (Design option 1).

Each stimulation site is approximately 72 µm in diameter with a spacing of 150 µm between each other. At the tip of the MEA a "Horse-Shoe" recording site is closely incorporated with the stimulation site. The aim in having this "Horse-Shoe" shaped structure is to record simultaneously the neural activity during the neural stimulation process in the close vicinity of the stimulation site. This recording site was connected to the bond pads by a 10 µm thick metal track which differed from the rest metal tracks used for stimulation sites which is 5 µm. This was done

purposely to identify the recording track and for the optimum use of the available space in the MEA design.

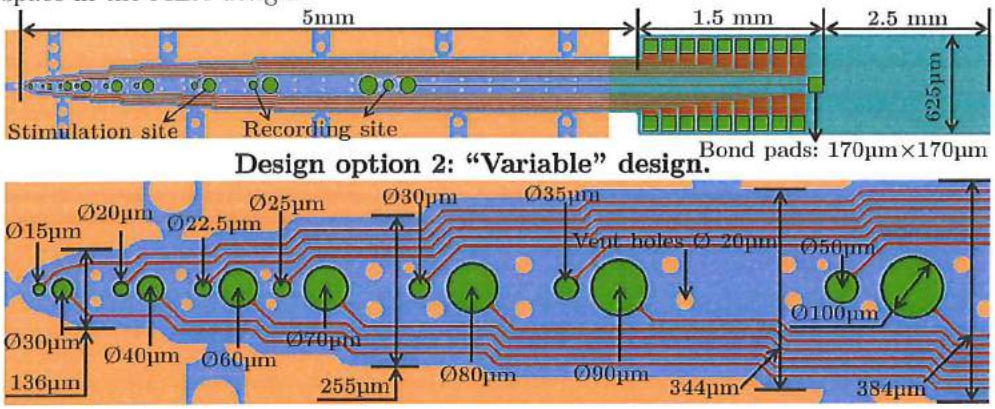

Figure 5.9 CAD illustration of the "Variable" design (Design option 2).

The other design version referred to as the "Variable" design was done to include various sizes (diameters) of stimulation and recording sites placed close to each other. The various different sizes are listed in Table 1, with the related geometrical dimensioning as seen from Figure 5.9. The design difference between the option 1 and 2 is in placing the recording site with the stimulation site. In design option 1 there is one "Hors-shoe" recording site surrounding the stimulation site to demonstrate the circular concept design of recording site with stimulation site. The variable design was to see the effect on the stimulation and the recording performance as the diameter changes and to check the microfabrication constraints in manufacturing them.

Size variations for stimulation and recording sites.									
Stimulation Site Ø (µm)	30	40	60	70	80	90	100	120	140
Recording Site Ø (µm)	15	20	22.5	25	30	35	50	60	80

Table 1. Dimensions for "Variable design" (Design option 2).

In the variable design the width varies from 384 µm at the base to 136 µm at the tip of the MEA. All the sites (stimulation and recording) are been connected in the similar manner with 4 µm width metal tracks to the Al bond pads which in turn are connected to the outside world by a programmable biphasic stimulator chip. This is to be placed in the space provided behind the basal bond pad area of the MEA. In both the design versions there were through holes of 20 µm each been created in midst of the stimulation sites along the complete length of the MEA. These holes are

specially designed as vent holes in order to facilitate the process of wet etch removal (detail process explained in Chapter 6) of the sacrificial pure aluminium (light orange colour as seen in both designs) layer present underneath each of the flexible devices.

5.5 Design aspects of "Flexi-Stiff" MEA (2nd generation)

The "Flexi-Stiff" MEA makes use of the experience gained in the stiff electrode and the completely flexible MEA. The idea behind designing the "Flexi-Stiff" array

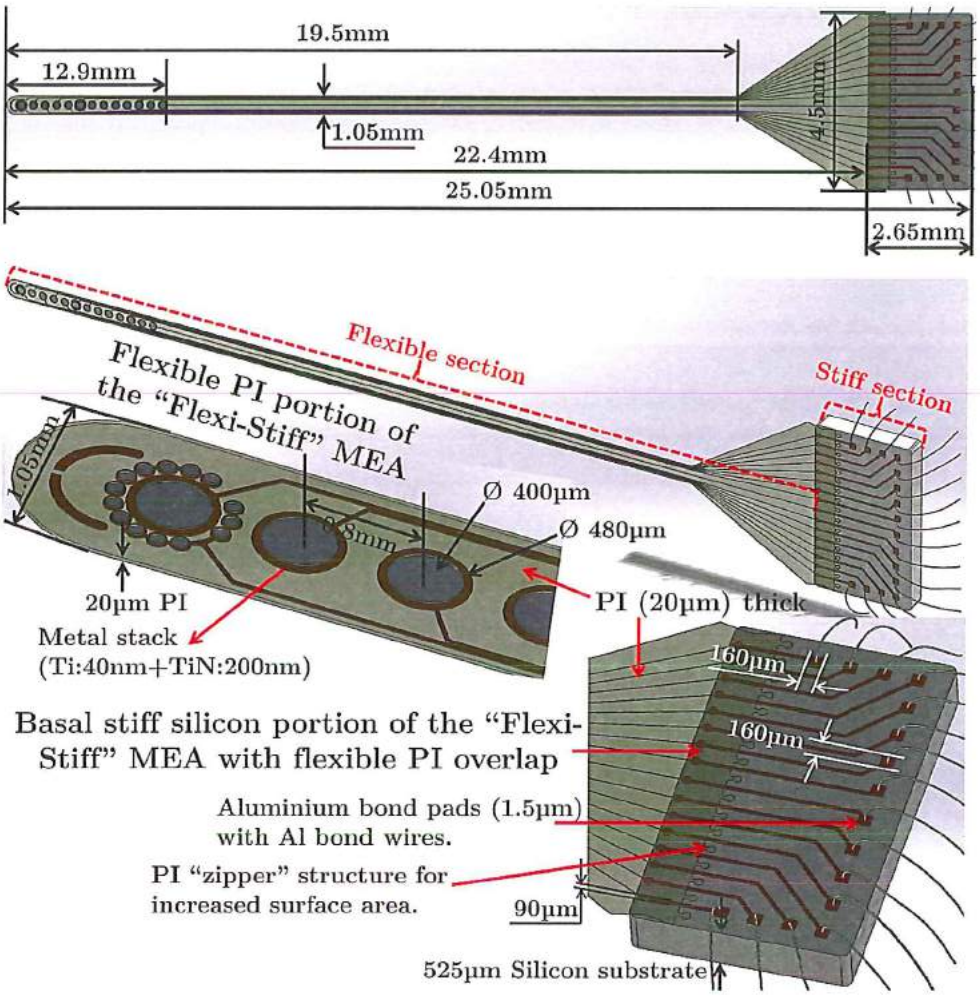

Figure 5.10 CAD illustration of the "Flexible-Stiff" MEA with major dimensions.

was to separate the flexible part (electrode stimulation area) from the stiff part (connection possibilities of the stimulation electronics). As illustrated in CAD schematics (Figure 5.10) the flexible part (22.4 mm (L) × 1.05 mm (W)) houses the

TiN stimulation site material in between the two polyimide (PI2611) layers which are 10 µm thick. The upper PI layer is selectively patterned by lithographic techniques (explained in the next chapter) to expose the metal sandwiched between the two PI layers. This sandwiched metal layer (240 nm thick) along with the flexible PI layers (20 µm thick) which runs over the stiff silicon (525 µm thick) which houses the Aluminium bond pads that ensure the connection to the electronics aimed for driving the stimulation sites. The PI layer at the edge where the transition goes from the flexible part to the stiff silicon is patterned to give a "zipper" like structure (Figure 5.10) which helps to add up more surface area in contact with the silicon in comparison with the straight line edges of the PI layer. Apart from the adhesion promoters used in the microfabrication process (explained in detail in the next chapter) this geometrical shape ("zipper" like) will add up to the overall adhesion surface area. The "Flexi-Stiff" MEA design and its dimensions shown in Figure 5.10 are for one type of design configuration displayed, the other design configurations with changes in number of stimulation sites, its shapes are mentioned in the appendix at the end of the thesis. The idea behind having different designs helped to identify the manufacturing limitations and to see the influence of different geometries on the stimulation parameters during in-vitro experimentation. The details of the microfabrication process for the "Flex-Stiff" MEA with its supporting subsequent results and associated problems will be explained in the next chapter.

5.6 Electric field density distribution analysis

Electrical neural stimulation of the auditory neurons by MEA of CI assists the auditory information to pass from the outer world to the auditory cortex which helps deaf people. Microstimulation of the auditory neurons at a micron level can activate a population of neurons than possibly done by a large electrode area implanted in the ST of the cochlea. Over stimulation of the neurons via the implanted electrodes may seldom lead to damage of the surrounding tissue causing permanent auditory loss from the residual hearing. This may cause electrode failure or corrosion of the metal due to increased electrochemical reactions occurring at the electrode tissue interface [9]. The purpose of this simulation exercise was to find answers by finite element method (FEM) to the questions concerning the electrical field distribution caused by the metal microelectrode stimulation site in combination with the polymer in the saline environment. This FEM analysis will help us to understand the spatial distribution of the potential electric field density distribution of the metal microelectrode occurring due to the electrochemical reactions taking place at the electrode electrolyte interface. Along with the spatial distribution the geometrical influence due to various shapes and sizes on this potential electric density

distribution is also studied. This will allow to choose an optimum design configuration of the stimulation site with the polymer to reduce the potential electric density effects in the ST. The prior information of the generated potential by the stimulus helped us to develop the correct geometry required for the stimulation electrodes prior to the microfabrication. The other objective of this study was to develop a FEM model for arbitrary substrate with a modelling environment and different shapes of microelectrode contact sites to determine the conditions influencing the potential electrical field distribution. Here in this section we demonstrate the FEM model used for the simulation and the subsequent results on the different design configurations in saline environment.

5.6.1 FEA modelling for stiff probe design

Multichannel implants which normally consists of multiple electrodes stimulates/excites the auditory nerve fibres in a simultaneous fashion at the different locations inside the Cochlea for coding different acoustic frequencies. The sequence in which the electrodes need to be activated largely depends on the frequency components existing in the spectrum of the incoming speech signals [10]. The threshold values for electrical neural stimulation and the patient pitch perception are affected through the generated electric field which are in turn dependent of stimulation parameters such as the electrode array configuration, pulse stimulation rate, pulse duration and stimulus intensity [11]. Due to these interdependent factors its necessary to understand the relationship between the stimulation parameters and the electric field generated in the physiological tissue in order to develop more efficient and spatially focused electric stimulation process inside the cochlea. FEM analysis helped to numerically understand the relationship between the electric fields generated inside the cochlear medium around the stimulation electrode array and the stimulation parameter especially the geometrical electrode array configuration.

The electric field potential $\varnothing$ produced by the CI stimulation inside a conduction volume is given by [12]:

$$\varnothing\left(x^{'},y^{'},z^{'}\right)=\frac{1}{4\pi\left(\sigma+j\omega\varepsilon\right)}\int_{V}\frac{i(x,y,z)e^{-jkR}}{R}dV \qquad (1)$$

where i is the current source per unit volume provided by the CI stimulation, σ and ε are the conductivity and dielectric permittivity of the medium, ω is the angular frequency of the excitation current, (x,y,z) and $\left(x^{'},y^{'},z^{'}\right)$ are the 3-D coordinates of the current source and of the point where the potential is computed,

$R^2 = (x-x')+(y-y')^2+(z-z')^2$, $k^2 = -j\omega\mu\sigma_c$, where μ is the permeability of the medium and σ_c is a complex conductivity that includes pure conductive effects, dielectric losses, and dielectric displacement, defined as [13]:

$$\sigma_c = \sigma\left(1 + \frac{j\omega\varepsilon}{\sigma}\right) \tag{2}$$

A quasi-static approximation can be used in order to simplify (1) in which an assumption that at each instant of time the electric potential field satisfies Poisson's equation, and that the boundary conditions always relate to a stationary condition. This quasi-static approximation is only possible to apply if the following three effects are neglected in a typical neural stimulation process [12]:

$$\omega\varepsilon/\sigma << 1 \text{ (capacitance effects)}$$

$$kR_{max} << 1 \text{ (propagation effects)}$$

$$\left(kR_{max}\right)^2 << 1 \text{ (inductive effects)}$$

These above mentioned assumptions are true for a frequency range normally related to the commercially available CI current stimulus (i.e. up to 20-80 kHz), for a purely resistive behavior of the cochlear hair cells or tissues [12,14,15] as dielectric properties [16], and for $R_{max} = 0.004$m (where R_{max} is the maximum value R to be considered in the conductor volume V). So for this quasi-static approximation, equation 1 becomes as:

$$\emptyset\left(x',y',z'\right) = \frac{1}{4\pi\sigma}\int_V \frac{i(x,y,z)}{R}dV \tag{3}$$

which is equal to the Poisson's equation solved in our FEM analysis:

$$\nabla^2\emptyset = -\frac{i}{\sigma} \tag{4}$$

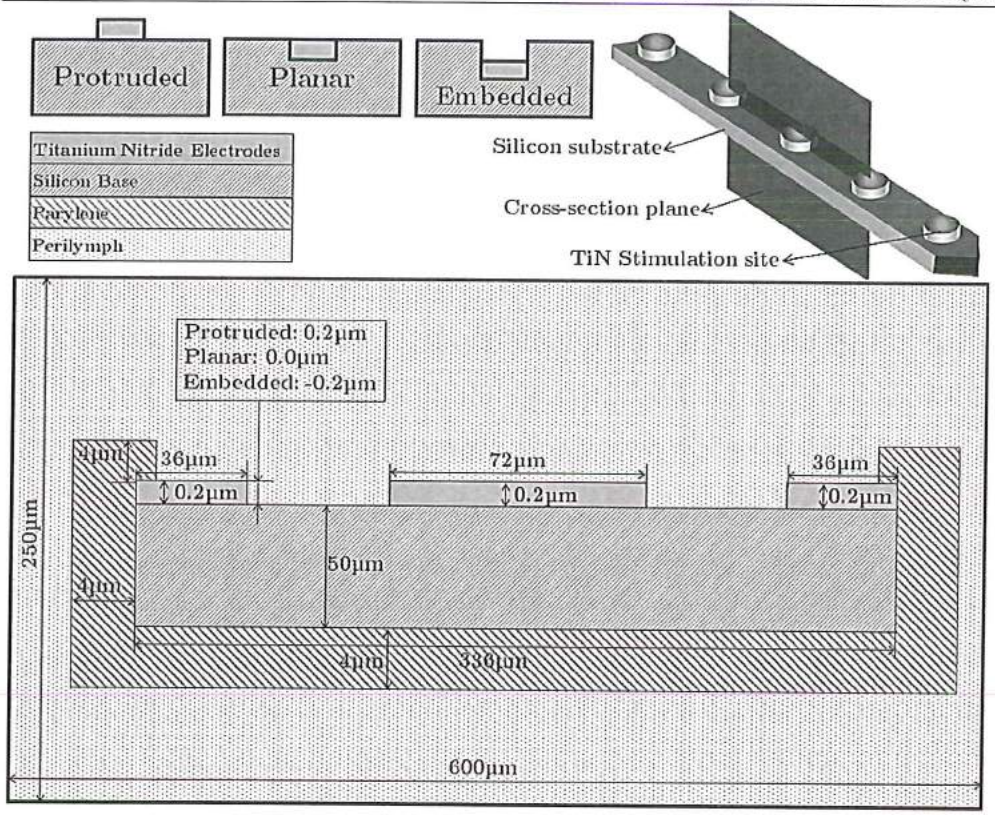

Figure 5.11 Part of the stiff probe with the cross-section model (not to scale) used during simulation studies along with different cases for the electrode site.

This quasi-static assumption here as mentioned is only applicable in the 20-80 kHz range. In an FEM process the solution to Equation 4 can be easily found by sub dividing the conduction volume (in this case the assumed perilymph environment) into small tetrahedral elements. The solution process is done by progressively refining the mesh subdivision of the considered conduction volume unless and until an error energy percent is achieved which eventually is the degree of how close you arrive in satisfying the Equation 4 in comparison with the specified target value. For Comsol Multiphysics 4.2a the energy error was $\leq 2\%$. Finite Element Analysis (FEA) was performed prior to fabrication of the stiff probes to understand the electric field spatial distribution inside the assumed medium. In this study we computed a 2D electric potential induced inside the medium (perilymph in this case) by using a FEA software (Comsol Multiphysics 4.2a). For the simulation purposes the part of the silicon stiff probe (as shown in Figure 5.11) was considered. The electric field distribution in the saline solution is dependent on some factors: the potential of the metal, the dimensions of the stimulation electrode site, the thickness of the isolation

layer on top of the metal layer and the dielectric constant of the saline (perilymph) solution space (600 µm×205 µm), as in Figure 5.11. Three different design configuration (protruded, planar and embedded) possibilities are considered for the stiff electrode MEA design. These proposed options are easy to validate for electric potential by FEM analysis in comparison to the experimental way.

Material	Conductivity (S/m)	Relative Permittivity (ε_r)
Silicon (undoped)	4.3×10^{-4} [17]	11.7 [18]
Titanium Nitride	5×10^{3}	100
Perilymph	2 [19]	109 [19]
Parylene	5×10^{-20} [5]	2.2 [5]

Table 2. Material properties considered during FEA analysis.

The 2D simulation model (Figure 5.11) consists of a cross-section of the part of the stiff electrode array which consists of one complete stimulation electrode site (72 µm) in the centre and two halve electrodes (36 µm each) at the sides. This model uses Parylene, an isolating material around the stiff MEA which has TiN stimulation electrode sites on an undoped silicon substrate. For simulation purpose the whole model is assumed to be enclosed in a defined perilymph environment. The simulations have been done using the AC/DC module of Comsol Multiphysics 4.2a, specially the Electric Currents (ec) physics. This physics has some predefined nodes: current conservation, electric insulation and initial values. A monopolar type of electrode stimulation is considered where normally in CI's a single electrode inside the cochlea is active with an return electrode is far from the target neuron, the stimulating flied is essentially that of the mono-pole, the return electrode is assumed at infinity [15]. In the simulation model one electrode is stimulated (active centre electrode) and there is an extracochlear electrode which is modelled as an ground electrode i.e. a ground node is added (in our case the bottom boundary of the perilymph). In this simulations no biphasic waveforms were used. For the stimulation purpose the current stimulus been used in order to stimulate the electric potentials inside the medium (perilymph) was stationary with a 1 mA amplitude. All components are initialized on 0V, except for the stimulated electrode which has the maximum electric potential of +544 mV for monopolar configuration adapted from the findings of G. Tognola [13]. Other material properties used during the simulation are listed in Table 2.

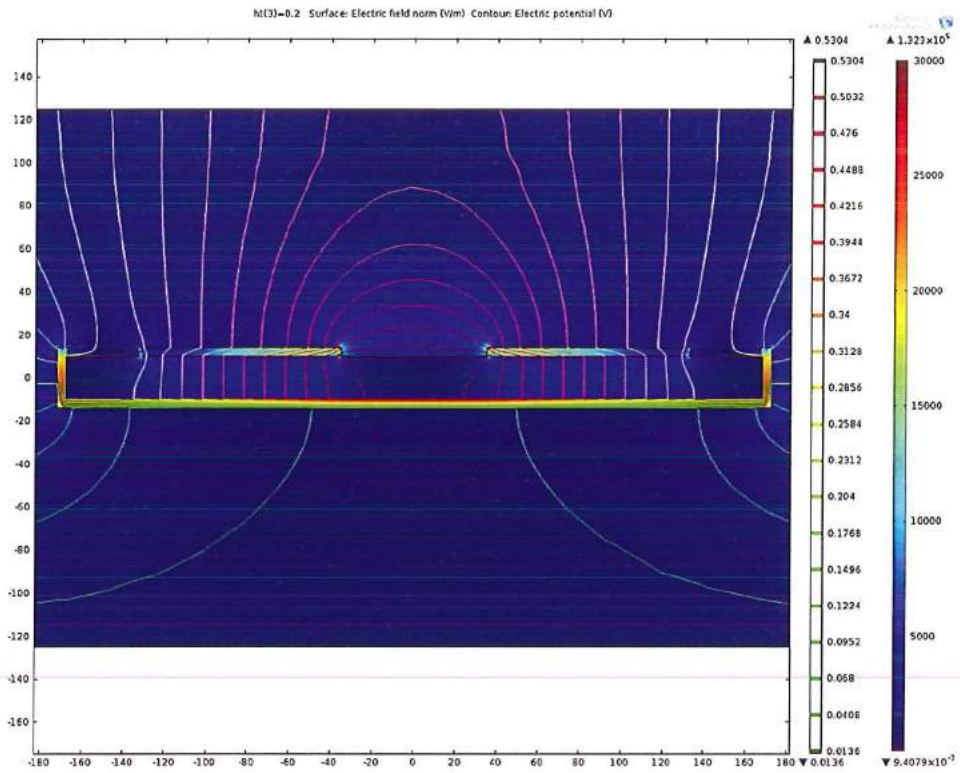

Figure 5.12 Colour plot showing the electric field (surface colour) and the potential (contour lines) of the protruded design configuration.

To study the three different design configurations (protruded, planar and embedded) a parameter sweep function in COMSOL is used. The parameter sweep simulates the three options in one go, creating the possibility to extract figures with the three results in one graph. The dimensions that have been used for these configurations in the parameter sweep method are marked with a box as in Figure 5.11. For simulation process a mesh with sufficient elements is required. Meshing of models with high aspect ratios, like the one described here, can be problematic, because the difference between the smallest dimension (200 nm) and the largest (600 nm) is very big. This means that both relatively large elements and very small elements need to be created. That is why a free triangular mesh is chosen with a maximum edge size of 40.2 µm, a minimum size of 5 nm, a maximum element growth rate of 1.2, resolution of the curvature of 0.3 and a resolution of narrow regions of 1. In that way the relatively thin electrodes and the regions around the corners are sufficiently meshed. The final mesh is as shown in Figure 5.13. It can be observed that the electrodes are meshed many elements and the elements increase in size when

they are further from the array due to the growth rate. Minimum element size gives the option of having sufficient meshing at the corners. Narrow regions like the electrodes are meshed correctly, because the resolution of narrow regions is 1, it is a factor between 0 and 1, where 1 gives the highest resolution. There are no curved boundaries, so the resolution of curvature (also a factor between 0 and 1) does not contribute to this model.

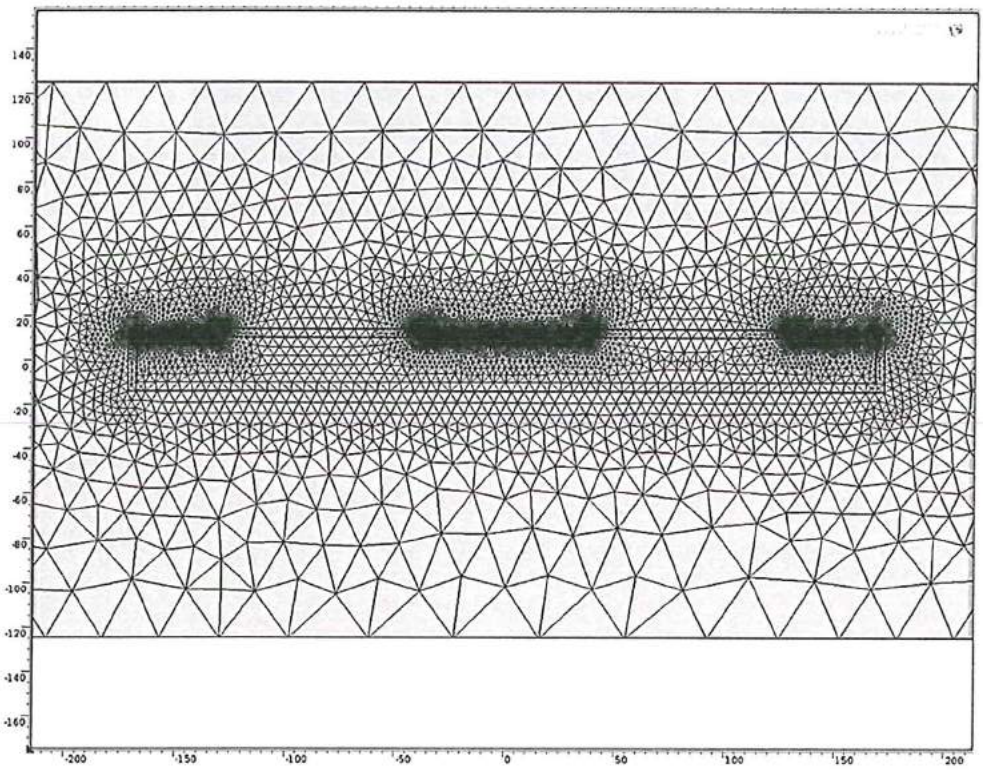

Figure 5.13 The mesh used in the model with correct aspect ratios.

The simulation is done using a stationary solver with a parametric sweep of the three options. The configuration of the solver is kept with its default values. When the simulation is finished, there are some ways to extract the data. One is the model with an overlay of the electric field and the potential. This shows only one step of the parametric sweep, the protruded version in this case. For electric field comparisons of 3 designs a 2D graph is created. The data used in this graph is the potential of the perilymph at 30 µm from the surface of the silicon substrate (Figure 5.14). From this it is clear that the difference in potential distributions is very small.

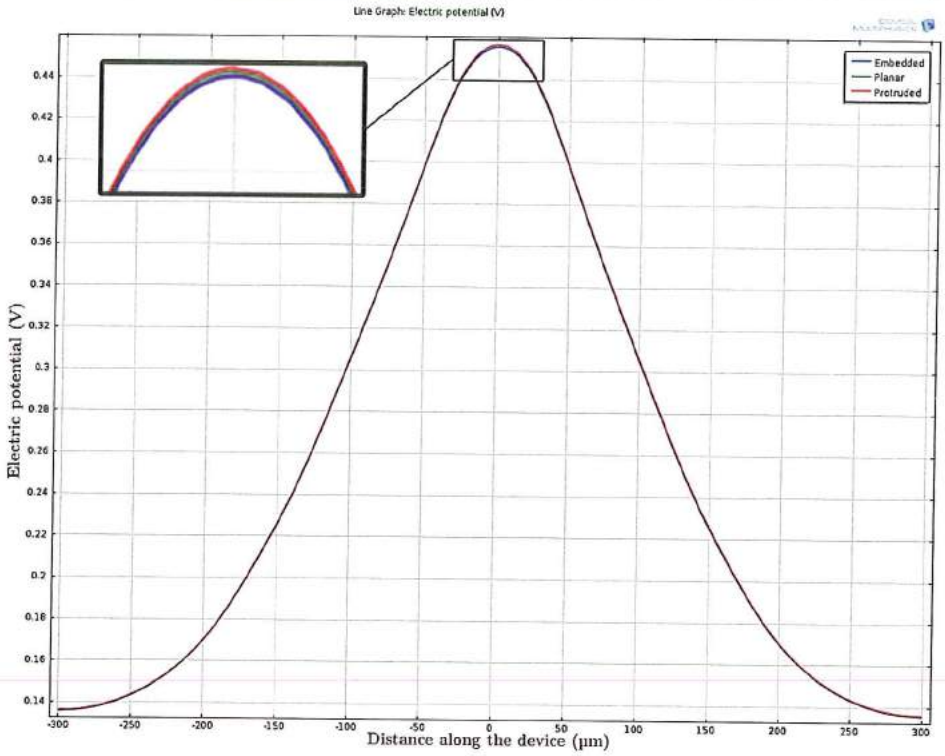

Figure 5.14 2D graph representing the electric potential in perilymph at 30 µm from the electrode surface for the three design configurations.

5.6.2 FEM modelling for flexible devices

Similar FEA was performed for the flexible section of the "Flexi-Stiff" MEA using COMSOL Mutliphysics 5. The model used for this simulation is as shown in Figure 5.15. The 2D model consists of the stimulation site metal stack (Ti: 40 nm + TiN: 200 nm) on top of a 10 µm thick polyimide (PI2611). This whole 2D assembly is inside a fixed perilymph environment of 2400 µm × 1600 µm. The remaining dimensions are as specified in Figure 5.15 with the properties as stated in Table 3. The other time varying bio-electric fields, currents and voltages for the biological medium can be studied by the conventional quasistatic limitations [12]. As per these conditions, the electric potential, (V) in the biological (perilymph) medium is defined by solving the Laplace's equation:

$$\nabla.\left\{\left(\sigma + i\omega\varepsilon_0\varepsilon_r\right)\nabla V\right\} = 0 \qquad (5)$$

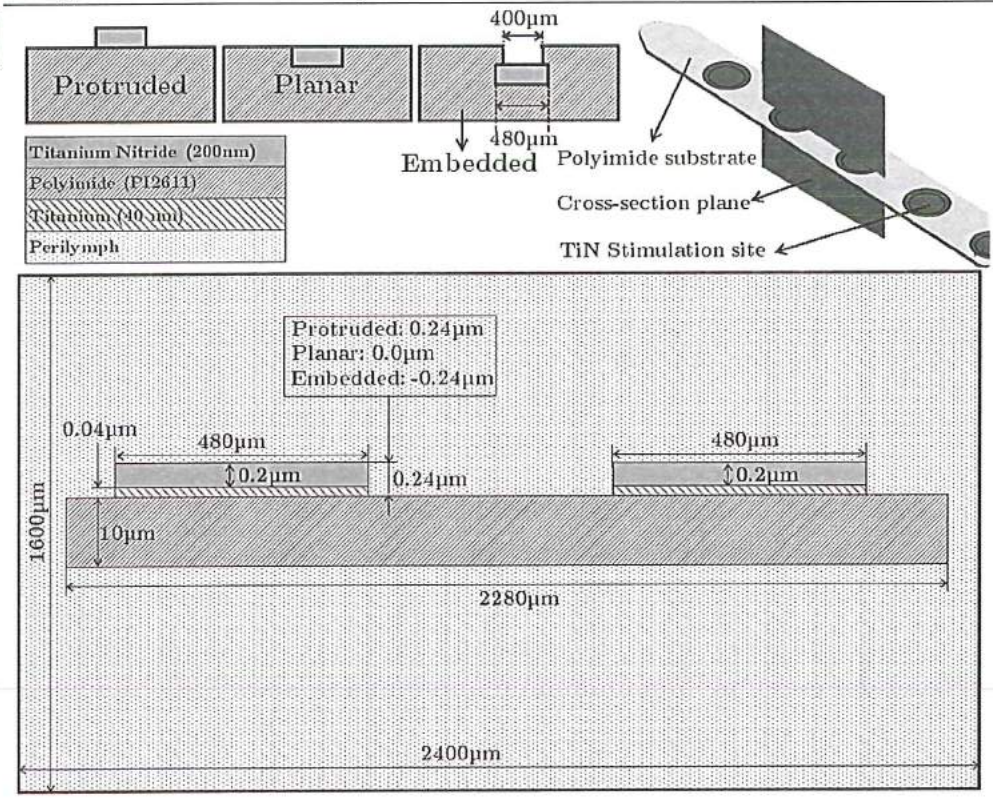

Figure 5.15 Part of the "Flexi-Stiff" MEA been used for FEA.

Material	Dimensions (Width × Thickness) µm	Conductivity σ (S/m)	Relative Permittivity (ε_r)
Titanium	480 × 0.04	2.6×10^6 [17]	80 [18]
TiN	480 × 0.2	5×10^3	100
PI2611	2280 × 10	1×10^{-17} [20]	4 [20]
Perilymph	2400 × 1600	2 [19]	109 [19]

Table 3. Material properties considered FEA analysis of the flexible device.

where σ and ε_r are the conductivity and relative permittivity of the medium correspondingly, ω is the frequency with which the stimulus is driven which is $\omega = 2\pi f$, ε_0 is the vacuum permittivity, and i is an imaginary number. The current density (J) of electrode site in relation to V is stated as [20]:

$$J = -\left(\sigma + i\omega\varepsilon_0\varepsilon_r\right)\nabla V \tag{6}$$

Kasi *et al.* [20] had similar simulation findings concluded that the potential drop across electrode is negligible in comparison to the potential drop across the tissue impedance. Also the capacitive component of tissue impedance is higher in magnitude than the resistive component. In this situation the simulation problem can be reduced to a simple and less computational frequency independent DC model with an purely resistive biological medium with the neglected electrode interface impedance [20]. Similar situation was considered where a simple DC model was considered for our FEA analysis. Simulations were performed with Comsol Multiphysics® 5 finite element simulation environment. A 2D axisymmetric finite element model as shown in Figure 5.15 for the electrode sites placed in a saline environment was created with a mesh of 713809 nodal elements. In the finite element modelling, the solution space for the given model to be analysed is divided into a series of nodes that define the corners of enclosed elements.

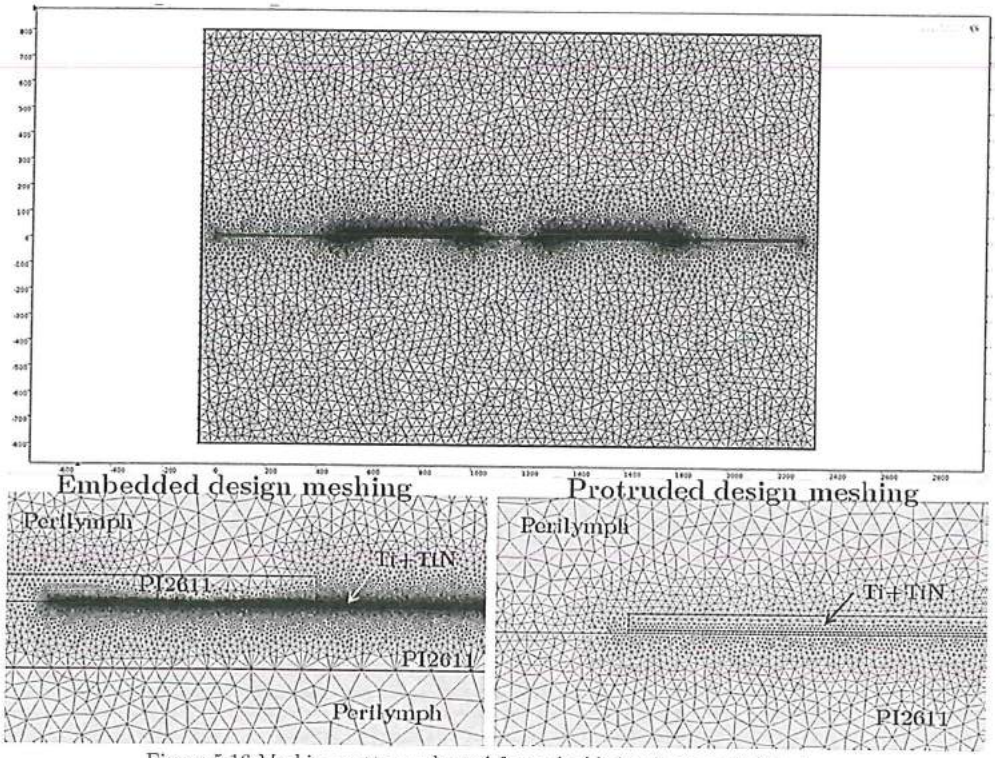

Figure 5.16 Meshing pattern adapted for embedded and protruded designs.

Each element is transformed locally onto a rigidly defined master element and the equation are approximated linearly across the element. The results are mapped onto

a system matrix and solved as a series of simultaneous equations to determine the overall electric potential field. The meshing, by default is Delaunay (normal or advancing front) triangulation meshing algorithm of Lagrange-quadratic element type was utilised in Comsol for meshing the simulation environment. The triangular mesh consists of a maximum element size of 48μm, minimum of 0.18 μm, a maximum element growth rate of 1.2 with a curvature factor of 0.25. The meshing pattern is as shown in Figure 5.16. In the simulation process the quasistatic and/or AC-DC module environment was used for the FEM model. Appropriate boundary conditions were used to define the electrode-perilymph interfaces, the considered simulation environment box. The other boundary conditions used in the simulation environment are listed in the Table 4 which were used for the quasistatic and/or AC-DC simulation performed using the FEM model. Simulations were performed under electrostatic conditions with an applied DC voltage between the stimulation electrode and the assumed ground boundary.

Domain/boundary name	Condition	Equation (s)
• All domains	Current conversation	$D=\varepsilon_0\varepsilon_r E$
• Simulation box (Upper and lower boundaries)	Electric insulation	$-n.J=0$
• Stimulation electrode	Electric potential	$V=V_{stimulation}$
• Simulation box (Left and right boundaries)	Ground	$V=0$
• TiN layer (perimeter)	Electric potential	$V=V_{stimulation}$
Equations used to compute electric potential (V) of the medium caused due to an electrode stimulation		$\nabla.J=Q_j$ $J=\sigma E+J_e$ $E=-\nabla V$

Table 4. Boundary/domain conditions and the equations of AC-DC module. *Notations:* J - current density of electrode; E - electric field vector; $V_{stimulation}$ - Voltage stimulus amplitude; n - normal vector; σ - medium conductivity.

In this model two different stimulation techniques were implemented in which the first stimulation method was similar to the stiff probe stimulation method where one stimulation site was used to stimulate with a maximum electric potential of +544 mV for monopolar configuration adapted from the findings of G. Tognola [13]. The result of the electric peak potential in the perilymph at 30 µm from the electrode surface plotted for three different design configurations is as seen in the graph of Figure 5.17. As seen from the plot there is not much difference observed in the three design (protruded, planar and embedded) configurations. The only visible difference was observed between the protruded and the embedded designs. So these two design configurations were further investigated for electric field density distribution.

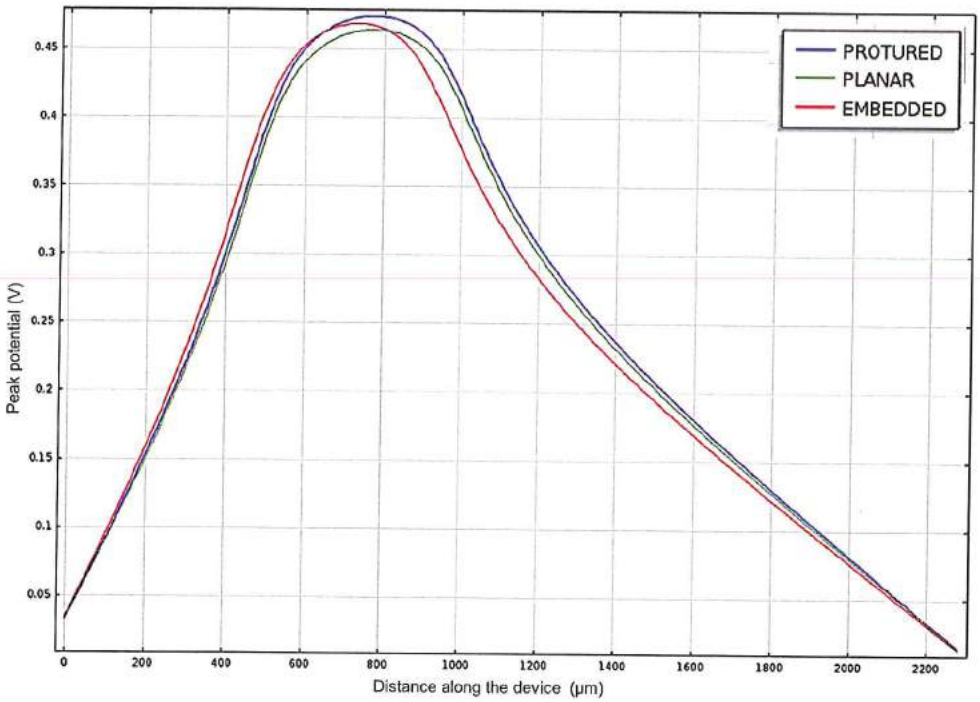

Figure 5.17 Electric peak potential for 3 designs with single electrode stimulation.

In the second type of stimulation method two electrode stimulation sites were considered for stimulation where similar conditions (maximum electric potential of +544 mV) was used as per the first method the only difference was the electric potential distribution plots where plotted at various distances from the electrode stimulation site surface. The current density streamlines were plotted at 50 µm, 100 µm, 200 µm, 300 µm, 400 µm until 800 µm from the electrode surface as shown in Figure 5.18.

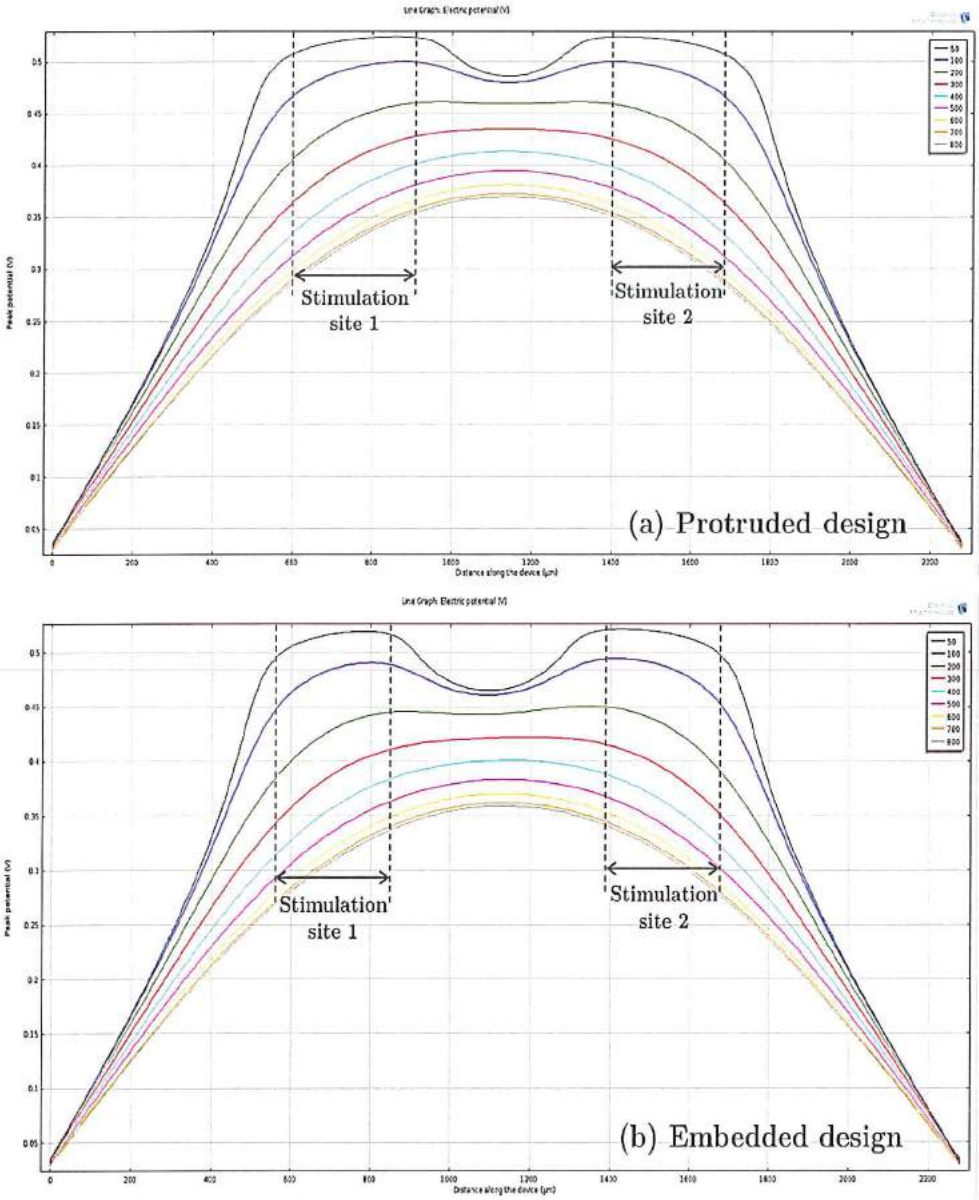

Figure 5.18 Current density streamlines for (a) Protruded and (b) Embedded designs with two electrode stimulation site stimulation method.

As seen from the plots of the electric peak potential for protruded and the embedded designs there is an similar pattern observed. The only difference seen in the electric potential was at 50 µm from the electrode stimulation site surface which has different peaks due to the design structure in both the configurations. In protruded design the electric potential distribution of one electrode influences the

electric field of the neighbouring stimulation site. This potential distribution effect influences individual electric field distribution resulting in lowering the overall neural stimulation process. This might lead to overstimulation of the neurons causing fatal damage to them which are present in the basilar membrane of the cochlea.

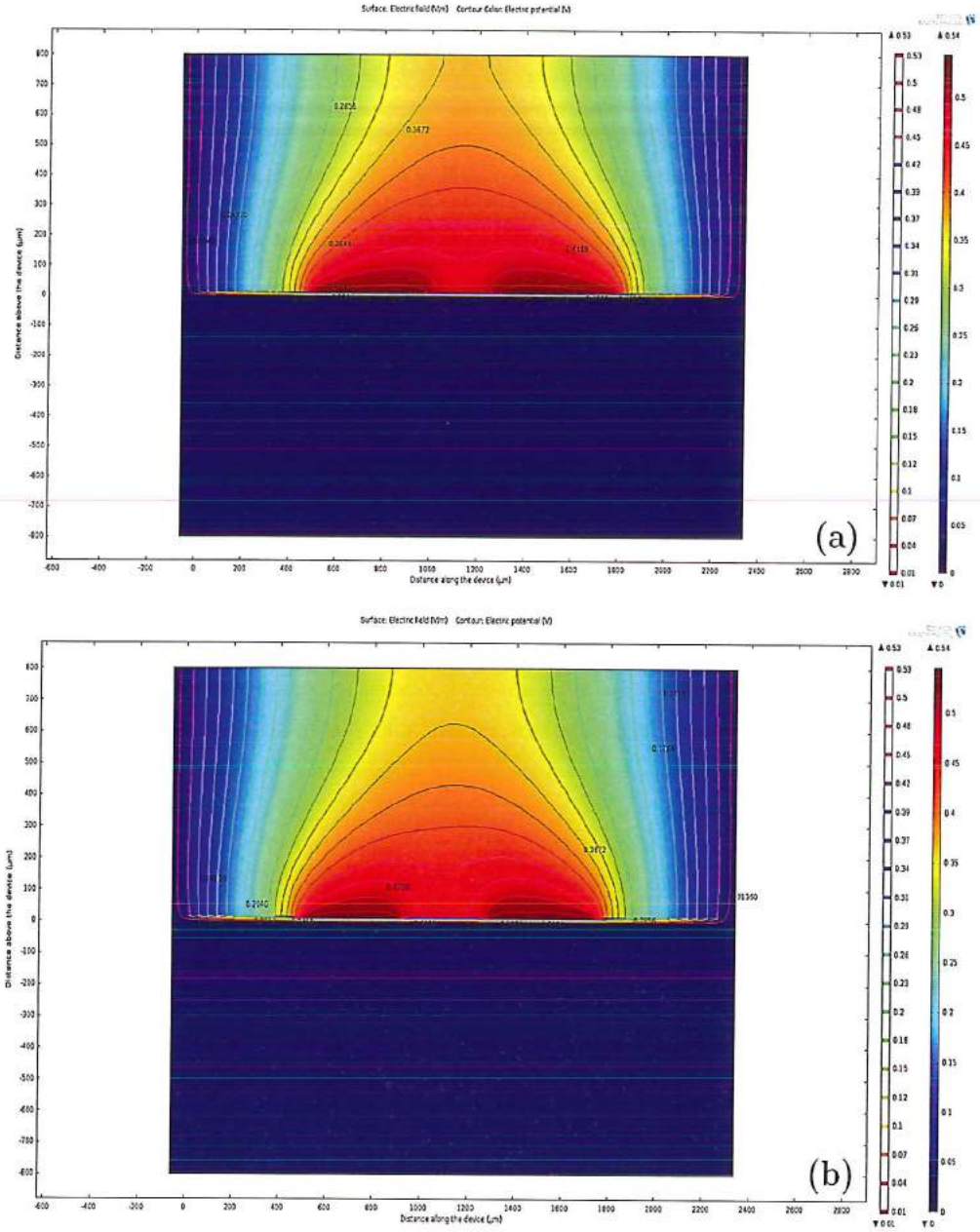

Figure 5.19 Colour plot showing the electric field (surface colour) and the potential (contour lines) of the a) protruded design and b) embedded designs.

An indication of the subsequent surface voltage contour profiles for the stimulation electrode process for the two electrode stimulation sites considered as per the model (refer to the FEA model in Figure 5.15) is as presented in Figure 5.19. The contour plots representing the electric density distribution for the two design configurations shows a less significant difference. The electric potential inside the perilymph ranges from 0.28 to 0.54 mV for both the design configurations as seen in the plot. The contour colour plots representing the density distribution as shown in Figure 5.19 are the results of the electrode stimulation sites of two different design configurations (protruded and embedded) when subjected to an electric potential of +544 mV. The remaining contour plots for other potential values (+50 mV, +110 mV and +170 mV) when applied to both the design options were also studied and which can be referred in the Appendix sections.

5.7 Conclusions

In this chapter various design and fabrication aspects of the stiff silicon probe, with its subsequent fabrications issues, were stated. Further in the development process the design features of the 1st generation completely flexible MEA is mentioned followed by the 2nd generation "Flexi-Stiff" MEA. The fabrication of the 1st generation and the 2nd generation devices will be dealt in the next chapter. Further in the FEA analysis performed by COMSOL® on the stiff electrode and the flexible electrode array in which the electric field density distribution studies showed a negligible difference between the three (protruded, planar and embedded) design variations. The embedded design was selected due to its lower effects of the electric field on the neighbouring electrode sites which also results in less influence on the neural tissues which are exposed to the electrical stimulation process. Moreover the microfabrication process used for the embedded design configuration of the stimulation sites for the MEA is less complicated in comparison with the other two design configurations. The material investigations along with subsequent FEA analysis performed and mentioned in this chapter helped us to go in the direction where we can choose the favourable CMOS compatible material (TiN) with the design configuration which will ease the overall microfabrication process of MEA.

5.8 References

1. Stieglitz, T., T. Miniaturization of electrodes towards single cell stimulation in neural prostheses - potentials and limitations. In *4th MATHMOD, IMACS Symposium on Mathematical Modelling 2003. Proceedings. Vol.1: Abstract volume*; 2003.

2. Rahman, S.; Sahin, M. Finite element analysis of a microelectrode on a substrate. *Conf. Proc. Annu. Int. Conf. IEEE Eng. Med. Biol. Soc. IEEE Eng. Med. Biol. Soc. Annu. Conf.* **2004**, *6*, 4157–9.

3. Lertmanorat, Z.; Durand, D. M. Electrode array for reversing the recruitment order of peripheral nerve stimulation: a simulation study. *Conf. Proc. ... Annu. Int. Conf. IEEE Eng. Med. Biol. Soc. IEEE Eng. Med. Biol. Soc. Annu. Conf.* **2004**, *6*, 4145–8.

4. McIntyre, C. C.; Grill, W. M. Current density and electric field analysis of microelectrodes using finite element modeling. In *Proceedings of the 22nd Annual International Conference of the IEEE Engineering in Medicine and Biology Society (Cat. No.00CH37143)*; IEEE, 2000; Vol. 3, pp. 2010–2011.

5. Coatings, S. Medical Coatings (SCS) http://scscoatings.com/parylene-applications/medical-coatings.

6. Briaire, J. J.; LUMC Cochlear implants from model to patients, Faculty of Medicine, Leiden University Medical Center (LUMC), Leiden University, 2008.

7. Frijns, J. H. M.; Briaire, J. J.; Schoonhoven, R. Integrated use of volume conduction and neural models to simulate the response to cochlear implants. *Simul. Pract. Theory* **2000**, *8*, 75–97.

8. Ngamkham, W.; van Dongen, M. N.; Serdijn, W. A.; Bes, C. J.; Briaire, J. J.; Frijns, J. H. M. A 0.042 mm^2 programmable biphasic stimulator for cochlear implants suitable for a large number of channels. **2015**, 13.

9. McCreery, D. B.; Agnew, W. F.; Yuen, T. G. H.; Bullara, L. Charge density and charge per phase as cofactors in neural injury induced by electrical stimulation. *IEEE Trans. Biomed. Eng.* **1990**, *37*, 996–1001.

10. Wilson, B. S.; Finley, C. C.; Lawson, D. T.; Wolford, R. D. Speech processors for cochlear prostheses. *Proc. IEEE* **1988**, *76*, 1143–1154.

11. Busby, P. A.; Whitford, L. A.; Blamey, P. J.; Richardson, L. M.; Clark, G. M. Pitch perception for different modes of stimulation using the Cochlear multiple-electrode prosthesis. *J. Acoust. Soc. Am.* **1994**, *95*, 2658.

12. Plonsey, R.; Heppner, D. B. Considerations of quasi-stationarity in electrophysiological systems. *Bull. Math. Biophys.* **1967**, *29*, 657–664.

13. Tognola, G.; Pesatori, A.; Norgia, M.; Parazzini, M.; Di Rienzo, L.; Ravazzani, P.; Burdo, S.; Grandori, F.; Svelto, C. Numerical Modeling and Experimental Measurements of the Electric Potential Generated by Cochlear Implants in Physiological Tissues. *IEEE Trans. Instrum. Meas.* **2007**, *56*, 187–193.

14. Strelioff, D. A computer simulation of the generation and distribution of cochlear potentials. *J. Acoust. Soc. Am.* **1973**, *54*, 620.

15. Rattay, F.; Leao, R. N.; Felix, H. A model of the electrically excited human cochlear neuron. II. Influence of the three-dimensional cochlear structure on neural excitability. *Hear. Res.* **2001**, *153*, 64–79.

16. Gabriel, S.; Lau, R. W.; Gabriel, C. The dielectric properties of biological tissues: II. Measurements in the frequency range 10 Hz to 20 GHz. *Phys. Med. Biol.* **1996**, *41*, 2251–2269.

17. Pearson, G.; Bardeen, J. Electrical Properties of Pure Silicon and Silicon Alloys Containing Boron and Phosphorus. *Phys. Rev.* **1949**, *75*, 865–883.

18. Honsberg, C.; Bowden, S. General Properties of Silicon
http://pveducation.org/pvcdrom/materials/general-properties-of-silicon (accessed Jan 1, 2013).

19. Van Rienen, U.; Flehr, J.; Schreiber, U.; Schulze, S.; Gimsa, U.; Baumann, W.; Weiss, D. G.; Gimsa, J.; Benecke, R.; Pau, H.-W. Electro-Quasistatic Simulations in Bio-Systems Engineering and Medical Engineering. *Adv. Radio Sci.* **2005**, *3*, 39–49.

20. Kasi, H.; Bertsch, A.; Guyomard, J.-L.; Kolomiets, B.; Picaud, S.; Pelizzone, M.; Renaud, P. Simulations to study spatial extent of stimulation and effect of electrode-tissue gap in subretinal implants. *Med. Eng. Phys.* **2011**, *33*, 755–63.

Section III

Micro-technologies

Chapter 6
"Flexi-Stiff" microelectrode array (Microfabrication process)

Discovery consists of looking at the same thing as everyone else and thing something different.

Albert Szent-Györgyi (Noble Prize in Physiology or Medicine, 1937)

This chapter starts with review of the work on thin-film cochlear microelectrode arrays (MEAs) and their results. Further a detailed novel microfabrication process for the "flexi-stiff" MEA is demonstrated which was developed at Else Kooi Laboratory (formerly referred as DIMES). Some of the micro-fabrication steps are based on the Flex-to-Rigid (F2R) technology platform also developed at the same lab, where the devices are first fabricated on the silicon wafers which further are transferred onto polyimide by backside silicon deep reactive ion etching (DRIE) process, thus enabling the partially flexible state. This flexibility permits the devices to be folded or wrapped around in desired shape to stiff MEA carriers such as silicone. The rigid part of the MEA contains the necessary bond pad area which allows standard wire-bonding for connecting to the driving electronics. The cleanroom processing steps and their improvement methods to optimize the microfabrication process are also discussed with the problems related to polyimide etching and post etch corrosion encountered in the path of the process flow chart. Subsequent measures were taken to solve them to end up in a "Flex-Stiff" MEA.

6

6.1 Introduction to thin-film Cochlear multielectrodes

In the recent years, MEA fabrication techniques have developed in combination with the microelectromechanical systems (MEMS) to extend the MEA fabrication possibilities from macroscopic to microscopic world. Photolithography, physical vapour deposition techniques, metal sputtering, etching etc. explained in earlier chapter facilitates to fabricate micrometer size features which were not possible by traditional manufacturing methods. Different groups conducted research in the MEAs area to obtain consistent recording signals from a small group of neurons without losing microstimulation capabilities, while maintaining low-impedance pathways for charge injection, high-charge transfer, and high-spatial resolution by altering the material composites and geometries of the arrays [1].

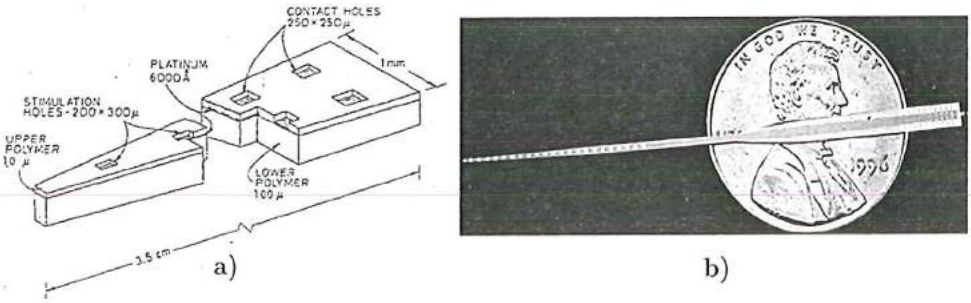

Figure 6.1 (a) Schematics of the polymer-Pt-polymer thin-film scala tympani electrode [4]; the first generation silicon-substrate MEA from WIMS, Michigan featuring 22-sties of 250 μm diameter with a pitch of 750 μm [5].

The various known advantages of photolithographic techniques from IC industry motivated Sonn and Feist in the 1900's [2] followed by Clark and Hallworth [3] in 2007 to develop the first flexible MEA prototype using a polymer-metal-polymer sandwich intended to use in the scala tympani. Sonn and Feist used Teflon and Platinum (Pt) to build their flexible MEA, similarly Clark and Hallworth showed an MEA with 17 Pt stimulation sites (0.5 mm^2 diameter) connected by Pt interconnects. These Pt interconnects were rf-sputtered on a 0.1μm thick fluorinated ethylene-propylene Teflon substrate. The device ends with an another upper passivation Teflon (0.3 μm) layer pattered with a lift-off process. Inspite of successful bending tests to prove the flexibility of the device during insertions other tests showed delamination, insulation and continuity problems. Researchers (White *et al.* [4]) at Stanford University developed both a stiff modiolar and a flexible scala tympani array using photolithographic techniques to fabricate an eight-site thin-film MEA [4]. The first version designed to directly stimulate the auditory nerve by exiting the

cochlea consists of a silicon substrate, gold interconnects and silicon dioxide (SiO_2) as an insulating layer. SiO_2 peeling and gold interconnect dissolution was occurred due to extended exposure of the MEA to saline environment. In various stages of development the substrate material was started from silicon to tungsten to molybdenum and ended on sheets of single crystal sapphire. Similarly a SiO_2 dielectric was later changes to silicon nitride and tantalum pentoxide providing good adhesion to the tantalum (Ta) interconnects. A polyimide (Pyralin PI-2555) for the required biocompatibility and elasticity was spin coated on a silicon wafer serving as a substrate and also as an top layer insulator. This polymer was patterned to the required dimensions after the first soft bake process and then later was hard baked to finish the two stage curing/baking process. Pt was used as an stimulation metal which was patterned to form stimulation sites (Figure 6.1).

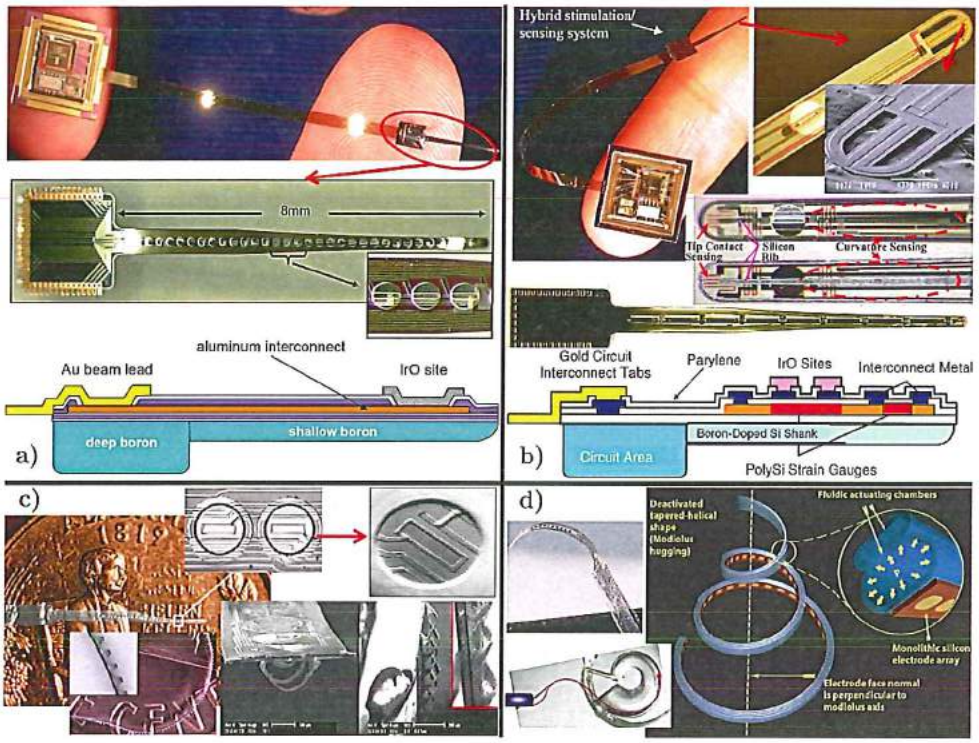

Figure 6.2. (a) P. Bhatti *et al.*: 32 site 4-channel high-density MEA [6]; (b) J. Wang *et al.*: An integrated position-sensing system in thin-film cochlear electrode array [7]; (c) A. Johnson *et al.*: An active thin-film cochlear MEA with monolithic backing and curl [10]; (d) B. Arcand *et al.*: Fluid actuator for safer placement of the thin-film MEA inside the scala tympani [11].

Re-sputtering of polymer surface followed by a thin Ta layer helped to adhere Pt to polyimide. MEA release was done by cutting the wafers with a diamond saw and

then later a quick dip into hydrofluoric acid to free from the silicon substrate. Initial *in-vivo* testing was not successful due as the sharp edges of the MEA caused damage of the basilar membrane, but in the second attempt to prevent insertion trauma and easy insertion a silastic carrier was used along with the MEA. A researcher (Bell *et al.*) from the Wireless Integrated Microsystems Engineering Research (WIMS) headed by K. D. Wise at the University of Michigan exhibited the first successful thin-film MEA with silicon-substrate [5]. This MEA consists of 22 iridium-oxide (IrO) stimulation sites of 250 µm diameter and a pitch of 750 µm (Figure 6.1). The passive MEA's were fabricated using a substrate which has boron-doped silicon of 4 µm thick with a deeper portion of 12 µm thick which holds the bonding pads. The devices were released from the wafer by an boron-doped etch stop process in which Ethylene-diamine pyrocatechol (EDP) was used for this purpose. In these devices polysilicon was used as an interconnect material.

Auditory threshold currents of 78 µA and 250 µA with monopolar and bipolar stimulation were applied during *in-vivo* experiments with these MEA's in guinea pigs to record electrically evoked auditory brainstem responses. Even though the electrochemical etch device release was well demonstrated for this application, but the large device width (640 µm) required lateral etch time that compromised mask integrity. Interconnect and device areas were attacked by HF during the etching process. Further in the cochlear implant research Bhatti *et al.* [6] from Michigan, in 2006 developed a 32 site 4-channel high-density passive intracochlear MEA. The array contains 180 µm contacts with a pitch of 250 µm. Combination of MEMS with active circuitry helped to realize a thin-film device with a stimulating site density which is three times that of the available commercial systems, delivering 500 µA biphasic current levels with 8-bit resolution and less than 1% charge mismatch Figure 6.2 (a). J. Wang *et al.* [7] with the goal to improve the thin-film cochlear electrode array integrated a polysilicon piezoresistive position-sensing system with bulk micromachining techniques Figure 6.2 (b) [8]. This MEA is based on the similar boron-doped silicon micromachining method where the tip contains a wall contact sensor with eight segmented polysilicon position sensors along the length and the encapsulating dielectrics. Each positon sensor was arranged in a half Wheatstone bridge, the signal from which is time-multiplexed, amplified (gain=10 or 30) and band limited. The effective gauge factor of the sensors is 15, permitting implant depth to be determined within 50 µm while providing wall-contact output signals of more than 50 mV at the tip [9]. Parylene-C is monolithically integrated into the fabrication process to improve the silicon array robustness with the flexibility to facilitate a modiolus-hugging shape during the insertion. Pre-defined curling of array was achieved using in-situ residual stress or post-release thermal actuation. A.

Johnson *et al.* effectively making using of parylene-C developed a 32-site, four channel, flexible CI prototype of 128-site eight-channel human prosthesis. The MEA comprises of metal layers embedded in parylene-C with parylene rings and self-curling parylene layers to achieve minimum radius of curvature [10] (Figure 6.2 c). Substrate stiffness can be adjusted from 0.2 to 1.4 kN.μm^2 with the help of parylene rings to increase rigidity in comparison to a flat parylene array. Insertion depths up to 6.5 mm ($>360^0$) was achieved during *in-vivo* experiments with guinea pig arrays without visual damage to scala media. The ASIC (application specific integrated circuit) (size: 2.2 mm×2.5 mm; power supply: ±2.5 V @ clock speed up to 500 kHZ) for the CI was designed to support a wide range of multisite multipolar stimulus configurations. Maximum power consumption was 2.5 mW with an output of monopolar 500 µA biphasic pulses [10].

Taking into consideration the small size and the delicate internal structures of the cochlea B. Arcand *et al.* [11] presented a miniature fluid actuator system to steer a thin-film MEA developed at the WIMS group. The actuator works in response to the change of the internal fluid pressure within one or more flattened and curled polymer micro-tubes, expanding the highly elliptical cross section of each tube, making it more stiffer and causing a change in its curling radius. *In-vivo* insertion tests showed that the actuator can place the thin-film MEA to a depth of more than one turn in the scala tympani under open-loop, manual control Figure 6.2 d [11]. All these CI MEAs development until now has enabled to move ahead in addressing and making attempt to solve these problems. There has been a mechanical challenge to make thin-film MEAs which is neither too flexible restricting the insertion inside cochlea nor too rigid (stiff) to intracochlear damage. These devices have yet to solve the long term stability issue in relation with material biocompatibility when used in harsh human body environment. Choosing the process with appropriate materials which are IC compatible with simple fabrication steps was the goal to solve the problem. Here we present the development towards microfabricating a thin-film "Flexi-Stiff" MEA process. In the following sections the issues related to the microfabrication process and results of the 1st generation (completely flexible MEA) will be described. Similarly, the 2nd generation "Flexi-Stiff" MEA will be presented which addresses the fabrication issues related to the 1st generation devices. The solution suggests the necessary changes required to be implemented in the overall design which aims towards *in-vivo* experimentation.

6

6.2 Flexible MEA (1st generation)

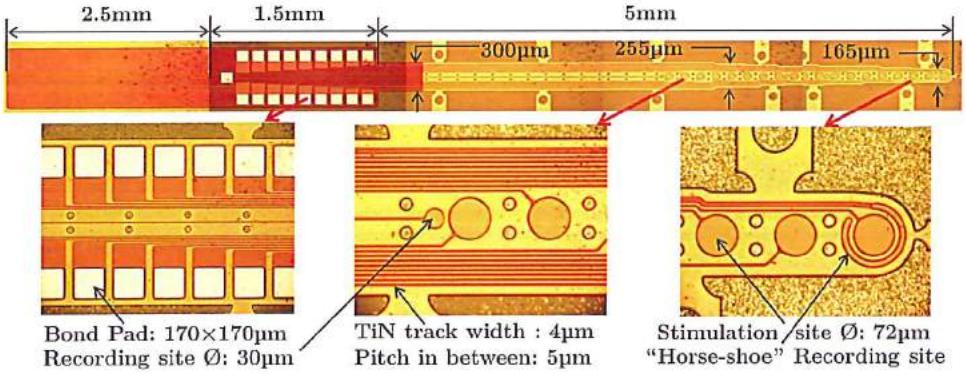

Figure 6.3 Images of the microfabricated Flexible MEA with dimensions and space at the basal end to accommodate the stimulation electronics.

Based on the design aspects mentioned in the earlier chapter (chapter 5) the completely flexible MEA consists of two Polyimide (PI 115A) layers of 10 µm thickness, each sandwiching a metal stack of Titanium (Ti: 40 nm) and Titanium Nitride (TiN: 200 nm) between the two PI layers. The upper PI isolation layer is selectively etched to expose the upper metal (TiN) which is acting in this case as an stimulation material. During the whole microfabrication process silicon is used as an supporting substrate which at the end is been removed when the sacrificial material in between the polyimide and the silicon is been etched away. The details of the microfabrication of this MEA is in the following sections.

6.2.1 Fabrication process flow chart description

The fabrication took place in a class 100 cleanroom using 4 inch wafers as the substrate carriers. The P type wafers (<100>) are single-sided side polished with low resistivity (2 – 5 Ωcm) and 525 ± 15 µm thickness. By thermal oxidation process at 1000 ^{o}C a 1 µm thick Silicon Oxide (SiO_2) layer was first grown on both sides of the wafer. Then pure Aluminium (Al) metal of 200 nm was sputtered on the front side (FS) by DC magnetron sputtering at 25 ^{o}C and was patterned by standard lithography wet etching techniques Figure 6.4 (a). This layer acts as a sacrificial layer to release the flexible devices at the end. After Al patterning, a 20 µm thick polyimide (Biomedical grade PI 115A) was spun on the wafer and was subsequently wet patterned to remove the polyimide (PI) from the edges using an positive photoresist (AZ9260) as a masking layer. The wet etching at the edges was done by a 2.5% TMAOH (Tetramethylammonium hydroxide) etchant. An adhesion promoter (primer VM 562) is initially applied before the PI spinning process in order to achieve a good adhesion between the thermal oxide and the PI layer. After solvent

evaporation (110 ^{o}C for 2 min) the PI layer is cured for 2 hours at 400 ^{o}C in vacuum oven with nitrogen environment. Due to evaporation of the soluble compounds in the PI its thickness was reduced to approximately 8 to 10 µm Figure 6.4 (b). The metal stack (Ti-TiN-Al) was then deposited by DC magnetron sputtering machine (Sigma 204 SPTS deposition system) Figure 6.4 (c). Ti of 40 nm was used as an adhesion layer between PI and the TiN of 200 nm which is sputtered above Ti. TiN is the microelectrode material which will be the stimulating material for stimulation of the auditory nerve fibres. Al of 1.5 µm was sputtered and patterned above TiN which is used for bond pads to connect the electronics with stimulation sites Figure 6.4 (d).

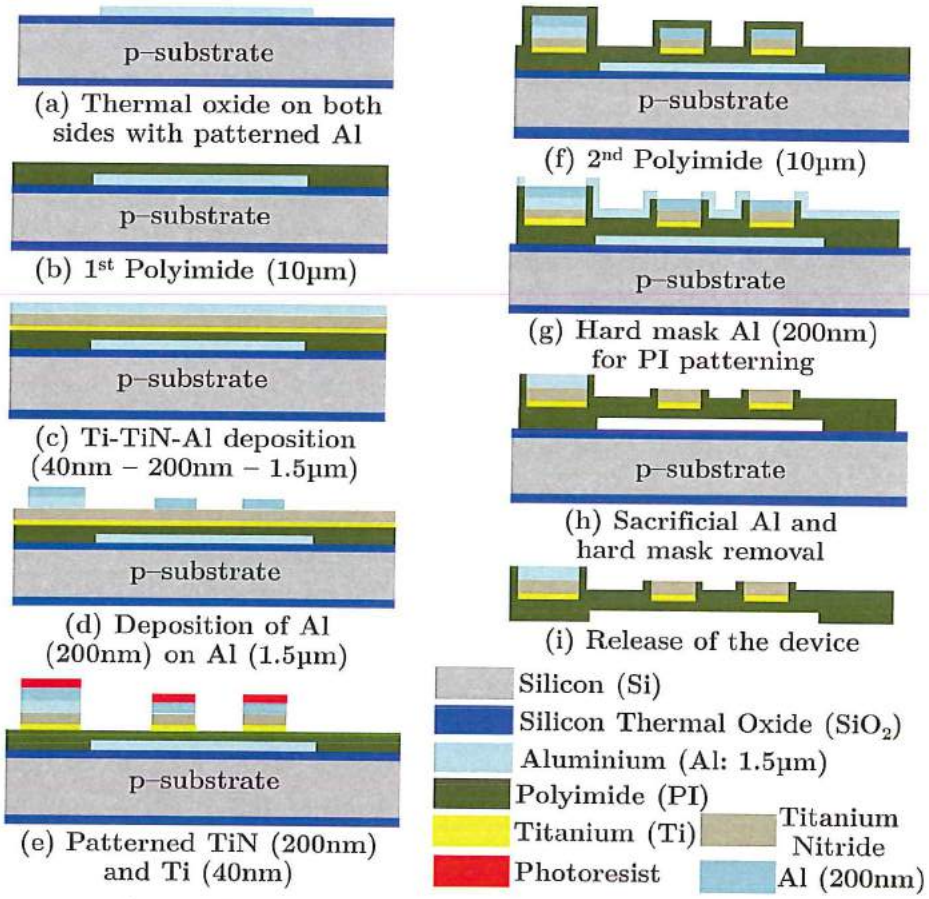

Figure 6.4 Cross-section schematics of the fabrication steps of flexible MEA.

The whole metal stack was deposited in one go by the puttering machine at 25 ^{o}C with pre-sputter clean of the Ti target after each TiN deposition to avoid N_2 contamination. After the dry patterning of the metal stack (Figure 6.4 (e)) the 2nd PI

layer is deposited in the similar process to achieve a thickness of 10 to 12 µm after curing Figure 6.4 (f). The whole PI layer (20 µm thick) was then dry patterned in oxygen plasma by using 200 nm of Al as a hard mask Figure 6.4 (g). After etching the PI, the underneath sacrificial Al (20 nm) and the Al hard mask (200 nm) were removed by a wet Al etching process in a single etch. The PES etchant used for this step is a combination of phosphoric acid (H_3PO_4; 85%), nitric acid (HNO_3; 65%), concentrated acetic acid (CH_3COOH; 100%) and deionized demi water (Mixing ratio - 4:4:1:1). After this step a freeze drying process was carried out. The devices (Figure 6.3) were released at the end by cutting off the PI strings attached as supports to the device. Some of manufacturing issues related to the device are stated below:

- The completely flexible device faced releasing problems due to the design in which the necessary vent holes which were meant to etch underneath the sacrificial Al layer caused the polymer device to adhere. Increasing the etching time in order to etch the sacrificial Al resulted in losing the Al bond pads. To solve this an additional mask was required to safeguard the Al bond pads in order to etch the sacrificial Al layer.
- The adhesion between the thermal oxide and the polyimide chosen (PI 115A) was not adequate enough to withstand the entire fabrication process which eventually resulted in delamination and cracking (thus making the PI and the underneath oxide layer unsuitable for our process and its application.
- PI 115A is known for its high moisture absorption (1.7% @ 50% RH [12]) capability which cause delamination during the fabrication process, also the mechanical properties such as the Young's modulus (3.3 GPa [12]) and the tensile strength at break (260 MPa [12]) are lower in comparison to other ones thus making it inappropriate polymer for our microfabrication process.
- Wire bonding and handling were also some of the main concerns for the completely flexible MEA.

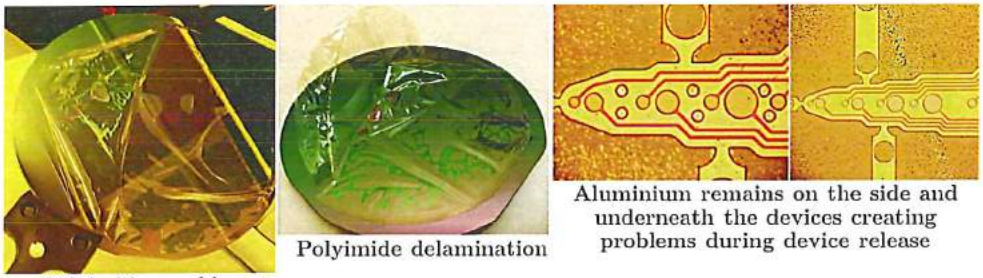

Figure 6.5 Images of the polyimide (PI 115A) delamination and cracking.

These manufacturing and material issues were a starting point to develop the 2nd generation "Flexi-Stiff" MEA.

6.3 "Flexi-Stiff" MEA (2nd generation)

The 1st generation completely flexible device was manufactured and design and manufacturing issues were identified. The necessary changes helped in the design and fabrication process for the 2nd generation MEA. The "Flexi-Stiff" MEA consists of a flexible polyimide part which contains the stimulation/recording electrode sites and a stiff silicon part which houses the bond pads for the connection to the external world such as stimulator circuit and other related electronics. The details of the various design variants present for the "Flexi-Stiff" MEA is discussed in the earlier chapter (Chapter 5).

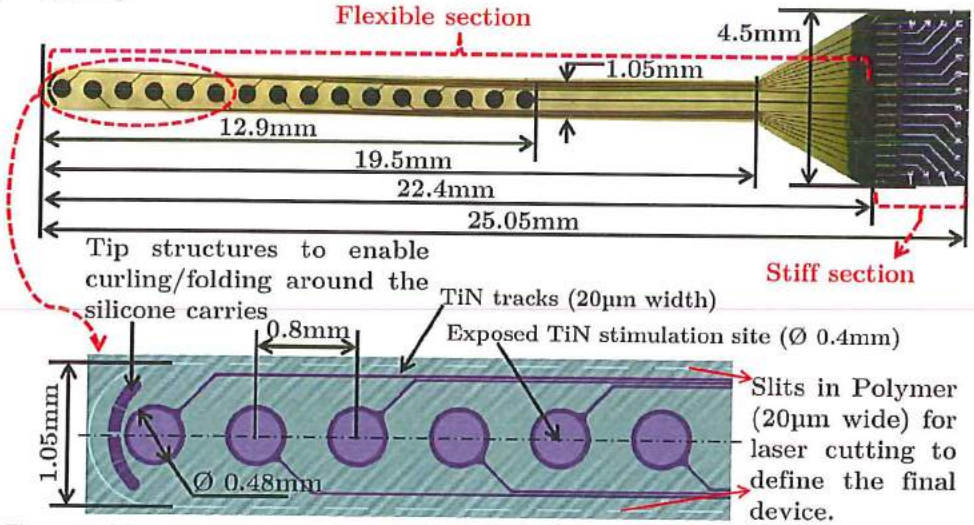

Figure 6.6 Microscopic image of the microfabricated "Flexi-Stiff" MEA with major dimensions and a closer view schematics of the tip.

In the following sections the details of the steps involved in the microfabrication process are mentioned. A step by step microfabrication process flow chart is given in the Appendix.

6.3.1 Fabrication process flow chart description

In this section the main fabrication process flow chart developed to fabricate the "Flexi-Stiff" MEA will be described. Some of the steps are based on the Flex-to-Rigid (F2R) technology platform, where the flexible devices are fabricated on silicon wafers are transferred onto a PI which at the end are made partially flexible by a backside deep reactive ion etching (DRIE) process [13]. The microfabrication steps from the F2R technology were accordingly changed in order to suit and realise the "Flexi-Stiff" MEA. A schematic representation of the main processing steps is given in as Figure 6.7.

The microfabrication process starts with plain 4 inch Si P type wafers (<100>) which are single side polished with low resistivity (2 – 5 Ωcm), 525 ± 15 µm thickness and a diameter of 100.0 ± 0.2 mm. Plasma enhanced chemical vapour deposition (PECVD) process was used to deposit Silicon dioxide (SiO_2) at 400 ^{o}C, on both sides (Front side: FS and Back side: BS) of the wafer with various thicknesses serving different purposes Figure 6.7 (a). On the FS a 1 µm thick PECVD SiO_2 serves as an base layer for supporting the upcoming polyimide and metal layers and also as an stop layer during the DRIE etching process while etching the Si from the BS of the wafer at a later stage of the fabrication process. On the BS the 6µm thick PECVD SiO_2 serves as a hard mask when selectively etching the 525 µm thick Si during the DRIE process. This BS 6 µm PECVD oxide layer was patterned selectively in a dry etching process carried in a Drytek 384T plasma etcher to land on Si Figure 6.7 (b).

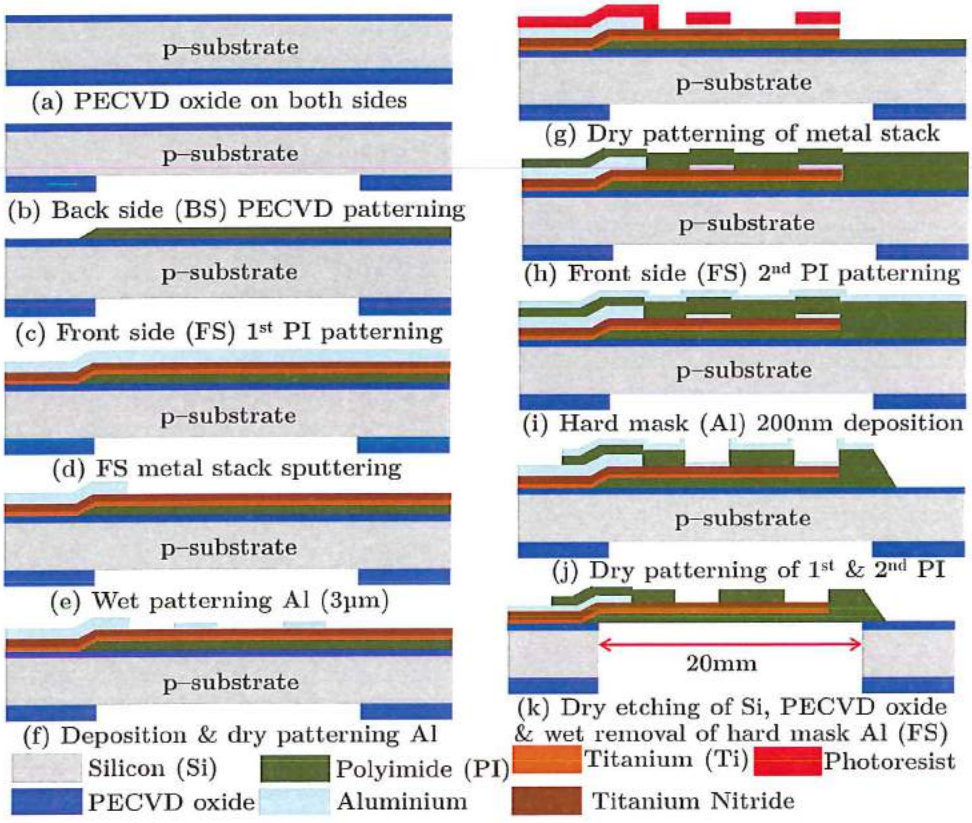

Figure 6.7 The major process fabrication steps for the "Flexi-Stiff" MEA.

After this an adhesion promoter (VM-651 from HD Microsystems) was spin-coated on the FS in order to improve the adhesion between the PI and the SiO_2

surface. After VM-651 application, polyimide (PI2611) was spin-coated and soft baked at 120 ^{o}C for 8min in order to remove most of the solvents to achieve an approximate thickness of 15 µm. The wafers were then hard cured at 350 ^{o}C for 2 hours in a low pressure (200 mbar) nitrogen atmosphere. The final curing produced an fully imidized 10 µm thick PI layers. The thickness of the cured polyimide layer can vary from 2.5 µm to 10µm depending on the PI been used (PI-2574 from HD microsystems using self-priming polyimide or PI2600 series using separate adhesion promoters) in combination with the spinning parameters. In the later part of this chapter an explanation for the choice of non-photodefineable PI2611 for fabricating the "Flexi-Stiff" MEA's is given in addition to the process parameters used in the coating and the curing process of the PI.

After this the masking layer was deposited. Normally oxides and metals are used as masking materials during the dry etching of PI. We used a 200 nm thick pure sputtered Aluminium (Al) as an hard mask to pattern the PI by dry etching process. In order to achieve a desired curved residue-free profile of the PI in the dry patterning process a combined anisotropic and isotropic dry etching process was used Figure 6.7 (c). The details of the combined etching process and the choice of the masking layer will be discussed in detail in the later sections. This residue-free PI etching profile step was adapted from Mimoun *et al.*, [14] processing steps with changes to process parameters tuned for PI2611 etching since Mimoun *et al.*, used a self-primed polyimide (115A from Fujifilm) used for a different application. Once the desired curved profile of the PI is prepared the metallisation step was performed in a TRIKON Aviza Sigma 204 sputtering machine. The metal stack consists of a adhesion layer Ti: 40 nm, TiN: 200 nm and a pure Al: 3 µm all deposited at 300 ^{o}C by the standard DC-Magnetron PVD (sputtering) process Figure 6.7 (d). The upper 3 µm Al was patterned wet by using a PES etchant (similar as in earlier section 6.2.1) during the wet Al etching process to define the bond pads for connection of the MEA to the external circuitry and the re-routing metal layer between the different TiN stimulation sites on the device and the bond-pad metal for subsequent wire bonding process done later Figure 6.7 (e). After wet etching and cleaning another pure Al (200 nm thick) was similarly sputter deposited at 25 ^{o}C which acts as an protective layer for the underneath TiN layer to be protected against the further steps in which plasma and other etching gases may change the surface microstructure of the columnar TiN. This Al layer along with the underneath metal stack (Ti: 40 nm and TiN: 200 nm) was patterned dry using a TRIKON Ωmega 201 plasma etcher Figure 6.7 (f) and (g). A spray coated negative photoresist (AZ® nLOF® 2000 series) of 14 µm was used to pattern the complete metal stack. The choice of negative resist was the result of an in-appropriate miniature dimensions litho definitions due to preferred positive resist (AZ® ECI 3027) as per the flow chart. The reason of using

the negative photoresist due to processing issues occurring because of the positive resist are explained in detail later in the section 6.4.3.1. Here during the litho steps NMP (N-Methylpyrrolidone) at 70 ^{o}C was well suited for stripping off the completely cross-linked AZ® nLOF® 2000 series negative resist which does not attack the polyimide underneath. After patterning of the metal stack the second PI layer was spin coated and cured in similar manner as the first PI layer Figure 6.7 (h). A 200 nm thick pure Al layer was sputtered in the same way as in step (f). This Al layer will be acting as a hard mask to etch the two PI layers (1st and 2nd PI) in one step Figure 6.7 (i). Dry patterning of PI was done by using a TRIKON Ωmega 201 plasma etcher to achieve an anisotropic etching profile as seen in Figure 6.7 (j).

After this step the back side (BS) processing step was began where an anisotropic silicon DRIE using a Bosch process was done to define the flexible part of the "Flexi-Stiff" MEA. The back side DRIE process etches the exposed Silicon parts completely through the wafer thickness (525 µm) to stop on the 1µm thick PECVD SiO_2 etch-stop layer deposited in step (a) on the front side (FS) of the wafer. The DRIE process was followed by a PECVD oxide (1 µm) removal from the BS. This dry etching was done in a Alactel GIR300 fluorine etcher in CH_4:CF_4:N_2=50:25:40 sccm environment at 500 mbar and a power of 60 W to achieve a etch rate of 390 Å/min. This dry etching of SIO_2 can also be done wet in BHF 1:7 (Buffered Hydrofluoric acid) but the dry process was chosen over wet due to handling and cleaning issues of the wafer holding the delicate devices to the Si substrate by the PI hinges at the edges as explained in the earlier chapter describing the die design of the MEA. After BS SiO_2 removal the FS 200 nm Al hard mask was removed along with the 200 nm protective Al covering the TiN layer at the same time by a wet etching process. The wet Al etch process is carried out by using a PES etchant (similar as in earlier section 6.2.1), thus exposing the PI and the TiN stimulation site surface to the atmosphere Figure 6.7 (k). The whole device per die of the wafer remains attached to the wafer by specially designed polyimide zipper like hinges that can be easily laser cut in order to remove the device from the support substrate Si wafer.

6.4 Fabrication Modules

This section describes the basic modules which were used to fabricate the "Flexi-Stiff" MEA devices developed in this thesis as well as other stiff microprobes used for other nerve stimulation applications. In the later sections all the important fabrication steps along with the main process flow chart will be explained in accordance with sketches to support the description.

6.4.1 Deposition and patterning of dielectric layers

Silicon (Si) being the dominant semiconductor material been used in the IC technology is largely been attributed for its passivating oxide layers or also referred as dielectric layer which are readily been formed on its surface. Dielectric layers are normally used as insulation layers to isolate metal layers from the silicon substrate and the harsh biological environment in which they have to withstand during their working period without degradation in properties and performance. In relation to MEA or any stiff probe application, the deposited dielectric materials have to be pinhole free, exhibit a high electrical resistance, and avoid any type of degradation by the biological environment of the human system [15]. Also on the other hand, the availability of appropriate deposition parameters and patterning techniques are necessary during the fabrication of MEA's. Especially in the stiff neural probes, the control of the residual stress of the deposited layers is crucial to avoid bending of the slender probe shafts during fabrication [16]. Oxides and nitrides of silicon, i.e., SiO_x and Si_xN_y are well known for their excellent material properties to serve for the electrical insulation of electronic components in micro devices [17].

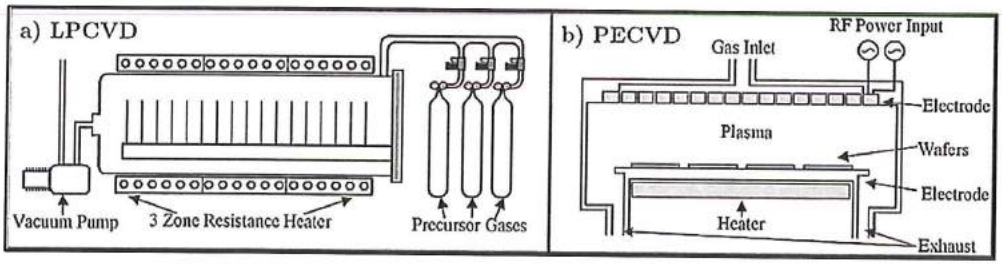

Figure 6.8 Schematics of a typical (a) LPCVD and a (b) PECVD system along with property comparison between silicon dioxide and silicon nitride [17].

Oxide deposition is a thermally driven conversion process which occurs over a wide range of temperatures, including ambient conditions. If grown/oxidized at room temperature a "native oxide" of 1-2 nm can be grown on a bare silicon surface in couple of hours or days, depending on surface conditions, and similar thin oxides from easily in oxygen plasma or in oxidizing wet environment. When a SiO_2 has to be grown directly on a silicon surface which is normally done by a low pressure chemical vapour deposition (LPCVD) process (Figure 6.8) with temperatures ranging between 400 – 1000 ^{o}C. A typical LPCVD system consists of a long, horizontal fused quartz reactor tube sized in length and diameter with vacuum sealed end caps. The contents of the reactor are heated up to 1000 ^{o}C by a resistive heater that envelops the reactor tube. Precursor gases are introduced via a gas manifold connected to

atleast one of the end caps [18]. Thermally grown SiO_2 is an standard reference material with a relative permittivity ε_r of ca. 4 (dielectric constant $\varepsilon=\varepsilon_r\varepsilon_0$) [17].

Property	SiO_2	Si_3N_4 (LPCVD)
Resistivity (Ω-cm), 25 °C	10^{16}	10^{16}
Density (g/cm^3)	2.2	2.9–3.1
Dielectric constant	3.8–3.9	6–7
Dielectric strength (V/cm)	12×10^6	10×10^6
Thermal expansion coefficient (ppm/°C)	0.5	1.6
Melting point (°C)	1700	1800
Refractive index	1.46	2.00
Specific heat (J/g °C)	1.0	0.7
Young's modulus (GPa)	87	~300
Yield strength (GPa)	8.4	14
Stress in film on Si (MPa)	200–400 C	1000 T
Thermal conductivity (W/cm K)	0.014	0.19
Etch rate in Buffered HF (nm/min)	100	1

Table 1. Comparison of properties between silicon dioxide and silicon nitride layers [17].

When a SiO_2 is needed on the materials other than silicon, it is done by chemical vapour deposition (CVD) or plasma enhanced CVD (PECVD). A typical PECVD system as shown in Figure 6.8 consists of a vacuum chamber, a vacuum pumping system and a gas manifold used for a PECVD deposition process. PECVD system is not only used to deposit dielectrics such as SiO_2 and Si_3N_4 but also amorphous and polycrystalline semiconductors like silicon can also be deposited. The chamber consists of an internal resistive heater that is connected directly to the substrate mounting stage. In addition to heater two large electrodes are used to generate a plasma inside the chamber by connecting the substrate stage to ground and other electrode to an RF power supply. The RF supply typically operates at 13.56 MHz and enables the formation of the high electric field required for the plasma [18].

In the processing of the "Flexi-Stiff" MEA to start with, PECVD oxide was chosen as the first layer of deposition which acts both as an adhesion layer for the forthcoming polyimide layer on the front side as well as an masking material on the back side for silicon DRIE etching (Figure 6.7 (a)). In addition to the properties of

the SiO_2 mentioned in the Table 1 the other main reasons for choosing PECVD oxide over LPCVD oxide are the low deposition temperature (300 ^oC) and the porous film quality. For PECVD, <0.1 pinholes/cm^2 is a good value. If the film is less dense than bulk, it can be either because of porosity or because of pinholes [17]. PECVD was utilized to deposit the low temperature SiO_2 layers by using a Novellus Concept One system. The mechanical quality of the deposited layers by PECVD is slightly lower than that of the high temperature LPCVD process. However, in contrast to the high temperature process this deposition method offers advantages such as higher deposition rates and the required pinhole surface which increases adhesion to the polyimide layer. The patterning or etching of SiO_2 on the back side of was done by dry etching which is driven by ion bombardment plasma etching so isotropic etching is therefore difficult but high-enough radical concentration will result in reasonable isotropic etch rates. Any fluorine-containing gas can be used as an etchant for oxide, CF_4 or SF_6, for example. However, both gases etch silicon too, and they are suitable for non-selective etching only. CHF_3 is used as oxide etch gas when selectively etching against silicon. This provides fluorine and carbon for etching (SiF_4, CO_2 etch products), and CF_2 radicals, which are polymer precursors. Polymerization takes place on silicon surfaces. Whereas on oxide surface $(CF_2)_n$ polymerization does not take place due to oxygen supply: ion bombardment induced reactions on oxide result in CO_2 formation [17]. The patterned SiO_2 will act as an hard mask to etch Si in the DRIE process.

6.4.2 Polyimide selection, properties and process parameters

Polyimide (PI) is a general term used to describe a group of polymers which vary widely in their physical and chemical properties. Polyimides are a class of thermally stable engineering polymers that are often based on stiff aromatic backbones exhibiting an exceptional combination of thermal stability (> 500 ^oC), mechanical strength and chemical resistance. Due to their high ductility and low CTE (coefficient of thermal expansion) these polymers are easily been realized into different microelectronic applications [19,20]. Various previous studies in the neural domain have involved different types of polyimides, giving a more generalized status of these polymer groups. The PI used in the microfabrication of the "Flexi-Stiff" MEA in this thesis is the BPDA-PPD type (or BPDA-DPA). Depending on the nomenclature (e.g., U-Varnish S from UBE or PI2611 from HD Microsystems) and is named after its precursor molecules biphenyl dainhydride (BPDA) and p-phenilene diamine (PPD) (for properties refer Table 2). Until now, for biomedical applications this PI appears to be the best suitable type as it is the least polar of all the polyimides [19,21,22], with the significance of having the lowest water uptake of only 0.045% [19,23,24]. Due to this less plasticization of material [25] is observed during

its application to human body and this as a consequence of low stress resulting in much lower volume increase in the device [26].

Sr. No.	Properties	PI-2611 (Non-photodefinable)	PI-2741 (Photodefinable)
	Mechanical properties		
1	Tensile strength	600 MPa	330 MPa
2	Elongation to break	60%	50%
3	Young's Modulus	6.6 GPa	6.1 GPa
4	Water intake in % weight @ 50%RH	0.5%	1.2%
	Electrical properties		
5	Dielectric constant (at 1kHz, 50% RH)	2.9	3.0
6	Dissipation factor (at 1kHz)	0.002	0.0018
	Thermal properties		
7	CTE	5 ppm/ ^{o}C	10 ppm/ ^{o}C
8	Decomposition temp.	620 ^{o}C	620 ^{o}C
9	Glass transition temp.	400 ^{o}C	365 ^{o}C
10	Residual stress	10 MPa	20 MPa
11	% Weight loss (500 ^{o}C in air, 2 hours)	1.0	1.5

Table 2. Properties of cured PI-2611 and PI-2741 polyimide [38]

In comparison to the other often used PI's, which tend towards absorbing more moisture and in some PI's for e.g. Kapton, BPDA-ODA, fluorinated or photodefineable PI exhibits dissolution in water thus leading to reduced reactivity [27–30]. This is also observed in the results after long-term aging tests aiming for mechanical properties required for a particular application in the human body [23]. On the other hand, other PI in-stability in such harsh environment is the major cause for delamination as shown in Figure 6.5. Certain techniques were adapted during the microfabrication process to avoid such delamination which will be addresses topic in the later sections. PI-2600 series (PI2610 and PI2611) are well known and characterized by the IC industry to be used frequently as interlayer dielectrics due to a desirable combination of high performance cured film properties to impact good mechanical and electrical properties. The cured PI from PI-2600 series offers a low residual stress level (around 2 MPa in a 10 µm thick film), low CTE (coefficient of thermal expansion), lowest moisture/water uptake within the group of Pyralin (HD microsystems) polyimides [26,31,32], high Young's modulus (8.5 GPa) and a high degree of ductility for microelectronic applications. Their CTE

of 5 ppm/^{o}C suits well to that of silicon. This material is supplied in the form of a liquid precursor of polyamic acids and N-Methyl-2-pyrrolidone (NMP) as the solvent.

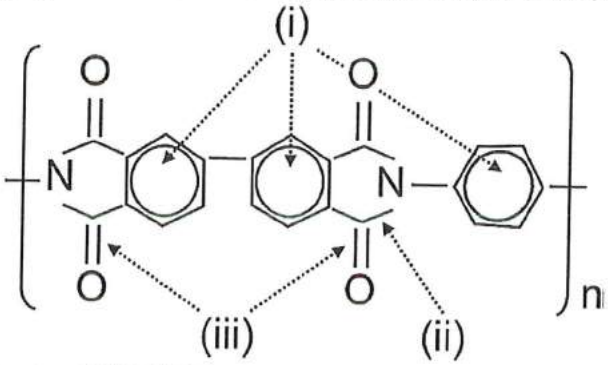

Figure 6.9 Chemical structure of BPDA/PPD of polyimide 2611 with arrow indication for the chemical bonding between carbon, N_2 and O_2: (i) C-C bonding in the benzene rings, (ii) C-N bonding, (iii) C= O carbonyl groups [33].

The chemical structural formula of the BPDA/PPD backbone of the PI2611 polyimide is as shown in Figure 6.9. The main chemical bonds as seen here are: (i) aromatic C-C; (ii) carbonyl groups C=O and (iii) imide groups (O=)=C-N. The sp^2 hybrid orbitals of the benzene carbon atoms overlap to form σ-bonds between neighbouring C atoms and the hydrogen atom. The overlap of the remaining carbon p-orbitals gives an π orbital system encompassing the benzene ring 'above' and 'below' the plane of the six C atoms. This delocalized π electrons system contributes to the relatively high stability of the benzene ring. The carbonyl groups form a plane between the oxygen and the carbon and the two more atoms – N and C – bound to the carbon. They exhibit a high dipolarity as a result of the relatively high electronegativity differences between oxygen and carbon. Thus, electrophilic groups attack the oxygen– and nucleophilic groups the carbon-side group. The nitrogen forms four sp^3 hybrid orbitals which result in non-planar bonds with the three neighbouring C atoms plus one N(2p) lone pair orbital [33,34]. These above mentioned properties for this PI makes it an ideal candidate suitable as a dielectric layer for most semiconductor IC industry or in thick film isolations or where metallization layers are stacked. PI patterning here is typically done by dry etching techniques (Figure 6.7 (c)) or by laser ablation techniques. PI-2611 provides a high molecular weight and fully aromatic PI based on BPDA/PPD backbone chemistry. The rigid rod PI structure of cured PI2611 exhibits essential film properties such as low stress, low CTE, low moisture uptake, high modulus and good ductility for heterogeneous microelectronic integration application thus anonymously making this material an ideal choice for the microfabrication of our "Flexi-Stiff" MEA.

6.4.2.1 *Polyimide (PI2611) processing (coating and dry etching)*

The PI versions (PI-2610 and PI-2611) from the PI-2600 series are highly viscous solutions which are deposited by a spin coating process. Due care has to be taken during PI dispensing since it is important to avoid trapped air in the solution causing bubbles to occur and one should allow them to dissipate out of the solution. Otherwise these bubbles will result in poor adhesion resulting delamination of the PI film. Also proper substrate surface preparation is important prior to PI application. As per the flowchart (Figure 6.7), after the amorphous PECVD SiO_2 deposition an organosilane-type adhesion promoter (VM-651 from HD Microsystems) was spin-coated (10 sec at 350 rpm and 45 sec at 3500 rpm) on SiO_2 layer in order to improve the adhesion between the PI and the SiO_2 surface. There are alternative ways for depositing the adhesion promoter in large volume batch processing, includes dip-coating substrates in adhesion promoter or dispensing the adhesion promoter by means of an automatic dispenser. The substrates are then dried on a hotplate for 60 seconds at 100 °C. After selective VM-651 application and drying, polyimide (PI2611) was then spin-coated.

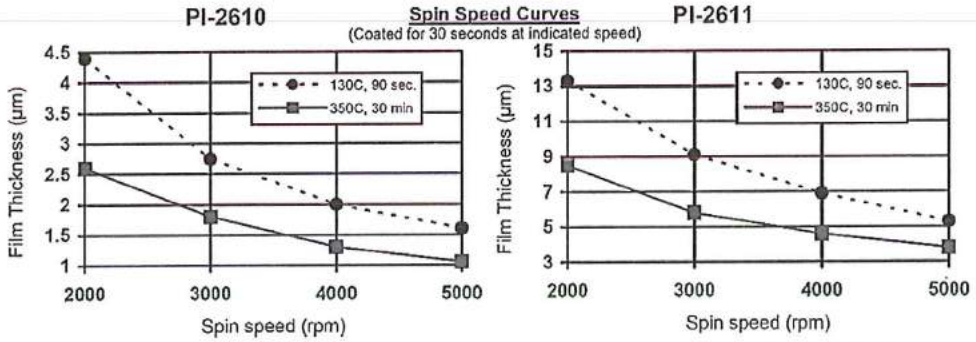

Figure 6.10 Curve showing the spinning speeds and thicknesses for PI-2600 series [31].

As seen from the Figure 6.10, the maximum soft baked film thickness of the PI layer is approximately 13 to 15 µm which is built of with several PI layers. The PI application is as follows: the PI is first dispensed on the substrate, rotated at 350 rpm for 15 sec (for a good spread of the material on the substrate) and then accelerated to 1000 rpm to rotate for 45 sec at this speed with further acceleration to 4000 rpm for 15 sec. The reason for spinning the PI at 4000 rpm is to limit the edge bead, i.e. a local thicker layer of PI at the edge of the substrate after spin-coating. The lower the final speed during spin-coating process, the thicker the final thickness of the spin-coated layer, but the more edge bead there will be at the edges of the substrates. After this a soft baked at 120 °C for 8 minutes done on a hotplate in

order to remove most of the solvents to achieve a thickness of 15 µm. The wafer edge bead (if any) and the back side PI contamination were chemically etched away by using 2.5% TMAOH (Tetramethylammonium hydroxide) as an etchant and a 3 µm thick positive photoresist (SPR3017M of MEGAPOSIT SPR3000 series photoresist from Shipley) as a masking layer. The wafers were then hard cured at 350 ^{o}C for 2 hours in a low pressure (200 mbar) nitrogen atmosphere. Cured layer thicknesses for PI-2611 were depicted as per the spin curves specified in Figure 6.10. An achievable thickness after final curing was between 9 to 10 µm which was an fully imidized PI layer. The hard curing process for was done in a vacuum oven at 350 ^{o}C, using the following standard curing steps adapted at the DIMES lab:

- Creating a vacuum (20 mbar pressure) in N_2 gas atmosphere and then heating the vacuum oven along with the wafers from room temperature (25 ^{o}C) to 200 ^{o}C with a ramp rate of 6 ^{o}C.
- Keeping the system at this temperature for 25 to 30 minutes.
- Then ramp up the heating from 200 ^{o}C to 350 ^{o}C with a ramp rate of 3 ^{o}C per minute.
- When reached at 350 ^{o}C the whole system is kept for 120 minutes at this temperature for the hard curing process.
- After the specified time a gradual cooling down is done to room temperature without any alteration to the N_2 atmosphere.

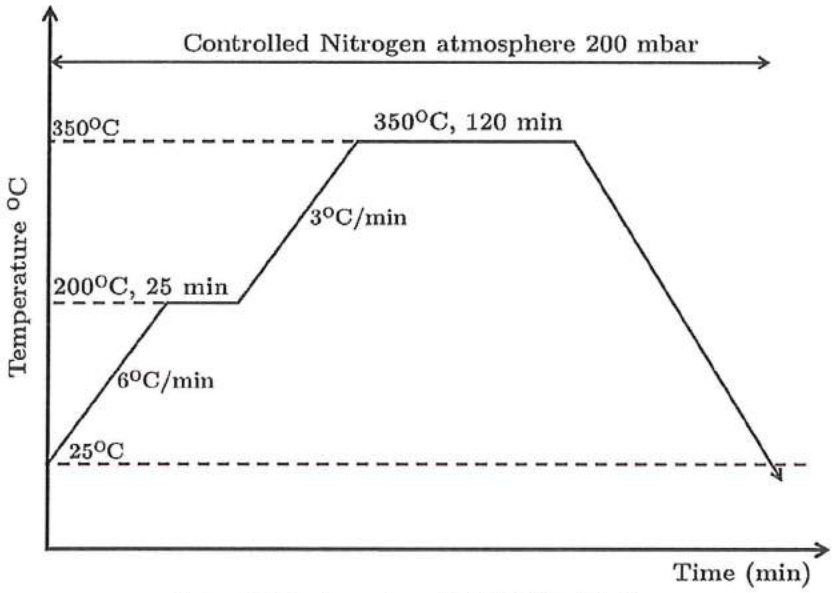

Figure 6.11 Curing cycle used for PI2611 polyimide.

During this curing cycle (Figure 6.11) the N_2 gas flow rate is used for a better removal of water and solvents evaporating from the spin-on PI. Patterning or etching PI was done by different methods depending upon the field of application. Using a dry sacrificial isotropic etch process of PI to release the top functional layer stiction problems normally encountered in wet sacrificial etching process can be eliminated [35]. In situations where PI was used as a dielectric layer or a substrate material in flexible applications anisotropic type of etching is required to obtain vertical electrical vias for subsequent electro(less) plating of metal [36,37]. By such process good anisotropy can be achieved after etching, however when interconnect material which is normally sputtered or evaporated on top of underneath PI layer has the requirement of good step coverage and electrical conduction. This is easily realized by a wet-etching process using a TMAH-based etchant using a thicker photoresist (usually 3 to 4 µm) before the hard curing of PI [38], or by using dry-etching methods after hard curing with parameters favouring the tapered via walls [39,40]. Various studies have been carried out in the area of PI etching using dry etching with different etch chemistries and related parameters [34,41–43]. At DIMES, Mimoun *et al.* [14] developed a residual-free plasma etching technique which is based on a two-step combination of both isotropic and anisotropic dry etching to etch polyimide to make residue-free fine pitch wine-glass shaped vias for subsequent metal deposition. It was shown that adding small content of fluorine gas to the etching mixture results in a residue-free polyimide at the end. In this etching process the possibility of using both, a metal or oxide masks were effectively demonstrated [44]. The polymer used here was a self-primed PI (115A from Fujifilm) using an additional adhesion promoter (VM-652 from HD microsystems) with combined etching recipes using a barrel-type plasma etching tool (Tepla IPC Plasma 300) and an inductively coupled plasma-reactive ion etching (ICP-RIE) tool (Trikon Ωmega 201). The complete etching procedure for the mentioned PI materials and the subsequent masking materials is explained in the research work [44] and publications [13,14]. In the microfabrication of the "Flexi-Stiff" MEA a non-photosensitive polyimide (PI 2611: BPDA-PPD type) along with a organosilane-type adhesion promoter (VM-651) provided from HD Microsystems was used. In this situation a slightly different approach in comparison to the etching technique developed by Mimoun *et al.* was adapted in order to achieve a desired curved profile of the 1st PI (10 µm) thick layer which facilitates a good step coverage for the next metal stack layer to be sputtered on top of the curvedly patterned PI layer. The curved etch profile of the PI for good step coverage was characterised using a scanning electron microscope (SEM) and the etch rates were measured using a profile-meter. Similar machines, such as the barrel-type etching tool (Tepla IPC Plasma 300) and an inductively coupled plasma-

reactive ion etching tool (ICP-RIE; Trikon Trikon Ωmega 201), were used but with different etching combination approach to achieve the desired PI profile which suits our application towards fabricating the "Flexi-Stiff" MEA. The two etching combination approaches with the etching tool explanations in detail are as follows:

1st etching approach using Tepla IPC Plasma 300 and Trikon Ωmega 201: In this combined two step etching procedure the first step etching machine (TEPLA IPC Plasma 300) which is a barrel-type plasma etching tool is based on a dry etching technique mostly used for stripping photoresist residues. A gas is introduced into the vacuum chamber and is ionized in reactive plasma with the help of a R.F. generator that excite a magnetron. Due to the ionization process of the gas, the undefined motion of the ions inside the chamber reach the target wafer to etch the PI in a purely chemical etching process. As a result, volatile reactions are extracted by a pumping system. The second step etching machine (Trikon Ωmega 201) which is an reactive ion-etching tool (ICP-RIE) is based on the same principle of the Tepla IPC Plasma 300. The only difference is that in this case the etching chamber's top electrode is grounded with the substrate (target wafer) to etched is acting as an excitation electrode. Due to this setup, where the target wafer is connected to R.F. signal instead of ground, the highly reactive electron species are often adsorbed by target wafer in comparison to heavier positive ions. On the other hand the electrons in the generated plasma which are positively charged ions are accelerated towards the target wafer thus resulting in an physical etch mechanism in which the layer to be etched is physically sputtered-off due to the impact of the ions on the wafer. The plasma generated by a magnetic field is aimed towards achieving an high ionization rate to improve the RIE process thus resulting in a physico-chemical etching process. As already known for etching PI atomic oxygen (O_2) is the main etching component used to add and/or abstract of O_2 atoms to unsaturated groups [19]. In both the mentioned etchers oxygen (O_2) gas in the main etchant but only atomic O_2 is not sufficient to remove unharmed structures. So in addition to this ion bombardments and natural defects in PI coatings are necessary in order to serve the purpose of the etching process. In addition to O_2 the presence of atomic fluorine in the plasma enhances O_2 production [34] resulting in increased etching efficiency. Also atomic fluorine reacts with PI surface in two ways to increase the overall etch rate; (a) fluorine addition to unsaturated benzene rings produces an intermediate saturated polymer having lower activation energy and (b) HF molecules are generated by combination of atomic fluorine with hydrogen atoms from PI surface, leaving behind a free surface radical sites for successive oxidation through atomic oxygen [42]. This combined approach which is similar to the "wine glass" residue free etching method from Mimoun *et al.* [14] in which the first step where the usage of the barrel-type

etcher (Tepla IPC Plasma 300) gives an isotropic etching profile with a thin residue layer (400 nm thick) is in accordance to our findings where the same residue layer was observed for our case during first isotropic etching in Tepla IPC 9200. The only difference that lies in our situation was in the second anisotropic PI plasma etching done in the ICP-RIE (Trikon Ωmega 201) etcher.

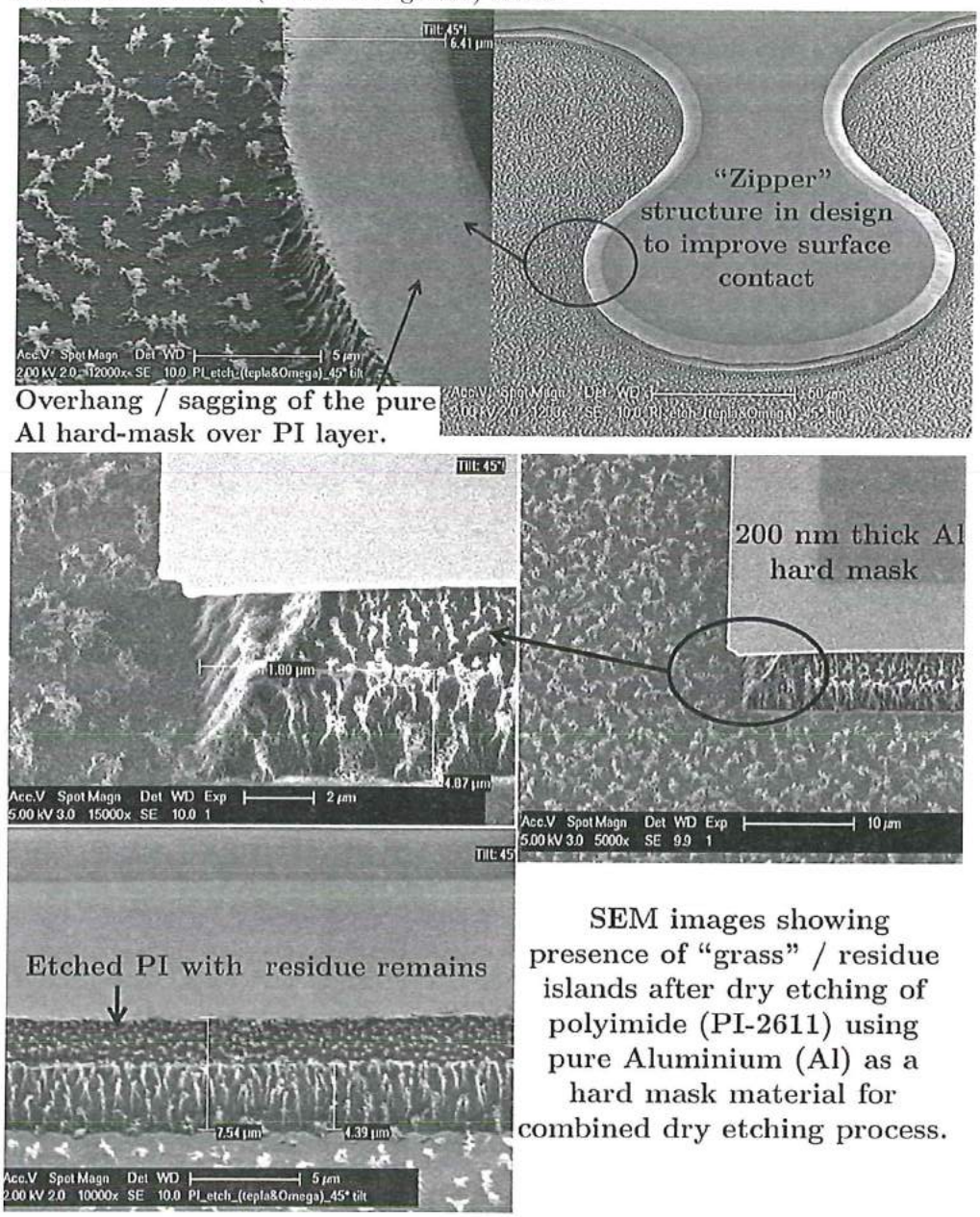

Figure 6.12 SEM images of combined dry etching using two machines.

As per Mimoun's findings [44] the gas mixture (80% O_2, 13% N_2 and 7%CF_4) used in the ICP-RIE etching chamber with 20 mTorr pressure and power of 500 W resulted in the removal of the residual layer while etching 10 µm PI (115A from Fujifilm) with an approximate etching rate of 1µm/min. Using this same etching recipe to etch PI (PI2611) for the 2nd step at the ICP-RIE etcher did not completely eliminate the residue layer, but resulted in lowering the thin residue layer to islands or "grass" type of structure as seen in Figure 6.12 which was not observed after the complete combined etching procedure adapted by Mimoun *et al.* This type of "grass" formation was earlier reported during etching PI in pure O_2 plasma which occurs due to inability of the ion bombardment to generate enough reactive sites to successfully destroy all the polyimide chains, resulting in non-volatile components and causing local micro-masking [42]. This micro-masking can also take place due to deposition of re-sputtered aluminium atoms from the hard mask been used during the etching process [39]. This "grass" like islands are mainly composed of the silicon-containing active ingredient (a-aminopropyltriethoxysilane) present in adhesion promoter (VM-651) which is used to improve adhesion by formation of Si-O bonds between the applied PI and the layer underneath (in this case PECVD SiO_2) [44]. The two reasons for the remaining "grass" islands, even though after using the same process conditions are; (a) The use of a different polyimide (PI-2611) and primer (VM-651) in process in comparison with the self-primed PI-115A and, (b) the open areas in the mask design along with large under etching due to longer etch times to etch the strong Si-O bonds present in the adhesion promoter (Figure 6.12). Taking these conclusions from this approach motivated to take the 2nd approach where only one etcher (Trikon Ωmega 201) was used.

2nd etching approach using the podule module and the ICP chamber of the Trikon Ωmega 201 etcher: The 1st approach involved the use of Tepla Plasma 300 to perform the 1st etch step. The drawback of that system is that the etch rate is uncontrollable and influenced by the amount of wafers that are loaded. Also the system must always be cooled down to room temperature before starting a process, to improve the reproducibility between batches. This formed the base of a new approach, in which the dry the complete PI is done in a single machine, a Trikon Ωmega 201 plasma etcher. This system is equipped with a special module (called podule), in addition to a standard ICP (Inductively Coupled Plasma) etch chamber (Figure 6.14 a). The podule etches polymer isotropically and is intended to strip the remaining resist from a wafer when the etching in the ICP chamber has finished. It is mainly used for an "Anti-corrosion" treatment after a metal etch process. In the new approach the PI layer is first etched in the podule, which allows for much better process control than the earlier used Tepla system.

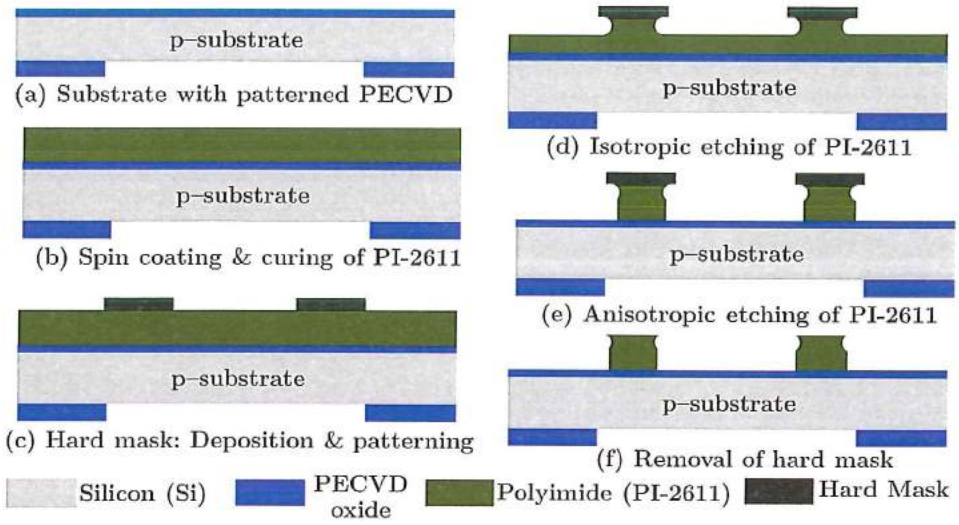

Figure 6.13 Schematics for PI etching process done in Trikon Ωmega 201 etcher.

At the bottom the podule is equipped with a 1 kW lamp (Figure 6.14c) which is normally used for heating the substrate wafer which accelerates the etching (resist removal) process of the PI (or photoresist) to be etched away. This lamp is surrounded by a metal cylinder casing (Figure 6.14d), which houses a reflector (Figure 6.14e) that evenly spreads the light on the backside of the wafer to heat it up. This will accelerate the polymer etch process. The lamp assembly is mounted underneath the podule chamber (Figure 6.14f) and is separated from the vacuum by a transparent glass plate directly under the wafer carrier ring. The wafer is supported on that ring at its edge by lifting pins. Above the wafer, a ceramic funnel shaped chamber is mounted (Figure 6.14g), where the plasma is created. The gas mixture consisting of oxygen, nitrogen and ammonia flows in from the top and is ignited with a 13.56 MHz RF coil around the ceramic tube. The ceramic chamber is enclosed in a metal box (Figure 6.14h) which protects it and shields off the RF radiation. A fan is mounted to avoid overheating of the chamber. As mentioned earlier the polyimide layer (PI2611)) is now first etched isotropically in the podule. Here 5 to 6 µm will be removed. Then the wafer is transferred into the ICP reactor without breaking the vacuum. There the remaining PI is anisotropically plasma etched with a gas mixture consisting of 80% O_2, 13% N_2 and 7%CF_4. The details of the process are represented schematically in Figure 6.13. The structures pattered for the 1st PI layer consists of either small features of 50 µm wide, or the larger features of approximate 2 mm×14 mm (L×W) with thickness of 10 µm. Hence the largest horizontal distance to be etched for a structure release is below 25 mm. In order to limit the etching process to

achieve the desired curved profile, the etching of the PI layer(s) consists of an isotropic etch step done in the "resist strip podule" module followed by an anisotropic etch done at the ICP-RIE chamber of the Trikon Ωmega 201 ICP etching tool as shown in Figure 6.14. As mentioned the isotropic etching takes place in the resist strip podule chamber where the reactive gases etch the PI layer up to 6 µm with an etch rate of 750 nm/min. The remaining (5 µm) PI etching process is done anisotropically in ICP-RIE chamber with an etch rate of 200 nm/min.

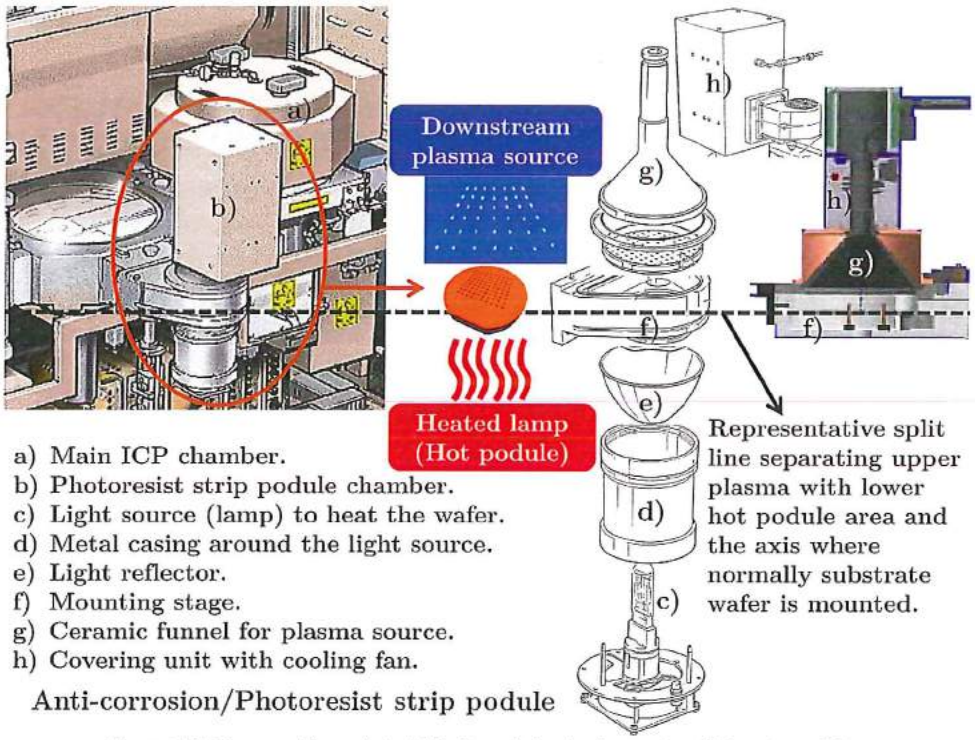

Figure 6.14 Image with exploded 3D view of the Anti-corrosion/PR strip podule.

The results of this etching approach are displayed in the SEM images as shown in Figure 6.15 and Figure 6.16.

6.4.2.2 Polyimide (PI2611) adhesion improvement

Various adhesion definitions and theories are mentioned by many researchers but to date it is difficult to have a common definition for adhesion due to different mechanisms involved in various conditions especially ranging in from thick films to thin films adhesion to different substrates. Depending on the predictor's perception, adhesion can be construed or stated as a force required to separate or hold together two bodies (materials), as an energy stored at the interface between the adhered and the adhesive to create the necessary binding forces to be operative.

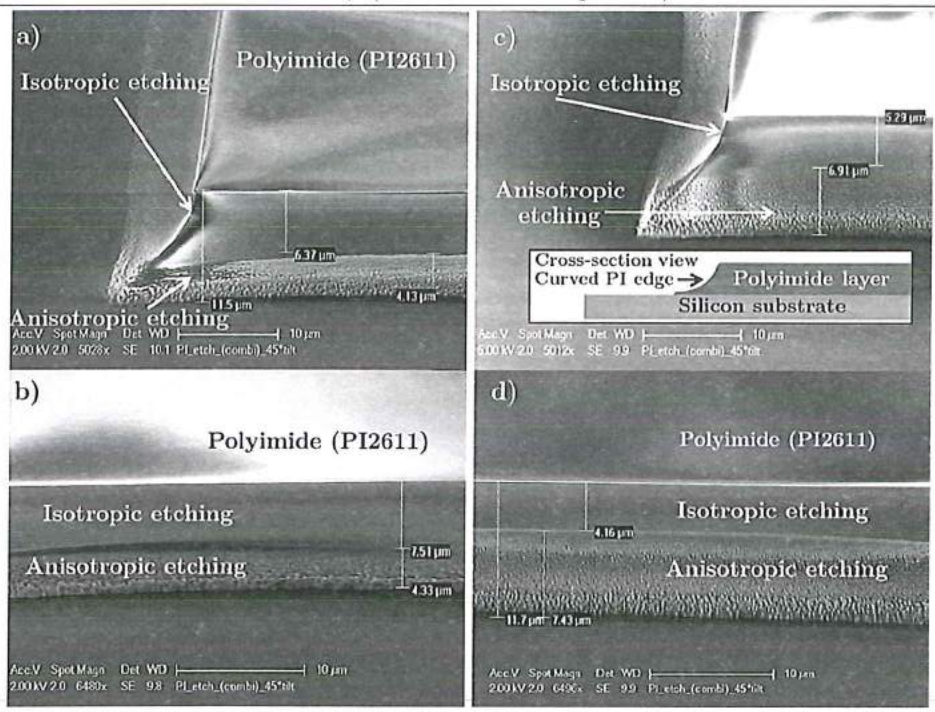

Figure 6.15 SEM images using combined etching in Trikon Ωmega 201 etcher with longer (a and b) and less (c and d) etch time in the "resist podule module".

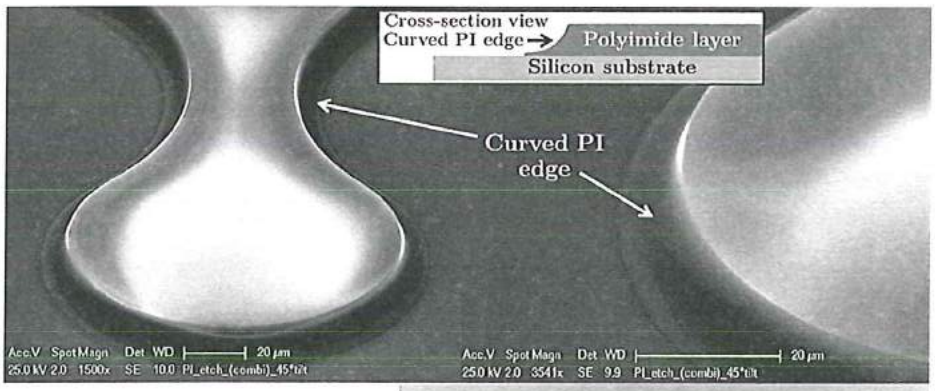

SEM images showing no traces of "grass" / residue islands after the combined etching of PI-2611 in the PI etch podule and the ICP etching chamber of the Trikon Ωmega 201 ICP etching tool.

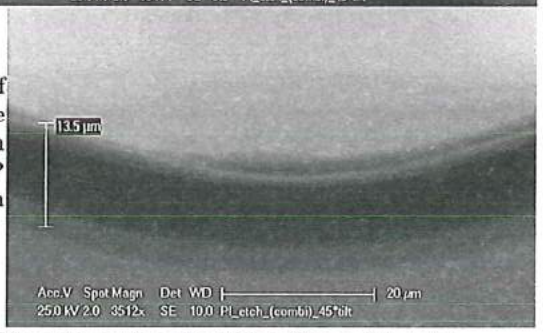

Figure 6.16 SEM images of combined dry etching using Trikon Ωmega 201 etcher.

At a molecular level four binding classes can exist between two molecules to be bonded which can be metallic, ionic, covalent and van der Waals bonds [45]. In the list the chemical ionic and covalent bonds exhibit the strongest connection in comparison to the weakest links created by the more generalized van der Waals or physical bonding. On the other hand, all these bonding mechanisms generally are confined within the bulk of the material which at the end defines the cohesiveness, binding force or the in-built energy of the particular material. When looked at an macro and microscopic level of two material the connection between their surfaces involves not only a combination of physical and chemical bonds but also a micro-mechanical engagement provided that both the material surfaces are never perfectly planar. In line with the micro-mechanical engagement interdiffusion of joining materials can also be considered an important addition to the overall binding process.

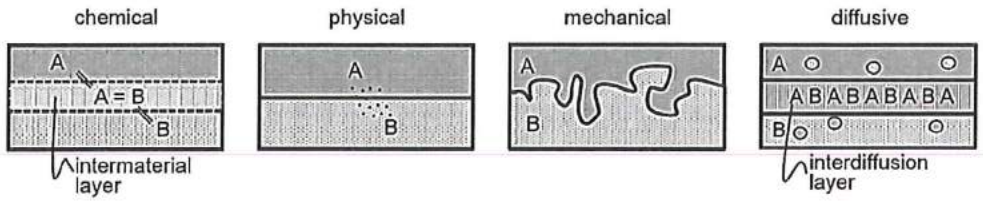

Figure 6.17 Adhesion mechanisms between two binding surfaces (A and B) [45].

Figure 6.17 illustrates the fundamental or ideal adhesion schemes mentioned here [45]. For an reliable and an working flexible MEA especially in an biological environment the adhesion of the polyimide to the base substrate (PECVD SiO_2) (Figure 6.7c) and the adhesion of the metal-polymer interface (Figure 6.7d) which comes after PI deposition and curing step is important. The harsh biological environment which is aqueous and contains salts, ions and proteins are the major responsible items causing the failure of the devices. Polymers up to some extent are already shown to be permeable to gases, including water vapour [25], which makes it difficult to avoid any type of water molecule incursion into the polymer-metal or polymer-substrate interface. Moreover, apart from the diffusion process, all the PI's absorb water to a percentage leading to material damage by plasticizing effect in the PI which is directly related to the expansion of the polymer chains [26]. Due to this effect it makes easy for the other items such as salts, ions and proteins to further diffuse in the PI thus altering the inherit properties of the PI. This water absorption process has two effects; first it encourages stretching or enlarging of the PI, which is already been proven for in-plane thin PI layers [26] where significant stresses are developed in the adjacent layers. Secondly the physical bonding forces between two layers (metal-PI interface) is also weakened which are decreased by a factor of six in

proportion to the distance [46,47]. This water influence is sufficient enough to disrupt the physical binding between the two surfaces by its in between presence or by incorporating polarity changes in the PI. Also the plasticization effect due to water and ionic absorption adds to the failure of mechanical adhesion. If there are no covalent bonds present between the two surfaces the mechanical weakening causes to lose the mechanical adhesion favouring any force (e.g. due to residual stress) to delaminate the assembly.

Over the years many researchers have studied various approaches to improve PI adhesion, most of them targeted towards PI chemistry. The use of inorganic interlayer dielectric materials (PECVD SiO_2 or Si_3N_4) between PI and Silicon substrates is mostly used during fabrication to improve the adhesion as well as the micro-hardness. SiO_2 (Silicon oxide) and Si_3N_4 prepared by PECVD techniques exhibit interesting properties such as low refractive index, low gas permeability and an easy-to-integrate deposition process [48]. These silica induced materials have been used not only for the IC industry as dielectric layers, diffusion barriers and hard masks [49,50] but also used in food and medical packaging industry [51]. H. Li *et al.* [48] deposited the adherent thin film PECVD SiO_2 and Si_3N_4 on PI, Kapton HN by using three types of gas mixtures; of tetraethyl orthosilicate (TEOS) and O_2, of SiH_4 (silane) and N_2O, and SiH_4, NH_3 and N_2. In the research it was proven that the silica and nitride films underwent chemical interactions with the underneath PI films via the formation of C–N–Si bonds thus improving the chemical binding and enhancing the dynamic surface micro-hardness of the PI film which was dependent on the thickness of silica and nitride film deposited [48]. In our fabrication process for the "Flexi-Stiff" MEA PECVD SiO_2 of 1µm at 300^{o} C was considered over PECVD Si_3N_4 due to the porous microstructure of PECVD SiO_2 which enhances adhesion. Although having low deposition temperatures excellent moisture barrier properties Si_3N_4 has a high dielectric constant which cannot be used as a gapfill material, and does not planarize the underlying topography [52], thus not fulfilling as an ideal candidate for our process. Another important property of the PECVD SiO_2 is the well matched coefficient of thermal expansion (CTE) of 3.9 ppm/^{o} C not only to silicon (CTE of 2.3 ppm/ ^{o}C) [53] but also to the upcoming PI-2611 (CTE of 5 ppm/ ^{o}C) [38].

The adhesion properties of PI films are extremely dependent on the surface chemistry of the substrate and the PI, substrate cleanliness and roughness, deposition conditions and curing process of PI. Apart from using an appropriate intermediate layer (PECVD SiO_2) layer between the silicon substrate an organosilane-type adhesion promoter (VM-651 from HD Microsystems) was applied between the PI (PI-2611) and the amorphous porous SiO_2 surface in order to further

improve the adhesion and stability in the harsh saline environment during characterisation tests. This adhesion primer is supplied in concentrated state which needs to be diluted with deionized (DI) water. Less adhesion effects are observed when the VM-651 concentration varies between 0.01% to 0.1% with the expiry of diluted solution of not more than 24 hours. The preparation of the mixed VM-651 can be done either with a 0.1% solution of VM-651 in DI water or with a mixture of 95% methanol, 5% DI water and one to two drops of concentrated VM-651. The addition of methanol here accelerates the drying process. In the DIMES process the first approach was used in which initially the cleaned and dried rough SiO_2 surface was flooded with the prepared mixture and kept for 20 seconds before starting the coating program specially build for this process. After spinning (spin speed 10 sec @ 500rpm + 45 sec @ 3500rpm) the wafer is placed on the covered hot plate at 115 ^{o}C for 2 minutes before proceeding for PI deposition. Primer application experimental experience indicated that only a thin monomolecular layer is sufficient to promote adhesion since too much primer (adhesion promoter) molecules staying on the surface of the substrate prevents air to escape during the baking process. On a molecular level the component 3-Aminopropyl triethoxysilane (APTES) inside the VM-651 primer when diluted with DI water which acts as an catalyst to create a monolayer of APTES creating a strong chemical bonding with the SiO_2 layer. Chemical bonded interface contains a high packed density of amino groups (67-92 NH_2 groups/mm^2) between PECVD SiO_2 and APTES creating a highly cross-linked APTES film. The stability of amino groups on PECVD SiO_2 is much higher in comparison to other hydroxyl-bearing materials thus PECVD SiO_2 films find application as biomaterial coatings and as an intermediate adhesion layers in salinization processes [54].

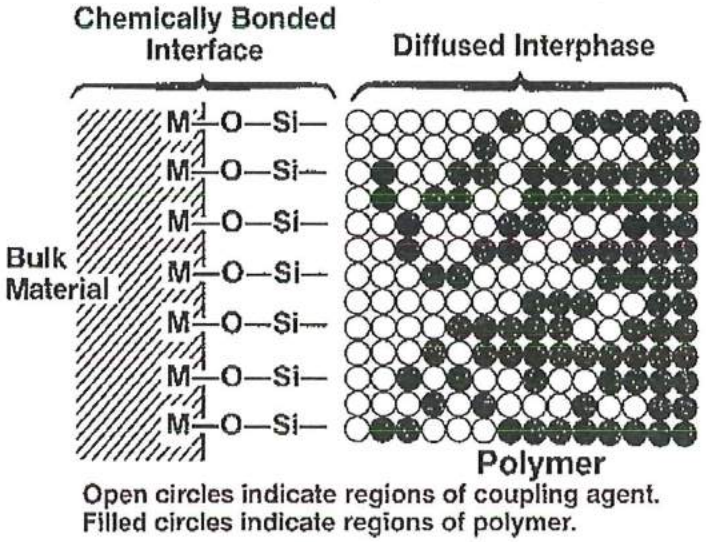

Figure 6.18 Interdiffusion model of silane-primed material and PI bonding system [55].

The adhesion mechanism of the primer to polymer can be considered in three ways; in the first type of adhesion where the primer is adequately cross-linked to adhere to the PI to from an interface where little or no interdiffusion of two phases take place, thus resulting in a reduced bond strength which completely depends on the surface free energy of the applied primer monolayer. In the second type the primer and PI undergo interdiffusion (Figure 6.18) into each other resulting in increased effective contact area between two phases and thus having an greatly improved adhesion strength. This adhesion system depends on solubility parameters of the two phases which is maximum when they are equal to each other [55]. In our process the interdiffusion of organosilane-type VM-651 with the cross linkable polymer (PI-2611) is the probable bonding mechanism. Bond strength strongly improves if the two phases undergo interdiffusion and crosslinking which is comparable to or exceeds the cohesive strength of the PI. Bonding in this way through formation of interpenetrating PI network forms the third type of adhesion mechanism [55].

6.4.3 Metal sputter deposition and patterning

As per our process flow chart, described in section 6.3.1, where after PI deposition and patterning process the combined metal stack of Ti: 40 nm, TiN: 200 nm and pure Al: 3 µm was deposited by using the Sigma 204 (Trikon) DC-Magnetron sputtering machine fitted with a high vacuum assembly fitted with a diffusion pump system yielding a base pressure of about 1.332×10^{-5} Pa. Prior to this step the wafers containing PI had undergone a short Oxygen plasma etch in the barrel-type etching tool (TEPLA IPC 9200). The use of oxygen plasma, previous to metal deposition is one of the successful approach to roughen the surface in order to achieve a good mechanical interlocking of the thin-film metallic layers [56–58]. The exposure of the PI surface to oxygen plasma to have an etch like surface helps to remove the exposed and the developed photoresist residuals. At atomic levels the remains of these residues contaminate the surface thus hindering the adhesion process. The use of short oxygen plasma before sputtering has also shown an increase in oxygen concentration on the surface, which alters the amount of carbonyl groups and produces active binding locations for the upcoming metallic layers [59,60]. The whole metal stack was sputtered on PI pattered wafers in one go without breaking the vacuum to maintain the continuity of the process. A circular, 332 mm sputtering target of high-purity Ti (99.99%) was used. The sputtering system was evacuated to 7×10^{-9} Torr by using a Cryogenic pump. The working base pressure was fixed at 1×10^{-7} Torr and it was controlled mainly by using a high-purity Argon (Ar: 99.99%) gas with a uniform flow rate of 100 sccm. In the first chamber with Ti sputter target Ti was deposited at 300 ^{o}C with an r.f. power of 5 KW after cleaning (2 mins) and

pre-sputtering (3 mins) the target to achieve a thickness of 40 nm on the activated PI surface.

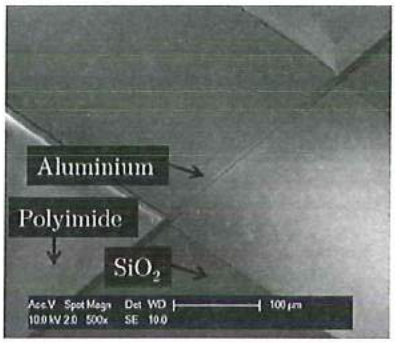

Uniform step coverage of sputtered Al on Polyimide layer

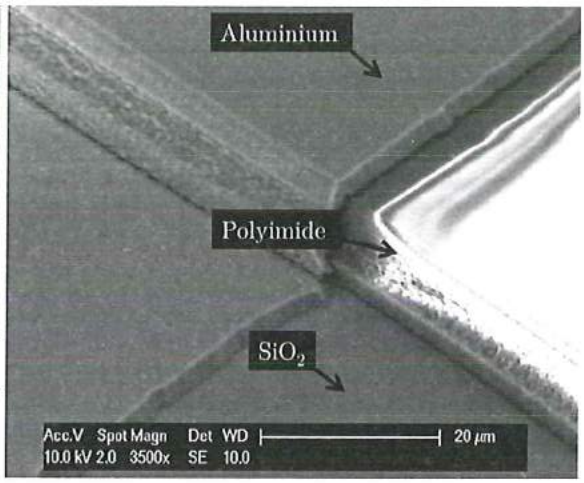

Figure 6.19 SEM image showing only pure Al step coverage over PI surface.

The cleaning and pre-sputtering of the Ti target was done by Ar plasma without the wafer presence in the chamber. Immediately after Ti deposition, without breaking the vacuum or the removal of the wafer form the chamber, TiN was deposited in the same chamber at 300 ^{o}C with an r.f. power of 5KW in the presence of gas mixture including 70 sccm of pure nitrogen (N_2) gas and 20 sccm of Ar to achieve a thickness of 200 nm. After the Ti and TiN deposition, without breaking the vacuum, the wafers were transported to another chamber where pure Aluminium (Al) was sputtered using similar sputtering conditions of Ti except the sputtering time in order to achieve a thickness of thickness of 3 µm. A simple example showing the uniform step coverage where only pure Al sputtered over a PI on silicon oxide layer can be seen from the SEM images as shown in Figure 6.19.

6.4.3.1 Photoresist patterning issues

The realisation of the metal tracks and the stimulation sites on the flexible substrates requires the patterning of the conducting lines (the metal stack) onto flexible substrates (PI-2611). Gold (Au) and Platinum (Pt) are the materials of choice for tracks and the contacts in neural interfaces. In comparison to Pt and Au other transition metals like titanium (Ti), chromium (Cr), nickel (Ni) and tungsten (W) lack the capability of forming carbides [61]. This is the reason why the thin-film devices reported use WTi, Ti and Cr metallization's as adhesion promoting and starting metal layers for Au and Pt metallization's. Theses metal transition interlayers layers create a chemical bonding through carbide formations at the PI

metal interface and an crystallised intermetallic transition to the upcoming metal of interest. In addition to the use of such interlayer metals to improve the adhesion bonding process in our process flow chart a short oxygen plasma etch as explained in the earlier paragraph was done. This promoted to the adhesion properties yielding to a stronger chemical bond between the PI and the upcoming sputtered metal stack. Such type of plasma treatment is proven step from researchers where such process on PI is the means of modifying the PI surfaces in order to improve the adhesion process while maintaining the desirable bulk properties [60,62]. The metal stack deposition as explained in the earlier section 6.3.1 was performed out of which the upper most Al layer (3 µm) was patterned by wet etching process by PES etchant (as explained earlier in section 6.2.1) to form the bond pads for electrical connections (Figure 6.20 (1)). As per the flow chart the next step is to safeguard the TiN layer from the further plasma involving processing steps. In reference to this a 200 nm thin pure Al layer was sputtered by PVD techniques at 50 ^{o}C (Figure 6.20 (2)). This hard mask protective layer needs to be patterned in order to define the stimulation sites and the subsequent metal tracks connecting to the bond pads. In order to do so initially, positive resist (AZ® ECI 3027) of 6 µm thick with a special recipe developed at DIMES for coating higher aspect ratios was used. But unfortunately this resist did not gave proper results due to its inability to develop at curved slopes of PI thus forming a mask which did not allow to etch the underneath Al during the dry patterning step.

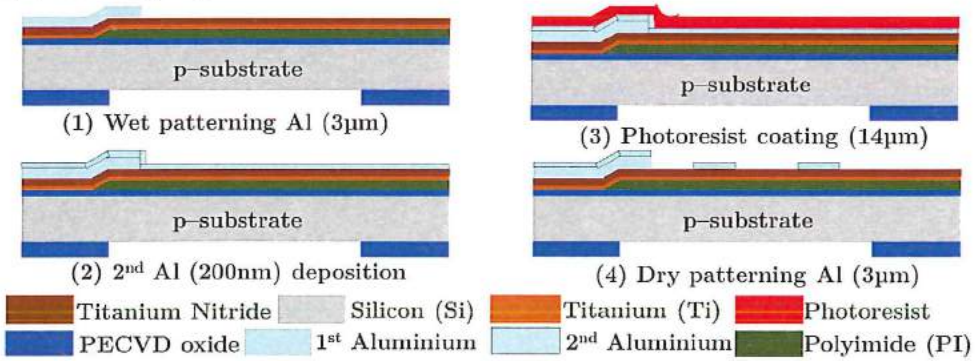

Figure 6.20 Part of the flow chart where photoresist patterning issues exist.

As seen from Figure 6.21 the Al remains after dry patterning caused the short circuiting between the two metal tracks. Use of a negative resist (AZ® *n*LOF™ 2000) of 12 µm thick which was spray coated on the substrates with a special recipe developed within DIMES gave a residue free development process thus resulting in a clear definition of the metal tracks. The details of the coating process is mentioned later in the appendix.

6.4.4 ICP, its associated issues and solutions

Inductively coupled plasma (ICP) etching is a dry etch technique which uses a chemically reactive plasma to etch away the material that has to be removed from the substrates. This reactive plasma is generated by the ionization of a gas (or gas mixture) in an electrical field at a low pressure (vacuum), and contains amongst others charged ions and neutral radicals.

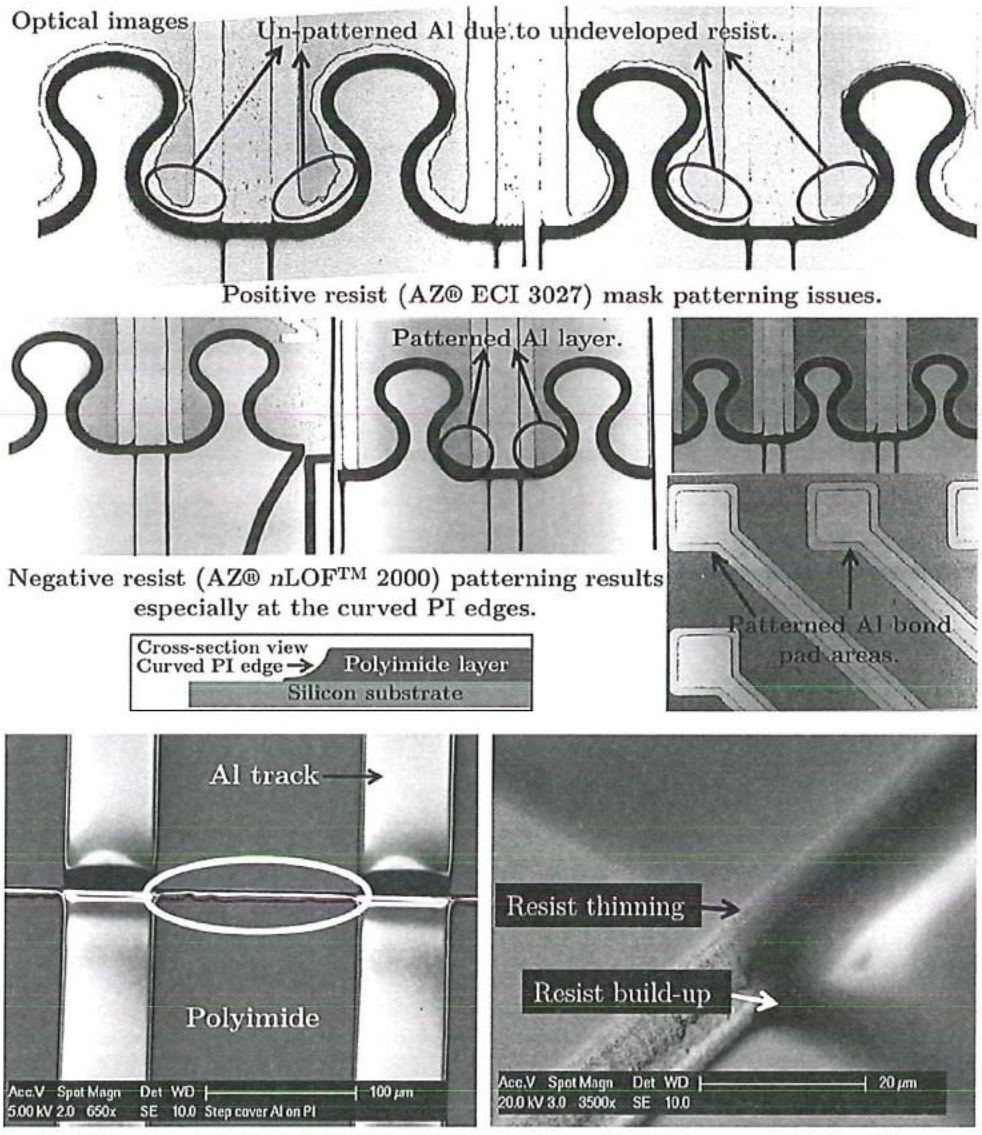

Figure 6.21 Optical and SEM images showing photoresist patterning issues.

The electrical field is created with an RF generator connected to a coil around the ceramic reactor chamber. A second RF generator connected to the top and bottom electrode is used to attract and accelerate positively charged ions towards this bottom electrode as it becomes negatively charged. The wafer to be etched is clamped on the bottom electrode by electrostatic force, which is applied with the help of embedded ESC (Electrostatic Clamping) electrodes (Figure 6.22). Electrostatic clamping is advantageous over the cheaper mechanical clamping, as there is no shielding of the edge of the wafer by a clamp ring and the clamp force is more evenly spread over the wafer than just on that edge. This type of clamping is beneficial and preferable for critical processes where thin fragile wafers are used in the process. During the etching process the substrate is cooled and kept at a constant temperature by circulating a cooling liquid through the bottom electrode with a chiller. Helium (He) is applied between the electrode and the backside of the wafer to ensure a good thermal contact, hence the name He backside cooling (Figure 6.22).

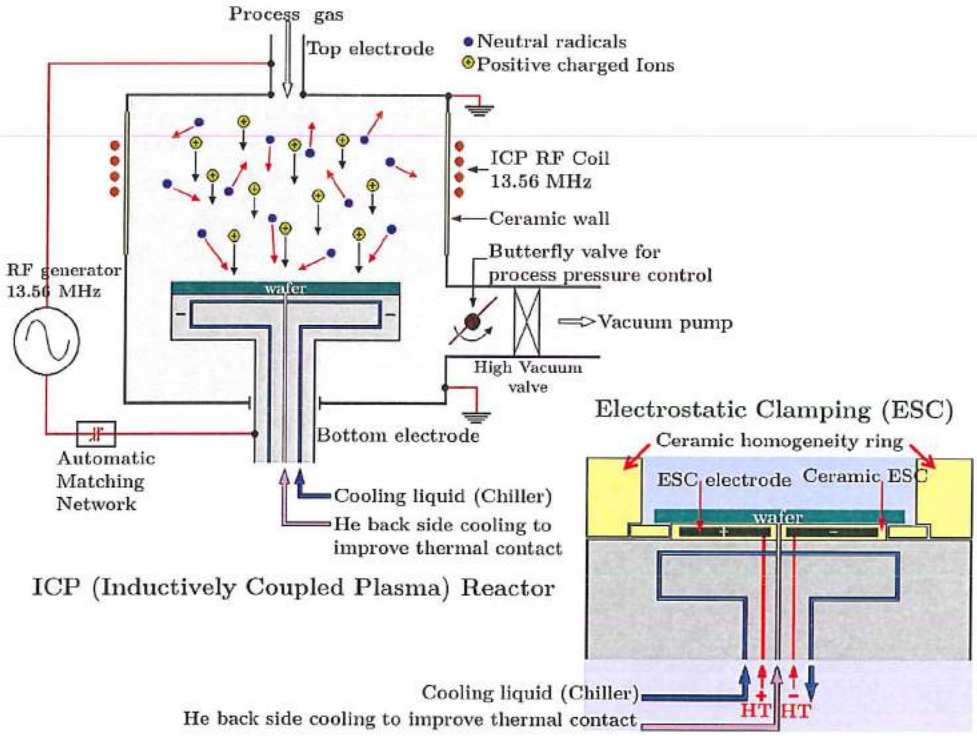

Figure 6.22 RIE reactor and Electrostatic Clamping of the wafer.

The accelerated positively charged ions in the plasma have a physical bombardment action on the wafer surface, resulting in damage to molecule bonds or

even sputtering molecules away. The neutral radicals (unstable and very reactive particles with unpaired electrons) cause a chemical reaction to the damaged surface. The volatile reaction products which are formed during the etching process are continuously pumped away by a vacuum pump which together with a butterfly valve controls the process pressure. If the reaction products formed in the process are not volatile, then there is a risk of these products to build up on the wafer surface and act as a protective layer, which may cause undesired effects (micro masking) or even stop the etch process. The RIE process is influenced by process parameters such as gas chemistry and ratio, process pressure, RF power and electrode temperature, as well as external conditions like the type of resist being used, extra treatments (e.g. bake steps) before etching etc. The available reactive gasses in the ICP chamber of the Trikon Ωmega 201 in DIMES are Chlorine (Cl_2), Hydrogen Bromide (HBr), Sulphur hexafluoride (SF_6), carbon tetrafluoride (CF_4) and Oxygen (O_2).

6.4.4.1 Issues during and after Al etching

For ICP etching of Al metal layer (200 nm) Cl_2 and HBr were the main reactive gases used, along with a negative resist (AZ® *n*LOF™ 2000) as a masking layer. The etch process was at 25 °C substrate temperature with an RF power of 50 Watts. During Al etching three type of issues did occur, causing damage to the layer.

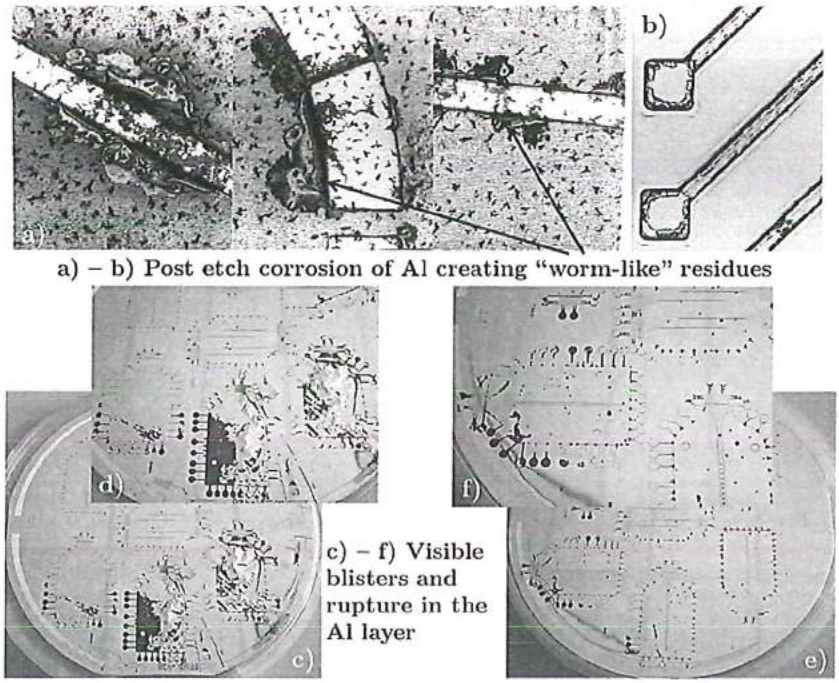

Figure 6.23 Microscopic images after RIE; a) & b) Visible "Worm-like" residues occurring at the Al metal tracks; c) – f) Visible cracks and ruptured blisters with corrosion around the periphery of the blister.

Below are those issues mentioned with the steps undertaken to solve them.

(a) Damage caused during etching due to machine malfunction.

The Al etching was carried out in an industrial plasma etcher (Trikon Omega 201). Although this machine is very reliable, an error can always occur due to machine malfunction. When this happens during the etch process, the machine will stop etching by switching off the RF power, which stops the plasma formation. Unfortunately the gasses keep flowing when that happens, which will cause isotropic etching and thus damages the Al layer. This is caused by the Chlorine gas. When the process has already removed the native Al_2O_3 layer, the Chlorine gas is able to etch the bare Al layer which is now directly exposed to it. Chlorine is capable of causing an exothermic reaction with Al which is very uncontrolled, even without a plasma being present. This results in undercutting of the masking layer which is not desired.

(b) Post-etch corrosion due to a reaction of adsorbed Chlorine products with moisture from the air.

During the plasma etch process, Chlorine products (Cl_2, $AlCl_3$) will be adsorbed on the sidewall of the photoresist masking layer. The type of photoresist that is being used influences the amount of adsorbed reaction products. When the process has finished and the wafer is removed from the vacuum into the atmosphere, these Chlorine products will attract moisture from the air and react to form Hydrochloric acid. This acid will etch the Al layer and thus damages the layer. Following are the reactions that occur in this corrosion process :

$$Cl_2 + H_2O \rightleftharpoons HOCl + HCl \quad [63]$$

$$Cl_2(g) + H_2O(l) \rightleftharpoons OCl^-(aq) + 2H^+(aq) + Cl^-(ag) \quad [64]$$

Chlorine (Cl_2) reacts with water to produce hypochlorite, OCl^-. The position of the equilibrium depends very much upon the pH of the solution. Both the above equations are same in which HCl and HOCl (hypochlorous acid) attacks the Al, as they both are acids, but HCl is stronger than HOCl.

There are three ways to prevent this corrosion form happening:

(i) The simplest, oldest and cheapest way is to submerge the wafers immediately into a container with water after breaking the vacuum, which will create the Hydrochloric acid but also dilutes it.

(ii) Another method is to replace the Chlorine products with Fluorine products by exposing the wafers to a fluorine plasma (e.g. SF_6) directly after the etching of the Al layer. It is important not to break the vacuum.

(iii) The in the industry now mostly used method is to remove the photoresist layer directly after Al etching (without breaking the vacuum), which also

removes the Chlorine products. This is done in the podule. This is the most expensive method, but it has the advantage that it saves a separate resist removal process step. This will improve wafer throughput.

(c) Post-etch pitting corrosion.

The Al etch recipe which was used in our process resulted in Al pitting type of corrosion which is caused mainly due to the Chloride ion interactions with the oxide covered Al. This overall corroding process creates a "worm" like residues which is easily spotted under an optical microscope as seen in Figure 6.23 a)-b). To explain this phenomenon P.M. Natishan *et al.*. [65] in his review paper focused on the interaction of Cl^- with the passive oxide film on pure aluminium by reviewing and summarizing the available experimental data concerning Cl^- interactions. The goal was to answer the question; what is the nature of the interaction of aggressive anions such as Cl^- with the passive film, adsorption and/or absorption leading to pitting? [65]. From all the review papers reviewed by P.M. Natishan it has been established that in environments that contain aggressive anions such as chloride, Cl^- is adsorbed and is incorporated in the oxide film of the metal layer. This causes the passive film to become unstable and degrades locally causing the film breakdown and pit nucleation with corrosion at the end. However the resolution of these techniques and modelling abilities were only to establish that Cl^- was observed in different chemical environments, being most often referred to as surface/near surface Cl^- and bulk Cl^- [65]. In order to simulate the Cl^- attack and breakdown of the passive oxide film, William E. O'Grady *et al.*. [66] generated molecular simulations where chloride was substituted for oxygen in either OH^- or an O^{2-} position. There are four basic positions of oxygen in the oxide surface that could be potentially attacked by a chloride ion. Two kinds of OH^- surface sites; OH^- recessed and OH^- elevated and the two O^{2-} positions; the normal bridging position and the terminal position at the end of an octahedron as seen in Figure 6.24 (a). Simulations and theoretical calculations showed that the OH^- recessed site is the most likely point of the initial attack by the Cl^- ions as seen from Figure 6.24 (b). Other two models; the one as seen in Figure 6.24 (c) illustrated two chlorides substituted in the diaspora molecule for one elevated OH^- site and the other one as seen in Figure 6.24 (d) depicted a chloride ion in the site of an aluminium atom in the (111) surface plane [66]. Normally pure Al is etched away easily in a Chlorine (Cl_2)plasma by itself but the native oxide layer which covers the whole aluminium layer. In this scenario the pure chloride (Cl^-) does not etch this native oxide so HBr is added to increase the sputtering amount and to scavenge the oxygen in the aluminium oxide (Al_2O_3). In our fabrication process negative photoresist (AZ® *n*LOF™ 2000; 12 µm) which is used to pattern the Al layer showed similar effect where the Cl^- ions from the

reactive gas mixture of Cl^- and HBr is not only been adsorbed by the remaining resist but also replaces the OH^- position of the passive oxide film. Post-etch corrosion is one of the main concern in this process which can be either purely chemical (observed in our process flow chart) or galvanic. This chemical corrosion is in association with residual chlorides present on the wafer, especially on the sidewalls. Even though the temperature at the wafer surface goes to 50 – 80 ^oC to allow the volatilization process of the etched by-products, some $AlCl_3$ is embedded as sidewall deposits (Figure 6.25), leading to chemical reactions with the moisture in the air [67,68].

$$AlCl_3 + 3H_2O \rightarrow Al(OH)_3 + 3HCl,$$

$$Al(OH)_3 + 3HCl + 3H_2O \rightarrow AlCl_3 \cdot 6H_2O,$$

$$2AlCl_3 \cdot 6H_2O \rightarrow Al_2O_3 + 9H2O + 6HCl$$

Al during the process is also be consumed by the aqueous HCl:

$$2Al + 6HCl \rightarrow 2AlCl_3 + 3H_2$$

As explained earlier the corrosion process continues to corrode the Al, creating "worm" like residues.

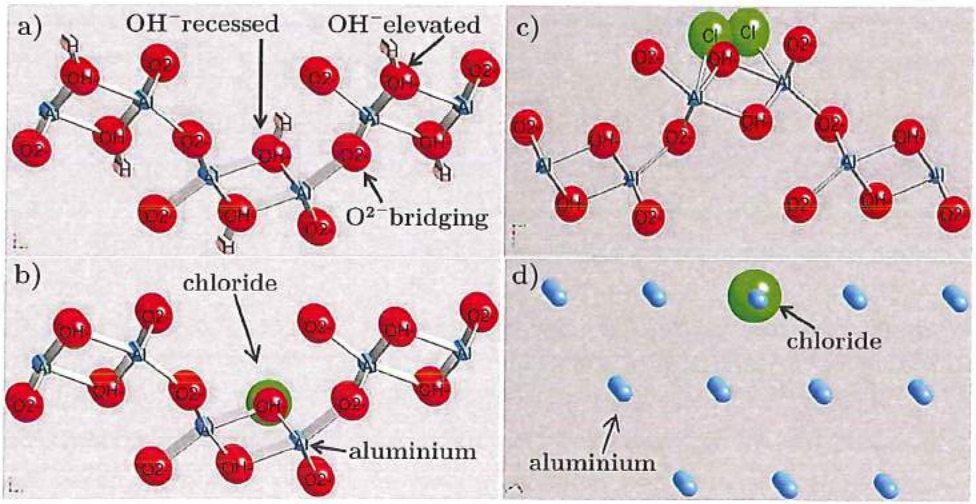

Figure 6.24 Molecular simulations showing Cl^- interacting with different sites in Al oxide models to understand the breakdown mechanism of passive films [66].

In addition to purely chemical corrosion explained above a small amount of galvanic corrosion is also responsible to Al rupture since a galvanic cell is formed between two dissimilar metals (aluminium and titanium nitride in our case) in

presence of the electrolyte which is nothing but the residual chlorides dissolved in water when they come in contact with the moisture present in the atmosphere. This galvanic corrosion is different than the pure chemical one which is characterized by voids leading to film rupture as shown in Figure 6.23 c)–f). In this situation the underneath TiN layer remains intact which normally is oxidized to prevent the galvanic cell reaction but might be different due to irregularities in the TiN during the sputtering process causing this galvanic corrosion at certain sites. This also can be prevented by reducing the sidewall deposits, a QDR (quick-dump-rinse) in Demi water or spin rinse, and a post-etch rinse in adequate Demi water. Common steps adapted to avoid the pure type of chemical corrosion are:

- Substrate wafer heating to its maximum operating temperature that will not reticulate the photoresist and then use a passivation step in combination with a partial or complete stripping of the photoresist. This passivation or stripping step is normally done in a separate strip resist chamber (similar to resist strip podule explained earlier) where oxygen plasma as a major component with a small amount of fluorine is used in order to replace the chlorides with the fluorides. This resist strip is a common process carried out *in-situ* using an O_2 plasma with fluorine gas [69]. The intention of this step is to convert the residual chlorides to volatile HCl and is achieved by hydrogen-containing plasmas, typically water vapour [70].
- Another approach is to heat the wafer after the passivation step on a hot stage in the etching tool itself in vacuum until the whole batch is etched and then rinse with water immediately after venting it to dissolve the residues that are left as water will dilute the HCl formed as per the above mentioned reactions thus stopping the corrosion further. This can be later followed by another resist removal step along with chemical sidewall removal to ensure complete resit removal.

In our situation where the landing material is polyimide does not permit us to use the first option mentioned above and the second option of heating the wafer was not possible due to machine limitations. Also to avoid the galvanic type of corrosion the solution for QDR was tried for one batch which was effective but not feasible due to practical restrictions as some time was lost in transferring the whole batch of wafers which resulted in initiating the corrosion process. Keeping all the machine limitations and the probable solutions in mind part of the first option mentioned above of replacing the corrosive chlorides with the noncorrosive fluorides was considered. In reference to this CF_4 gas was introduced for two minutes immediately after the timely etched process of the Al layer was stopped. This timely etched process was

worked out in accordance with the end point detection technique used in the etching recipe of the RIE etching machine. This passivation step which includes the introduction of CF_4 enabled us to replace the corrosive chlorides with the non-corrosive fluorides thus solving the post etch corrosion problem along with safeguarding the landing layer (polyimide: PI2611 in our case) without exposing it to any oxygen plasma environment which would result in PI etching which is not desirable.

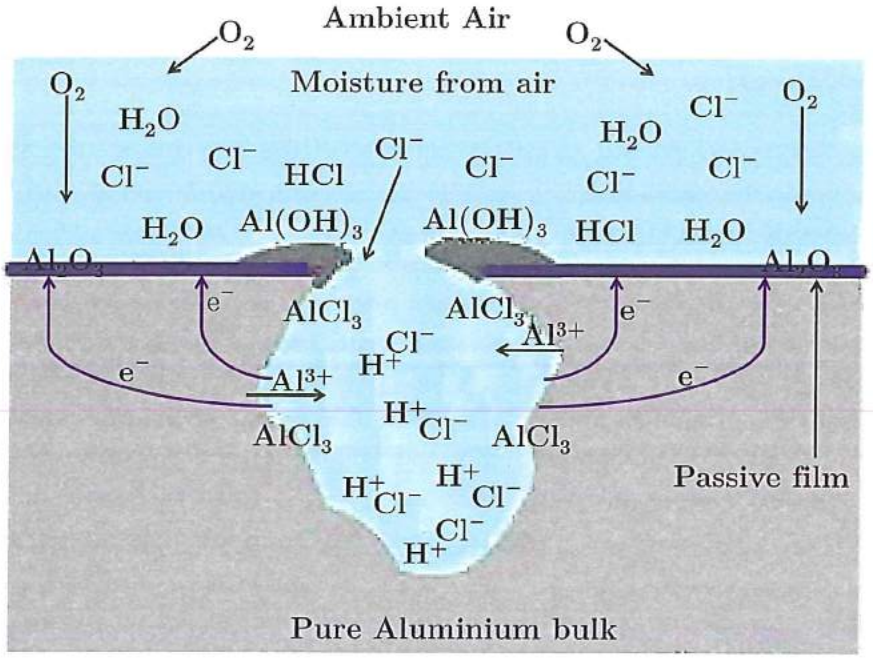

Figure 6.25 Schematics showing the pitting corrosion mechanism.

6.5 Conclusions

The novel microfabrication process developed at DIMES successfully demonstrated the possible application of the IC microfabrication technology towards the development of a "Flexi-Stiff" MEA. The problems encountered in developing the 1st generation completely flexible MEA and the stiff electrode explained in earlier chapter formed an motivational base towards making the 2nd generation "Flex-Stiff" MEA. Also in the 2nd generation devices which faced photolithographic issues with positive resist due to high aspect ratios was solved accordingly by using a custom coating recipe for the negative photoresist. The polyimide patterning process using Al metal as a hard mask was altered by using a two-step RIE process which is a combination of isotropic and anisotropic dry etching process developed in the lab to get the desired polyimide (PI2611) curved surface profile. This curved profile was

necessary in order to achieve the uniform metal step coverage for the oncoming metal stack while retaining the high density of the metal tracks. The PI etching process presented in this chapter exhibits a new method of PI etching which is done in two steps by using only one machine (Trikon Ωmega 201 ICP etcher) without the hassle of using two different machines working on different principles which is normally preferred in PI etching. For the metal patterning the post etch corrosion which caused the hurdle after the metal etching enabled to have additional step after etching process which included the passivation step to replace the corrosive chlorides with the non-corrosive fluorides.

The complete novel microfabrication process presented in this chapter significantly enables the fabrication process to fabricate the "Flexi-Stiff" polyimide based MEA where high-density metal tracks embedded in polyimide coatings are required for the concerned application.

6.6 References

1. Ward, M. P.; Rajdev, P.; Ellison, C.; Irazoqui, P. P. Toward a comparison of microelectrodes for acute and chronic recordings. *Brain Res.* **2009**, *1282*, 183–200.

2. Sonn, M.; Feist, W. M. A prototype flexible microelectrode array for implant-prosthesis applications. *Med. Biol. Eng.* **1974**, *12*, 778–791.

3. Clark, G. M.; Tong, Y. C.; Black, R.; Forster, I. C.; Patrick, J. F.; Dewhurst, D. J. A multiple electrode cochlear implant. *J. Laryngol. Otol.* **2007**, *91*, 935–945.

4. Shamma-Donoghue, S. a.; May, G. A.; Cotter, N. E.; White, R. L.; Simmons, F. B. Thin-film multielectrode arrays for a cochlear prosthesis. *IEEE Trans. Electron Devices* **1982**, *29*, 136–144.

5. Bell, T. E.; Wise, K. D.; Anderson, D. J. A flexible micromachined electrode array for a cochlear prosthesis. *Proc. Int. Solid State Sensors Actuators Conf. (Transducers '97)* **1997**, *2*, 1315–1318.

6. Bhatti, P. T.; Wise, K. D. A 32-Site 4-Channel High-Density Electrode Array for a Cochlear Prosthesis. *IEEE J. Solid-State Circuits* **2006**, *41*, 2965–2973.

7. Wang, J.; Gulari, M.; Wise, K. D. An integrated position-sensing system for a MEMS-based cochlear implant. In *IEEE InternationalElectron Devices Meeting, 2005. IEDM Technical Digest.*; IEEE, 2005; Vol. 00, pp. 121–124.

8. Wise, K. D.; Bhatti, P. T.; Wang, J.; Friedrich, C. R. High-density cochlear implants with position sensing and control. *Hear. Res.* **2008**, *242*, 22–30.

9. Wang, J.; Wise, K. D. A Hybrid Electrode Array With Built-In Position Sensors for an Implantable MEMS-Based Cochlear Prosthesis. *J. Microelectromechanical Syst.* **2008**, *17*, 1187–1194.

10. Johnson, A. C.; Wise, K. D. An Active Thin-Film Cochlear Electrode Array With Monolithic Backing and Curl. *J. Microelectromechanical Syst.* **2014**, *23*, 428–437.

11. Arcand, B.; Shyamsunder, S.; Friedrich, C. A Fluid Actuator for Thin-Film Electrodes. *J. Med. Device.* **2007**, *1*, 70.

12. Fujifilm Technical Product Information (Durimide ® 100)
http://www.fujifilmusa.com/shared/bin/Durimide 100_US12.pdf.

13. Mimoun, B.; Henneken, V.; van der Horst, A.; Dekker, R. Flex-to-Rigid (F2R): A Generic Platform for the Fabrication and Assembly of Flexible Sensors for Minimally Invasive Instruments. *IEEE Sens. J.* **2013**, *13*, 3873–3882.

14. Mimoun, B.; Pham, H. T. M.; Henneken, V.; Dekker, R. Residue-free plasma etching of polyimide coatings for small pitch vias with improved step coverage. *J. Vac. Sci. Technol. B Microelectron. Nanom. Struct.* **2013**, *31*, 021201.

15. Stieglitz, T. Considerations on Surface and Structural Biocompatibility as Prerequisite for Long-Term Stability of Neural Prostheses. *J. Nanosci. Nanotechnol.* **2004**, *4*, 496–503.

16. Herwik, S.; Paul, O.; Ruther, P. Ultrathin Silicon Chips of Arbitrary Shape by Etching Before Grinding. *J. Microelectromechanical Syst.* **2011**, *20*, 791–793.

17. Franssila, S. *Introduction to Microfabrication*; John Wiley & Sons, Ltd: Chichester, UK, 2010.

18. Polcawich, R. G.; Pulskamp, J. S. *MEMS Materials and Processes Handbook*; 2011.

19. Ghosh, M. *Polyimides: Fundamentals and Applications*; 1996.

20. Ohya, H.; Kudryavsev, V. V; Semenova, S. I. *Polyimide Membranes: Applications, Fabrications and Properties*; 1997.

21. Sacher, E.; Susko, J. R. Water permeation of polymer films. I. Polyimide. *J. Appl. Polym. Sci.* **1979**, *23*, 2355–2364.

22. Sacher, E.; Susko, J. R. Water permeation of polymer films. III. High-temperature polyimides. *J. Appl. Polym. Sci.* **1981**, *26*, 679–686.

23. Rubehn, B.; Stieglitz, T. In vitro evaluation of the long-term stability of polyimide as a material for neural implants. *Biomaterials* **2010**, *31*, 3449–58.

24. Buchhold, R. A Study on the Microphysical Mechanisms of Adsorption in Polyimide Layers for Microelectronic Applications. *J. Electrochem. Soc.* **1998**, *145*, 4012.

25. Massey, L. K. *Permeability Properties of Plastics and Elastomers - A Guide to Packaging and Barrier Materials (2nd Edition)*; William Andrew Publishing/Plastics Design Library, 2003.

26. Buchhold, R.; Nakladal, A.; Gerlach, G.; Sahre, K.; Eichhorn, K.-J. Mechanical stress in micromachined components caused by humidity-induced in-plane expansion of thin polymer films. *Thin Solid Films* **1998**, *312*, 232–239.

27. Deiasi, R. Thermal regeneration of the tensile properties of hydrolytically degraded polyimide film. *J. Appl. Polym. Sci.* **1972**, *16*, 2909–2919.

28. Campbell, F. J. Temperature Dependence of Hydrolysis of Polyimide Wire Insulation. *IEEE Trans. Electr. Insul.* **1985**, *EI-20*, 111–116.

29. Hetke, J. F.; Lund, J. L.; Najafi, K.; Wise, K. D.; Anderson, D. J. Silicon ribbon cables for chronically implantable microelectrode arrays. *IEEE Trans. Biomed. Eng.* **1994**, *41*, 314–21.

30. Vora, R. H.; Krishnan, P. S. G. Poly (amic acid) s and their ionic salt solutions : Synthesis , characterization and stability study. In *Polyimides and other high temperature polymers: synthesis, characterization and applications Volume 2*; Mittal, K. L., Ed.; VSP, The Netherlands, 2003; Vol. 2, pp. 3–35.

31. H.D.Microsystems Product information: PI 2600 http://hdmicrosystems.com/HDMicroSystems/en_US/pdf/PI-2600_ProcessGuide.pdf.

32. Niyogi, S.; Maiti, S.; Adhikari, B. Chemical durability of polyimide blend films. *Polym. Degrad. Stab.* **2000**, *68*, 459–464.

33. Rojahn, M. Encapsulation of a retina implant, University of Stuttgart, 2003.

34. Turban, G. Dry Etching of Polyimide in O[sub 2]-CF[sub 4] and O[sub 2]-SF[sub 6] Plasmas. *J. Electrochem. Soc.* **1983**, *130*, 2231.

35. Bagolini, A.; Pakula, L.; Scholtes, T. L. M.; Pham, H. T. M.; French, P. J.; Sarro, P. M. Polyimide sacrificial layer and novel materials for post-processing surface micromachining. *J. Micromechanics Microengineering* **2002**, *12*, 385–389.

36. Aggarwal, A. O.; Raj, P. M.; Tummala, R. R. Metal–Polymer Composite Interconnections for Ultra Fine-Pitch Wafer Level Packaging. *IEEE Trans. Adv. Packag.* **2007**, *30*, 384–392.

37. Sugitani, S.; Onodera, K.; Aoyama, S.; Hirano, M.; Tokumitsu, M. Etching method for fabricating ultracompact three-dimensional monolithic microwave integrated circuits. *J. Vac. Sci. Technol. B Microelectron. Nanom. Struct.* **2002**, *20*, 1019.

38. Licari, J. J. *Coating Materials for Electronic Applications: Polymers, Processing, Reliability, Testing*; William Andrew, 2003.

39. Till, S. J.; Brown, A. G.; Deshmukh, V. G. I. Reactive ion etching of polyimide for multi-level resist and contact hole applications. *Microelectron. Eng.* **1985**, *3*, 491–498.

40. Deschler, M.; Balk, P. Optimization of via hole plasma etching in polyimide for overlay interconnections. *Microelectron. Eng.* **1986**, *4*, 207–219.

41. Vanderlinde, W. E. Reactive ion beam etching of polyimide thin films. *J. Vac. Sci. Technol. B Microelectron. Nanom. Struct.* **1988**, *6*, 1621.

42. Buder, U.; von Klitzing, J.-P.; Obermeier, E. Reactive ion etching for bulk structuring of polyimide. *Sensors Actuators A Phys.* **2006**, *132*, 393–399.

43. Bliznetsov, V.; Manickam, A.; Chen, J.; Ranganathan, N. High-throughput anisotropic plasma etching of polyimide for MEMS. *J. Micromechanics Microengineering* **2011**, *21*, 067003.

44. Mimoun, B. A. Z. Flexible Sensors for Minimally Invasive Medical Instruments 2013.

45. Ordonez, J. S. Miniaturization of neuroprosthetic devices and the fabrication of a 232-channel vision prosthesis with a hermetic package, Freiburg im Breisgau, 2012.

46. Woodruff, D. . *The Chemical Physics of Solid Surfaces*; The Chemical Physics of Solid Surfaces; Elsevier, 2002; Vol. 10.

47. Gnanou, Y.; Fontanille, M. *Organic and Physical Chemistry of Polymers*; John Wiley & Sons, 2008.

48. Li, H.; Sharma, R. K.; Zhang, Y.; Tay, A. A. O.; Kang, E. T.; Neoh, K. G. Surface Modification of Polyimide Films via Plasma-Enhanced Chemical Vapor Deposition of Thin Silica and Nitride Films. *Langmuir* **2003**, *19*, 6845–6850.

49. Maier, G. Low dielectric constant polymers for microelectronics. *Prog. Polym. Sci.* **2001**, *26*, 3–65.

50. Schulz, A.; Baumgärtner, K.-M.; Feichtinger, J.; Walker, M.; Schumacher, U.; Eike, A.; Herz, K.; Kessler, F. Surface passivation of silicon with the Plasmodul®. *Surf. Coatings Technol.* **2001**, *142-144*, 771–775.

51. Chatham, H. Oxygen diffusion barrier properties of transparent oxide coatings on polymeric substrates. *Surf. Coatings Technol.* **1996**, *78*, 1–9.

52. Yota, J. Interlevel Dielectric Processes Using PECVD Silicon Nitride, Polyimide, and Polybenzoxazole for GaAs HBT Technology. *J. Electrochem. Soc.* **2009**, *156*, G173.

53. Lee, J.-B.; English, J.; Ahn, C.-H.; Allen, M. G. Planarization techniques for vertically integrated metallic MEMS on silicon foundry circuits. *J. Micromechanics Microengineering* **1997**, *7*, 44–54.

54. Szili, E. J.; Kumar, S.; Smart, R. S. C.; Voelcker, N. H. Generation of a stable surface concentration of amino groups on silica coated onto titanium substrates by the plasma enhanced chemical vapour deposition method. *Appl. Surf. Sci.* **2009**, *255*, 6846–6850.

55. Chaudhury, M. K.; Gentle, T. M.; Plueddemann, E. P. Adhesion mechanism of polyvinyl chloride to silane primed metal surfaces. *J. Adhes. Sci. Technol.* **1987**, *1*, 29–38.

56. Lago, N.; Yoshida, K.; Koch, K. P.; Navarro, X. Assessment of biocompatibility of chronically implanted polyimide and platinum intrafascicular electrodes. *IEEE Trans. Biomed. Eng.* **2007**, *54*, 281–90.

57. Rubehn, B.; Bosman, C.; Oostenveld, R.; Fries, P.; Stieglitz, T. A MEMS-based flexible multichannel ECoG-electrode array. *J. Neural Eng.* **2009**, *6*, 036003.

58. Stieglitz, T. Development of a micromachined epiretinal vision prosthesis. *J. Neural Eng.* **2009**, *6*, 065005.

59. Girardeaux, C.; Druet, E.; Demoncy, P.; Delamar, M. The polyimide (PMDA/ODA)-titanium interface. Part 1. Untreated PMDA/ODA: an XPS, AES, AFM and Raman study. *J. Electron Spectros. Relat. Phenomena* **1994**, *70*, 11–21.

60. Egitto, F. D.; Matienzo, L. J.; Blackwell, K. J.; Knoll, A. R. Oxygen plasma modification of polyimide webs: effect of ion bombardment on metal adhesion. *J. Adhes. Sci. Technol.* **2012**.

61. Ham, D. J.; Lee, J. S. Transition Metal Carbides and Nitrides as Electrode Materials for Low Temperature Fuel Cells. *Energies* **2009**, *2*, 873–899.

62. Egitto, F. D.; Matienzo, L. J. Plasma modification of polymer surfaces for adhesion improvement. *IBM J. Res. Dev.* **1994**, *38*, 423–439.

63. Chemistry of Chlorine: The Dynamic Chemistry E-textbook http://chemwiki.ucdavis.edu/Inorganic_Chemistry/Descriptive_Chemistry/p-Block_Elements/Group_17%3A_The_Halogens/Chemistry_of_Chlorine.

64. WebElements Chlorine: reaction of elements https://www.webelements.com/chlorine/chemistry.html.

65. Natishan, P. M.; O'Grady, W. E. Chloride Ion Interactions with Oxide-Covered Aluminum Leading to Pitting Corrosion: A Review. *J. Electrochem. Soc.* **2014**, *161*, C421–C432.

66. O'Grady, W. E.; Roeper, D. F.; Natishan, P. M. Structure of Chlorine K-Edge XANES Spectra During the Breakdown of Passive Oxide Films on Aluminum. *J. Phys. Chem. C* **2011**, *115*, 25298–25303.

67. Donnelly, V. M.; Kornblit, A. Plasma etching: Yesterday, today, and tomorrow. *J. Vac. Sci. Technol. A Vacuum, Surfaces, Film.* **2013**, *31*, 050825.

68. Cameron, G.; Chambers, A. Successfully addressing post-etch corrosion. *Semicond. Int.* **1989**, *12*, 142 – 147.

69. Selamoglu, N. Tapered etching of aluminum with CHF3/Cl2/BCl3 and its impact on step coverage of plasma-deposited silicon oxide from tetraethoxysilane. *J. Vac. Sci. Technol. B Microelectron. Nanom. Struct.* **1991**, *9*, 2530.

70. Czuprynski, P.; Joubert, O.; Heitzmann, M.; Louis, D.; Vizioz, C.; Lajoinie, E. Efficiency evaluation of postetch metal stack anticorrosion treatments using chemical analyses by x-ray photoelectron spectroscopy and wide dispersive x-ray fluorescence. *J. Vac. Sci. Technol. B* 1997, *15*, 1000–1007.

Chapter 7
Assembly, packaging and characterisation

Manufacturing is more than just putting parts together. It's coming up with ideas, testing principles and perfecting the engineering, as well as the final assembly.
James Dyson (Industrial designer and founder of Dyson)

In order to show the feasibility of the assembly process and its compatibility in performing in-vitro experiments the wire bonding, packaging are the important steps to be considered regarding the microelectrode arrays. In this chapter all the necessary steps from releasing individual devices from the silicon wafer to the lasering process to get a finished device is explained. The device mounting on a flexible silicone stiffener and other possible solutions to stiffen the flexible MEA in order to use it for the insertion process during the animal experiments. Three electrode electrochemical cell test set up which is used for in-vitro experimental characterisation tests is explained. In-vitro experiments such as cyclic voltammetry, electrochemical impedance spectroscopy and voltage transients were performed in order to determine cathodic charge storage capacity (CSC_c), charge injection capacity (Q_{inj}) of the microelectrodes of the fabricated "Flexi-Stiff" MEA. The fabricated design options are plotted on the Shannon plot to find the charge density changes with increasing charge per phase for a pulse width of 300 µs/phase concerning the tested MEA devices. The chapter proceeds further with in-vivo experimentation performed on Guinea Pig which were carried out at the ENT department of LUMC, Leiden. During the in-vivo measurements the device successfully stimulated and measured the neural response back with an adjacent stimulation site of the MEA. Therefore the "Flexi-Stiff" MEA device was able to demonstrate a basic stimulation and neural response measurement, comparable to electrode designs used in CI recipients.

The part of this chapter which contains the data of the *in-vitro* and *in-vivo* experiments with its subsequent results were performed and provided by J.J. de Vos from the ENT department of LUMC.

7 Assembly, packaging and characterisation

7.1 Introduction

Medical devices and other implantable prosthesis which interface with human parts (e.g. muscles, organs, peripheral nerves, brain etc.) have been developing rapidly in the past decades. These devices, before using in the human beings, are first investigated fundamentally by performing studies (mostly neuro-scientific) tests in lab (*in-vitro*) followed by rigours testing in animals (*in-vivo*) and finally they have to be approved by the FDA. In this process most of the concepts, devices are filtered out and some of them then get transferred into clinical practice in terms of diagnosis, therapy and rehabilitation etc. The hard work behind the successful usage of these medical devices is only possible because of the latest cutting edge technologies and precision machines used during the manufacturing process. For example devices to restore hearing (CIs), vision, neural diseases etc. However there is a demand for more complex systems, greater degree of miniaturization and larger scales of heterogeneous integration to manufacture and perform. Developing these devices with advanced manufacturing techniques packaging is an important aspect to not only secure all the components together but also to functionally perform without failure for the intended period of time in harsh environment.

Many researchers via various research groups, universities, hospitals etc. are working in the area of neural stimulation by an electrical signal through a micro-machined device in order to record the bioelectrical signals indicating the neural activity. The focus of some of them is to investigate the fundamental neuro-scientific challenges but some of them face the challenges to transfer their prototype devices for human use as per the medical device directive (MDD) or active implantable medical device directive (AIMD) in order to achieve the CE mark in EU, the FDA approval in USA or other relevant approvals as per countries like Canada, Japan or Australia [1]. With the aim of designing and developing a long term stable implant without hindering its functionality while interfacing with the tissues/nerves of the human being. These medical devices have to undergo the technical requirements along with fulfilling the legal aspects of its final usage.

Whenever a medical or a neural implant (active type) is designed for a neural stimulation process, it needs to satisfy certain requirements, taking into consideration its application and the material tissue interface at a molecular level. During the device implantation procedure may sometime result in implantation trauma causing an chemical reaction on the tissue side which is initiated immediately after insertion and can last for weeks and months. In this situation the important requirement from the implant side is that it should not disturb the normal neural activity during the implantation process (Figure 7.1). In the nerve stimulation or recording process a stable input output signal performance is expected with minimal tissue damage

which is important for the therapy reliability and the rehabilitation process [1]. International standard ISO 10996 (Biological Evaluation of Medical Devices) are the established standards where the required tests are mentioned in order to evaluate the properties of the implant.

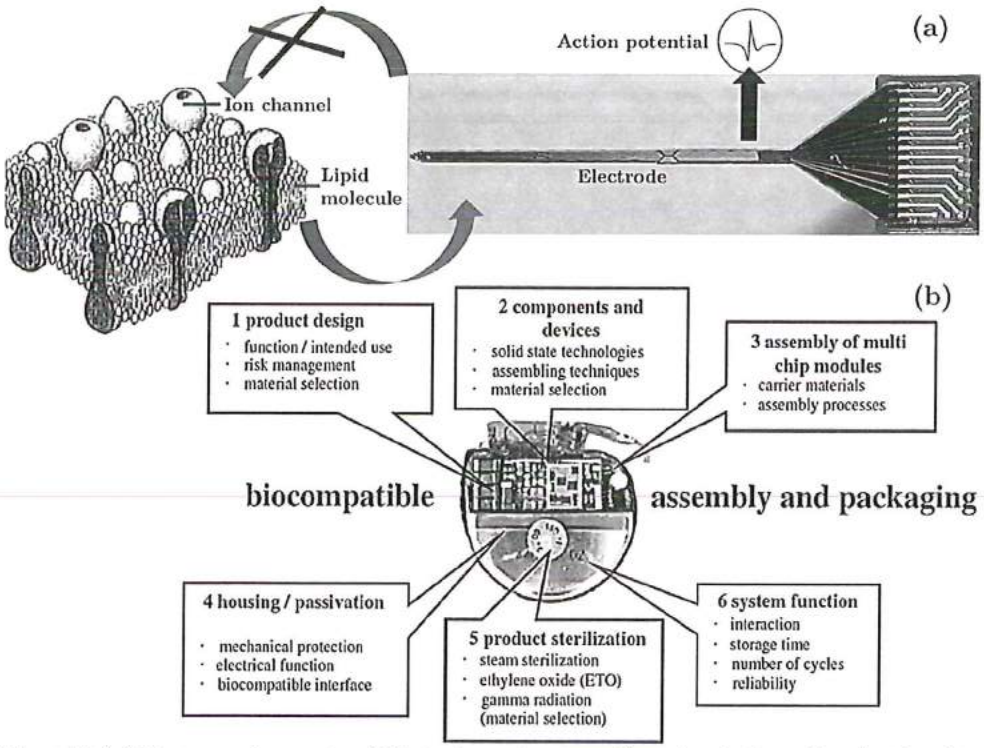

Figure 7.1 (a) Human environment and Electrode must not modify each other's working functionality; (b) Design and development aspects for implantable medical device: Cardiac Pacemaker (*Adapted and reprinted from* [1]).

The term "biocompatibility" coined from these standards is an important material property where the surface of the device must not only contain any left-over residues from the fabrication process but also must not release any toxic products when comes in contact with the tissue environment. For implants intended for long-term usage in the human being have to prove its material stability and its functionality. The structural biocompatibility of the device is affected by the implant tissue reaction and the implant intended use. Depending upon the intended use and the application of the implant apart from the assembly and packaging part, other aspects as mentioned and drafted out T. Stieglitz *et al.* (Figure 7.1 (b)) are worth considering during the overall development of the medical device [1].

7

7.2 Device assembly and packaging

The MEA is the main element in performing the electrical neural stimulation process and recording back of the bioelectrical signals from the tissues or nerves and transfer the audio information. It forms an important interfacing device between the biological and the technical system. The application of the MEA device defines the target design requirements concerning the electrode stimulation site sizes and its count. The MEA is normally connected to the central processing electronics via flexible cables, in most cases a single wire enclosing tiny individual wires to a plug or a connection pad near the base of the device making connection to the outer electronics which is the configuration in our "Flexi-Stiff" MEA. In our case individual electrode stimulation site is connected by separate metal tracks which run at the base of the device where the stiff connection pad (bond pad area) is glued and wire bonded to the PCB where by appropriate connectors connection is made possible with the required driving electronics.

7.2.1 Device release

In the development and design procedure of the MEA along with the microfabrication aspects, equal importance has to be given for assembly, packaging and encapsulation of the device from the biological environment. Depending upon the intended application, biological boundary conditions (for e.g. fluid environment, anatomy etc.) has to be considered in advance to determine the system complexity.

The first step in the assembly of "Flexi-Stiff" MEA is its individual release step from the completed microfabricated wafer holding all the devices (refer Figure 7.3). The CAD design process and the subsequent microfabrication process was designed accordingly in order to obtain the "Flexi-Stiff" device, where the flexible part containing the thin PI foil and the metal is firmly held during the entire fabrication process by the PI supports at the edges. The red dotted line as shown in Figure 7.3. is a guideline for the cutting (laser process or with sharp blade) procedure to be followed for releasing the individual device from the wafer. Results showing the released device from the complete wafer can be seen in Figure 7.2 where the support PI structures are easily visible along with the rectangular Silicon (525 µm thick) islands kept for folding and handling purposes during the assembly procedure. The remains of the PI holding structures especially at the stiff Silicon (bond pad area) part are then carefully lasered out to avoid further problems in glueing and the wire bonding steps.

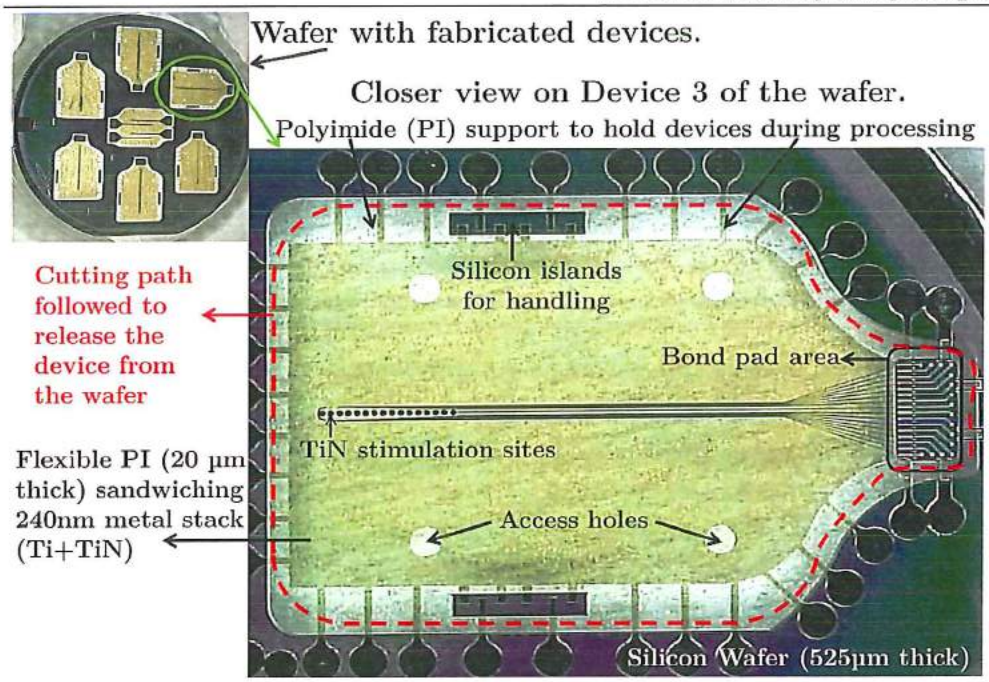

Figure 7.2 Fabricated devices on wafer with a closer look up to one of the device.

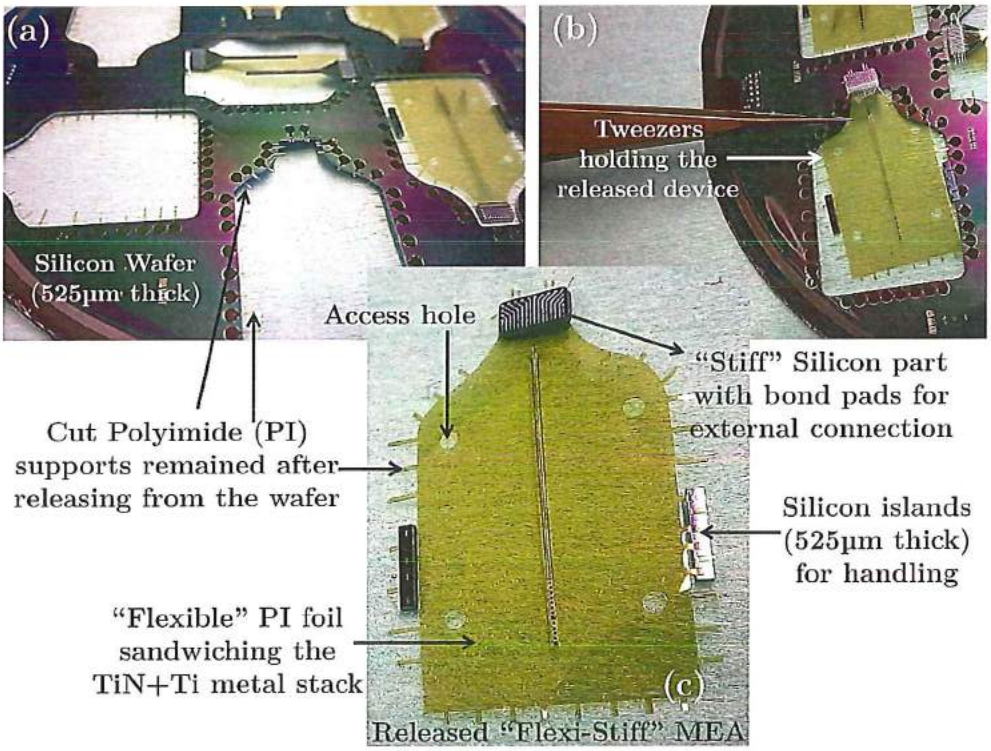

Figure 7.3 Released device separated from wafer and ready for gluing on PCB.

7.2.2 Glueing, wire bonding and Silicone encapsulation

After the releasing step the next step was to perform the glueing and the wire bonding of the "Flexi-Stiff" MEA on the PCB's. Two different PCB's were designed in order to accommodate the microfabricated MEA's with subsequent connectors. The details of the two PCB's (CAD impressions and images) with the connectors are as shown in Figure 7.4. The mounting and encapsulation procedure for one type of PCB (Design 1) is explained here. Each PCB has a specified area where the stiff part (Silicon) of the "Flexi-Stiff" MEA will be glued on. A non-conducting glue (ABLEBOND® 84-3) from Ablestik™ , Henkel was used to glue the stiff part to the PCB's intended place. The glueing step was followed by a room temperature (25 ^{o}C) curing step for 2 hours before it is wire bonded. A normal wire bonding procedure using aluminium, as the bonding material was done followed by soldering the 18 Pin two row connector on the PCB from the back side. A special steel cage was designed which fits on the surroundings of the PCB. The steel cage was designed in two parts (upper and lower cage) such that it closely fits at the side edges of the PCB with an clearance at the tip of the cage allowing the flexible foil to pass through it.

The mounting of the steel cage created a cavity where encapsulating silicone material can be added. The encapsulating material used for our case was a medical grade transparent silicone (Sylgard® 184 Silicone Elastomer) material supplied as a two-part liquid. This two-part free flowing flexible silicone elastomer after pouring into the desired cavity is cured for 30 minutes at 80 ^{o}C. This cured flexible elastomer which normally is used for the protection of electrical and electronic devices. After curing it gives a hardness of 50 Durometer, Shore A with a minimal shrinkage which ensures minimal stress levels on the aluminium wire bonds which are bonded with a step height difference of 525 µm from the hard Silicon bond pad area to the PCB surface. After curing and the de-moulding of the cages extra silicone (flash) is cleaned out with the help of special tweezers or by Excimer laser for smaller intricate shapes. The entire packaging steps are illustrated in Figure 7.5.

7.2.3 Wrapping and mounting to silicone carriers

The "Flexi-Stiff" device which resulted by the steps shown in Figure 7. was well suited for *in-vitro* experimentation purposes, the procedure of which is explained in the later sections of this chapter. In order to perform *in-vivo* experiments in guinea pig cochlea's the planar flexible part of the device needs to be either circular or have to be glued and mechanically supported by a flexible biocompatible silicone tubing (hollow or solid) which must be able to have easy insertion while inserting inside the upward going circular cross-section of the animal cochlea. For this three different approaches were undertaken.

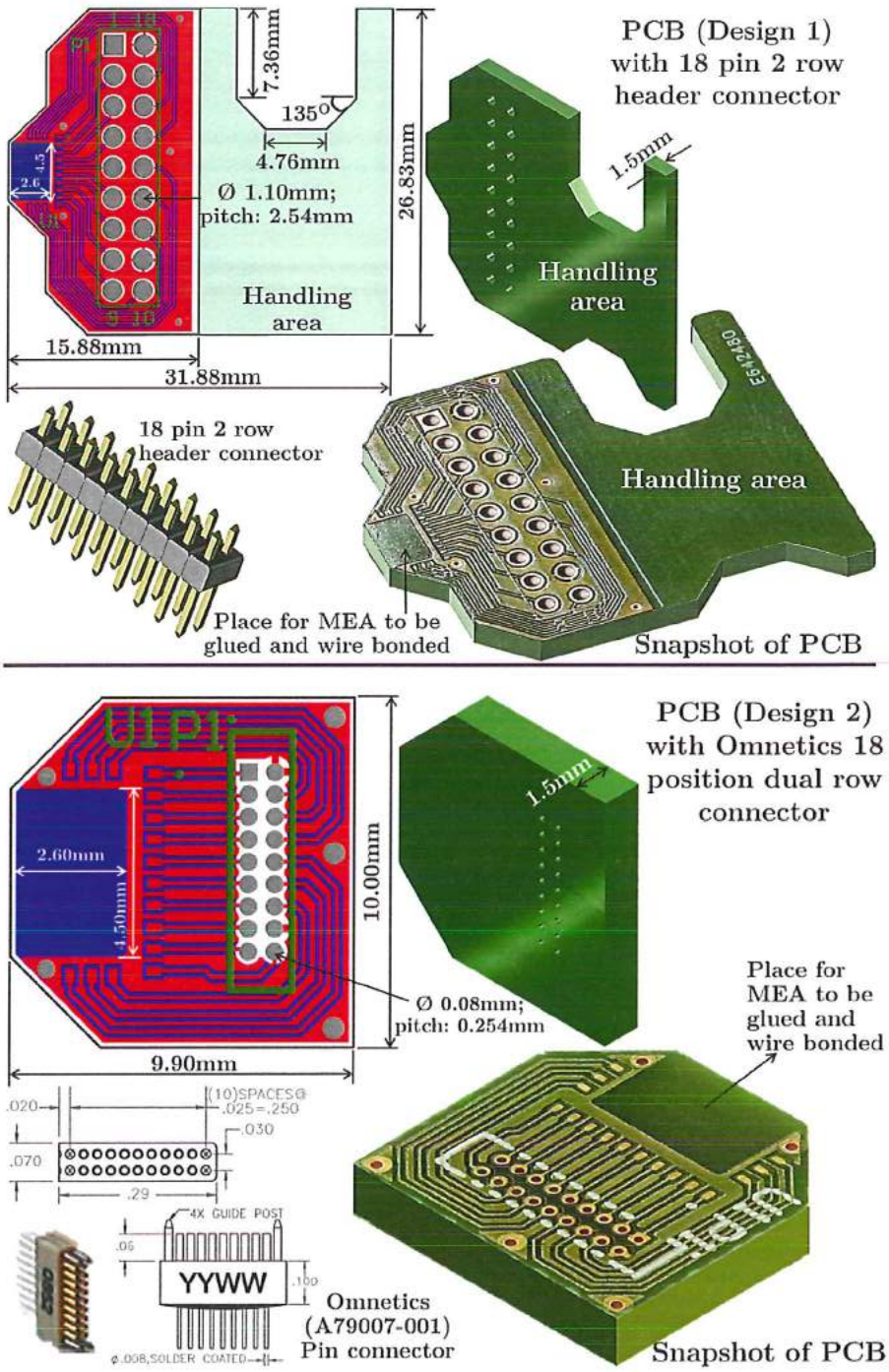

Figure 7.4 PCB's (Design 1 and 2) with various dimensional and other details.

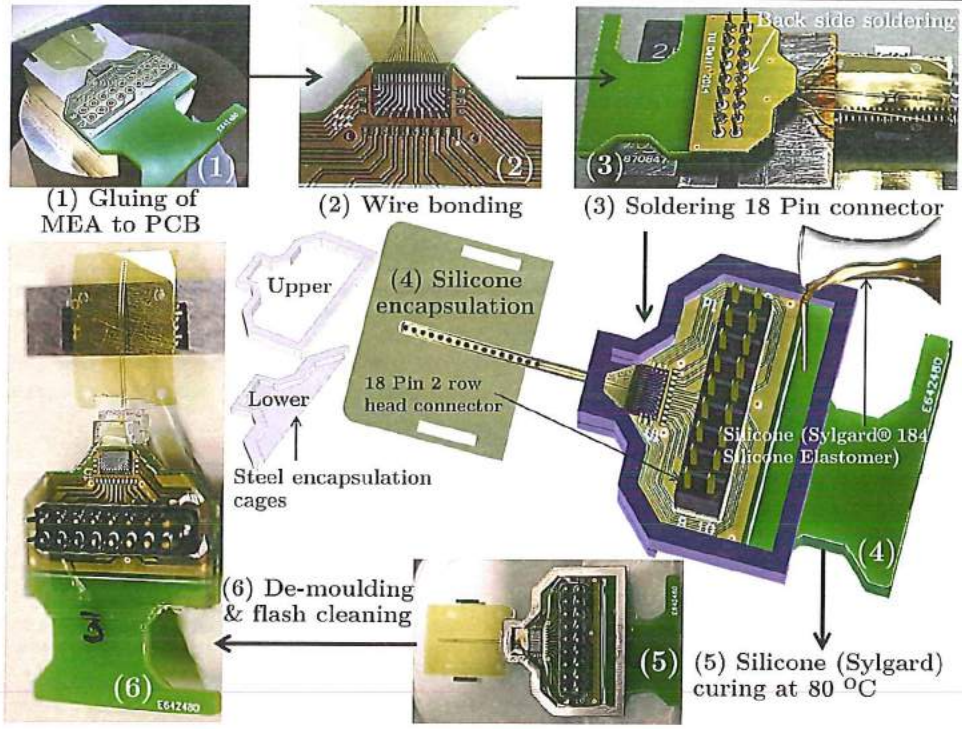

Figure 7.5 Different packaging steps involved for the fabricated MEA.

Figure 7.6 Mounting and folding of the "Flexi-Stiff" MEA.

(a) Mounting and folding of the flexible foil with the flexible MEA: In this method a special brass fixture was manufactured (Figure 7.5) which included steel guiding pins for aligning the pre-fabricated holes in the flexible part of the "Flexi-Stiff" device. The flexible part including the MEA with upside down was placed in the guiding pins with a support on the PCB to compensate for the fixture height. A flexible hollow silicone tube (0.35 to 0.4 mm OD Ø) was centrally placed on the back side of the MEA. Before placing a transparent silicone adhesive (MED-2000 and MED-1511; NulSil Silicone technology) was applied on the hollow silicone tube and the back side of the flexible MEA PI foil. This silicone adhesive is a special adhesive which is used for bonding silicone elastomers to each other and some synthetics and metals. This part which is self-levelling, solvent-free silicone adhesive cures at room temperature upon exposure to atmospheric moisture. After the adhesive application and proper placement of the parts is dine with the help of purposely kept silicon islands during the microfabrication process, the flexible PI foil is folded around the flexible silicone tubing. After folding, the whole assembly is kept in an Heraus oven for 20 minutes at 80 ^{o}C which speeds up the curing process of the adhesive. The folding result is as shown in Figure 7.5. After curing process, excess PI is cut out by an Excimer laser machine (details explained in section 7.2.4) to obtain a flexible circular MEA device with the stiff Silicone part which is already wire bonded to the PCB. This process was reasonably successful but unfortunately the yield was low (<30%) so alternative options had to be sought. The reason for low yield was the manual folding and handling process of the flexible part which created fracture stresses at the junction where the foil is attached to the stiff silicon part. These stresses propagated further into cracks leading to loosening and breakage of the foil from the stiff silicon part.

(b) Attaching a 3D printed silicone carrier with a flexible solid silicone tube: In this process a separate 3D printed silicone carrier which was designed and manufactured in such a manner that this 3D printed part fits from the back side of the PCB adding mechanical stability to the flexible part leaving the stiff silicon in conjunction with the PCB. The CAD impression and the resulted 3D printed fabricated silicone carrier (Material: "Flexible": Photo-reactive Resin for Form1, From 1+ from FormLabs) is as shown in Figure 7.7 (a). In order to also add stability to the flexible PI foil a flexible circular silicone rod (0.4 mm Ø) was separately manufactured and then glued to the 3D printed part. The material of this circular flexible silicone rod is MED-4970 (Liquid Silicone Rubber from NulSil Silicone technology).

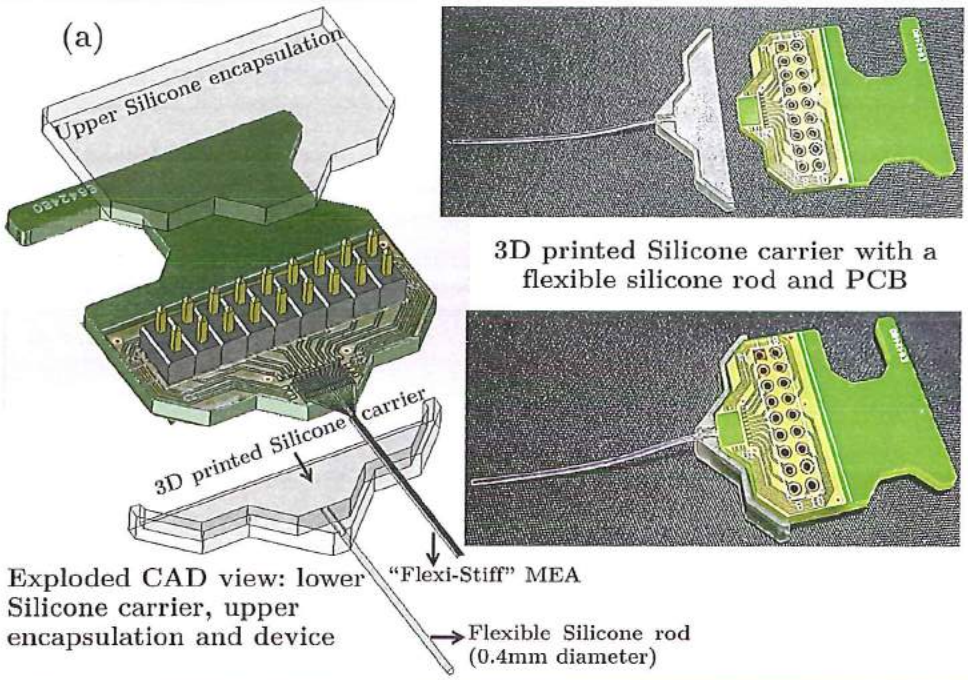

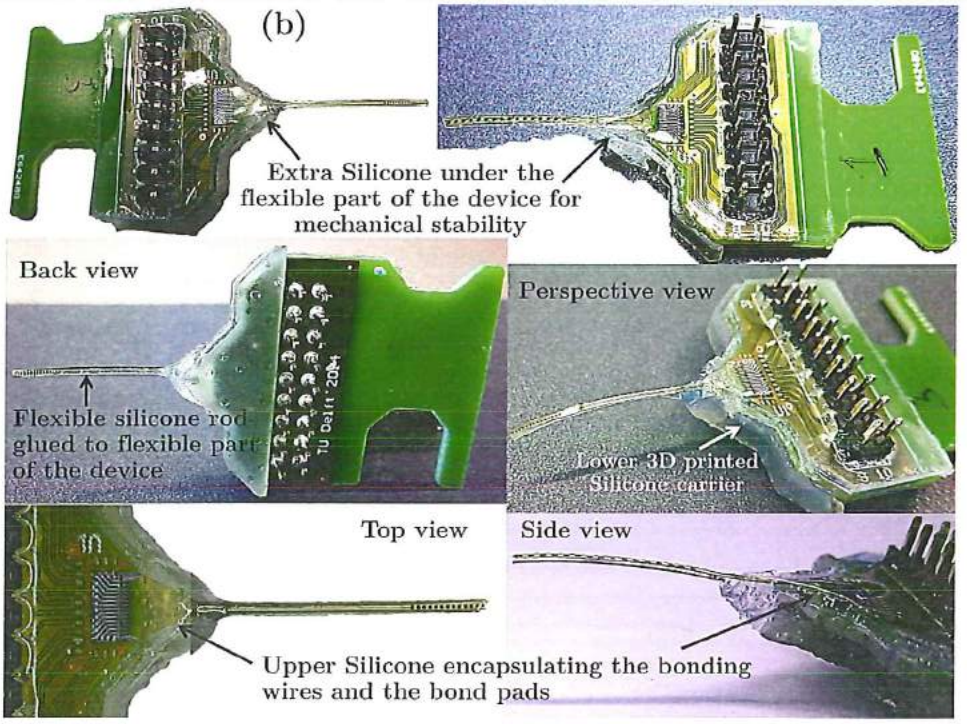

Figure 7.7 3D printed Silicone carrier: (a) CAD impression and manufactured 3D printed Silicone parts; (b) Final assembly of "Flexi-Stiff" device after gluing 3D printed Silicone carrier along with the flexible solid silicone tube.

This two-part (1:1 Mix ratio of part A and part B), translucent silicone system was manufactured by injection moulding process to obtain the desired dimensions. The flexible silicone rod was glued to the 3D printed part with the help of the transparent silicone adhesive (MED-2000 and MED-1511; NulSil Silicone technology). Making use of the same adhesive the whole assembly (3D printed silicone carrier and the flexible silicone rod) was glued to the back side of the PCB. After glueing, the final assembly was cured in an oven (Heraus oven) for 20 minutes at 80 ^{o}C. The results after curing and flash cleaning are shown in Figure 7.7 (b).

(c) Using a Silastic carrier of the non-functional CI electrode array: This approach was used for the smaller PCB designs (Design 2) where space restrictions with the available material was a priority. The smaller PCB based devices were assembled in similar manner as the larger PCB's, the only difference being the 3D printed silicone carrier which was not manufactured in this case for excluding one packaging step. In this case a Silastic carrier of the non-functional pre-fabricated CI electrode was used. This carrier was first glued (glue used: MED-2000 NulSil Silicone technology) to the flexible part of the device which is initially laser cut to define the MEA dimensions. Then a silicone elastomer (Sylgard® 184 Silicone elastomer kit) was used to encapsulate the upper and the lower part of the PCB along with creating a slope with the same material that runs from the PCB to the flexible part of the MEA, thus adding mechanical support to the entire assembly. The whole assembly was then cured in a similar manner as done earlier. The resulting device, after curing and flash cleaning, is as seen from the device images in Figure 7.8.

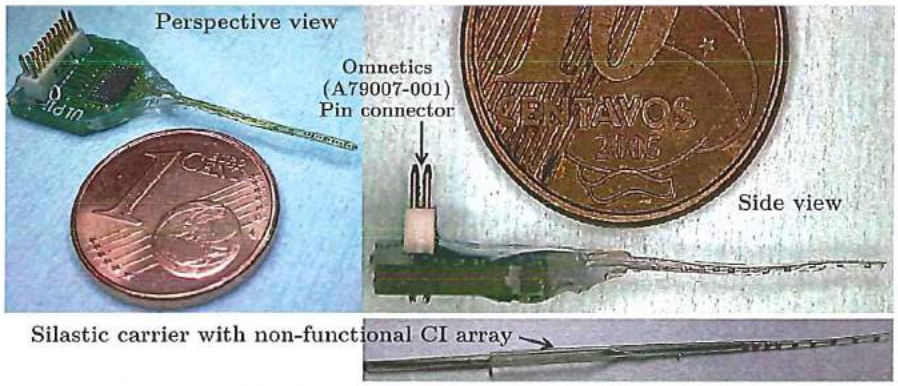

Figure 7.8 "Flexi-Stiff" MEA with smaller PCB version and silastic carrier of CI array.

Out of the three approaches mentioned above the last two options were finally considered for assembly and packaging of the "Flexi-Stiff" device depending upon the simplicity and the number of steps involved.

7.2.4 Laser micromachining or structuring of the device

Laser micromachining is a material removal or an ablation process using a laser beam suitable for that particular material. The knowledge from the laser manufacturing technology, which is widely used for precise machining with tight tolerances, has been extensively applied to neural implant field in order to overcome the spatial and manual manufacturing limitations within the working frame of the approved materials to be used for chronic implantation in the human beings. Schuettler *et al.* [2] uses Laser technology to manufacture stimulation electrodes for retinal prostheses with the help of Pt as an electrode and interconnection material along with Silicone rubber as a substrate as well as an insulation material. Similar combination of material and laser technologies were used by other researchers to manufacture recording electrodes for brain machine interfaces [3] and flexible MEAs for impedance tomography of the brain [4]. With the help of advanced CAD design software it is possible to construct complex MEA design and geometries. These can be further transferred directly to advanced laser machines in their compatible formats in order to construct the MEA by patterning the metal or the silicone. The electrode material (mostly noble metals) normally is sandwiched between two polymer or silicone rubber layers which later are opened from the top side to get in touch with the tissue or the nerve where stimulation/recording is necessary. Silicone rubber not only electrically insulate the metal from the biological environment but also adds mechanical support to the whole device. By laser micromachining, feature sizes less than 300 µm with a pitch of at least 150 µm is achievable. Laser micromachining technology until now seems to be a process adapted in research as well as industry to produce the MEAs based on modern CAM and CAD data used in the overall design process of MEAs. Table 1 reviews the common lasers used for structuring different materials [5].

As mentioned earlier the laser micromachining which is an material ablation process, is a complex method where the lasering procedure is dependent on the laser properties such as wavelength, pulse width, duration and intensity, and the material (surface microstructure, absorption spectra, ease of material removal) to be removed. In our microfabrication process we have used an Excimer laser (MicroMaster, distributed by OPTEC S.A. laser micromachining systems, Belgium) machine to structure the outer shape of the flexible part of the "Flexi-Stiff" MEA device. Excimer micromachining relies on the interaction between UV pulsed laser radiation and the material to be machined. The shorter wavelength means that radiation is efficiently absorbed in the surface layers except few materials; the short pulse duration ensures high peak absorbed power densities. The combination of UV and short pulse results in the removal of surface layers by a number of mechanisms:

vaporisation in the case of metals and ceramics, molecular disintegration (photo-ablative decomposition) for many polymers at <300 nm, or interface effects (stripping by exfoliation of thin films up to a few µm thick). Successive laser pulses cause further material ablation, and thus controls the localized milling into the part, which constitutes the basic act of machining as shown in Figure 7.9 (a). Energy densities are typically in the range of 1-10 J/cm^2 at repetitive rates up to a few hundred Hz; machining takes place at rates on the order of tenths of µm/shot. As a minimum condition Excimer micromachining requires a laser and a beam delivery unit. This unit is nothing but a combination of lenses along with process control systems which makes it possible to get an appropriate beam of correct wavelength, intensity and pulse duration at the desired location. **Masks:** Excimer laser machines use laser beams which have typically broad spatial profile, and poorly defined mode structure. Unlike other lasers, focal point applications are rare; most of the processing is performed by using projection optics, where the beam is used to illuminate a mask, whose de-magnified image is then focussed on the part in accordance with the formula $1/u + 1/v=1/f$, where f is the focal length of the projection lens used, u and v are the object (mask) and image (part) distances respectively. The mask may be defined as a simple motif, e.g. circle, slit (the situation in our case) or more complex motifs which are then projected as a whole onto the part, e.g. alphanumeric characters. The final machining pattern on the part can be built up from the repetition of selected motifs associated with part motion in X, Y and laser firing and the machining depth is mainly controlled by local shot dose. Fixed masks may be mounted on a motorized selector carousel.

Type	Wavelength	Pulse Width	Pulse energy	Target materials
Excimer (ArF, KrF, XeCl)	193, 248, 308 nm	~ 20 ns	0.01 – 1J	Polymers
Nd YAG	1.064 µm	~ 10 ns	10 mJ	
Co_2	10.6 µm			High throughput application
Fluorine vapor	157 nm			
Nd YAG	355 nm, 266 nm	~ 10 ns	<1 mJ	PTFE, PMMA, Polyimide
IR	10 µm			Metals, ceramics
Copper vapor	255, 271, 289 nm			
Diode Lasers	808 – 980 nm			

Table 1. Summary of common lasers been used for micromachining materials (*Adapted and reprinted from S. Rajaraman et al.)* [5].

Dynamic masks use e.g. motorized slit or rectangular variable aperture (RVA). The choice of mask type is determined by the processing requirements, whereas we used a fixed steel mask (Figure 7.9 (b)) with a hole diameter of 0.30 mm and a standard demagnification of 10 giving a 0.030 mm hole projection. Following are the Laser specifications used for our lasering process:

- Wavelength = 248 nm
- Repetition rate = 300 Hz max
- Pulse energy = 18 mJ Max

Positioning: X,Y travel range of 200 mm with an resolution of 1 µm. The total focus range is 25 mm, adjustable in steps with 2.5 µm.

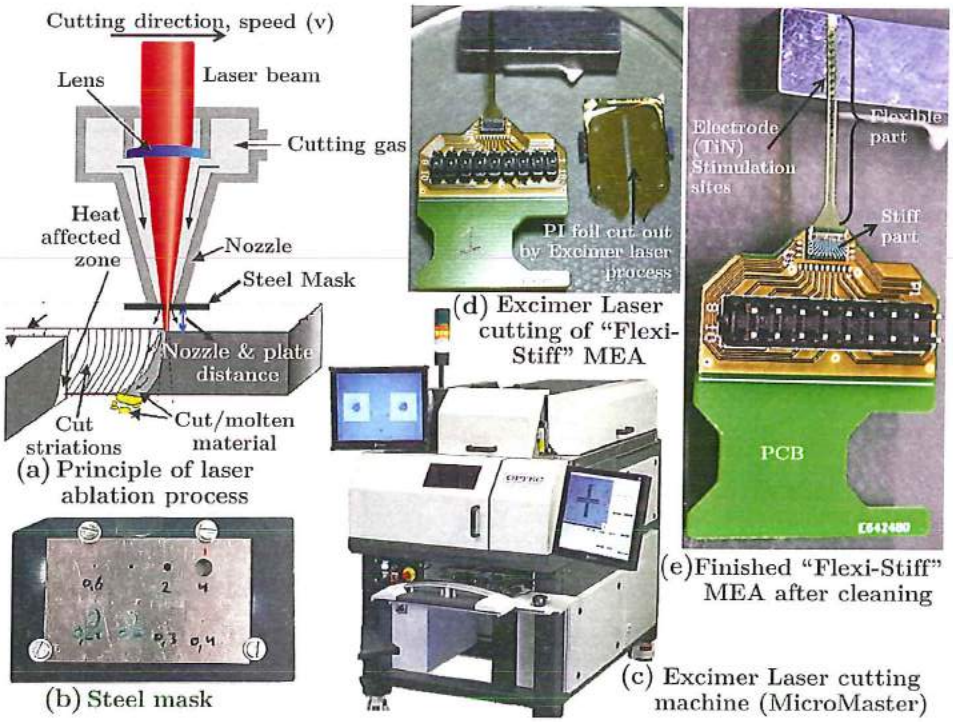

Figure 7.9 Excimer laser micromachining process and subsequent results.

7.3 Electrochemical characterisation

The most common techniques used in the electrochemical characterisation process for characterising MEAs or bio-electrodes are cyclic voltammetry (CV), electrochemical impedance spectroscopy (EIS), and potential transient measurements. These techniques can be applied both for *in-vitro* or *in-vivo*

applications but for the characterisation of our devices we present our *in-vitro* results of the characterisation tests done at LUMC.

7.3.1 Cyclic Voltammetry (CV)

CV is the most effective and versatile electro-analytical measuring technique which is normally used to identify and study the nature of the electrochemical reactions caused by the electroactive species at the electrode-electrolyte interface. Generally CV is one of the first experiments in a typical electrochemical studies performed on compounds, a biological material or an microelectrode surface. CV experiments demonstrate the ability to observe rapidly the redox reaction behaviour at the interface over a wide potential range. This experiment results, given in a voltammogram, convey information as a function of an energy scan [6]. CV experimentation involves the usage of electrodes; the working electrode whose potential is cycled by immersing or soaking it in an unstirred solution (for e.g. phosphate buffered saline-PBS) and which is controlled against a reference electrode such as a standard calomel electrode (SCE) or a silver/silver chloride electrode (Ag|AgCl). A controlling potential (normally an excitation signal in a triangular waveform as shown in Figure 7.10) is applied across or in other terms is swept cyclically at a constant rate between these two electrodes.

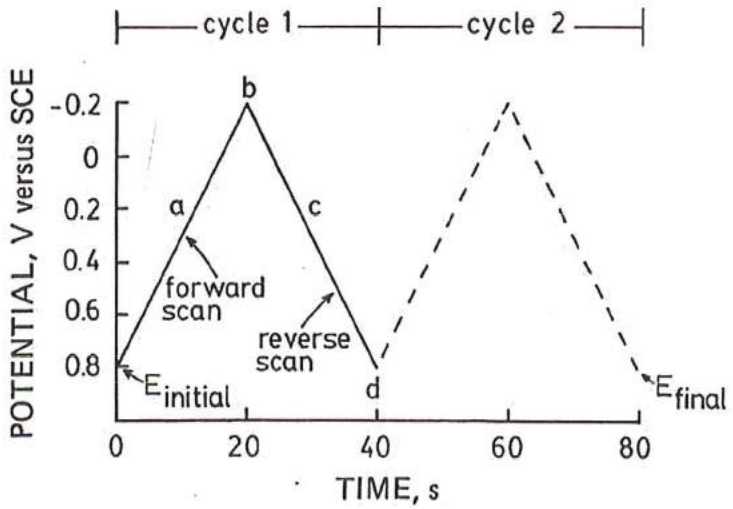

Figure 7.10 Nature of an excitation signal used for CV experimentation [6].

This triangular potential excitation signal sweeping action normally sweeps the electrode potential between two potentials referred to as switching potentials. Such a applied triangular excitation signal causes the potential to scan from positive (+0.8 V) to a negative value (– 0.2 V) at which point the scan direction gets reversed to scan back to its original potential (+0.8 V). Since the reference electrode is an non-

current-carrying electrode, the current generated by these excitation signals flows between the working electrode and an additional counter electrode. This generated current is directly proportional to the redox reaction rate occurring at the electrode-electrolyte interface. The CV experimentation results in a cyclic voltammogram which is obtained by the current measurement done during the potential scan at the working electrode.

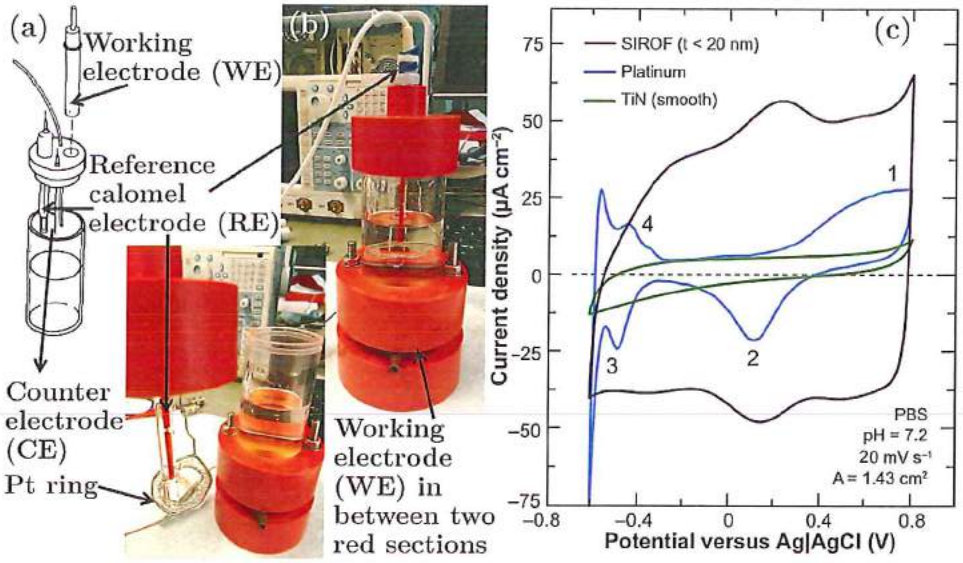

Figure 7.11 (a) Schematics of an electrochemical cell [6] and (b) a typical one; (c) Voltammogram's for different materials in PBS at a sweep rate of 20 mVs^{-1} [7].

This voltammogram shows the current variations (vertical axis) for the respective voltage potential (horizontal axis) applied at the electrode surface. The shape of this graph (voltammogram) depends on the sweep-rate, the electrode material and its roughness and the exposed geometric area [7]. With the help of these voltammograms it is able to enumerate the amount of charge which is provided by the micro-electrode when subjected to stimulations under a normal stimulation experiment. This charge value is normally referred as charge storage capacity (CSC) and is obtained by performing a standard cyclic voltammetry experiment at slow sweep rate over a potential range within the water electrolysis window and then integrating the measured cathodic current. Figure 7.11 (a) [6] and (b) shows a typical electrochemical cell with three electrode configuration. The potentiostat that applies a desired potential between a working and a reference electrode is normally used in an electrochemical setup. The working electrode is the electrode under investigation where the electrolysis reaction of interest occurs. The current which is required to

withstand this electrolysis reaction at the working electrode is delivered by the counter electrode. This three electrode configuration thus prevents the passage of large current through the reference electrode which could change its potential. As shown in Figure 7.11 (a) and (b) such type of cell is housed in a glass container containing a electrolyte (generally phosphate buffered saline: PBS solution) sealed by a cap having holes for electrode insertion. Also in some cases holes for allowing nitrogen flow via tubes are done in order to allow oxygen removal from the electrolyte by replacing it with nitrogen, thus maintaining an oxygen free environment in the cell. The reference electrode (RE) is a standard calomel electrode (SCE) or a Ag|AgCl electrode (used in our case). The auxiliary or a counter electrode (CE) is a platinum wire or a ring which is immersed in the solution. In any voltammetry experimentation the peak (or limiting) current is temperature dependent and the cell should be thermostated for accurate measurements. In most cases this is not required [6]. Figure 7.11 (c) [7] represents a comparison of cyclic voltammograms of sputtered iridium oxide (SIROF), Pt and TiN (smooth) macroelectrodes (geometric surface area; GSA=1.4 cm^2) in PBS at a sweep rate of 20 mVs^{-1}. The difference in the voltammograms provides information on different electrode materials. SIROF graph represents the largest area which indicates a higher CSC with an higher electrochemical activity at the electrode-electrolyte interface. Referring to Pt graph (Figure 7.11 (c)) points 1 and 2 show the Pt oxidation and reduction process and 3, 4 indicates the hydrogen atom plating and stripping on Pt respectively. On the other hand, TiN (smooth surface) shows an approximate rectangular form which relates to the capacitive behaviour of this material. CV electrochemical tests were carried out on the fabricated devices (fabrication as explained in earlier chapter) at LUMC. The image shown in Figure 7.12 is a part of the complete setup showing electrochemical cell. This cell consists of a glass container with Phosphate Buffered Saline (PBS) solution (NaCl, $Na_2HPO_4 \cdot 12H_2O$, $NaH_2PO_4 \cdot 2H_2O$, pH=7.4) was used which is the place to hold the three electrodes; working electrode (WE), reference (RE) and counter electrode (CE). The WE in our case is the "Flexi-Stiff" MEA with the PCB connector as shown in Figure 7.12 connecting to the external circuitry. The RE is the Ag|AgCl electrode wire from A-M systems, USA. The CE is a standard pure Pt or Ag (99.99%) wire. LABSTIM stimulation and measurement software developed at LUMC was used to improve the efficiency of experiments which was controlled by a personal computer. A sequence of coded pulses, transmitted via two input/output digital lines, determine all the stimulation parameters. Pulse width, frequency, and amplitude of stimulation can be preset by the computer. Pulse parameters can also be updated during stimulation, which allows the generation of burst of stimuli with gradually changing the pulse widths, frequencies, or amplitudes. The pulse width ranges from 10 µsec to 10 msec

and the frequency range is from 0.1 Hz to 1 KHz. All the measurements done were analysed and controlled by NI USB-6215, a bus powered isolated USB M series multifunctional data acquisition (DAQ) module which is optimized accordingly for accuracy and faster sampling rates. The DAQ module here was used as an interface between the cell and the instrumentation where on one side it is connected to the electrochemical cell and on the other side to the PC where the signals are generated. The whole experimental setup used for CV measurements is represented in a block diagram as shown in Figure 7.13. As seen from the block diagram the electrochemical cell with the three electrodes (reference, counter and working) are connected to the DAQ module.

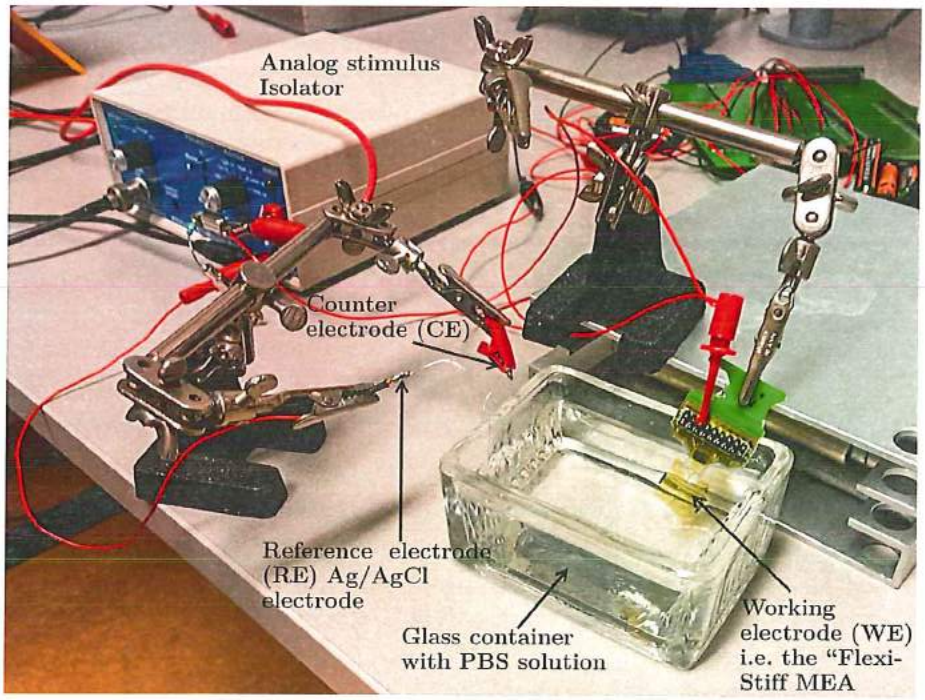

Figure 7.12 Electrochemical cell as a part of the electrochemical setup characterising the "Flexi-Stiff" MEA *(Image courtesy: J.J. de Vos, LUMC Leiden).*

A potential was applied between the working and the reference electrodes and is swept cyclically with a constant rate between two potential limits, while the current flows between the WE and the CE. The detailed procedure is explained as below:

1) Cleaning of the electrodes ensures a good electron transfer. The "Flexi-Stiff" working MEA array, the Ag|AgCl reference electrode, and the Ag counter electrode were placed in a standard PBS solution (pH 7.4). All the electrodes were connected by connection clips as per the diagram.

2) The electrode was cycled in a positive range for 10 min at lower scan rate (20 mV/sec). These parameters were used in the CV technique with large number of scans. Cyclic voltammograms were stopped after 10 min. Here step 1) and 2) ensured a clean electrode.
3) CV was then repeated from + 0.8 V to − 0.8 V at a rate of 50 mV/sec. Further three different scan rates (100, 200 and 300 mV/s) were used to show the peak currents and peak splitting variation with the scan rate.
4) After CV experiments the electrodes were thoroughly rinsed with acetone and isopropyl alcohol (IPA) before storing back into their respective boxes.
5) MatLab was used to plot the cyclic voltammograms.

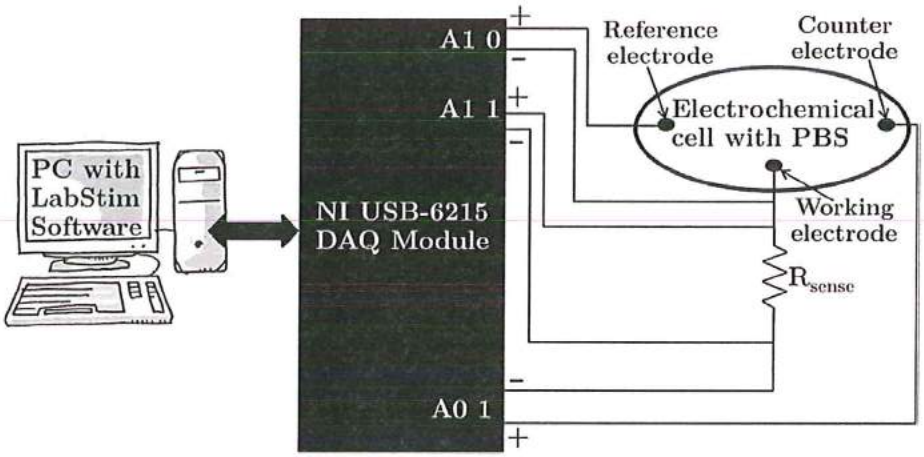

Figure 7.13 Block diagram showing the experimental setup for CV measurements.

Cyclic voltammograms obtained in phosphate buffered saline (PBS) solution from the microelectrode surface of the sputtered rough TiN of the "Flexi-Stiff" MEA is as shown in Figure 7.14. The nature of the CV obtained in our experimentation is in accordance with the rectangular shape profile obtained by S. Cogan *et al.* [7] during the experimentation for smooth sputtered TiN film. This shape is as expected for TiN which exhibits a double-layer capacitance behaviour at the electrode-electrolyte interface. This behaviour is similar in the case of Pt (refer Figure 7.11 (c)) where no faradic processes were observed with only distinctive peaks associated with oxidation and reduction of surface oxide (peaks 1 and 2) and hydrogen-atom plating and stripping (peaks 3 and 4) which may result in changes in surface properties due to long term stimulation [7].

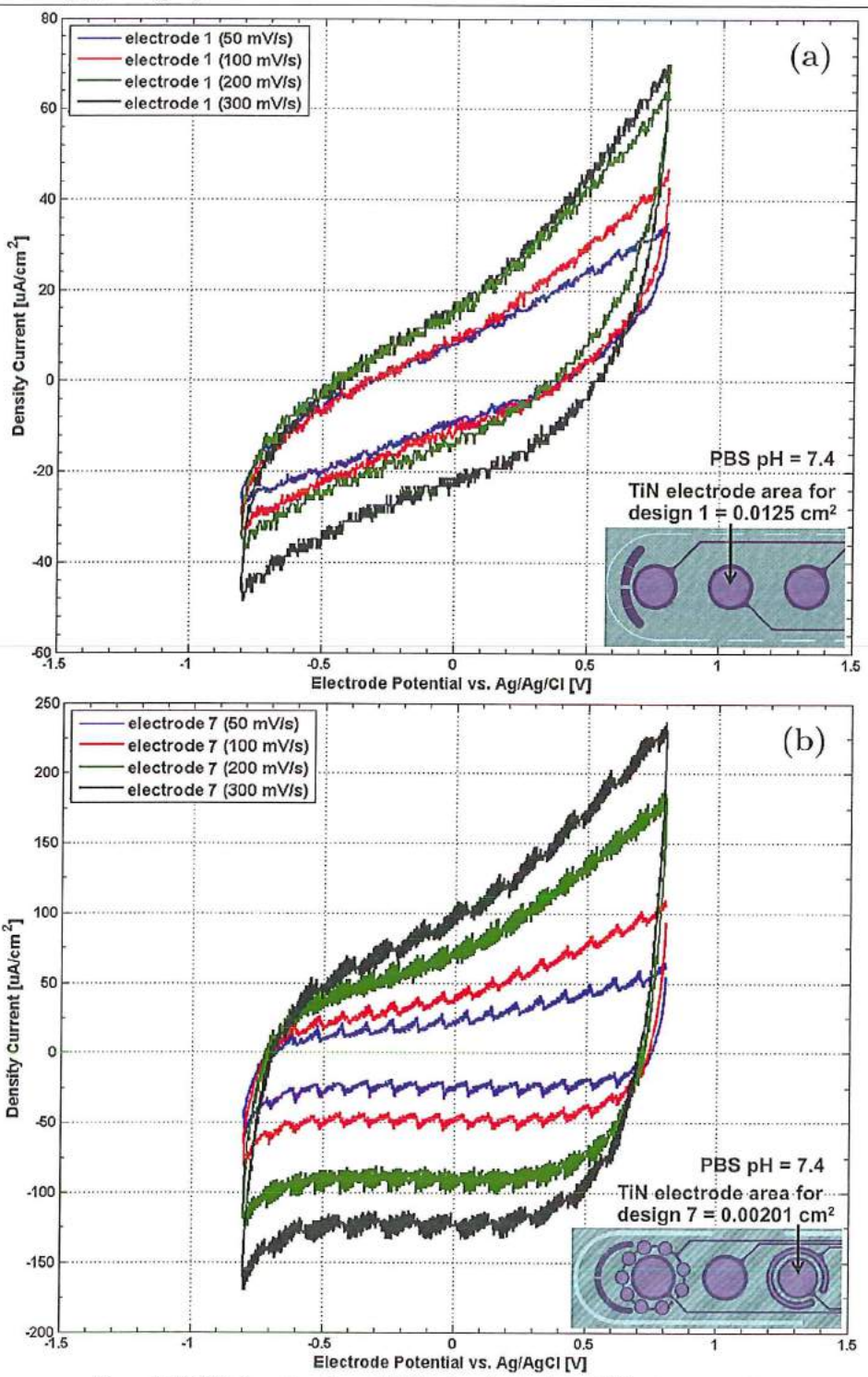

Figure 7.14 CV of sputtered rough TiN microelectrodes at different sweep rates.

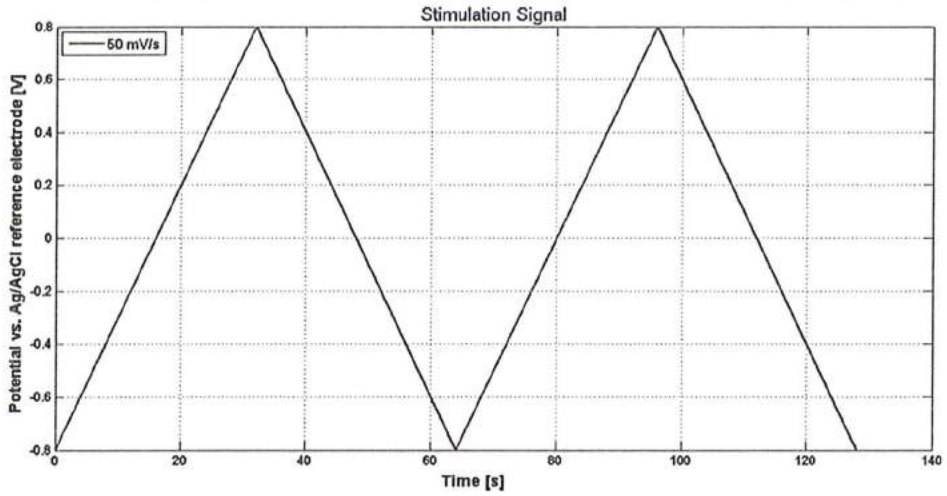

Figure 7.15 A typical excitation signal with a sweep rate of 50 mV/s.

On the other hand, SIROF based electrodes exhibit a significantly higher charge storage capacity (5 times the available charge for the same geometric surface area-GSA). The rectangular CV for SIROF though proposes a capacitive behaviour, but the charge is substantially faradic involving the reversible Ir^{3+}/Ir^{4+} couple [7]. A common technique to characterize the stimulation microelectrodes is by calculating their **C**athodal **C**harge **S**torage **C**apacity (CSC_c). The CSC_c is a quantitative figure of merit which provides information regarding the amount of charge a particular material can deliver in its cathodal part of the cyclic voltammetry. It's value represents the maximum amount of charge that can be transferred by the electrode while remaining in a set potential window. The CSC_c is calculated from the time integral of the cathodic current in a slow-sweep-rate cyclic voltammogram over a potential range that is just within the water electrolysis window.

$$CSC_c = \int_{t_1}^{t_2} D dt \qquad (1)$$

where; t_1 is the measurement starting time which is the upper positive peak of excitation signal (0.8 V in our case), t_2 is the measurement finishing time which is the lower negative peak of the excitation signal (– 0.25 V) (refer to Figure 7.16) and D is the current density (A/cm²). This equation was used along with a MatLab script to calculate the CSC_c's for different designs of the stimulation electrode site of the "Flexi-Stiff" MEA. The CSC_c of the respective electrode designs as shown in Figure 7.14 are 235 µC/cm² (electrode design 1) and 732 µC/cm² (electrode design 7). The remaining CSC_c values with their respective cyclic voltammograms can be

referred in the Appendix. The CSC_c is principally a tool to measure the amount of charge available for a particular stimulation material for a stimulation pulse. On the other hand the CSC_c which is obtained by this process under low-current-density, near equilibrium conditions has limitations in predicting the charge-injection capacity for the neural stimulation process. Normally for an implanted microelectrode of certain material an equilibrium potential which is between the upper and lower potential limits is used to generate the cyclic voltammogram for the CSC_c integration. For example, AIROF which has an *in-vivo* equilibrium potential close to 0.0 V (Ag|AgCl), and without the use of positive bias which has a slimmest advantage over Pt in the stimulation process [8]. At high current densities more relevant factors like pore resistance and activation over-potential also play a role in the overall reduction of the charge-injection capacity of electrode relative to CSC_c [7].

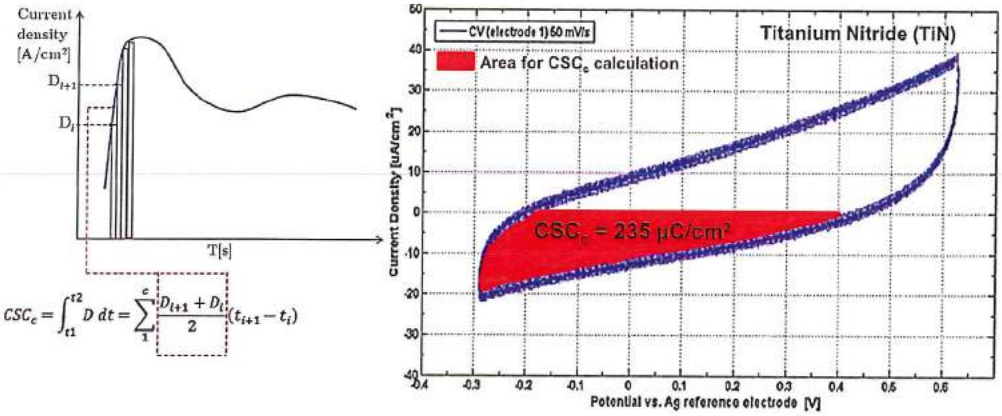

Figure 7.16 Integral calculation for CSC_c with CV of TiN in PBS at 50 mV/s. Time integral of the negative current, shown by red region of the voltammogram which represents a CSC_c of 235 $\mu C/cm^2$.

7.3.2 Electrochemical Impedance Spectroscopy (EIS)

EIS is a standard non-destructive characterisation technique used for many material systems and applications (for e.g. corrosion, plating, batteries, fuel cell etc.) This method can provide a time dependent information about the ongoing processes such as corrosion or the battery discharge process, the reactions in fuel cells, batteries or any other electrochemical process. EIS consists of the measurement of the electrical impedance and the phase angle obtained with an sinusoidal voltage or the current excitation of the electrode. The measurement usually is made over a broad frequency range (<1 Hz to 10^5 Hz), and the magnitude of the excitation is sufficiently smaller than the linear current-voltage response obtained at each frequency. For voltage excitation, the root-mean-square magnitude of excitation

source is typically 10 mV but generally not more than 50 mV [7]. EIS also referred to as AC impedance or simply Impedance spectroscopy is capable enough to distinguish between the contributions of the individual components which are investigated, for instance an approximate behaviour of the coating on the metal when immersed in salt solution can be predicted by EIS method in which a value of the resistance and the coating capacitance can be evaluated through modelling of the electrochemical data. This modelling process involves usage of electrical circuits which are built from components such as resistors and capacitors to represent the electrochemical behaviour of the coating and the metal. Any change in individual component values represent their behaviour and performance. The greatest strength but at the same moment the greatest weakness of the technique is that one can develop models that completely embed the observed behaviour without worrying about what physical processes are actually being represented. Listed below are some of the advantages and the disadvantages of this technique:

Advantages of EIS:

1. Beneficial for high resistance materials used for coatings and paints.
2. Time dependent output data is available.
3. It is an non-destructive analysing technique.
4. Makes use of the service environments.

Disadvantages of EIS:

1. It is an expensive analysis method to perform.
2. A relative complex data for quantification.

In a typical EIS experiment, an electrode (investigation material) is biased at some potential (normally an open circuit potential) and a small sinusoidal voltage is applied over a wide frequency range (10^5 to 10^{-3} Hz), therefore this is an alternating current (AC) technique. A computer system then measures and records the magnitude of the current induced by the potential and the phase angle between the potential and the current maxima. This is repeated over a range of frequencies, building sequentially a complete spectrum. EIS is normally measured using a small excitation signal. This is done so that the cell's response is pseudo linear. In a linear (or pseudo-linear) system, the current response to a sinusoidal potential will be a sinusoid at the same frequency but shifted in phase (Figure 7.17). The excitation signal is expressed as a function of time as:

$$V\left(t\right) = V_0 \, sin\left(\omega t\right) \qquad (2)$$

In a linear system the response signal $I\left(t\right)$ is shifted in phase (φ) and has a different amplitude:

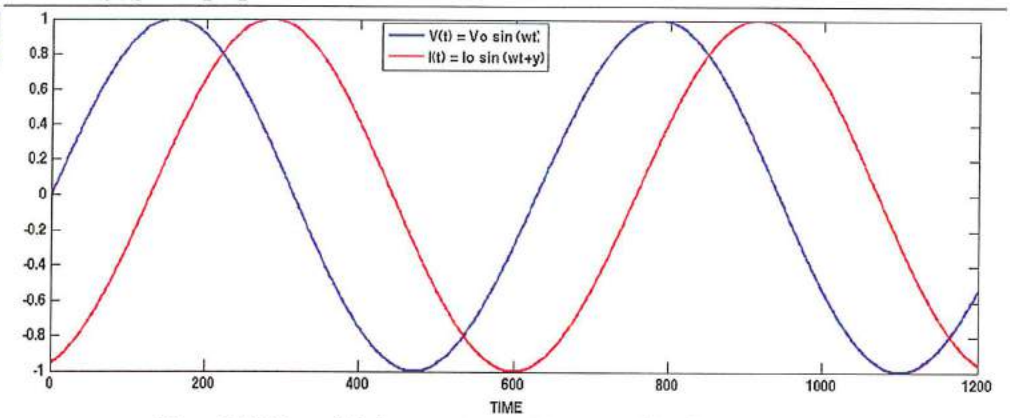

Figure 7.17 Phase shift between sinusoidal potential (blue) and current (red).

$$I\left(t\right) = I_0 \, sin\left(\omega t + \varphi\right) \tag{3}$$

An analogous to Ohms law for impedance calculation of the system is:

$$Z = \frac{V_t}{I_t} = \frac{V_0 \, sin\left(\omega t\right)}{I_0 \, sin\left(\omega t + \varphi\right)} = Z_0 \frac{sin\left(\omega t\right)}{sin\left(\omega t + \varphi\right)} \tag{4}$$

where Z is the impedance of the system. From this modified Ohms Law for AC conditions the impedance can be calculated by setting the input potential and measuring the induced current. By Euler's relation the impedance can be represented in a complex form as:

$$Z\left(\omega\right) = Z_0 e^{j\varphi} = Z_0 \left(cos\,\varphi + j \, sin\,\varphi\right) \tag{5}$$

When the phase angle (φ) between the voltage applied and the current induced is zero, then a pure resistance is present, while a phase angle (90^o) measured between the voltage and current at same frequency, gives a pure capacitance. Angles between these values gives a combination of a capacitor and resistor. Thus it is essential to plot the log of impedance (Z_0), in addition to phase angle (φ) both as a function of frequency. These are known as Bode plots. A typical example is shown in Figure 7.18 with an simple equivalent electrical circuit representing a double layer capacitance at the electrode and electrolyte interface which suits our EIS setup. It consists of a resistor and a capacitor in parallel. This circuit simulates the type of data found for our experimentation purpose. When the circuit has a maxima in the phase angle as shown in this case, it is caused by a combination of a resistance and a capacitor in parallel and referred to as a RC circuit. It also leads to models of electrochemical

interfaces. In electrochemistry, a Randle-type equivalent circuit ([9] Figure 7.18 (b)) is frequently used to model electrode/electrolyte interface. The model also referred as the double layer model where at the interface the metal in electrolyte is envisioned as a layer of ions adjacent to the electrode surface with a further layer of solvated ions further away from the surface. The two layers of ions leads to a capacitor as they store charge, called the double layer capacitance (C_{dl}) or the interfacial capacitance which is directly proportional to the effective surface area. It is usually approximated as a parallel-plate capacitor which is defined as:

$$C_{dl} = \varepsilon\varepsilon_0 \frac{A_{eff}}{d} \tag{6}$$

where ε is the dielectric constant of the medium and ε_0 is the dielectric permittivity of vacuum, d is the distance between the two charged plates or surfaces, and A_{eff} is the effective surface area. The presence of even a thin oxide film on the electrode surface can influence or sometimes even dominate the interfacial capacitance. Equation 6 holds true for an ideal capacitor which is different for the practical electrode-electrolyte interface where normally a constant phase element (CPE) is often used instead of pure capacitance. CPE is responsible for the non-ideal capacitive behaviour, the impedance for which is given as follows [10]:

$$Z_{CPE} = \frac{1}{K_{dl}(i\omega)^{\beta_{dl}}} \tag{7}$$

where i is the imaginary number, ω the angular frequency, K_{dl} is an constant, and β is a mathematic constant ($0 \leq \beta \leq 1$). For an ideal capacitor, $\beta = 1$ and K_{dl} is the capacitance [10].

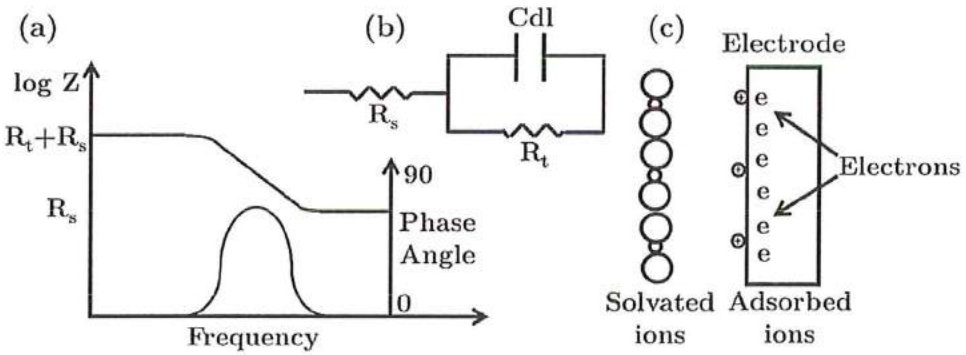

Figure 7.18 (a) A typical Bode plot example; (b) Randles electrical circuit; (c) A metal electrode in electrolyte representing a double layer model.

This double layer model also leads to a resistor as charge leaks across the capacitor (C_{dl}), called the charge transfer resistance (R_t) or the polarization resistance at open-circuit conditions which is strongly influenced by surface conditions. R_t can be obtained by electrochemical polarization and EIS measurements at the open-circuit potential (OCP). Therefore these interface (electrode-electrolyte) models are represented as a capacitor and resistor in parallel. In series with this, is a resistor representing the solution resistance (R_s) or the electrolyte resistance. This typical interface is shown along with its electrical analogue in Figure 7.18. By using the electrical circuit analogue approach, the data can be modelled to provide quantitative values for R_s, C_{dl} and R_t. R_t usually is proportional to the corrosion resistance of the electrode. The higher this value the more resistant to corrosion.

The experimental setup for EIS is similar to CV as shown in Figure 7.19. The difference is the addition of instrumentation amplifiers. These amplifiers were used in order to compensate for the high input capacitance occurring due to the NI USB-6215 DAQ module which will be effecting the measurements done at higher frequencies. The EIS experiments were performed using a electrochemical cell set up similar to the one used for CV. All EIS spectra were collected using an electrochemical interface (NI USB-6215 DAQ module) controlled by a computer comprising LabView used for excitation signal in together with frequency analysis. The external data processing and plotting was done with MatLab.

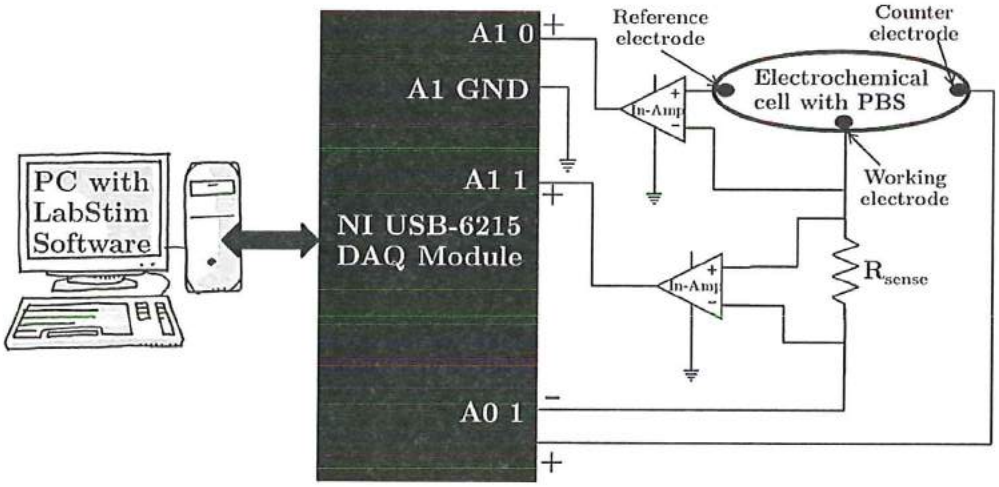

Figure 7.19 Experimental setup block diagram used for EIS measurements.

The measurements were performed at the open circuit potential over a frequency range from 1 Hz to 10 kHz. As in block diagram (Figure 7.19) a resistor (R_{sense}) is added in the to reduce the noise in the circuit. Even though this improved the SNR, but the measurements performed at lower frequencies were still affected by noise.

The perturbation amplitude is 50 mV. All the measurements were performed at room temperature. The output current signal was always checked during measurements to verify the non-linarites caused by high-amplitude stimulations. The output signal linearity was considered sufficient with the mentioned voltage amplitude.

EIS can be used to investigate both the tissue and the electrode properties. The resistive contribution of tissue conductivity to the overall electrode impedance is estimated from the impedance measured at high frequency, where the contribution to the impedance due to the charge transfer at the electrode-electrolyte interface is negligible [7]. The EIS measurements were performed on the electrode stimulation sites of various microfabricated design options. The corresponding EIS spectra for Design 1 option is shown in Figure 7.20 (b). From the magnitude plot we can observe that impedance stays more or less constant after that it has a linear decreasing trend. The maximum value of the TiN electrode impedance is 560 KΩ while the minimum is 1.7 KΩ. For the phase initially it shoots to a positive value (80^{O}) with later a dip to 40^{O} for a frequency of about 2.5 Hz it increases very quickly and gets again to a value of 80^{O} and then starts a low decline again to arrive at 60^{O} for a frequency of 10 KHz. It is worth noting here that there was no substantial difference observed in the EIS spectra of other electrode designs. The spectra of all the samples exhibits one time constant feature, and a simple equivalent circuit (Refer Figure 7.18 (b) Randles electrical circuit) explained earlier which is sufficient for modelling the electrode/electrolyte interfaces. The spectra were fitted to the equivalent electrical circuit to obtain the interfacial capacitance (C_{dl}) and the charge transfer resistance (R_t). The simulated spectra using fit parameters in comparison with the measured spectra is as shown in Figure 7.21. The results of the spectra fitting is compared to the similar spectra fitting studies done by A. Norlin *et al.* [10] in the table below:

Material	R_t (Ω/cm^2)	K_{dl} $\left(\left(\Omega s^{-\beta_{dl}}\right)/cm^2\right)$	β_{dl}
Smooth Pt [10]	7.4-8.6 × 10^5	4.3-5.7 × 10^{-5}	0.91
Smooth Ti [10]	2.3-3.4 × 10^7	1.6-1.7 × 10^{-5}	0.97
Smooth TiN on Ti [10]	2.1-5.6 × 10^7	4.7-5.5 × 10^{-5}	0.91-0.94
Rough TiN [10]	6.6-8.8 × 10^3	1.8-2.2 × 10^{-2}	0.82
TiN [this work]	6.5 × 10^3	3.5 × 10^{-8}	0.89

Table 2. Comparison of EIS spectra fitting for various metals with this work.

Cogan *et al.* [7] showed the benefit of high-charge-capacity coatings in reducing the charge-transfer resistance of electrodes by showing the Bode plots for smooth and

porous TiN electrodes in PBS electrolyte with identical shape and GSA. As seen (Figure 7.20 (a)), both the electrodes exhibit the same high-frequency impedance, whereas a marked reduction in low-frequency impedance was observed with the porous coating over a frequency range of 0.2–10^5 Hz.

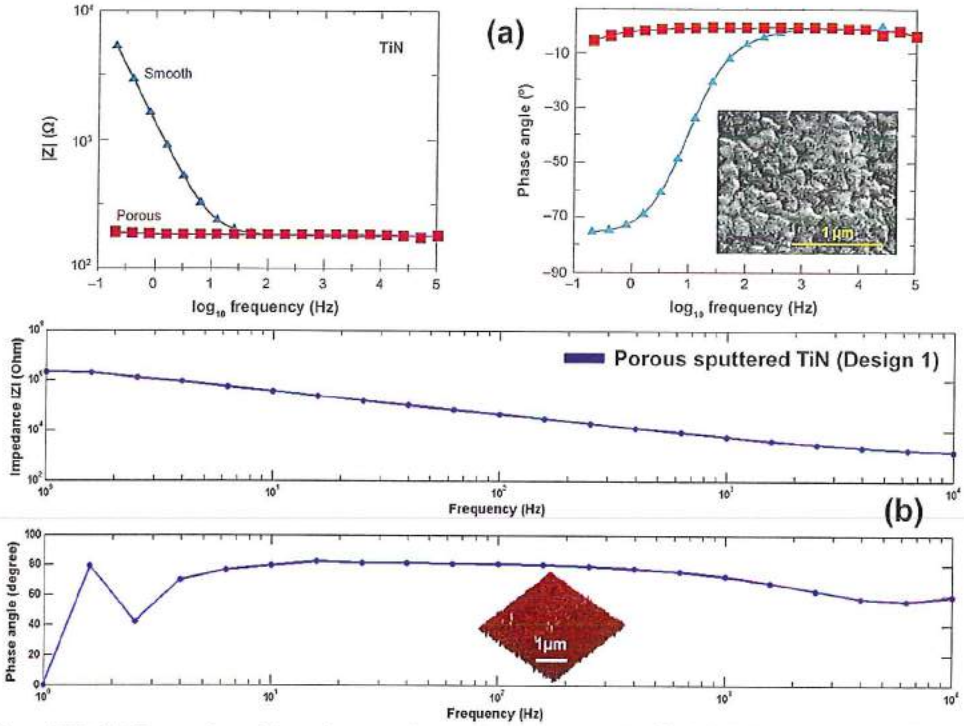

Figure 7.20 (a) Comparison of impedance with smooth and porous TiN [7]; (b) EIS spectra obtained for sputtered TiN for electrode of "Flexi-Stiff" MEA.

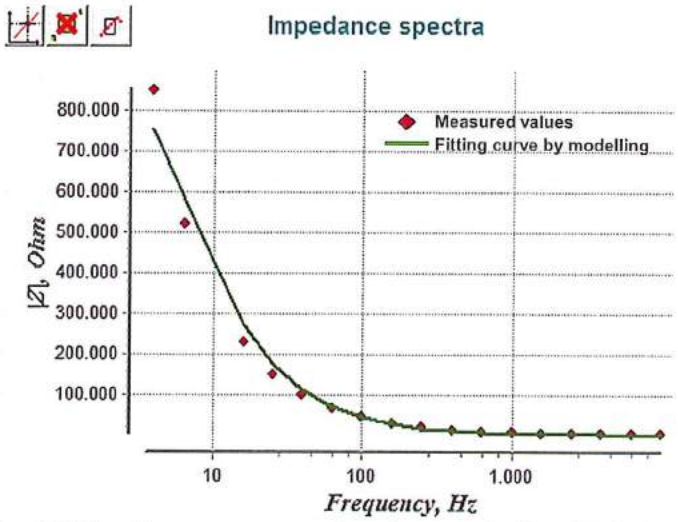

Figure 7.21 Impedance spectra comparison of measured and modelled values.

The porous film exhibits a near-resistive phase angle (approaching 0^{o}) and an impedance modulus (|Z|) which is almost the entire solution resistance [7]. Our obtained EI spectra from the EIS experiments was in accordance with the findings from Cogan *et al.* The electrode surface roughness and porosity results in an non-ideal capacitive behaviour explained by Equation 7. This is due to the increased surface area of the electrode causing increase in the double layer capacitance (C_{dl}). On the other hand, due to the solution impedance which is present inside the porous structure does not allow the high frequency AC signals to reach thus resulting in lower penetration depths in comparison to the low frequency ones. In the absence of faradaic reactions, for porous electrodes the geometric factors such as pore size, depth and pore size distribution are important ones which have an influence on the total impedance [10]. The total impedance also referred as electrode impedance, has to be designed as low as possible during the neural stimulation and recording process. During a neural stimulation process when high impedance electrode are been used, then in order to reach a sufficient current density it is necessary to apply a high-amplitude voltage which might result in extreme harmful reactions in the near vicinity of the cells [11]. In performing high impedance electrode recordings a high Johnson (i.e. thermal) noise is generated which decreases the capacity for current injection in stimulation resulting in a low signal to noise ratio (SNR) [12,13]. This thermal noise shows an relation to the electrode impedance by Nyquist equation[14]:

$$V_{th}^2 = 4kTBR(V) \qquad (8)$$

where, k is the Boltzmann constant (1.38×10^{-23} JK^{-1}), T is the temperature (Kelvin), B is the bandwidth (Hz) and R is the real part of the electrode-electrolyte impedance (Ω) [14].

7.3.3 Voltage Transients

Normally voltage transient (VT) measurements are used to evaluate the maximum charge that can be injected in a current-controlled stimulation pulse. It is been used to study the response of the nerve fibres to a variety of stimulus waveforms by investigating the generation of action potentials caused by the stimulation process. These VT measurements are measured in a standard three electrode electrochemical setup with the help of a large-area return electrode and a noncurrent carrying reference electrode. Analysis of this voltage transients is done to define the maximum polarization, both the most negative (E_{mc}) and most positive (E_{ma}), across the electrode-electrolyte interface. Further these positive and negative potentials are compared with the established maximum potentials (listed in Table 3

are potential limits for typical stimulation material [7] which are typically water oxidation and reduction potentials) beyond which it is considered unsafe to polarize the electrode.

Material	Mechanism	Maximum Q_{inj} (mC cm^{-2})	Potential Limits V versus Ag|AgCl	Comments
Pt and PtIr alloys	Faradaic/capacitive	0.05–0.15	−0.6–0.8	
Activated iridium oxide	Faradaic	1–5	−0.6–0.8	Positive bias required for high Q_{inj}. Damaged by extreme negative potentials (<−0.6 V)
Thermal iridium oxide	Faradaic	~1	−0.6–0.8 V	Positive bias required for high Q_{inj}
Sputtered iridium oxide	Faradaic	1–5	−0.6–0.8 V	Benefits from positive bias. Damaged by extreme negative potentials (<−0.6 V)
Tantalum/Ta_2O_5	Capacitive	~0.5		Requires large positive bias
Titanium nitride	Capacitive	~1	−0.9 to 0.9	Oxidized at positive potentials
PEDOT	Faradaic	15	−0.9 to 0.6	Benefits from positive bias

Table 3. Charge-injection limits of electrode materails (*Adapted and reprinted from Cogan et al.)* [7].

For the calculation of E_{mc} and E_{ma} different elements have to be considered which can be listed in summation formula for VT (ΔV) as:

$$\Delta V = i_c R_i + \eta_c + \eta_a + \Delta E_o \qquad (9)$$

where, ($i_c R_i$) is the ohmic voltage drop, in which i_c is the ionic conductivity of the electrolyte and R_i is the electrolyte resistance, η_c is the concentration over-potential which is related to the transport of the electroactive species (reactants or counter-ions) causing a concentration gradient between the electrode surface and the bulk electrolyte, η_a is the activation overpotential which is nothing but the voltage drop at the electrode-electrolyte interface necessary to maintain a net current flow

when the current is provided by reduction or oxidation reactions and ΔE_o is the equilibrium potential shift of the electrode [7].

From these parameters, η_c, η_a and ΔE_o are the time dependent parameters out of which η_a and ΔE_o only contribute towards the polarization across the electrode-electrolyte interface (ΔE_p). This ΔE_p is relative to the potential of the electrode at the start of the current pulse (the inter-pulse potential that determined E_{mc} or E_{ma}. Thus, for a cathodal current pulse [7]:

$$E_{mc} = E_{ipp} + \Delta E_p = E_{ipp} + \left(\Delta V - V_a\right) \qquad (10)$$

where the value of access voltage V_a can be taken either immediately after the current pulse or as the near instantaneous voltage change onset of the current pulse. V_a could be included over potential terms as well as the electrolyte $i_c R_i$ drop, and this takes an approximation into the value of ΔE_p. Based on these theoretical findings from Cogan *et al.* VT measurements with the subsequent calculations for charge injection capacities for different microelectrodes of the "Flexi-Stiff" MEA.

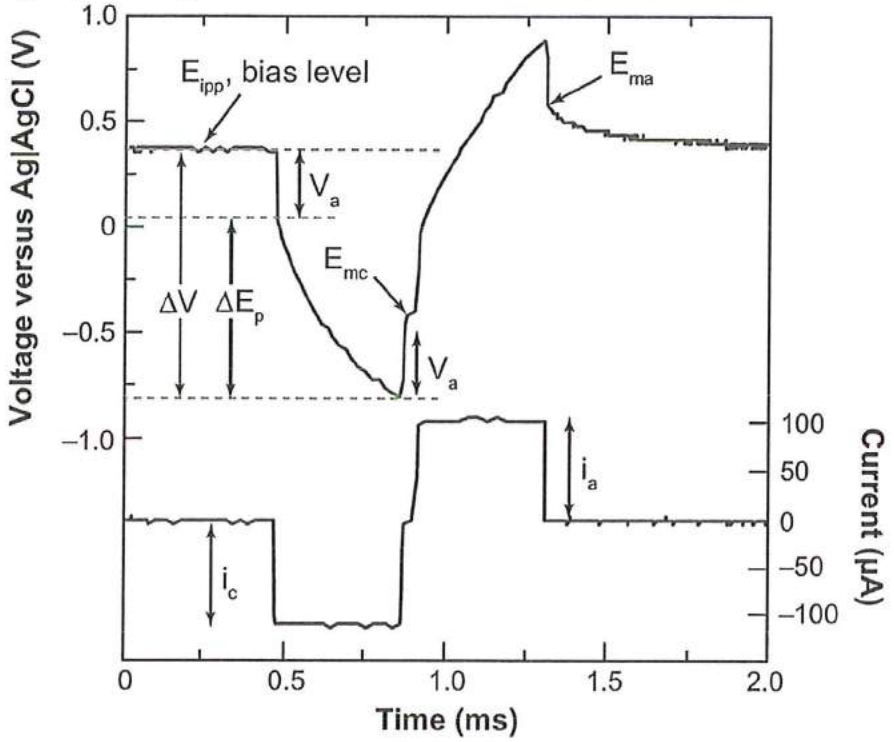

Figure 7.22 VT of AIROF microelectrode in response to biphasic pulse [7].

7.3.3.1 Charge injection capacity (Q_{inj}) of TiN microelectrodes.

Charge injection capacity (Q_{inj}) determination was done in a similar way by T. Rose and L. Robblee *et al.* [15]. In this method application of current pulses with different amplitudes to the electrode were done and simultaneously the potential was measured over time. With the help of determining the maximum current density for which the electrode potential remains within the reversible range, the charge injection capacity can be calculated by multiplying the current density with the pulse width. In our experimentation for TiN the reversible limits was taken between – 0.8 V and + 0.8 V vs. Ag|AgCl which is below the established maximum potentials as specified by Cogan *et al.* (refer Table 3).

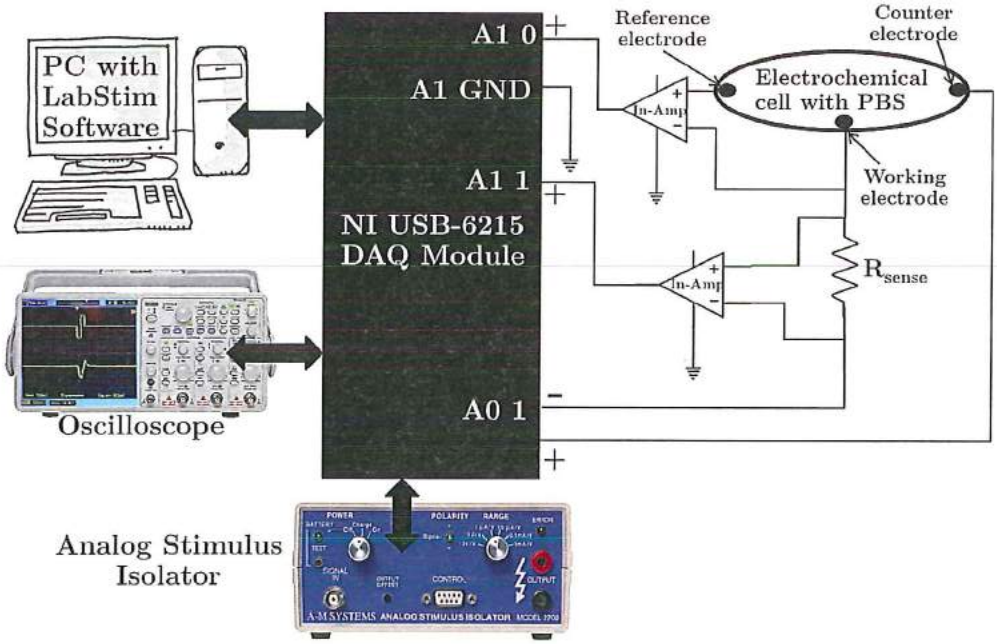

Figure 7.23 Set-up for VT and to determine charge injection capacity.

The measurement system is similar as used for CV and EIS measurements with additional components as shown in Figure 7.23. The stimulation signal is generated by a stimulator program (LabStim). The stimulator, biphasic, cathodic-first, square pulses with various current amplitudes between 1 µA and 5 mA and pulse widths between 10 µs and 500 µs could be generated. The three electrode electrochemical setup was similar to CV and EIS experimentation. The potential at the working electrode ("Flexi-Stiff" MEA) with respect to reference electrode (RE: Ag|AgCl electrode) was recorded by an amplifier and displayed by a digital oscilloscope (DSO1004A, Agilent Technologies). The oscillator was synchronous with the

stimulator. The measurement data was transferred to PC for further processing. The recorded potentials were corrected for the potential ohmic voltage drop ($i_c R_i$) in the electrolyte (as mentioned in Equation 6) [15]. The electrolyte resistance (R_i) was calculated by [16]:

$$R_i = \frac{\rho_E}{4r} + \frac{\rho_E h}{\pi r^2} + h_a \frac{\rho_E}{r} \qquad (11)$$

where, r is the radius of the electrode, h is the recessed electrode height inside the PI structures, ρ_E is the electrolyte conductivity (72 Ωcm [17]), and h_a is a correction factor (0.01 [16]). For $r = 200$ µm, $h = 10$ µm, value of $R_i \approx 995$ Ω was found for our situation. The stimulation electrode sites ("Flexi-Stiff" devices) were subjected to biphasic, cathodic-first square pulses and the potential response over the time was recorded. Figure 7.24 shows the excitation signal (a) and the corresponding potential response (b) of sputtered TiN metal microelectrode (Design 3 of the "Flexi-Stiff" MEA) for current pulses with a pulse width of 300 µs and with various amplitudes. It can been seen from the results that with the increasing current amplitude, the potential excursions become larger. In order to determine the charge injection capacity (Q_{inj}) of microelectrode material, the maximum and the minimum values for the electrode potential (refer Figure 7.24 (b)) were plotted versus the charge injected during a single pulse (i.e. the applied current amplitude multiplied by the pulse width). For 4 different designs of different surface areas the respective plots are shown in Figure 7.24 for a pulse width of 300 µs. Furthermore the established potential limits or in other sense the water windows (+ 0.9 V to − 0.9 V), brown dashed lines) for TiN from Table 3 and the considered ones in our experimentation case (+0.8 V to − 0.8 V, pink dashed lines) are shown in the plot. From Figure 7.25, the charge injection capacity can be predicted from the intersection points of the potential lines with the maximum and minimum safe potential limit lines (brown dashed lines). For our sputtered TiN metal for design 1 and design 7 the potential does not leave the upper and lower water windows but for design 3 and design 6 the potential leaves the reversible range at the lower limit rather than the upper potential limit. By linear interpolation, the following values concerning the Q_{inj} for 300 µs for our sputtered TiN is listed as below:

- Q_{inj} for Design 1 (Ø 0.04 cm) : 27 µC/cm²
- Q_{inj} for Design 3 (Ø 0.02 cm) : 95 µC/cm²
- Q_{inj} for Design 6 (Ø 0.018 cm) : 82 µC/cm²
- Q_{inj} for Design 7 (Ø 0.016 cm) : No intersection was observed.

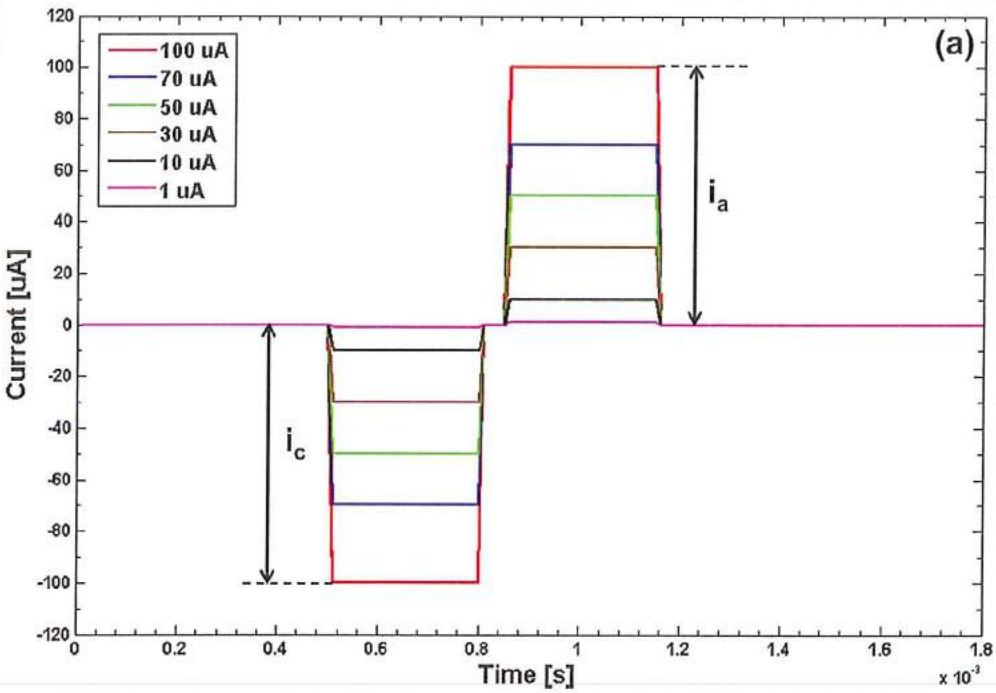

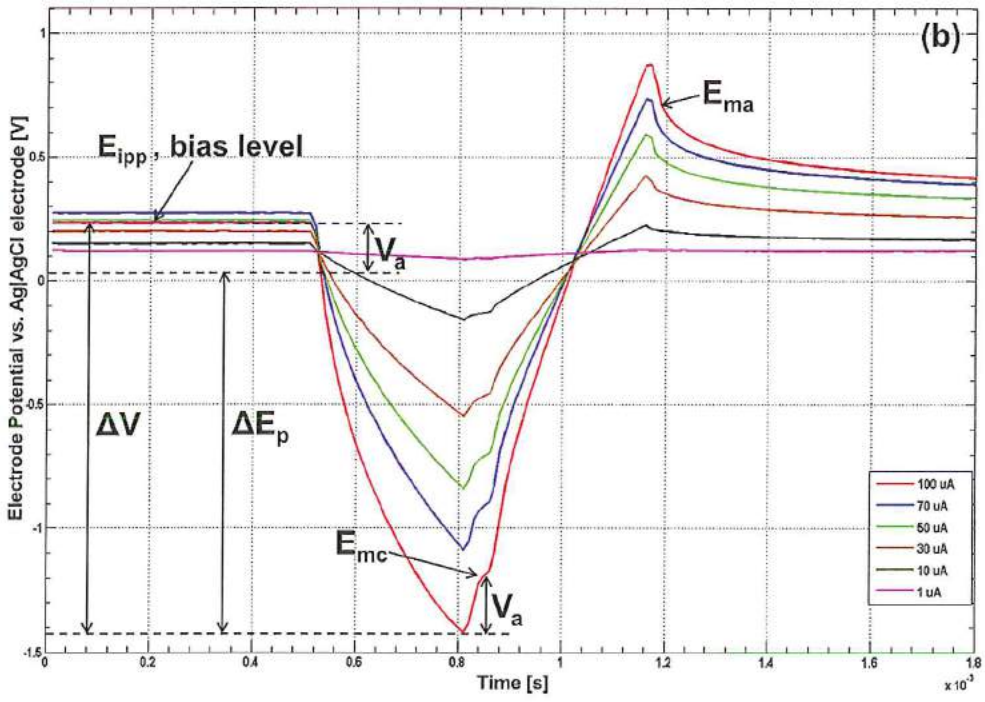

Figure 7.24 (a) Excitation signal (a biphasic pulse); (b) Potential response measured at electrode (TiN) site for various amplitudes (pulse width 300 µs).

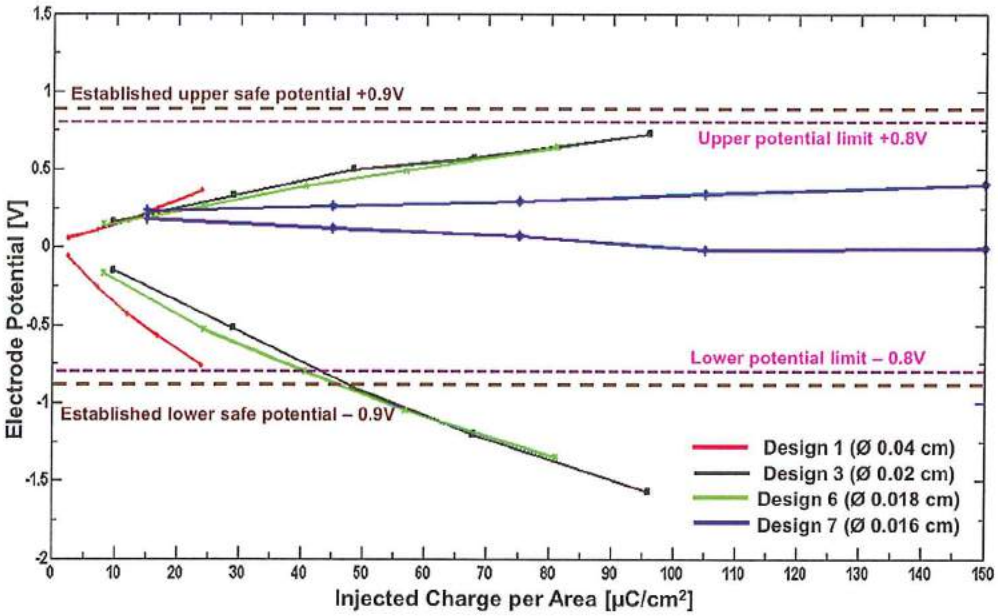

Figure 7.25 Electrode potentials for stimulation pulses (300 µs pulse width) of various amplitudes versus injected charge for TiN; charge where the potential leaves the reversible potential limits is called the charge injection capacity.

7.3.3.2 Dynamic range, safe limits for TiN and discussions.

One of the main advantage of the "Flexi-Stiff" MEA design is the greater number of closely spaces and smaller sites which can be implanted deeper inside the cochlea. It is well known that the total charge is the main factor causing the neural activation by electrical stimulation via. the electrode stimulation site [18]. On the other hand, the tissue damage caused due to the neural stimulation process depends on both the total charge dissipated and the charge density (i.e., total charge/surface area) [19]. A multi-study comparison done by Mc-Creery *et al.* [19,20] has provided a "threshold" for a tissue damage that can be modelled with a simple equation stated by R. V. Shannon [21] as follows:

$$log\left(D\right) = k - log\left(Q\right) \qquad (12)$$

where D is the charge density in µCoulomb/cm²/phase, Q is the charge in µCoulomb/phase and k is defined as a safety parameter with different changing lines as shown in Figure 7.26. When $k = 2$, the straight line falls in an area where the damage was observed. If this line is used to define the limit of safe stimulation, some stimuli would be expected to cause the damage to the stimulating tissue. The

curve for $k = 1.5$ defines a set of parameters where no damage was observed and is used for computations that follow [21]. Approximately similar activation levels (i.e., total charge) except Design 1 was observed for the remaining designs (Design 3, 6 and 7) of the fabricated "Flexi-Stiff" MEA. As stated by researchers [19,22] that greater tissue damage at much lower current levels can occur for the smaller electrode surface areas which leads to higher charge density values. Figure 7.27 shows the modelled charge per phase versus charge density per phase for different design option stimulation of the "Flexi-Stiff" MEA using Equation 12 derived by Shannon [21]. The measurements were done at a pulse width of 300 µs/phase.

The limits of safe stimulation were approximated by the thick dashed dark blue line (k =2). Although the Shannon model is based on specific stimulation parameters and brain regions, needs to be interpreted with carefulness [22], it still provides us with a reasonable approximation to compare the safety limits for electrodes of different dimensions. For our "Flexi-Stiff" MEA designs the stimulation levels fall under the non-damaging zone thus ensuring a safe stimulation process which can be stimulated safely for a 300 µs/phase pulses. For different designs following are the values predicted from the plots:

- For Design 1: charge: 0.00339 µC and charge density: 25 µC/cm^2
- For Design 3: charge: 0.005402 µC and charge density: 95 µC/cm^2
- For Design 6: charge: 0.0056532 µC and charge density: 81 µC/cm^2
- For Design 7: charge: 0.1884 µC and charge density: 150 µC/cm^2

The charge density values predicted above were also in line with the values found out in section 7.3.3.1. Thus it is apparent that the total charge range for our "Flexi-Stiff" MEA stimulation from threshold value to this safety limit is within the dynamic range and is much smaller than the normal stimulation.

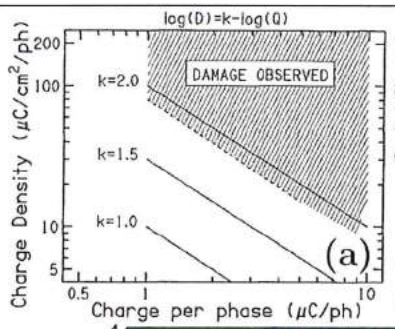

(a) "Shannon plot" with different safety lines (k = 1, 1.5, 2) defining limits of safe stimulation with damage observed zone.

(b) Studies performed by S.F. Cogan on different materials and it's depiction on "Shannon plot".

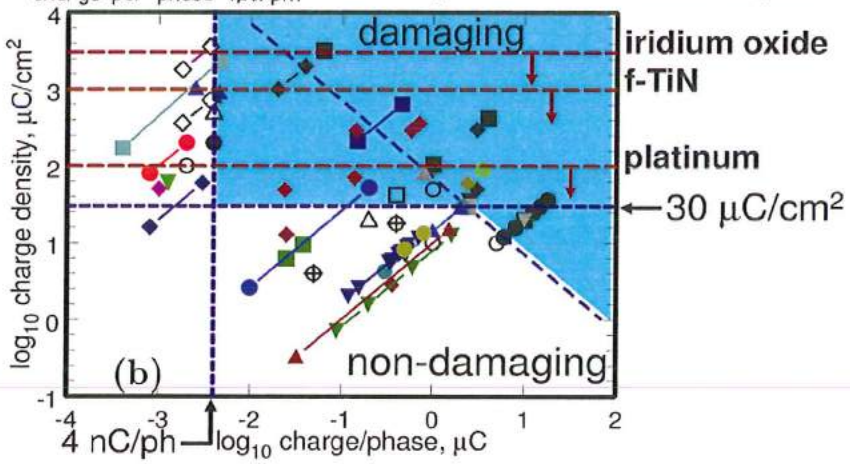

Figure 7.26 (a) Shannon plot showing damage and undamaged areas in neural stimulation [21]; S. F. Cogan's findings for stimulation materials.

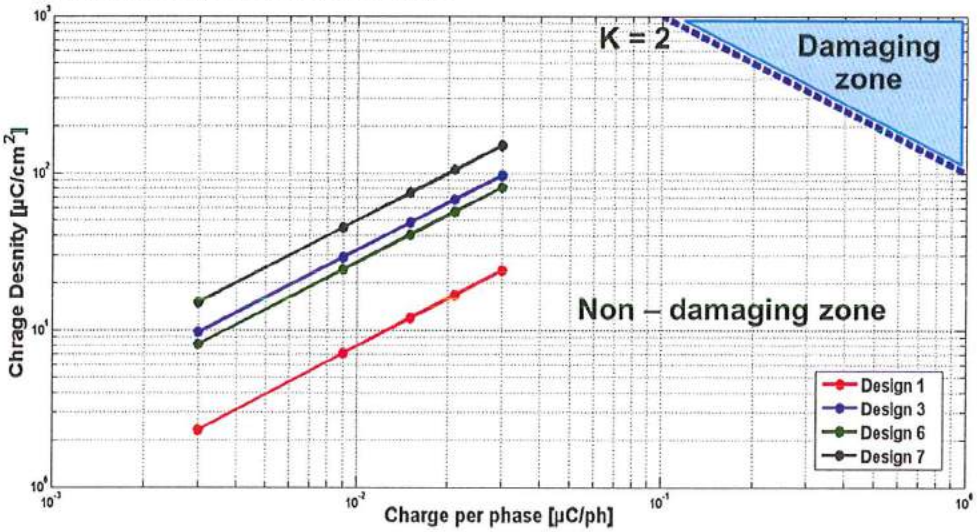

Figure 7.27 Modelled safe stimulation parameters for various "Flexi-Stiff design. Stimulation above the thick dashed dark blue line ($k = 2$) has been shown to induce the tissue damage and varies in proportion to the total charge and charge density per pulse phase. The various colour lines refer to different design options of the "Flexi-Stiff" MEA showing how the charge density changes with increasing charge per phase for a pulse width of 300 μs/phase.

7.4 *In-vivo* experiments, measurements and results

Before its use in human beings, a medical device has to undergo animal experiments (*in-vivo*) to demonstrate its capability and suitability, after a thorough *in-vitro* experimentation. *In-vivo* experiments are the implantation and testing of the fabricated MEA in living animals. *In-vivo* facilitates the use of functional anatomy, the environmental conditions (in our case exposure to perilymph fluid of the cochlea) and the means to test the actual function of the device. Also in our case is to elicit a neural response of the auditory nerve and measure it back intra-cochlear means. All the *in-vivo* experiments were carried out at Leiden University Medical Centre by Johan J. de Vos, who provided all the data described below.

7.4.1 Electrically evoked Compound Action Potential (eCAP)

Clinicians and audiologists are interested in measuring the electrically evoked responses of the auditory system, which provide information on the auditory nerve status, thus helping the clinician in the fitting procedure of the CI's speech processor. A commonly referred measurement is the electrically evoked auditory brain stem response (EABR). In EABR a series of potentials are recorded with scalp electrodes occurring within 10 msec after onset of a pulsatile stimulus. This response represents synchronized activity of fibres of the auditory nerve and brain stem nuclei [23]. More recently, attention has focused on the recording of electrically evoked compound action potentials (eCAPs) due to the introduction of Neural Response Telemetry (NRT) by Cochlear Ltd. (Sydney, Australia) and Neural Response Imaging (NRI) by the Advanced Bionics corporation (Sylmar, CA, USA). These systems facilitate easy acquisition of the eCAP through the CI system without the need of extra recording or stimulating electrodes such as a trans-tympanic needle [24]. The auditory CAP is commonly referred from the acoustically evoked equivalent, which is called the electrocochleogram. This is a common and reliable clinical practice to measure a frequency specific objective audiogram [24]. Compared to EABR and other methods for measuring neural responses to electrical stimulation, the eCAPS have several benefits. The eCAPs are recorded from electrodes positioned close to the nerve, eCAPs have relatively large amplitude [25]. The eCAPs can be recorded using an electrode positioned directly on the exposed nerve in research animals or through intracochlear recording sites in cochlear implant patients [23], thus not requiring any additional recording equipment or electrodes. Also this measurement does not have a negative influence of any nearby muscle activity, enabling to record in non-sedated patients.

A commonly used eCAP measurement method is the Amplitude Growth Function (AGF). In an AGF eCAP responses is measured with increasing stimulus amplitudes which are respectively plotted versus the corresponding stimulus level. The minimal current to evoke a neural response can be derived by using a linear fit through the eCAP amplitudes Figure 7.28. The AGF can be used to calculate threshold levels for cochlear stimulation. Besides threshold levels, eCAP measurements can also be useful to determine the functioning of the electrode and neural survival [26].

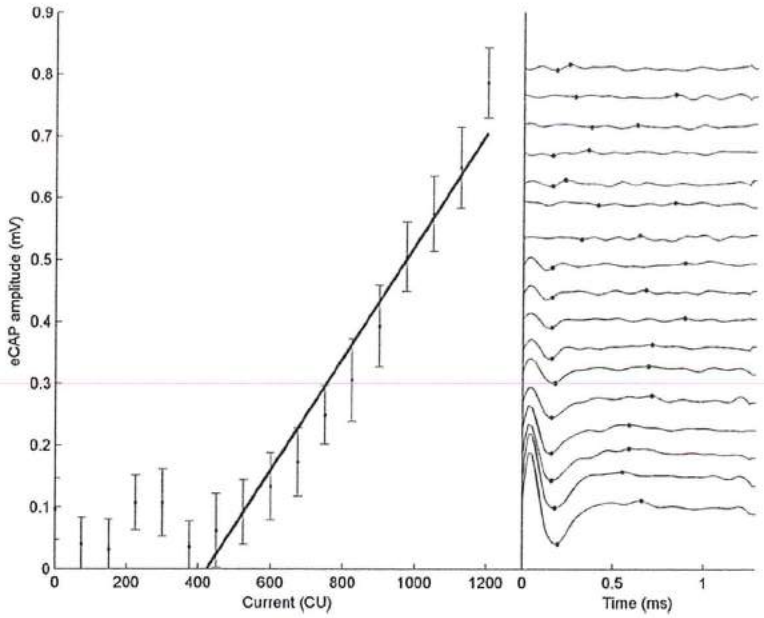

Figure 7.28 Amplitude Growth Function (left) with corresponding eCAP recordings (right). These eCAP responses are measured in a human patient by use of increasing stimulus amplitudes. By plotting the eCAP amplitudes against the stimulus levels, the eCAP thresholds can be predicted by use of a linear fit. (*Image courtesy: J.D. Biesheuvel, LUMC Leiden*).

7.4.2 *In-vivo* animal experimentation

For the animal experiments performed at LUMC, Guinea Pigs (*Cavia porcellus*) were the chosen animal model, since Guinea Pigs are commercially bred and available for experimentation and easy to handle. The hearing range of Guinea Pigs is relatively similar to humans, which is important for testing within the frequency range. Additionally, the cochlea of a Guinea Pig is embedded in a large air-filled bulla, which permits easy access to the cochlea and round window Figure 7.29. Apart from these benefits, the Guinea Pig animal model has some limitations in shape and structure of the cochlea, which has more turns than a human cochlea (4 turns in Guinea Pigs versus 2.5 turns in humans) and the diameter of the cochlea, which is

narrower than that of humans (< 0.5 mm), in particular after the first basal turn. Measured eCAP amplitudes are dependent on the relative position of the intracochlear electrodes used for recording and stimulation. In our setup we can simultaneously measure at multiple stimulating electrodes, which will provide information about the generated eCAPs at different sites in the cochlea.

When measuring the neural responses of the auditory nerve in patients with Cochlear Implants (CI's), the implanted electrode array from the CI is used both for stimulation and readout. By using the "Flexi-Stiff" MEA design, in which the stimulation electrode is placed alongside the recording electrode, measuring eCAPs at the exact site of stimulation is possible. The details of the "Flexi-Stiff" MEA design which was used during our *in-vivo* experiments is as shown in Figure 7.29. The MEA was implanted in anesthetized guinea pigs, in conjunction with a stimulator and amplifier circuit.

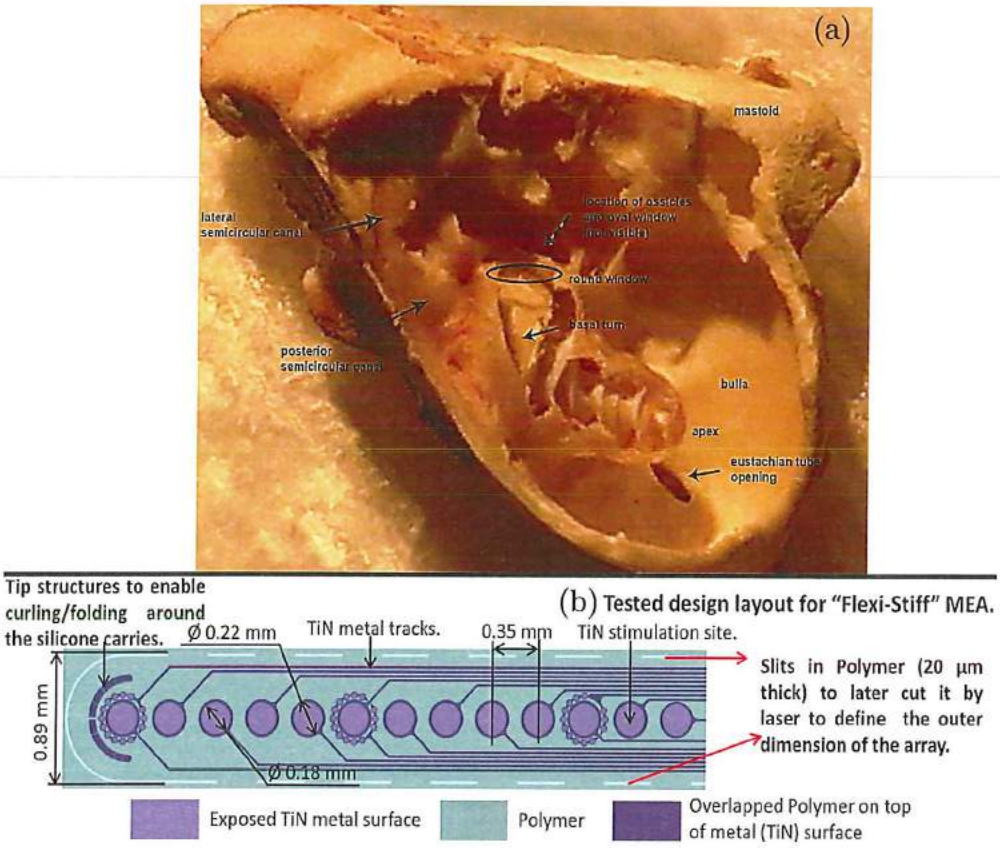

Figure 7.29 (a) Right side of the Guinea Pig bulla surrounding the cochlea, opened by use of a ball drill (*Image courtesy: J.J. de Vos, LUMC Leiden*); (b) CAD image of the flexible part of the "Flexi-Stiff" MEA design been used for *in-vivo* experimentation.

7.4.3 Experimental procedure and measurements

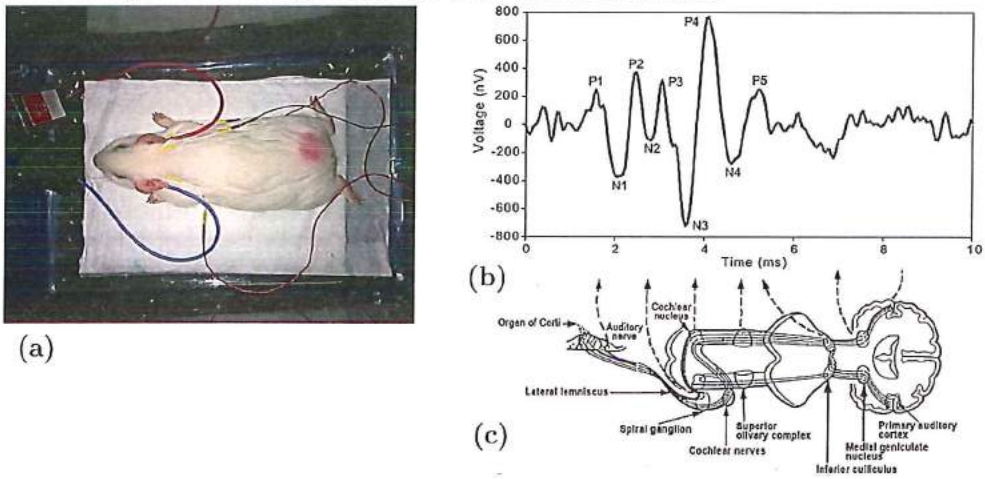

Figure 7.30 (a) Guinea Pig with electrodes attached for ABR measurements (*Image courtesy: J.J. de Vos, LUMC Leiden*); (b) Typical waveform (12 kHz, 80 dB SPL) showing peaks (P1: Auditory nerve; P2: Spiral Ganglion; P3: Cochlear Nucleus, P4: Sup Olivary Complex; P5: Inferior Colliculus-Brainstem) [40]; (c) Signal travel path from auditory nerve to the primary auditory cortex (*Image courtesy: Open access).*

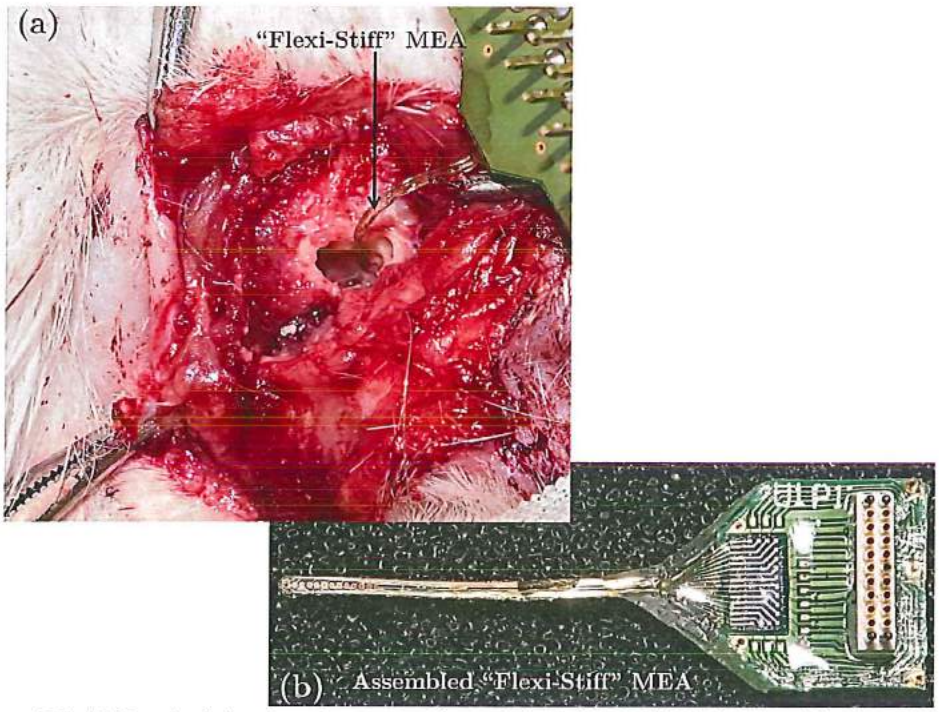

Figure 7.31 (a) Round window insertion, *in-vivo* of one of the "Flexi-Stiff" MEA device; (b) Image of the completely assembled and packaged "Flexi-Stiff" MEA device with a smaller PCB before *in-vivo* experimentation (*Image courtesy: J.J. de Vos, LUMC Leiden*).

For *in-vivo* experiments 6 female albino guinea pigs (strain: Dunkin Hartley; Harlan Laboratories, Horst, The Netherlands) weighing 250-600 grams were used. All animal procedures were approved by the Animal Ethics Committee of the LUMC (DEC LUMC nr. 13221). ABR measurement were used to objectively test acoustical hearing (hair cell function). For each ear, a click or tone burst at different frequencies is administered by ear inserts at the measured ear. By placing electrodes on the scalp, the small neural response from each part of the auditory pathway is measured. By use of this technique, processing of acoustical input by the auditory pathway can be measured Figure 7.30 (b).

After a minimal period of two weeks for acclimatization at the Animal Care Centre of LUMC the animals were measured with an ABR measurement to verify normal hearing in both ears. Only animals with normal hearing results (less than 50 dB SPL loss) were included. The ABR equipment consisted of NI LabView® (National Instruments corporation) based software in combination with a NI USB-6215 multifunction DAQ device, a DAM-80 differential amplifier (World Precision Instruments) a SA1 stereo amplifier (Tucker Davis Technologies, Alachua, USA) and ER-2 insert earphones (Etymotic Research inc.). The details of the ABR measurements, deafening procedure used along with the implantation and the animal monitoring procedure are explained in the Appendix section.

7.4.3.1 Electrophysiological measurements and preliminary results.

A system setup containing a NI USB-6215 multifunction DAQ device (16-bit), optically isolated voltage to current converter, "Flexi-Stiff" MEA design with small PCB and an instrumentational amplifier were used. The system was controlled by NI Labview based programming software (LabStim) developed by J.J. de Vos and J. Koolwijk. Biphasic pulses with a phase duration of 32 µs were used for stimulation. Every measurement (sweep) was repeated 200 times for noise reduction (averaging). Artifact rejection was performed by using the forward masking paradigm [27]. The forward masking paradigm consists of three frames containing a masker and probe stimulus. The details of this forward masking is explained in the Appendix.

Experiments were conducted with the implanted small pcb MEA for stimulation in combination with a platinum ball electrode for measurements as well as stimulating and measuring back with the MEA. The ball electrode was placed at the entrance of the round window (extracochlear). For intracochlear stimulation with the MEA, electrode 2 was used (this was the most deeply inserted functional electrode) and for measuring we used electrode 4, keeping some distance to the stimulating electrode. The first pilot *in-vivo* experiments gave us information about basic functioning of the measuring system and the MEA device behaviour *in-vivo*. The data discussed is preliminary and more measurements are necessary for definitive

conclusions. eCAP measurements with small PCB MEA: We were able to stimulate and measure a neural response by use of the MEA device. Stimulation on electrode 2 and measurement on electrode 4 at increasing current levels provided us with eCAP curves Figure 7.32.

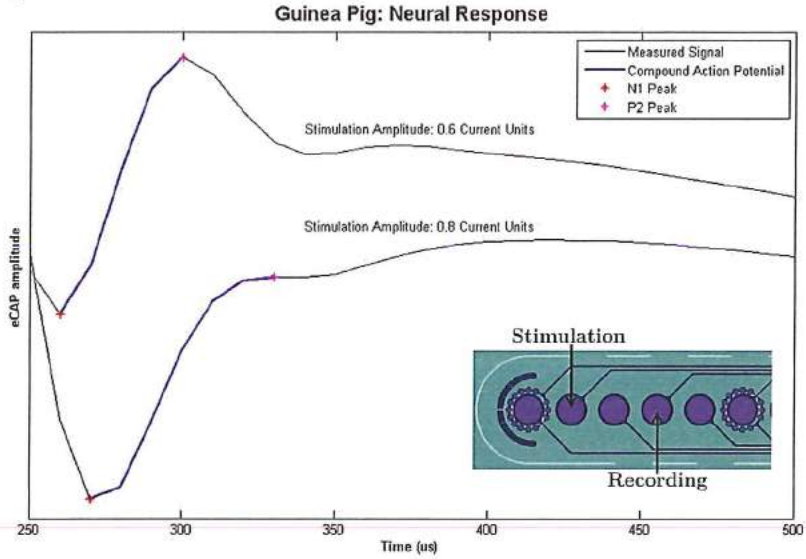

Figure 7.32 eCAP curves measured at 2 different stimulus amplitudes. Stimulation was performed at electrode 2 of the MEA device, the neural response is measured back at electrode 4 of the MEA device (*Image courtesy: P. S. Boot and J.J. de Vos, LUMC Leiden*).

7.4.3.2 MEA delamination and deterioration.

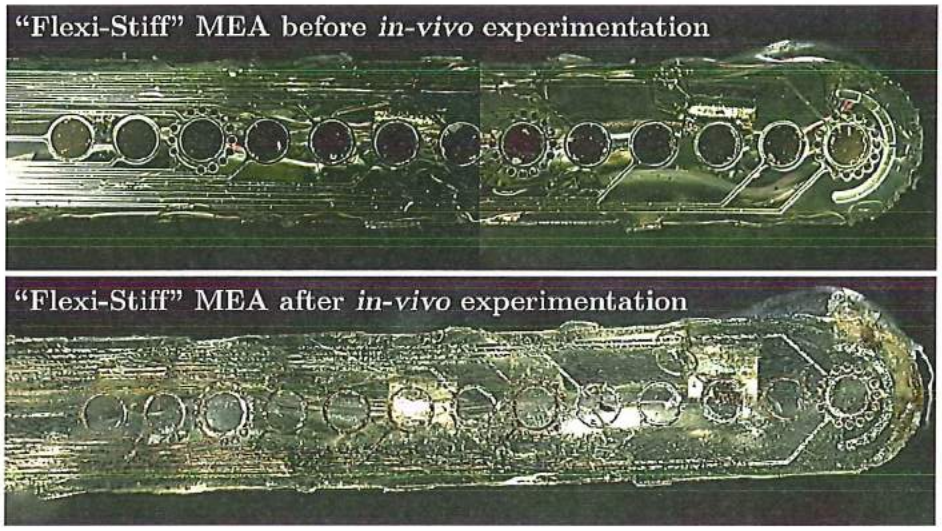

Figure 7.33 High-resolution part images of the "Flexi-Stiff" MEA before and after three implantation and stimulation sessions (*Image courtesy: J.J. de Vos, LUMC Leiden*).

The flexible part of the "Flexi-Stiff" MEA which was used in our *in-vivo* experimentation with Guinea Pigs encountered delamination from the Silastic carrier and stimulation metal deterioration after the measurement process as seen in Figure 7.33. This examination and analysis was done with the help of a high-resolution microscope, when the device showed a malfunction after three *in-vivo* round window insertions followed with multiple stimulation and measurement sessions.

7.4.4 Discussion and future scenarios

"Flexi-Stiff" MEA was used for neural stimulation and measurement, however, more work is required to obtain enough eCAP data to calculate a reliable Amplitude Growth Function (AGF). Also due to the drawbacks in the measuring hardware in combination with deterioration of the MEA device after successful implantations posing limitations on our measurement session. In Guinea Pigs, due to the closer proximity of the neural tissue (because of a smaller anatomy than humans), the neural response is measured closer to the stimulus artifact. Therefore a proper artifact reduction method is necessary. During the measurements we used the forward masking artifact rejection method (Refer Appendix for details). However, a significant part of the artifact was still present in the resulting graphs, forcing us to remove the first part of the graph (also the first part of the eCAP signal). Another challenge is the duration of the stimulus artifact, which is longer than desired because of the long saturation time of our amplifier. By using a different amplifier in combination with use of a compensation method [28] we hope to solve this problem.

The MEA deterioration caused during the *in-vivo* experimentation performed on Guinea Pigs opens discussions for referring back to the microfabrication process of building different thin film metal and polyimide layers. A likely reason for the delamination of the Silastic carrier from the flexible part of the MEA device is the poor adhesion between the silastic carrier and the polyimide (PI2611) from the glue (MED-2000 NulSil Silicone technology) used to adhere these two materials. Also an adequate curing process might affect the adhesion between these two surfaces. The stimulation metal (Ti+TiN) deterioration at some places is due to loose adhesion between the adhesion layer (Ti in our case) with the underneath polyimide layer. This adhesion might be due to the mechanical type of adhesion mechanisms (Figure 6.17) between two binding surfaces as explained in section *6.5.2.2* of chapter 6. In order to improve the adhesion between these two binding surfaces, an intermediate adhesion layer which either has a chemical bond or an interdiffusion layer based on diffusive principle (Figure 6.17) may be used. Various adhesion improvements are also described in detail in chapter 6, but the most promising one researched by Ordonez *et al.* [29] where Silicon carbide (SiC) is used as an interdiffusion layer

between Platinum (Pt) and PI to establish a chemical bond for their retinal implant application. By various long term studies (more than 6 months) [30] and experiments [31] carried, concluded that adhesion between PI and SiC is achieved by carbon bindings and not through oxide formation (which is in our case) and that the chemical adhesion of PI to SiC deteriorates only at a minimal rate [29].

The first *in-vitro* and *in-vivo* measuring sessions with the "Flexi-Stiff" devices provided us with the information about device functioning, measuring system setup, *in-vivo* implantation and processing of the measured data. Based on this information, we propose several improvements and additions to the current hardware and measuring protocol.

1) **Upgraded measuring hardware:** The currently used measuring system is based on a conventional low cost equipment to insure compatibility for testing the basic functioning of the MEA. The system requires an upgrade with new components, providing less signal interference and the possibility for a multi-channel measurements. A newly developed neural stimulator circuit developed at TU Delft by Ngamkham *et al.* [32,33] in combination with the MEA will provide us with the freedom of increased number of available channels. Additionally the usage of a newly developed neural amplifier for higher dynamic range will enable our neural response measurement through the stimulus artifact [34].
2) **Improved artifact rejection method:** In our experimentation we used an artifact rejection method with an forward masking (mp3) paradigm [35]. Next steps here are to improve the stimulus programming for the accuracy of measured frames. Besides the mp3 method, other improved versions of the mp3 protocol are proposed [36]. Using these methods in combination with MEA is the possible future step. An evident difference is between the cathodic-first and anodic-first forward masking artifact rejection [37], which has not been a part of our experiments until now. Future work will include cathodic-first and anodic-first forward masking in our next experiments.
3) **Optimizing the eCAP measurements:** Currently, animal experiments are being conducted with the goal to improve overall eCAP measurements by using different numbers of sweeps, inter pulse intervals (IPIs) and by looking at different artifact rejection methods. Based on this data, we want to extent the measurements to our animal model in conjunction with the MEA device.
4) **Different MEA designs:** In our *in-vitro* experimentation, various MEA design configurations were tested out to identify stimulation differences. However, for our *in-vivo* measurements only one type of MEA design (refer Figure 7.29 (b)) with one carrier design was used. The next goal here would be to use different MEA design configurations consisting of various electrode stimulation site shape and sizes along with new carriers for smoother insertion/implantation. By doing

so we will be able to gather information on the optimal size and shape of the electrodes for the stimulation and recording purposes. This aspect of the MEA can be used as a design tool to develop future MEAs.

5) **Impedance measurement by electric field imaging (EFI):** As described earlier, the CI electrode array consisting of multiple electrodes, each stimulating a certain part of the cochlea in a tonotopic manner. Ideally, each electrode will emit an electrical field which is limited to the neurons close by. However, in practice the electrical field of each electrode spreads through the cochlea and may excite the neurons at a larger distance than intended. This electrical field spread, limits the amount of available channels in CI's, reducing the amount of spectral information to the patient. It is therefore essential to get a better understanding of the spatial distribution of injected current in the cochlea. By use of Electrical Field Imaging (EFI), the internal electrode contacts are measured relatively to an external reference. This technique provides an intracochlear potential profile of all electrodes [38]. Due to the fact that it is not possible to stimulate and measure simultaneously at the same electrode contact, measurements at the stimulation electrode contact are calculated. By using our designs, we propose that it is possible to measure close to the stimulating electrode during EFI measurements, providing information about the electrical field characteristics at the site of stimulation (*in-vitro* testing shows the tested design to be functional during simultaneous stimulation and measuring process).

6) **Stimulus level effects on neural excitation and eCAP amplitude:** In the first batch of *in-vivo* experiments, basic forward masking artifact rejection methods was used. In basic forward masking, it is assumed that the measurement in which masker and probe are combined will excite the same fibres that are recruited by the probe alone. Westen *et al.* in her experiments concluded that at high current levels, the measured eCAP values are an underestimation of the real amount of excited nerve fibres [39]. Based on the work of Westen *et al*, a setup is proposed at LUMC in which the goal will be to search for the optimal IPIs, and use this value to measure interleaved forward masking. Additionally, using other stimulus shapes while injecting equal amounts of current has to be investigated.

7.5 Conclusions

In this chapter, a generic platform for assembly and packaging of the "Flexi-Stiff" MEA device has been presented. The necessary challenges in mounting, assembly and packaging relating to the materials, process simplicity, it's subsequent integration and optimisation were discussed along with illustrative images. A PCB was designed

for the *in-vitro* experiments and also for *in-vivo* insertion tests. A smaller PCB was designed for the *in-vivo* experiments described above.

In-vitro (electrochemical) characterisation was carried on the "Flexi-Stiff" devices at the LUMC and the successive experimentation procedure with the results mentioned. Electrochemical experiments (CV, EIS, VT) demonstrate the capability of the microfabricated demonstrator ("Flexi-Stiff" device) to be in the safe non-damaging zone when plotted in comparison to other neural stimulation materials, gave us a preliminary indication of the possible safe neural stimulation to the desired neurons of the intended application.

The preliminary results obtained during the *in-vivo* measurements demonstrate the capability of the "Flexi-Stiff" MEA for auditory neural stimulation application. The tested design achieved the desired dimensional requirements along with the mechanical property of showing an adequate balance between stiffness and flexibility favouring the intracochlear insertion process in Guinea Pigs. As per the information provided from the LUMC team the device was able to successfully survive the insertion and removal process within the set requirements and also handled a sufficient amount of current to elicit a neural response. The device successfully measured the neural response back at an adjacent stimulation site on the electrode array, thus proving the concept of simultaneous stimulation and recording on the same device at the stimulation area. Therefore the "Flexi-Stiff" MEA device was able to provide a basic stimulation and neural response measurement, comparable to electrode designs used in cochlear implant recipients.

7.5.1 Additional video material of the demonstrators

Videos for a) Steel cage and silicone encapsulation procedure and the subsequent b) mounting and glueing steps of the silicone carriers of the "Flexi-Stiff" device are respectively demonstrated and can be found using the following QR codes:

(a)

(b)

7.6 References

1. Stieglitz, T. Manufacturing, assembling and packaging of miniaturized neural implants. *Microsyst. Technol.* **2010**, *16*, 723–734.

2. Schuettler, M.; Stiess, S.; King, B. V; Suaning, G. J. Fabrication of implantable microelectrode arrays by laser cutting of silicone rubber and platinum foil. *J. Neural Eng.* **2005**, *2*, S121–8.

3. Cordeiro, J. G.; Henle, C.; Raab, M.; Meier, W.; Stieglitz, T.; Schulze-Bonhage, A.; Rickert, J. Micromanufactured electrodes for cortical field potential recording: *in-vivo* study. In *IFMBE Proceedings*; 2009; Vol. 22, pp. 2375–2378.

4. Schuettler, M.; Ordonez, J. S.; Henle, C.; Oh, D.; Gilad, O.; Holder, D. S. A Flexible 29 Channel Epicortical Electrode Array. *IFESS 2008 - 13th Annu. Int. FES Soc. Conf.* **2008**, -.

5. Rajaraman, S. Micromachined three-dimensional electrode arrays for in-vitro and in-vivo electrogenic cellular networks, Georgia Institute of Technology, 2009.

6. Smyth, M. Cyclic voltammetry. *TrAC Trends Anal. Chem.* **1994**, *13*, 341.

7. Cogan, S. F. Neural stimulation and recording electrodes. *Annu. Rev. Biomed. Eng.* **2008**, *10*, 275–309.

8. Cogan, S. F.; Troyk, P. R.; Ehrlich, J.; Plante, T. D. *In-vitro* comparison of the charge-injection limits of activated iridium oxide (AIROF) and platinum-iridium microelectrodes. *IEEE Trans. Biomed. Eng.* **2005**, *52*, 1612–4.

9. Gabrielli, C. Identification of electrochemical processes by frequency response analysis. *Tech. Rep. No. 004/83* **1998**, *4*, 130.

10. Norlin, A.; Pan, J.; Leygraf, C. Investigation of Electrochemical Behavior of Stimulation/Sensing Materials for Pacemaker Electrode Applications. *J. Electrochem. Soc.* **2005**, *152*, J7.

11. Bareket-Keren, L.; Hanein, Y. Carbon nanotube-based multi electrode arrays for neuronal interfacing: progress and prospects. *Front. Neural Circuits* **2012**, *6*, 122.

12. Franks, W.; Schenker, I.; Schmutz, P.; Hierlemann, A. Impedance characterisation and modeling of electrodes for biomedical applications. *IEEE Trans. Biomed. Eng.* **2005**, *52*, 1295–302.

13. Fung, A. O.; Tsiokos, C.; Paydar, O.; Chen, L. H.; Jin, S.; Wang, Y.; Judy, J. W.

Electrochemical properties and myocyte interaction of carbon nanotube microelectrodes. *Nano Lett.* **2010**, *10*, 4321–7.

14. Huigen, E.; Peper, A.; Grimbergen, C. A. Investigation into the origin of the noise of surface electrodes. *Med. Biol. Eng. Comput.* **2002**, *40*, 332–338.

15. Rose, T. L.; Robblee, L. S. Electrical stimulation with Pt electrodes. VIII. Electrochemically safe charge injection limits with 0.2 ms pulses. *IEEE Trans. Biomed. Eng.* **1990**, *37*, 1118–20.

16. West, A. C. Current Distributions on Recessed Electrodes. *J. Electrochem. Soc.* **1991**, *138*, 1620.

17. Kovacs, G. Introduction to the theory, design, and modeling of thin-film microelectrodes for neural interfaces. *Enabling Technol. Cult. Neural Networks (ed. Stenger DA, McKenna TM), San Diego, Acad. Press* **1994**, 121–165.

18. Rattay, F. Ways to approximate current-distance relations for electrically stimulated fibres. *J. Theor. Biol.* **1987**, *125*, 339–349.

19. McCreery, D. B.; Agnew, W. F.; Yuen, T. G. H.; Bullara, L. Charge density and charge per phase as cofactors in neural injury induced by electrical stimulation. *IEEE Trans. Biomed. Eng.* **1990**, *37*, 996–1001.

20. McCreery, D. B.; Agnew, W. F.; Yuen, T. G.; Bullara, L. a Comparison of neural damage induced by electrical stimulation with faradaic and capacitor electrodes. *Ann. Biomed. Eng.* **1988**, *16*, 463–481.

21. Shannon, R. V A Model of Save Levels for Electrical Stimulation. *IEEE T Bio-Med Eng* **1992**, *39*, 424–426.

22. Merrill, D. R.; Bikson, M.; Jefferys, J. G. R. Electrical stimulation of excitable tissue: design of efficacious and safe protocols. *J. Neurosci. Methods* **2005**, *141*, 171–98.

23. Abbas, P. J.; Brown, C. J.; Shallop, J. K.; Firszt, J. B.; Hughes, M. L.; Hong, S. H.; Staller, S. J. Summary of results using the nucleus CI24M implant to record the electrically evoked compound action potential. *Ear Hear.* **1999**, *20*, 45–59.

24. Briaire, J. J.; LUMC Cochlear implants from model to patients, Faculty of Medicine, Leiden University Medical Center (LUMC), Leiden University, 2008.

25. Versnel, H.; Prijs, V. F.; Schoonhoven, R. Round-window recorded potential of single-fibre

discharge (unit response) in normal and noise-damaged cochleas. *Hear. Res.* **1992**, *59*, 157–170.

26. Bierer, J. A.; Faulkner, K. F.; Tremblay, K. L. Identifying cochlear implant channels with poor electrode-neuron interfaces: electrically evoked auditory brain stem responses measured with the partial tripolar configuration. *Ear Hear.* **2011**, *32*, 436–44.

27. Brown, C. J.; Abbas, P. J.; Gantz, B. Electrically evoked whole-nerve action potentials: data from human cochlear implant users. *J. Acoust. Soc. Am.* **1990**, *88*, 1385–1391.

28. Klop, W. M. C.; Hartlooper, A.; Briare, J. J.; Frijns, J. H. M. A new method for dealing with the stimulus artefact in electrically evoked compound action potential measurements. *Acta Otolaryngol.* **2004**, *124*, 137–143.

29. Ordonez, J. S.; Boehler, C.; Schuettler, M.; Stieglitz, T. Improved polyimide thin-film electrodes for neural implants. *Conf. Proc. Annu. Int. Conf. IEEE Eng. Med. Biol. Soc. IEEE Eng. Med. Biol. Soc. Annu. Conf.* **2012**, *2012*, 5134–7.

30. Ordonez, J. S.; Boehler, C.; Schuettler, M.; Stieglitz, T. Long-term Adhesion Studies of Polyimide to Inorganic and Metallic Layers. *MRS Proc.* **2012**, *1466*, mrss12–1466–tt01–06.

31. Ordonez, J.; Boehler, C.; Schuettler, M.; Stieglitz, T. A blister-test apparatus for studies on the adhesion of materials used for neural electrodes. *Conf. Proc. Annu. Int. Conf. IEEE Eng. Med. Biol. Soc. IEEE Eng. Med. Biol. Soc. Annu. Conf.* **2011**, *2011*, 2953–6.

32. Ngamkham, W.; van Dongen, M. N.; Serdijn, W. A. Biphasic stimulator circuit for a wide range of electrode-tissue impedance dedicated to cochlear implants. In *2012 IEEE International Symposium on Circuits and Systems*; IEEE, 2012; pp. 1083–1086.

33. Ngamkham, W.; van Dongen, M. N.; Serdijn, W. A.; Bes, C. J.; Briaire, J. J.; Frijns, J. H. M. A 0.042 mm^2 programmable biphasic stimulator for cochlear implants suitable for a large number of channels. **2015**, 13.

34. Cees, J. B.; Sawigun, C.; Wouter, A. S. An additive instantaneously companding readout system for cochlear implants. In *2010 Biomedical Circuits and Systems Conference (BioCAS)*; IEEE, 2010; pp. 126–129.

35. Miller, C. A.; Abbas, P. J.; Brown, C. J. An improved method of reducing stimulus artifact in the electrically evoked whole-nerve potential. *Ear Hear.* **2000**, *21*, 280–90.

36. Klop, W. M. C.; Frijns, J. H. M.; Soede, W.; Briaire, J. J. An objective method to measure electrode independence in cochlear implant patients with a dual-masker forward masking

technique. *Hear. Res.* **2009**, *253*, 3–14.

37. Miller, A. L.; Morris, D. J.; Pfingst, B. E. Interactions between pulse separation and pulse polarity order in cochlear implants. *Hear. Res.* **1997**, *109*, 21–33.

38. Vanpoucke, F. J.; Zarowski, A. J.; Peeters, S. A. Identification of the impedance model of an implanted cochlear prosthesis from intracochlear potential measurements. *IEEE Trans. Biomed. Eng.* **2004**, *51*, 2174–83.

39. Westen, A. A.; Dekker, D. M. T.; Briaire, J. J.; Frijns, J. H. M. Stimulus level effects on neural excitation and eCAP amplitude. *Hear. Res.* **2011**, *280*, 166–76.

40. Dehmel, S.; Eisinger, D.; Shore, S. E. Gap prepulse inhibition and auditory brainstem-evoked potentials as objective measures for tinnitus in guinea pigs. *Front. Syst. Neurosci.* **2012**, *6*, 42.

Chapter 8

TiN; an initial evaluation for MEA/microelectronics hybrid device

If the experimental physicist has already done a great deal of work in this field, nevertheless the theoretical physicist has still hardly begun to evaluate the experimental material which may lead him to conclusions about the structure of an atom.

Johannes Stark (Noble Prize in Physics, 1919)

After demonstrating the technological and manufacturing feasibility of using titanium nitride (TiN) as one of the biocompatible material in microfabricating "Flexi-Stiff" MEA for our prototype (demonstrator) application, here in this chapter we present our initial findings of potentially using TiN as a gate electrode and interconnect material all fabricated in five lithographic steps to fabricate BiCMOS functioning devices. This demonstrated simple Bipolar Complementary Metal-Oxide Semiconductor (BiCMOS) process allows the on-chip integration for biomedical devices for instance in case microelectrode arrays (MEA's) with electronics to reduce the electrode wiring density and hence reduce the electrodes footprint. This approach can be useful for medical devices like cochlear implants (CI's) where a high density electrode array is applied in a small volume for the auditory nerve stimulation restoring back the sound for the deaf patients. This initial validation unlocks new research areas where two technologies (MEA fabrication and microelectronics) foresees a new application where these two technologies can be combined to lay a platform for developing the future hybrid cochlear implants.

This chapter is published in: Lawand, N. S.; van Zeijl, H.; French, P. J.; Briaire. J. J.; Frijns, J. H. M, Titanium Nitride (TiN) as a gate material in BiCMOS devices for biomedical implants., 2013 IEEE Sensors; IEEE, 2013; pp. 1 – 4.

8

8.1 Introduction

Titanium nitride (TiN), is one of the established biocompatible conductor because of its good mechanical properties, high corrosion resistance and capability of supplying high-density electrical charge for effective neural stimulation which seeks an potential application as an microelectrode material in novel biomedical devices. TiN films and surface coatings on other components are generally used in modern microelectronics, in glass and solar industries as reflecting materials, for protective coatings in automobiles and as surface finished golden colour coatings in jewellery items. Due to its low electrical resistivity, excellent mechanical properties, chemical and metallurgical stability, they are widely been used for various applications in semiconductor device technology [1] especially used as diffusion barrier metal layers for submicron metallization due to its superior thermal stability [2,3]. TiN thin layer have earlier been utilized as an interconnect barrier gate material for VLSI (Very large scale integration) CMOS local interconnect technology [4]. Several techniques of TiN deposition as a barrier layer for an Ohmic contact system in microelectronic devices have been explored; reactive DC sputtering from a pure titanium target [5], low pressure chemical vapor deposition (LPCVD) [6], sputter deposition from a TiN target [7] and nitridation of thin titanium layer by rapid thermal annealing process in a ammonium (NH_3) ambient environment [8]. From the mentioned processes reactive sputtering of TiN is one of the most commonly used deposition method because of its ease in processing and a good control of stoichiometry.

In the biomedical field metals are been used in implants since long time; in 1895 Lane implanted a metal plate for bone fracture fixation [9]. In the early developmental stages, metal implants encountered corrosion and mechanical instability problems. After the introduction of stainless steel in 1920's, which has superior corrosion resistance at that time attracted the interest of the clinicians. Platinum (Pt) and Platinum-Iridium (Pt-Ir) alloys are been widely used as microelectrode materials for fabricating neural, cochlear, deep brain stimulation (DBS) and other implants for stimulation and recording purposes. These materials exhibit excellent electrical and mechanical properties suitable for the nerve stimulation process. Apart from these materials TiN has found increasing interest because of properties, like high corrosion resistance, electro chemical stability, metal like conductivity and biocompatibility. So far TiN thin films have been fabricated by different deposition techniques and have also been studied extensively for their microstructural surface properties, surface chemical composition, mechanical and electrical properties. DC magnetron sputtering has been investigated intensively and has been proved and promoted to an industrial scale for many years [10]. These sputtered films possess great differences in crystal structure, morphology, electrical

and mechanical properties for different sputtering conditions. TiN is deposited by reactive physical vapour sputter deposition (PVD) techniques to obtain a micro-columnar structure. In this chapter we focus on the technology feasibility of using TiN as a gate electrode and interconnect material for building Bipolar Complementary Metal-Oxide Semiconductor (BiCMOS) devices with its future application of heterogeneous or monolithic integration of active devices in the biomedical MEA's to reduce the electrode metal track density to have improved functionality and performance. Characterisation results of the BiCMOS devices developed at the Delft Institute of Microsystems and Nanoelectronics (DIMES), Delft University of Technology with its performance will be discussed in detail.

8.2 TiN as a stimulation and gate material

In reference to the developmental obstacles associated to CI electrode arrays and the challenges for material requirement different manufacturing methods have to be considered. Silicon micromachining techniques and integrated circuit (IC) technologies is the path been undertaken by most of the researchers to tackle the various problems regarding the CI's. The first ever thin film microelectrodes fabricated using the micromachining techniques were constructed of gold electrodes supported on thin silicon substrate as a carrier [11]. The lengths of the electrode were in the range of 10μm to 50μm with the electrode-tip diameters to be as small as 2 μm. These electrodes were covered with a thin layer (0.4 μm) of silicon oxide which serves as the electrode insulating material. These probes where shown for the first time it's relevance of micromachined silicon substrates for the use in physiological applications [34]. However, the application is limited due to high complexity in the fabrication process and low yield. To add up these electrodes also show some technological and long-term failure due to their material incompatibility with the on-chip circuitry. The technological advances in the semiconductor industry and its associated fabrication processes for the IC consisting of photolithographic techniques with silicon etching enabled the path for the development and microfabrication of these microelectrode arrays (MEA's). These microfabricated MEA's were used for the long-term recording of extracellular neural bio-potentials from the neurons in the cortex [35,36].

Titanium Nitride (TiN), a material for MEA has been found increasing interest because of properties, like high corrosion resistance, IC compatibility, electro chemical stability, appreciable conductance and biocompatibility. A micro-columnar structure can be obtained when TiN is deposited by reactive physical vapor sputter deposition (PVD) techniques. M. Janders *et al.* [12] during his findings have reported charge injection capacities of 23 mC/cm^2 for transient current pulses for PVD TiN

electrodes with an surface area of 80 μm^2 and with a low impedance (|Zf=1kHz| = 150 kΩ) which is particularly useful for stimulating and sensing electrodes. The devices fabricated should satisfy the need via the electrode site for simultaneous stimulation and sensing neuronal activity requiring switching functionality with the corresponding wiring (metal interconnect lines) density in the microfabricated MEA as explained in Chapter 6 of this thesis and also mentioned elsewhere [13]. In such devices the performance is directly proportional to the electrode count hence a high electrode density and a corresponding large number of interconnect lines is required. Mechanical and electrochemical requirements does not allow a multi-level interconnect and with a one level interconnect only a limited electrode density can be realised. This wiring crisis can be solved by switching circuits that are integrated within the electrode array. Here the manufacturing cost, the mechanical and electrochemical requirements limits the process options for such integration. Furthermore, the integration process should not degrade the microelectrode performance.

In the following sections we demonstrate the fabrication and the Characterisation of the conventional BiCMOS devices such as npn, PMOS and NMOS transistors using TiN as a gate electrode and interconnect material in comparison with the standard aluminium and 1% silicon (Al+1%Si). This approach benefits in common material (TiN) being used for building microelectrodes as well as integrated electronics required to support the functioning of the same. This shows one possible step towards future electronics integration into MEA. In perspective of CI electrode array which contain only passive components for stimulation, thus missing the active components, the inclusion of which will provide more functionality of MEA by broadening the frequency spectrum of the device. The active components can be basic electronics performing the switching process of stimulation over different stimulation sites, thus intending to solve the wiring problem of MEA which restricts the addition of stimulation sites to current CI devices due to the anatomical space restrictions inside the cochlea. The MEA is permanently inside the human body, hence biocompatibility and reliability of the system is of utmost importance. This puts severe constraints on the integration of active devices into the MEA; either a very reliable and flexible packaging of electronics is required or the electronics itself must be fully biocompatible. The latter approach is proposed in this work; by modifying a simple and robust BICMOS process, an innate integration of electrodes with active devices is obtained. The modified BiCMOS process exhibits possible directions towards building biocompatible electronics for long term stable performance for intended in-vitro and in-vivo application.

8.3 BiCMOS devices and its fabrication process

In the semiconductor industry TiN is been widely used as a barrier metal for submicron metallization [2,3] and for local interconnect contact material in VLSI [4] technology for building CMOS devices due to its excellent thermal stability [2,3] and reduction in parasitic capacitance by the use of t use of minimum geometry junctions [4] thus improving the overall circuit performance. In our case TiN serves as an dual advantage multi-purpose material by exploiting its properties for MEA material as well as interconnect and gate material for the BiCMOS devices.

A schematic overview of the BiCMOS process flow is given in Figure 8.1. This BiCMOS process developed in Delft Institute of Microsystems and Nanoelectronics (DIMES) comprises of a five mask process that involves both Bipolar and CMOS transistors. This process, is primarily developed for education purposes. Its educational value is its simplicity yet showing both CMOS and bipolar transistors and its short turnaround time. However, a significant trade-off between the optimum settings of the various devices does not allow a full optimisation of the device parameters. Yet this process is robust, cost effective and enables the study of TiN MEA electrode material integrated in the fabrication of active devices.

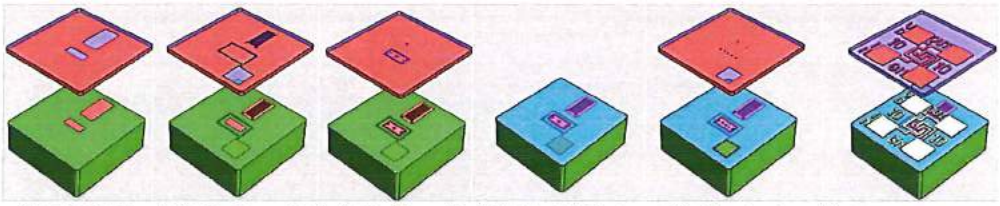

(a) N–Well (b) Shallow N (c) Shallow P (d) Field/Gate oxide (e) Contact opening (f) Interconnect

Figure 8.1 Schematic view of the 5 mask BiCMOS process [16].

The process sequence starts with a p-type wafer that is patterned for some to form deep n-type regions: the n-wells of the PMOS transistors and the collector for the npn transistors. This is done with a phosphor implant and a deep diffusion of 4 hours at 1150 ^{o}C (Figure 8.1 (a)). The second mask is used to create highly doped shallow type regions:- the source and drain of the NMOS transistors and the emitter of the npn transistors. An low energy high dose Arsenic implant is used for this purpose. The third mask is for the boron doped p-regions: the source and drain of the PMOS transistor and the base of the npn transistor, (Figure 8.1 (c)). The sequence n-type before p-type is chosen because the previous arsenic will amorphise the silicon which reduce the channelling of the subsequent boron implant, enabling a shallow boron profile for base of the npn-transistor. A mask less boron implantation over the whole wafer is used to tune the Threshold voltage of the MOS transistors. This

threshold voltage adjust implant is shallow enough not to alter the current gain of the NPN transistor. After the boron implant, the wafer is annealed/oxidized for 10 minutes at 1000 ^{o}C, this thermal process diffuses and activates the dopants and forms a silicon dioxide layer of 100 nm (Figure 8.1 (d)). This layer will act as an isolation layer between the interconnect and the substrate as well as the gate material of the PMOS and NMOS transistors. All of the connections to the shallow n- and p- layers need a contact opening (Figure 8.1 (e)). The fifth and final mask is used to pattern the interconnect layer made of AlSi(1%). This is the metallization step that creates a circuit by combining the different components (Figure 8.1 (f)) but is also used as a gate material. The schematic view of for the three types of transistors is as shown in Figure 8.2.

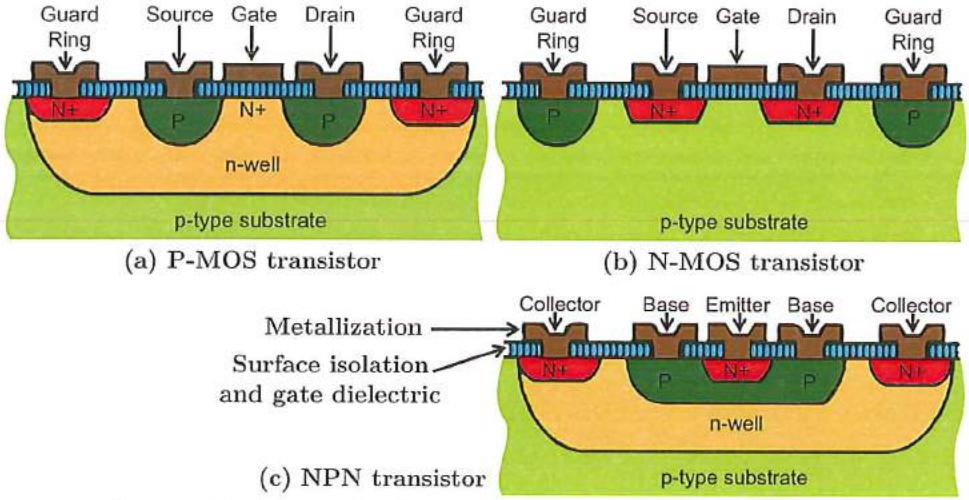

Figure 8.2 Schematic cross section of 3 types of transistors fabricated in BiCMOS.

As mentioned earlier, there are trade-offs in the process flow. The isolation layer thickness trade-off between the optimum gate layer thickness and the preferred isolation layer thickness between the substrate and the interconnect. Obviously, to enable practical threshold voltages of the MOS devices, the surface isolation layer is too thin for adequate isolation. The resulting parasitic devices are suppressed by the design of guard rings around each device. To form the guard rings, the shallow n- and p-implantations of the source/drain/emitter/base are used. These implantations are also used to form Ohmic contacts to the substrate and n-well. A contact of AlSi(1%) directly to the n-well will form a Schottky contact. High dopant concentrations generally results in low contact resistance, however, the contact resistance of the p contacts and source-drain dopant concentration of the PMOS transistor are limited by the current gain requirements on the npn transistor, a high

p-type dopant concentration, favourable for low contact and source/drain resistance will result in a low npn current gain and poor low current performance of this device.

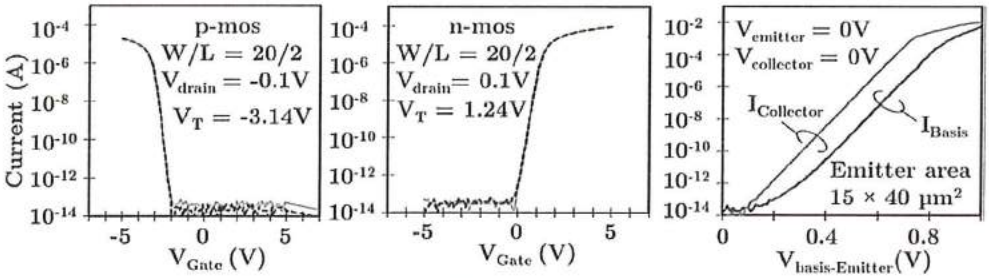

Figure 8.3 Typical characteristics of the PMOS, NMOS and NPN transistor fabricated with BICMOS5 process flow.

Obviously, a BiCMOS process with only five mask steps has a simple, and straightforward process flow yet, the device performance is highly compromised and may not be the most efficient solution for conventional applications. However, a simple process flow enables a re-engineering of the materials such that the fabricated circuits are bio-compatible even without packaging. Such intrinsic bio-compatible circuits can be used in applications where packaging is very critical or even impossible due to reliability or form factor issues. The BICMOS5 process, described above is converted into an intrinsic bio compatible process by replacing the SiO_2 surface isolation with LPCVD deposited silicon nitride while the AlSi(1%) is replaced by Ti/TiN, the main electrode material for the CI's.

8.3.1 BiCMOS device Characterisation results

For a better comparison for the gate metal (TiN) material, BiCMOS devices using thermal silicon oxide as an surface isolation layer with an standard aluminium and 1% silicon (Al+1%Si) were fabricated with the same process steps as described in section 4. Measurements were performed on the fabricated BiCMOS devices with standard Al+1%Si and TiN metallization using a controllable probe station with four probes. These are connected to an Agilent 4156C Precision Semiconductor Parameter Analyser which is also connected to a computer using GPIB. The probe station can be programmed for its movement in x-, y- and z-direction using a joystick or its movements can be programmed. Along with the basic BiCMOS structures, standard Greek Cross and Kelvin Cross were also fabricated and measured for sheet and contact resistance. These results can be used to discuss the characteristics of the transistors, as will be discussed in the following sections.

8.3.1.1 *Sheet and Contact resistance*

The sheet resistance is measured using the Greek cross structures as shown in figure 4. These structures make it possible to measure the sheet resistance of the different layers of the wafer. A current is passed from the top left pad to the bottom left pad and the potentials of the top right and bottom right pads are measured. The current flows through the centre cross from the top to the left. The sheet resistance is calculated with the equation [14]:

$$R_S = \frac{\pi R}{ln(2)} \tag{1}$$

where R_S the sheet resistance and R is the measured resistance. The current is passed using a voltage sweep of V_{force} from –0.5V to 0.5V. The current through that terminal I_{force} is measured. The potentials of the two measuring terminals are measured by keeping the current zero. The Greek cross was not only created using the interconnect layer, but also with other layers and combination of layers as shown in Figure 8.4.

The sheet resistance measurements for Al and TiN after annealing at 400 ^{o}C and 700 ^{o}C respectively are tabulated in Table 1. The annealing resulted in high sheet resistances for TiN as compared to Al. The probable reason is due to the growth of an oxide isolation layer on top of TiN which restricts sufficient contact between TiN and the measuring metal probe. Attempts to break through the isolation layer by applying high current resulted in a non-working device.

Material	R_S of the IC layer (Ω)	R_S of the SN layer (Ω)	R_S of the SN-SP layer (Ω)
TiN before annealing	4.6	0.81	1.6×10^2
TiN after annealing	3.7	1.7	3
Al after annealing	0.00044	0.06	0.031

Table 1. Sheet resistance measurements of various layers

The contact resistance is a measure for the resistance between two materials, in this case between the interconnect and the shallow n-type (SN) and shallow p-type (SP) layers. A contact resistance exists due to a bandgap difference between two contacting materials. It can be measured by using a Cross Bridge Kelvin Resistor, as

shown in Figure 8.4. The structure is much like the Greek Cross, only now the current goes from one material to the other in the centre of the cross.

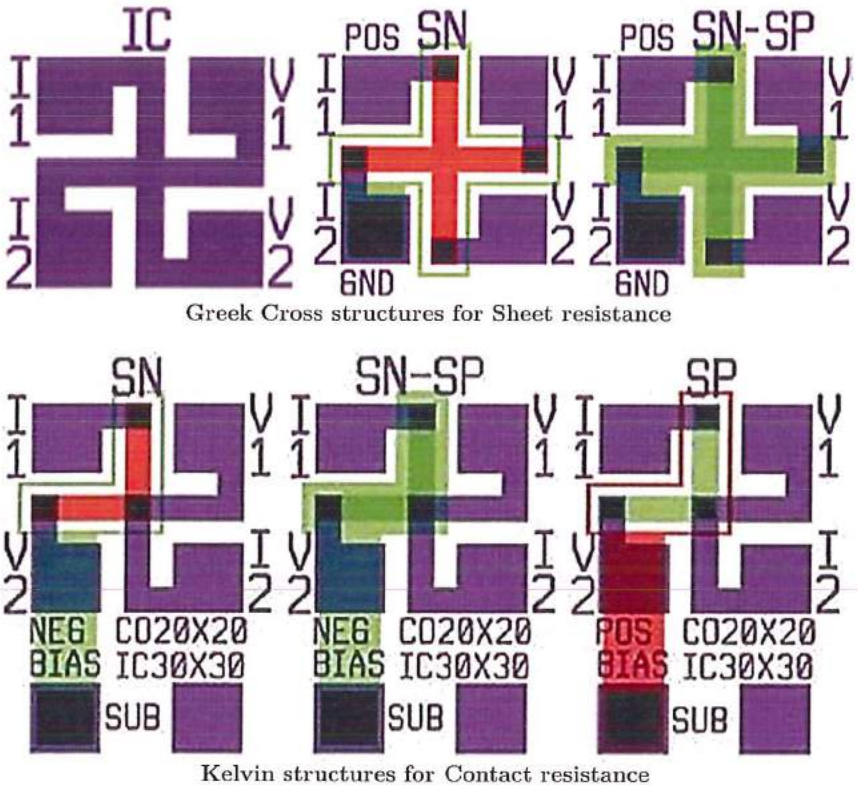

Figure 8.4 Schematics of various structures used for measurements.

The structure is much like the Greek Cross, only now the current goes from one material to the other in the centre of the cross. The contact resistance can be calculated using the following equation [15]:

$$R_K = R_C + R_{geom} \tag{2}$$

where R_K is the measured resistance, R_C is the resistance due to the voltage drop of the actual contact and R_{geom} is the is resistance due to the voltage drop around the contact opening. The above equation 2 can be further extended as:

$$R_K = \frac{\rho_C}{A} + \frac{4R_{sh}\delta^2}{3W_x W_y}\left\{1 + \frac{\delta}{2\left(W_x - \delta\right)}\right\} \tag{3}$$

where, A is the contact surface (30 × 30μm²), ρ_C the contact resistance, R_{sh} the sheet resistance of the underlying layer (SN or SP) and δ is the width of the region between the contact opening and the edge of the sidewall of the layers which is ideally zero, but in this case it is 5 μm. W_x is the width of the cross section (not the contact opening) in the x-direction and W_y is for y-direction, both are 40μm. This results in R_{geom} of 0.0027 Ω for contact resistance from the interconnect layer to the non-annealed SN layer, 0.0013Ω for the annealed SN layer, 0.0020 Ω for the non-annealed SP layer and 6.92 × 10^{-1} Ω for the annealed one. Due to data consistency the sheet resistance measurements of Al have been used. Contact resistance measurements of TiN and Al is tabulated in Table 2.

Material specifications	R_S of the SN layer (Ω)	R_S of the SN-SP layer (Ω)
TiN before annealing (Die 1, Die 2)	2.6, 2.4	0.0048, 1.4
TiN after annealing (Die 1, Die 2)	6.8, 4.3	0.0022, 0.0035
Al before annealing (Die 1, Die 2)	0.7, 0.53	0.0085, 0.0091
Al after annealing (Die 1, Die 2)	0.2, 0.21	0.0075, 0.0084

Table 2. Contact resistance measurements of TiN and Al layers

8.3.1.2 MOS transistors

Cross sections of NMOS and PMOS transistor is as shown in Figure 5 with a device top layout shown in Figure 8.5 (a) and (b). These were of different gate length ranging between 0.5 μm to 10μm and the gate width between 20 μm to 60 μm were fabricated. The devices were fabricated with thermally grown silicon dioxide (SiO_2) surface isolation with Al as interconnect/gate. All the devices were measured, and accordingly the transistor subthreshold characteristics with channel length of 2 μm and width of 20 μm are plotted as in Figure 8.5 (c) along with the Gummel plot as seen in Figure 8.5 (d). The measurements were performed sweeping the gate voltage (Vgate) from -4 V to 4 V. The plots were in accordance with the standard MOS device characteristics.

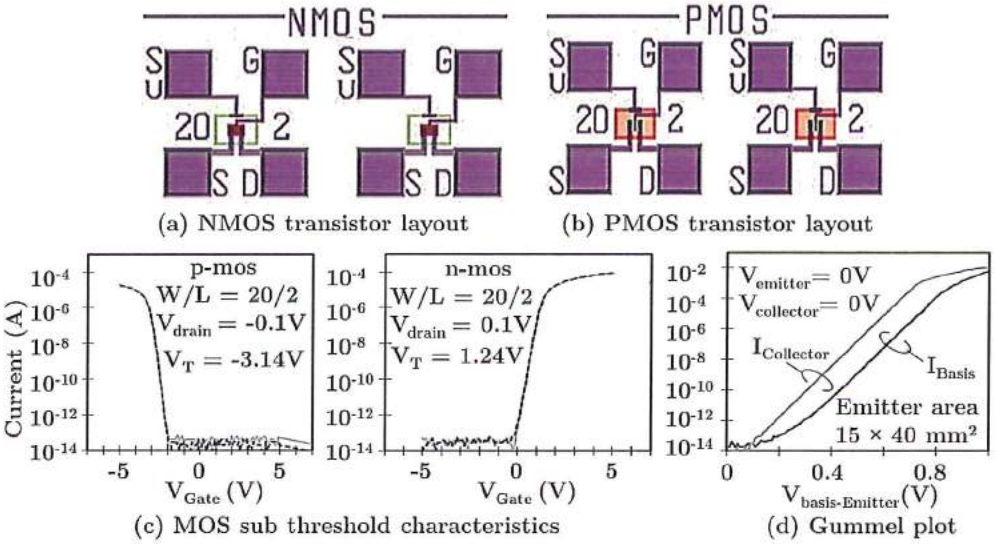

Figure 8.5 NMOS and PMOS layouts with their subthreshold characteristics with SiO_2 as surface isolation and Al as an interconnect/gate material.

8.3.1.3 Inverter and Oscillator

Inverter and Oscillator devices were also included in the fabrication process.

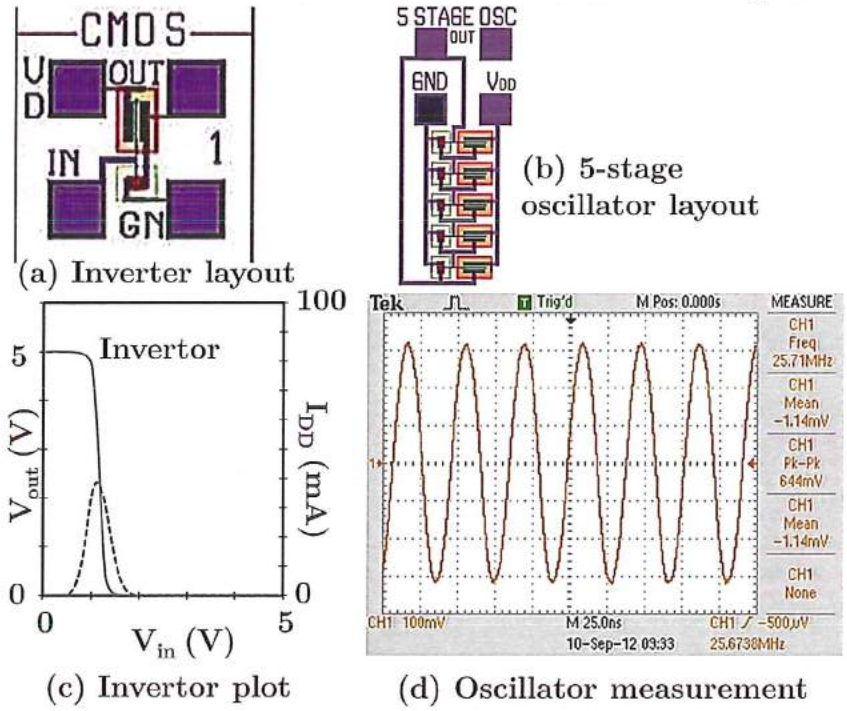

Figure 8.6 Inverter and 5 stage ring oscillator layout and their characteristics.

The respective device layouts on the die are as shown in Figure 8.6 (a) and (b). For plotting the inverter characteristics an input voltage Vin is swept from 0V to 5 V. These values are also applied to the V_{ss} and the V_{dd} terminals respectively. The output voltage V_{out} and current I_{DD} are accordingly plotted as shown in Figure 8.6 (c). A 5 stage ring oscillator processed with Si_3N_4/SiNx surface isolation and titanium nitride gate was fabricated and measured with an oscilloscope with the VDD terminal put on 5 V. The screen shot of the measurement is as shown in Figure 8.6 (d). The resulting frequency is 25.71 MHz with a peak-to-peak voltage of 644 mV.

8.4 Conclusions

In this chapter the basic idea to add active devices to the biocompatible MEA in such a way that the added active devices are biocompatible as well. This would simplify the requirements for packaging /sealing such systems for critical applications like cochlear implants. BiCMOS5 as it is a very straightforward process can be modified for this specific purpose. We fabricated simple devices with two gate materials; Ti/TiN and Al and two gate dielectrics; silicon dioxide and silicon nitride (SiNx). In the BiCMOS5 fabrication process flow, the gate material is also the interconnect and contact material. The devices are not alloyed. Measurement data so far indicates that the devices with TiN and Al gates on SiNx dielectric showed quite some leakage currents which is most likely due to the electric charge in the SiNx. On oxide the performance was better. The second batch of devices which were alloyed and subsequent measurements were performed on Ti/TiN gate on oxide and SiNx wafers. However, the measurements showed a high contact resistance on these wafers. The alloying process which was used is the standard process to improve the contact resistance for the Al interconnect devices but is in a temperature range where $TiSi_2$ can be formed and TiN can be oxidised. This can explain the high contact resistance. Ti contacts to silicon can be formed, there are several reports on this topic and is an increased p-type concentration would give a better Ti to silicon contacts. In BiCMOS5, the p-type dopant concentration can be increased to the required levels but this would kill the npn transistor. BiCMOS5 would then be CMOS5, which still is an useful process for the applications intended.

In this chapter a cost effective 5 mask BiCMOS process, proposed for integration in a MEA is been demonstrated. A low-stress silicon nitride/stoichiometric silicon nitride stack (Si_3N_4/SiNx, 20/80 nm thick) is used as surface isolation. The interconnect and gate are fabricated with TiN microelectrode array material. Such materials are also used in CI's. Compared with the results demonstrated here it is clear that the Si_3N_4/SiNx, surface isolation affects threshold voltage and low current characteristics of the mos and bipolar transistors. Furthermore a high contact

resistance is responsible for the low saturation current of the mos devices and low collector current in the bipolar device. Although further process and/or layout optimisation is required to improve the device performance, the results obtained clearly demonstrates the feasibility of integration of the active devices into the passive microelectrode arrays for biomedical applications.

8.5 References

1. Wittmer, M. Electrical characteristics of TiN contacts to N silicon. *J. Appl. Phys.* **1981**, *52*, 5722.

2. Wittmer, M. Barrier layers: Principles and applications in microelectronics. *J. Vac. Sci. Technol. A Vacuum, Surfaces, Film.* **1984**, *2*, 273.

3. Ting, C. Y.; Wittmer, M. The use of titanium-based contact barrier layers in silicon technology. *Thin Solid Films* **1982**, *96*, 327–345.

4. Tang, T. E.; Haken, R. A.; Holloway, T. C.; Hite, L. R.; Blake, T. G. W. Titanium nitride local interconnect technology for VLSI. *IEEE Trans. Electron Devices* **1987**, *34*, 682–688.

5. Ahn, K. Y.; Wittmer, M.; Ting, C. Y. Investigation of Tin films reactively sputtered using a sputter gun. *Thin Solid Films* **1983**, *107*, 45–54.

6. Raaijmakers, I. J.; Sherman, A. Contact hole fill with low temperature LPCVD TiN. In *Seventh International IEEE Conference on VLSI Multilevel Interconnection*; IEEE, 1990; pp. 219–225.

7. Brat, T. Characterisation of titanium nitride films sputter deposited from a high-purity titanium nitride target. *J. Vac. Sci. Technol. B Microelectron. Nanom. Struct.* **1987**, *5*, 1741.

8. Hara, T.; Tani, K.; Inoue, K.; Nakamura, S.; Murai, T. Formation of titanium nitride layers by the nitridation of titanium in high-pressure ammonium ambient. *Appl. Phys. Lett.* **1990**, *57*, 1660.

9. Lane, W. A. Some Remarks on the Treatment of Fractures. *Br. Med. J.* **1895**, *1*, 861–3.

10. Arnell, R. .; Kelly, P. . Recent advances in magnetron sputtering. *Surf. Coatings Technol.* **1999**, *112*, 170–176.

11. Wise, K. D.; Angell, J. B.; Starr, A. An Integrated-Circuit Approach to Extracellular Microelectrodes. *IEEE Trans. Biomed. Eng.* **1970**, *BME-17*, 238–247.

12. Janders, M.; Egert, U.; Stelzle, M.; Nisch, W. Novel thin film titanium nitride microelectrodes with excellent charge transfer capability for cell stimulation and sensing applications. In *Proceedings of 18th Annual International Conference of the IEEE Engineering in Medicine and Biology Society*; IEEE, 1996; Vol. 1, pp. 245–247.

13. Lawand, N. S.; Ngamkham, W.; Nazarian, G.; French, P. J.; Serdijn, W. a; Gaydadjiev, G. N.; Briaire, J. J.; Frijns, J. H. M. An improved system approach towards future cochlear implants. *Conf. Proc. Annu. Int. Conf. IEEE Eng. Med. Biol. Soc. IEEE Eng. Med. Biol. Soc. Annu. Conf.* **2013**, *2013*, 5163–6.

14. Smith, S. Sheet Resistance and Electrical Linewidth Test Structures for Semiconductor Process Characterisation, The University of Edinburgh, 2003.

15. Stavitski, N.; Klootwijk, J. H.; van Zeijl, H. W.; Kovalgin, A. Y.; Wolters, R. A. M. Cross-Bridge Kelvin Resistor Structures for Reliable Measurement of Low Contact Resistances and Contact Interface Characterisation. *IEEE Trans. Semicond. Manuf.* **2009**, *22*, 146–152.

16. Lawand, N. S.; van Zeijl, H.; French, P. J.; Briaire, J. J.; Frijns, J. H. M. Titanium nitride (TiN) as a gate material in BiCMOS devices for biomedical implants. In *2013 IEEE SENSORS*; IEEE, 2013; pp. 1–4.

Section IV

Conclusions, Future and Appendix

Chapter 9
Conclusions and future outlook

While day by day the overzealous student stores up facts for future use, he who has learned to trust nature finds need for ever fewer external directions. He will discard formula after formula, until he reaches the conclusion: "Let nature take its course".

Larry Bird (Retired basketball professional)

This chapter summarizes the main highlights of this thesis followed by recommendations for further research based on the research exploration carried out within the SMAC-it project.

9 Conclusions and future outlook

9.1 Conclusions

Due to the multifaceted delicate structure and its working of the human hearing organ (ear, especially cochlea), it is almost impossible to fully retrieve the natural hearing mechanism which a human being receives by birth. A step towards solving hearing loss (SNHL) are the advancements of medical devices. Cochlear Implant is one of the FDA approved device which is a proven invention to treat the people with severe–to–profound hearing loss. Apart from the medical and the technological challenges which were dealt under the SMAC-*it* project gave us the opportunity to look back on the fundamental material issues and other technological aspects which resulted in demonstrators of the device.

In this thesis, microfabrication technologies were used to demonstrate the design, fabrication and integration of a "Flexi-Stiff" device showing an exemplar which lays the foundation to develop future Cochlear Implant. In the path of arriving to this new material (Titanium Nitride) which was never used in the field of CIs was investigated and incorporated in the final demonstrator. This material having its application in microelectronics had to prove its application potential in developing the microelectrode arrays (MEAs). When designing the MEA (the demonstrator) used for animal cochlea's, the flexibility of the "Flexi-Stiff" array was an interesting challenge tackled in the final packaging. Apart from this challenge when fabricating such miniature sized devices, every other challenges of the development process which included design, microfabrication, handling, mounting and packaging also has to be equally weighted, particularly when aiming towards a sophisticated manufacturing process. This has to be realized within the permissible boundaries of material ease, biocompatibility and size which are crucial, especially while creating them in the cleanroom environment. The issues which were undertaken in this research project along with its major realizations are briefly summarized in the following sections:

- Before heading towards developing the product, a thorough understanding of both, the anatomical part with its location and the current device technological drawbacks is necessary. In parallel the different potential manufacturing technologies (the cleanroom ones) has to be considered before moving ahead. This has been dealt in detail under the chapters 2 and 3 which gives you a closer look at the structural aspects of the human ear and the CI device itself. This gives a brief technological overview from the traditional manufacturing to the latest MEMS based microfabrication technologies used for the microelectrode array.

- In quest to find a biocompatible electrode material which has to demonstrate its manufacturing capabilities and its microstructural material properties along with its electrical ones it has to be tested out to prove as an ideal candidate. To do so a thorough investigation of Titanium Nitride (TiN) was done in chapter 4. Various experiments (current density, electromigration, impedance, TCR etc.) were performed in comparison with the commonly used cleanroom materials (Al and Ti) which gave us an indication about its working capabilities. This laid the foundation with our understanding of its probable manufacturing boundaries which helped us in moving towards the subsequent microfabrication processes.
- Chapter 5 deals with the design approaches of the 1st and 2nd generation microelectrode array devices which were fabricated. Finite element analysis demonstrated a particular design configuration which has less influence on the potential electric field density distribution and is feasible to manufacture in the adopted microfabrication process for MEAs.
- The microfabrication process in developing the stiff and completely flexible MEA devices led our way to combine the knowledge gained in these two device approaches to come up with a "Flexi-Stiff" demonstrator. The selection of an appropriate polyimide (PI2611) along with the preferred thicknesses and the dry etching process to achieve the desired profile was an crucial processing step. This PI processing feature helped us to establish the flexible-stiff inter-conjunction of the device. The thin metal (TiN) layer sandwiched between the two PI layers had an important role to play in the functioning (electrical stimulation) of the device which has to be sputter deposited and patterned with utmost care. All the microfabrication challenges and the subsequent approaches gave solutions of the technological hurdles and its limitations in manufacturing the MEA.
- Assembly, packaging and testing are the final key elements to test the working of the device as a whole. The post fabrication, packaging and the folding techniques presented in chapter 7 where the selected processes as per the design feasibility and the manufacturing methods (e.g. laser micro-structuring) have been industrially used in manufacturing miniature components of medical devices. The in-vitro characterisation tests performed and the results achieved gave an indication that the charge densities generated by our "Flexi-stiff" devices are well inside the non-damaging zone as per the Shanon plot. Finally in chapter 8, by using TiN to build BiCMOS devices opens a new research area where by heterogeneous integration of basic electronics in the MEA to build hybrid devices and by multiplexing techniques might lead to solve the wiring crisis of the CI devices in future.

9.2 Recommendations for future work

The results based on the research outcome and the technological advances mentioned in this thesis enables to understand the frontiers to develop the future CIs. However, there is long way to realize the final product since it requires further research and development in different areas. This involves product development and calls for technology platform maturity to a certain level in addition to long term in-vivo material stability for the potential commercial use. Here below are some of the possible future research areas with some ideas for a hybrid device with added functionality. Future devices can be looked beyond cochlea usage for better hearing experience for the deaf ones.

- Although in this thesis a new metal (TiN) was investigated as a potential candidate material for future MEAs, this material has yet to demonstrate its full working capability for long term in-vivo stability. For doing so long-term ($\geq$ 6 months) in-vitro and in-vivo experimentation are required to be performed on devices build with such materials. Here the metal has to be investigated in combination with different biocompatible polyimides.
- As mentioned above and in this thesis the selection of appropriate materials in the microfabrication process is a crucial step. This determines the process compatibility and its stimulation capabilities during the final use. For long term in-vivo structural stability Prof. Thomas Stieglitz [1–3] *et al.* and Juan Ordonez *et al.* [4–6] have investigated various polymers and metals for developing neural and retinal implants. Out of the materials investigated by them the use of a thin intermediate Silicon Carbide layer (50 nm) is an important findings from Juan Ordonez which creates an chemical interlock bonding rather than mechanical with the polyimide layer been used underneath it. This makes it important for the long term material stability which the researchers have demonstrated by their long term experimentation.
- The cochlea anatomical features, especially the curling upward nature with its reducing volume creates an engineering challenge for designing it smaller and requires the functionality of curling around the inner wall of the cochlea to be placed closer to the auditory nerve. The present insertion tool which comes along with the CI device is adequate but there are still some shortcomings during surgery for its optimal placement inside the cochlea. Many researchers (J. Wang *et al.* [7] and B. Y. Arcand *et al.* [8]) have investigated MEMS and fluidic actuating techniques to have a proper insertion and placement system integrated inside the MEA. However, these efforts have not yet turned out into a commercial insertion and placement tool which makes the process

simpler during surgery. Hence further research and investigation in this area is required.

- One of the innovative ideas that came out of the discussion regarding insertion and curling was based on the idea of a "Party horn" as shown in Figure 9.1. which has its own structure in a curly manner which straightens up when air is blown into it. The microfabrication process of theses flexible MEAs involves thin layer deposition and patterning of different metal and polymer layers. To realize this idea, the thin layer deposition process can be tuned with respect to the stress level in individual layers in such a manner that the desired curled structure (similar to part horn) is achieved when released from the wafer substrates. These curled flexible structures before insertion can be straightened out with the help of a thin layer of intermittent piezoelectric or shape memory alloy (SMA) actuators which can be either deposited or glued to the back side of the device. The straightened part can be further inserted inside the cochlea with the help of an insertion tool.

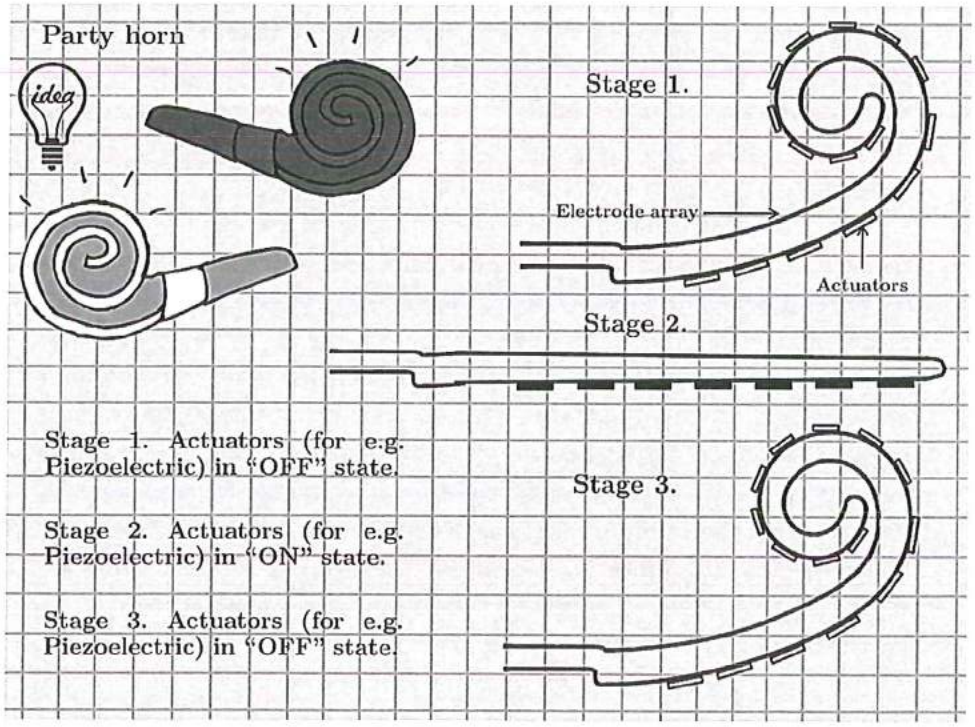

Figure 9.1 Schematic representation of an futuristic idea where micro-actuators (for e.g. Piezoelectric actuators) lined on the back side of an electrode array facilitates the desired curling and straightening process to help with the insertion procedure inside scala tympani of the cochlea.

After insertion intermittent switching off individual actuators along the length can be retrieved back. The curled structure thus enables to achieve the device been placed in close proximity of the cochlea. This is an initial idea which further has to be researched and developed in order to realise its applicability.

- One of the limitation of the CI is its limited capability for low frequency sound which are normally perceived deeper inside the cochlea. Moreover, due to anatomical space restrictions of the cochlea addition of more electrodes to current devices is not possible. In chapter 8 we have demonstrated a simple and robust BiCMOS microfabrication process. The device experiments performed showed good transistor characteristics. This proposed methodology will allow the number of electrodes to be increased without creating a wiring problem. The next research challenge would be to combine the fabrication process of the MEA (for instance "Flexi-Stiff" MEA) with the BiCMOS process. Therefore this approach showed a possible step towards future on-chip heterogeneous integration in the MEA to build hybrid devices.
- Final interconnecting technology, micro-assembly, micro-packaging and encapsulation of MEAs is an important area of future research to be undertaken for the actual working conditions and the reliability of such MEAs. The contribution of Prof. Thomas Stieglitz *et al.* [9] especially in developing the retinal implant addresses the main issues and its subsequent findings for these areas is beneficial for future research.
- Another potential research area would be to go beyond the cochlea towards the auditory cortex. This can be enabled by direct electrical stimulation of the cochlear nucleus complex which is mostly done for patients with neurofibromatosis type 2 (NF2). CIs which rely on the electrical activation of the peripheral neural processes within the cochlea, are not possible for patients suffering with NF2 due to their loss of integrity of the auditory nerve to bilateral vestibular schwanommas (acoustic tumours) [10]. In this situation auditory brainstem implant (ABI) is used which is surgically implanted and an external part is worn on the pinna of the ear. It works by electrical stimulation of the cochlear nucleus in the brainstem to produce a sensation of sound. ABI is similar in design and function to the multichannel CIs except for the differences in the stimulating electrode array design. Currently Nucleus ABI24 device (Cochlear Corporation, Englewood, CO, USA) uses 21 stimulating electrodes on a 2×8 mm pad shaped array (Figure 9.2) and MED-EL (Vienna, Austria) manufactures an ABI (Synchrony ABI) which have been approved for use in the cochlear nucleus (and inferior colliculus) [10].

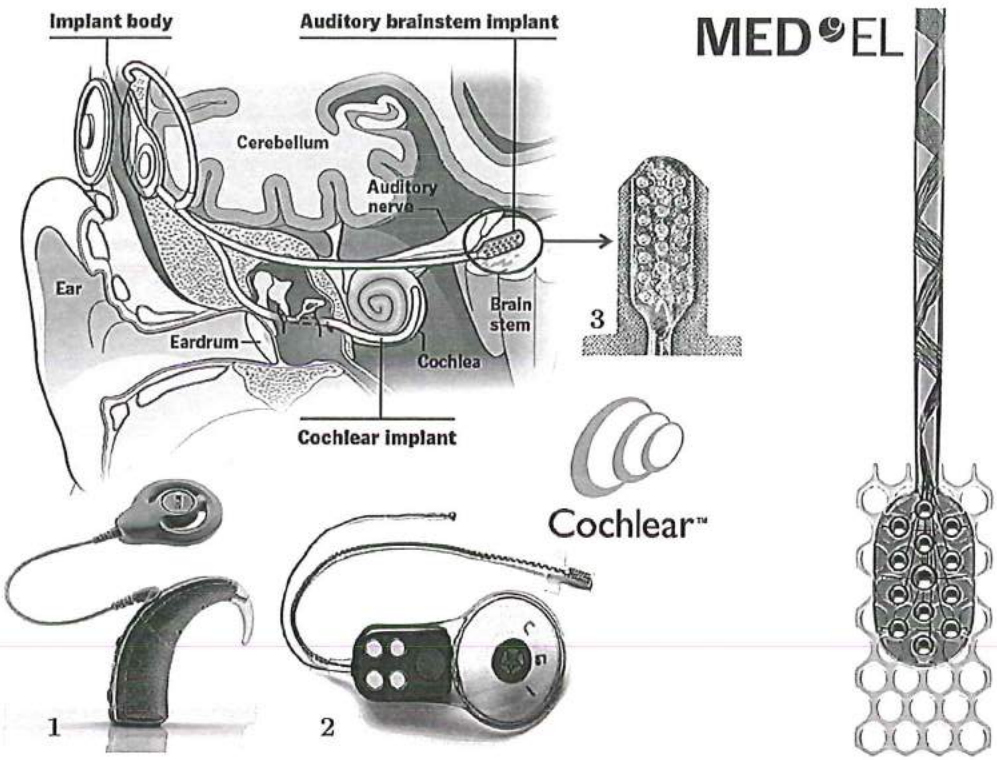

Figure 9.2 Auditory Brainstem Implant (ABI). From left to right. Nucleus® ABI24 from Cochlear® Corporation: 1. Signal Processor with microphone and transmitter coil, 2. Receiver-stimulator implant, 3. Implant placed at the auditory nerve *(Image courtesy: http://www.cochlear.com/)*. Image at the extreme right: MED-EL's ABI *(Image courtesy: http://www.medel.com/maestro-components-abi/)*.

9.3 References

1. Rubehn, B.; Stieglitz, T. In vitro evaluation of the long-term stability of polyimide as a material for neural implants. *Biomaterials* **2010**, *31*, 3449–58.

2. Hassler, C.; Boretius, T.; Stieglitz, T. Polymers for neural implants. *J. Polym. Sci. Part B Polym. Phys.* **2011**, *49*, 18–33.

3. Stieglitz, T. Considerations on Surface and Structural Biocompatibility as Prerequisite for Long-Term Stability of Neural Prostheses. *J. Nanosci. Nanotechnol.* **2004**, *4*, 496–503.

4. Ordonez, J. S.; Boehler, C.; Schuettler, M.; Stieglitz, T. Improved polyimide thin-film electrodes for neural implants. *Conf. Proc. Annu. Int. Conf. IEEE Eng. Med. Biol. Soc. IEEE Eng. Med. Biol. Soc. Annu. Conf.* **2012**, *2012*, 5134–7.

5. Ordonez, J. S. Miniaturization of neuroprosthetic devices and the fabrication of a 232-channel vision prosthesis with a hermetic package, Freiburg im Breisgau, 2012.

6. Ordonez, J. S.; Schuettler, M.; Ortmanns, M.; Stieglitz, T. A 232-channel retinal vision prosthesis with a miniaturized hermetic package. *Conf. Proc. Annu. Int. Conf. IEEE Eng. Med. Biol. Soc. IEEE Eng. Med. Biol. Soc. Annu. Conf.* **2012**, *2012*, 2796–9.

7. Wang, J.; Gulari, M.; Wise, K. D. An integrated position-sensing system for a MEMS-based cochlear implant. In *IEEE InternationalElectron Devices Meeting, 2005. IEDM Technical Digest.*; IEEE, 2005; Vol. 00, pp. 121–124.

8. Arcand, B. Y.; Bhatti, P. T.; Butala, N. V.; Wang, J.; Friedrich, C. R.; Wise, K. D. Active positioning device for a perimodiolar cochlear electrode array. *Microsyst. Technol.* **2004**, *10*, 478–483.

9. Schuettler, M.; Stieglitz, T. *Implantable Sensor Systems for Medical Applications*; Elsevier, 2013.

10. Fayad, J. N.; Otto, S. R.; Shannon, R. V.; Brackmann, D. E. Cochlear and Brainstem Auditory Prostheses "Neural Interface for Hearing Restoration: Cochlear and Brain Stem Implants." *Proc. IEEE* **2008**, *96*, 1085–1095.

Appendix

Supplementary information for Chapter 6

(Microfabrication process flow steps for "Flexi-Stiff" MEA)

A Appendix 1 Process flow steps for "Flexi-Stiff" MEA

Following are the major steps with its details which were used in the fabrication of the "Flexi-Stiff" microelectrode array. This process flow chart was developed and was processed accordingly at DIMES, The Netherlands.

1A Alignment Markers (Zero layer on the Front Side: FS)

1. Substrate information: Si p-type, boron wafer, Orientation: {1-0-0}, 0 degrees off orientation, Diameter: 100.0 ± 0.2 µm, Thickness: 525 ± 15 µm, Resistivity: 2-5 Ωcm.
2. Coating and Baking: EVG 120 Coater/developer was used to coat the wafers with resist (1.4 µm). The process consists of a treatment with HMDS (hexamethyldisilazane) vapour with nitrogen as a carrier gas, spin coating with Shipley SPR3012 positive photoresist, and a soft bake at 95 ^{o}C for 1.5 minute. The temperature of the hotplate (95 ^{o}C) and the relative humidity (48 ± 2 %) in the room is maintained during resist deposition.
3. Alignment, exposure and development: Mask alignment (COMURK mask), Exposure with energy of 140 mJ/cm^2 on ASML PAS 5500/80 automatic stepper wafer, post exposure bake at 115 ^{o}C for 1.5 minute, followed by a development step using Shipley MF322 developer (single puddle process), and a hard bake at 100 ^{o}C for 1.5 minute.
4. Inspection: Visually inspect the wafers through a microscope, and check the line width. No resist residues are allowed.
5. Plasma etching: With Trikon Ωmega 201 plasma etcher the alignment markers were etched with the platen temperature 20 ^{o}C.
6. Cleaning: Remove photoresist in Tepla plasma system (Program 1: 1000 watts power and automatic endpoint + 2 minutes over-etching), HNO_3 100% in 10minutes, demiwater in 5 minutes, HNO_3 65% at 105 ^{o}C in 10 minutes, demiwater in 5 minutes and drying procedure (non-metal procedure).

2A Oxide (PECVD) deposition (Front Side: FS and Back Side: BS)

7. Deposition: By Novellus Concept One system 1µm oxide is deposited at 400 ^{o}C.
8. Measurement of oxide: Oxide measured by Leitz MPV-SP measurement system.
9. BS cleaning: HNO_3 100% in 10minutes, demiwater in 5 minutes, HNO_3 65% at 105 ^{o}C in 10 minutes, demiwater in 5 minutes and drying procedure (non-metal procedure).
10. Deposition: By Novellus Concept One system 6 µm oxide is deposited at 400 ^{o}C.
11. BS coating and baking: EVG 120 Coater/developer was used to coat the wafers with resist (3 µm). The process consists of a treatment with HMDS

(hexamethyldisilazane) vapour with nitrogen as a carrier gas, spin coating with Shipley SPR3012 positive photoresist, and a soft bake at 95 ^{o}C for 1.5 minute. The temperature of the hotplate (95 ^{o}C) and the relative humidity (48 $\pm$ 2 %) in the room is maintained during resist deposition.

12. Alignment, exposure and development: Mask alignment (DRIE_BS), Exposure was performed on EVG 420 contact aligner, post exposure bake at 115 ^{o}C for 1.5 minute, followed by a development step using Shipley MF322 developer (single puddle process), and a hard bake at 100 ^{o}C for 1.5 minute.
13. Inspection: Visually inspect the wafers through a microscope, and check the line width. No resist residues are allowed.
14. Plasma etching: With Drytek 384T plasma etcher the back side (BS) oxide was etched as per the pattern using oxide etch recipe.
15. Inspection: Visually inspect the wafers through a microscope, and check if there is any silicon oxide left in the pattered areas.

3A Polyimide (1st layer) coating and patterning (Front Side: FS)

16. FS cleaning: Remove photoresist in Tepla plasma system (Program 1: 1000 watts power and automatic endpoint + 2 minutes over-etching), HNO_3 100% in 10minutes, demiwater in 5 minutes, HNO_3 65% at 105 ^{o}C in 10 minutes, demiwater in 5 minutes and drying procedure (non-metal procedure).
17. Spin coating of Primer (VM652): Manual LANZ wafer coater was used. Using a plastic pipette dispense VM652 primer over the wafer with primer recipe, Rotational speed: 10 sec @ 500 rpm + 45 sec @ 3500 rpm.
18. Spin coating of polyimide (PI2611): Manual LANZ wafer coater was used. Using a plastic pipette dispense PI2611 over the wafer with PI recipe, Rotational speed: 15 sec @ 350 rpm + 45 sec @ 1000 rpm. 2 sec @ 4000 rpm to decrease thickness at the edge. Estimated final polyimide thickness: 18 µm. Soft baking of PI layers for 6 minutes @ 120 ^{o}C.
19. FS coating and baking: Manual LANZ wafer coater was used. Dispense SPR3017 M for 10 sec @ 700 rpm + 30 sec @ 3510 rpm to achieve a thickness of 3µm.
20. Alignment and exposure: Mask alignment (EBR_3N), Exposure was performed on EVG 420 contact aligner, post exposure bake at 115 ^{o}C for 1.5 minute.
21. Development, etching and back side cleaning of PI2611: This step was performed in the SAL (Special applications laboratory). Development and etching was done by 2.5% TMAOH for approximate 15minutes. Resist strip and back side cleaning was done using Acetone + IPA + Demi water in a sequential manner in order to avoid PI residues remaining at end. Rinse the wafers in the glass beaker. Use the manual spinner SPIN 150 with the standard program to dry the wafers.

22. PI thickness (18 µm approximate) measurement done by Dektak profilometer.
23. Polyimide (PI2611) curing: PI2611 curing was carried in the MEMS lab with the help of Heraus oven @ 200 mbar in Nitrogen atmosphere. The curing was done for 2 hours @ 400 ^{o}C and was cooled to room temperature before removal.
24. Cleaning in SAL lab: Prepare separate cleaning line using Acetone + IPA + Demiwater in separate glass beakers only for this purpose. Rinse wafers in each glass beaker. Use the manual spinner SPIN 150 with the standard program to dry the wafers.
25. PI thickness (10µm approximate) measurement done by Dektak profilometer.
26. TEOS oxide (SiO_2) deposition: Deposition of TEOS oxide 200 nm deposition (@ 300 ^{o}C) by low stress, low pressure Plasma Enhanced Chemical Vapour Deposition (PECVD) process in Novellus Concept One.
27. Coating and Baking: EVG 120 Coater/developer was used to coat the wafers with resist (1.4 µm). Spin coating of Shipley SPR3012 positive photoresist, and a soft bake at 95 ^{o}C for 1.5 minute. The temperature of hotplate (95 ^{o}C) and the relative humidity (48 $\pm$ 2 %) in the room is maintained during resist deposition.
28. Alignment, exposure and development: Mask alignment (2N_PI1), Exposure was performed on EVG 420 contact aligner, post exposure bake at 115 ^{o}C for 1.5 minute, followed by a development step using Shipley MF322 developer (single puddle process), and a hard bake at 100 ^{o}C for 1.5 minute.
29. Inspection: Visually inspect the wafers through a microscope, and check the line width. No resist residues are allowed.
30. Dry patterning (etching) of PI2611: This was performed in Trikon Ωmega 201 plasma etcher using a polyimide etching recipe to pattern the 10 µm polyimide.
31. Resist stripping and cleaning: Resist is stripped in a dedicated beaker with NMP (N-methylpyrrolidone) heated at 70 ^{o}C. After this standard cleaning and rinsing using the manual spinner SPIN 150 with the standard drying program.

4A Metal stack deposition and subsequent patterning

32. Trikon Sigma 204 sputter coated used for deposition of the metal stack (40 nm Ti + 200 nm TiN + 3 µm Al) on wafers. Sputtering recipe was made to deposit the metal stack at 300 ^{o}C.
33. Coating and Baking: EVG 120 Coater/developer was used to coat the wafers with resist (12 µm). Spray coating of AZ® *n*LOF™ 2000 negative photoresist using special coating recipe, and a soft bake at 115 ^{o}C for 2 minute. The temperature of hotplate (115 ^{o}C) and the relative humidity (48 $\pm$ 2 %) in the room is maintained during resist deposition procedure.

34. Alignment, exposure and development: Mask alignment (3N_Al), Exposure was performed on EVG 420 contact aligner, post exposure bake at 115 ^{o}C for 1.5 minute. 15minutes idle time between exposure and development. Development was done using Shipley MF322 developer (double puddle process), and a hard bake at 100 ^{o}C for 1.5 minute.
35. Aluminium wet etching and cleaning: Wet etching Al (2 µm) was done in Al etchant which is PES. 1 litre buffered etch fluid contains: 770 ml concentrated phosphorus acid (H_3PO_4, 85%), 14ml concentrated nitric acid (HNO_3, 65%), 140ml concentrated acetic acid (CH_3COOH, 100%) and 76ml deionized water. The etch rate is ± 150 nm/min at 35 ^{o}C ± 1 ^{o}C. Etching is followed by cleaning in demiwater with further rinsing and cleaning in standard dryer machine.
36. Metal stack etching: The metal stack (Al: 1 µm + TiN: 200 nm + Ti: 40 nm) is patterned by dry etching technique using a Trikon Ωmega 201 plasma etcher using a standard dry etching recipe. Platen processing temperature 25 ^{o}C.
37. Resist stripping and cleaning: Resist is stripped in a dedicated beaker with NMP (N-methylpyrrolidone) heated at 70 ^{o}C. After this standard cleaning and rinsing using the manual spinner SPIN 150 with the standard drying program.

5A Polyimide (2nd layer) coating and patterning (Front Side: FS)

38. Repeating similar steps from 17 to 25.
39. Deposition of hard mask: 200 nm thin pure Al layer is deposited at 25 ^{o}C by Trikon Sigma 204 sputter coating machine.
40. Coating and Baking: EVG 120 Coater/developer was used to coat the wafers with resist (3 µm). Spin coating of Shipley SPR3017 positive photoresist, and a soft bake at 95 ^{o}C for 1.5 minute. The temperature of hotplate (95 ^{o}C) and the relative humidity (48 ± 2 %) in the room is maintained during resist deposition.
41. Alignment, exposure and development: Mask alignment (5N_PI2), Exposure was performed on EVG 420 contact aligner, post exposure bake at 115 ^{o}C for 1.5 minute, followed by a development step using Shipley MF322 developer (double puddle process), and a hard bake at 100 ^{o}C for 1.5 minute.
42. Inspection: Visually inspect the wafers through a microscope, and check the line width. No resist residues are allowed.
43. Dry patterning (etching) of Al(200 nm): This was performed in Trikon Ωmega 201 plasma etcher using standard dry etching recipe to etch 200 nm of Al.
44. Dry patterning (etching) of PI2611: This was performed in Trikon Ωmega 201 plasma etcher using a polyimide etching recipe to pattern together the two 10 µm thick polyimide (PI2611) layers to land on the underneath oxide layer.

45. Resist stripping and cleaning: Resist is stripped in a dedicated beaker with NMP (N-methylpyrrolidone) heated at 70 ^{o}C. After this standard cleaning and rinsing using the manual spinner SPIN 150 with the standard drying program.

6A Deep reactive ion etching (DRIE) and oxide removal (Back side: BS)

46. DRIE: DRIE of silicon was done by using a Adixen AMS100 on the BS of the wafer. In this process the 6 µm PECVD oxide mask was used to etch completely the 525 µm thick silicon wafer to land on the 1µm thick PECVD oxide and the polyimide (20 µm thick) from the back side of the wafer.
47. Removal of oxide: 1 µm PECVD oxide from the BS is removed by dry etching method by using a Alactel GIR300 F etcher enabling to land on the polyimide layer. The etching is carried out at room temperature (25 ^{o}C).

7A Hard mask removal for free standing devices.

48. Aluminium wet removal and cleaning: Wet etching or removal of the Al (200 nm) hard mask was done in Al etchant which is PES. 1 litre buffered etch fluid contains: 770 ml concentrated phosphorus acid (H_3PO_4, 85%), 14 ml concentrated nitric acid (HNO_3, 65%), 140 ml concentrated acetic acid (CH_3COOH, 100%) and 76 ml deionized water. The etch rate is $\pm$ 150 nm/min at 35 ^{o}C $\pm$ 1 ^{o}C. Etching is followed by cleaning in demiwater with further rinsing and cleaning in standard dryer machine.
49. Free standing flexible Polyimide devices hold by supporting structures attached to the etched Silicon wafer. The bond pad area is the stiff silicon part where the Al bond pads exist.

A

Appendix

Supplementary information for Chapter 7

(Clinical procedures and other information for in-vivo experiments)

A Appendix 2 Clinical procedures carried out at LUMC

1. Anaesthetic procedure

For ABR measurements, animals were anesthetized by use of Dexmedetomidine (Dexdomitor®, Orion, Finland; 0.25 mg/kg) and ketamine (Anesketin®, Eurovet, Bladel, The Netherlands; 40 mg/kg). During ABR measurements, subcutaneous needle electrodes were used, the active electrode behind the pinna at the side of measurement, the reference (negative) electrode was placed on the skull and the positive electrode behind the contralateral pinna. The measurements consisted of a click ABR at 90 dB to 0 dB followed by a frequency specific ABR measurements at frequencies of 16000 Hz, 8000 Hz, 4000 Hz, 2000 Hz and 1000 Hz tone bursts with an amplitude range from 90 to 0 dB. The data was processed by use of MATLAB®. After measurements, the animals were recovered from anaesthesia with atipamezol (Antisedan®, Orion, Finland; 1.75 mg/kg).

2. Deafening procedure

To provide less interference due to the residual hearing during the electrophysiological measurements, a ototoxic treatment with Kanamycin and Furosemide was conducted at least two weeks prior to intracochlear measurements. Before ototoxic treatment, an ABR measurement was conducted. Animals were anesthetized by use of Dexmedetomidine (Dexdomitor®, Orion, Finland; 0.5 mg/kg) and ketamine (Anesketin®, Eurovet, Bladel, The Netherlands; 40 mg/kg). After total anaesthesia was achieved (lack of pedal reflex), Kanamycin (Kanamycin sulphate, Sigma-Aldrich, St. Louis, MO, USA; 400 mg/kg) was administered subcutaneously followed by subsequent intravenous infusion of furosemide (Sandoz, Almere, The Netherlands; 100 mg/kg) by surgical cannulation of the right external jugular vein. This technique has proved to eliminate the majority of both inner and outer hair cells [1,2]. During anaesthesia, the animals were injected subcutaneously with the non-steroid anti-inflammatory drug carprofen (Rimadyl(3), Pfizer; 5 mg/kg)

Postoperatively, the animals were recovered from anaesthesia with atipamezol (Antisedan®, Orion, Finland; 2.5 mg/kg). During our pilot study for validation of our ototoxic treatment, ABR measurements were conducted before treatment and at day 3, 6, 10 and 14 post surgery. During regular experiments ABR measurements were only conducted before treatment and prior to intracochlear surgery.

3. Implantation procedure

For implantation surgery, the animals were pre-medicated with atropine sulphate (0.06 mg/kg) subcutaneously. The general anaesthesia was initiated with

Dexmedetomidine (Dexdomitor®, Orion, Finland; 0.25 mg/kg) by intramuscular injection followed by cap ventilation with a gas mixture of O_2 and pressurized air (1:1) mixed with 1-2% isoflurane. A tracheal tube was placed for continuous ventilation by an animal ventilator system (Delta Medic, Utrechts, The Netherlands) during measurements. The acoustic bulla was approached by making a retro auricular incision. After identification of the foramen stylomastoideus, the facial nerve was obliterated by opening of the foramen stylomastoideus with 0.5-1.0 mm diamond ball drills, providing direct access to the round window. The round window was opened with a sharp forceps, after which insertion of the electrode array found place. The wound was covered with moist bandages to prevent tissue dehydration.

4. Animal monitoring

The pO_2, pCO_2, heart rate, ventilation rate and rectal temperature were continuously measured during surgery and measurements. Anaesthetics were adjusted based on these values. The body temperature of the animals was kept at 38 ^{o}C by a water-based heating mat (less electromagnetic interference) for the duration of the measurements. During measurements, every 2 hours 2 ml of NaCl 0.9% was injected subcutaneously to avoid dehydration.

Appendix 3 Artifact rejection by forward masking paradigm

The electrically evoked compound action potential (eCAP) is a synchronous auditory nerve activity which is in response to an stimulated electrical pulse, and can be recorded in-situ with the help of CI electrodes. eCAPs are the clinical routine measurements carried out in order to measure objectively and determine the functionality of the auditory nerve stimulation process. During the measurement process a stimulation artifact results from a voltage decay following the biphasic current pulse. This artifact waveform is typically a several orders of magnitude larger than the eCAPs and is a decaying exponential with a time constant of several hundreds of microseconds, which is sufficiently long to overlap with the neural response. Various artifact rejection paradigms were demonstrated by W. M. C. Klop *et al.* [3]. In our case the forward masking (MP3) paradigm was used for the eCAP recordings. The MP3 technique consists of three frames containing a masker and probe stimulus (Figure.1). In the first frame, called the M (masker) frame, only a masker pulse is provided which is a high-level, short duration pulse. The second frame called the P (probe) frame, only a probe pulse is provided which is a high-level, short duration presented after a short delay. Both giving rise to neural excitation. In the third frame, called the MP (masker-probe), both masker and probe pulse are provided which represents a high-level, short-duration masker pulse, before

presenting a second, probe stimulus pulse. However, when providing the probe pulse most neurons are still excited due to the masker pulse, resulting in no or small neural response due to the probe. By adding the recordings of the first two frames (masker with eCAP and probe with eCAP) and subtracting the third frame (masker and probe combination without eCAP after the probe) the result is the neural response of the probe without any stimulus artifact.

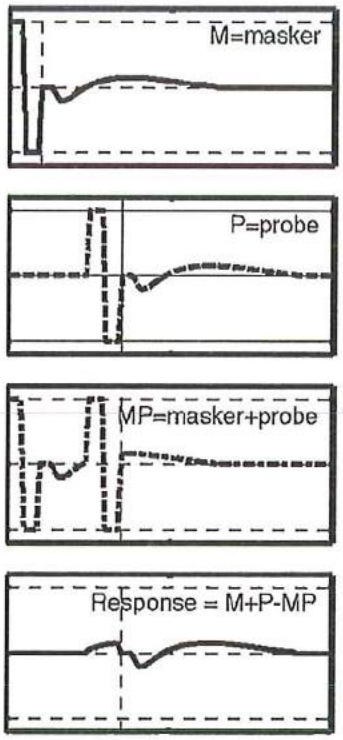

Figure.1 Forward masking artifact rejection paradigm [3].

References

1. West, B. A.; Brummett, R. E.; Himes, D. L. Interaction of kanamycin and ethacrynic acid: severe cochlear damage in guinea pigs. *Arch. Otolaryngol.* **1973**, *98*, 32–37.

2. Versnel, H.; Agterberg, M. J. H.; de Groot, J. C. M. J.; Smoorenburg, G. F.; Klis, S. F. L. Time course of cochlear electrophysiology and morphology after combined administration of kanamycin and furosemide. *Hear. Res.* **2007**, *231*, 1–12.

3. Klop, W. M. C.; Hartlooper, A.; Briare, J. J.; Frijns, J. H. M. A new method for dealing with the stimulus artefact in electrically evoked compound action potential measurements. *Acta Otolaryngol.* **2004**, *124*, 137–143.

Publications and Awards

1. **Lawand, N. S.**; French, P. J.; Briaire, J. J.; Frijns, J. H. M. Study of fabrication strategies for Silicon in Cochlear Implants. In *SAFE/ProRISC*; Veldhoven, **2009**; pp. 28–31.

2. **Lawand, N. S.**; French, P. J.; Briaire, J. J.; Frijns, J. H. M. Silicon Probes for Cochlear Auditory Nerve Stimulation and Measurement. In *Advanced Materials Research*; **2011**; Vol. 254, pp. 82–85.

3. **Lawand, N. S.**; French, P. J.; Briaire, J. J.; Frijns, J. H. M. Design and fabrication of stiff silicon probes: A step towards sophisticated cochlear implant electrodes. *Procedia Eng.* **2011**, *25*, 1012–1015.

4. **Lawand, N. S.**; French, P. J.; Briaire, J. J.; Frijns, J. H. M. Design and Simulation of Silicon Electrodes for Cochlear Auditory Nerve Stimulation. *Proc. 2011 Int. Conf. Microtechnologies Med. Biol.* **2011**, 255–256.

5. **Lawand, N. S.**; French, P. J.; Briaire, J. J.; Frijns, J. H. M. Development of probes for cochlear implants. In *2011 IEEE SENSORS Proceedings*; IEEE, **2011**; pp. 1827–1830.

6. **Lawand, N. S.**; French, P. J.; Briaire, J. J.; Frijns, J. H. M. Micromachined Silicon probes for cochlear auditory nerve stimulation. *Netherlands MicroNano Conf.* **2011**.

7. **Lawand, N. S.**; French, P. J.; Briaire, J. J.; Frijns, J. H. M. Thin Titanium Nitride Films Deposited using DC Magnetron Sputtering used for Neural Stimulation and Sensing Purposes. *Procedia Eng. Eurosensors* **2012**, *47*, 726–729.

8. **Lawand, N. S.**; French, P. J.; Briaire, J. J.; Frijns, J. H. M. Development of microelectrode material for nerve stimulation using TiN . In *Proceedings IC-MAST-2012*; **2012**; pp. 3–6.

9. **Lawand, N. S.**; French, P. J.; Briaire, J. J.; Frijns, J. H. M. Cochlear implant electrode development for improved implants. In *Proceedings IEEE Engineering in Medicine and Biology Society*; San Diego, CA, USA, **2012**.

10. **Lawand, N. S.**; Driel, J. Van; French, P. J. Electric Field Density Distribution for Cochlear Implant Electrodes. In *2012 COMSOL Conference Proceedings*; **2012**; pp. 1–4.

P

11. **Lawand, N. S.**; French, P. J.; Briaire, J. J.; Frijns, J. H. M. Titanium Nitride as a microelectrode material for auditory nerve stimulation and sensing purposes . In *Proceedings 4th International Conference on Neuroprosthetic Devices*; Freiburg, Germany, **2012**; pp. 99–100.

12. **Lawand, N. S.**; French, P. J.; Briaire, J. J.; Frijns, J. H. M. TiN as an microelectrode material for nerve stimulation and sensing. In *Proceedings of Annual IEEE EMBS Micro and Nanotechnology in Medicine*; 2012; Vol. 254, p. **2012**.

13. **Lawand, N. S.**; French, P. J.; Briaire, J. J.; Frijns, J. H. M. Long term Cochlear Implant electrode improvement for stimulation and sensing neuronal activity. In *2012 Sixth International Conference on Sensing Technology (ICST)*; IEEE, **2012**; pp. 533–537.

14. **Lawand, N. S.**; van Zeijl, H.; French, P. J.; Briaire, J. J.; Frijns, J. H. M. Titanium nitride (TiN) as a gate material in BiCMOS devices for biomedical implants. In *2013 IEEE SENSORS*; IEEE, **2013**; pp. 1–4.

15. **Lawand, N. S.**; Ngamkham, W.; Nazarian, G.; French, P. J.; Serdijn, W. a; Gaydadjiev, G. N.; Briaire, J. J.; Frijns, J. H. M. An improved system approach towards future cochlear implants. *Conf. Proc. Annu. Int. Conf. IEEE Eng. Med. Biol. Soc. IEEE Eng. Med. Biol. Soc. Annu. Conf.* **2013**, *2013*, 5163–6.

16. **Lawand, N.**; Lopez, V.; French, P. Electrochemical Study of Potential Materials for Cochlear Implant Electrode Array. In *2013 COMSOL Conference Proceedings*; **2013**.

17. **Lawand, N. S.**; French, P. J.; Driel, J. Van; Briaire, J. J.; Frijns, J. H. M. Sensing Technology: Current Status and Future Trends II. In *Sensing Technology: Current Status and Future Trends II*; Mason, A.; Mukhopadhyay, S. C.; Jayasundera, K. P.; Bhattacharyya, N., Eds.; Springer International Publishing, **2014**; Vol. 8, pp. 1–25.

1. Best Flash presentation award at the "SAFE, ICT.OPEN 2012" conference.

2. Best presentation award at the "International Conference on Materials and Applications for Sensors and Transducers – 2012"

Acknowledgements

In my PhD research journey, one of humans sensing capability "hearing" was addressed but now time comes to write/acknowledge about those "humans" whom I was "listening" to for all these years. While doing so I had to envision the "thinking" process by mentally contemplating through my PhD life to coherently mention the instants and the people who influenced and helped me to arrive at the end of this journey. This thesis represents a milestone achieved in TU Delft over the years. My experience at the university has been amazing and a memorable one. The supporters list includes people from various continents of the globe who showed affinity, interest and support towards this research without whom coming at this stage and presenting this thesis would not have been possible.

The first and foremost person I would like to thank is my promotor Prof. P. J. French (Paddy) who along with the supervision shared this roller-coaster ride of my PhD trip. He has been the sole person as a strong supporter for my both scientific and non-scientific life. I am utmost grateful for being the part of this adventure right from the interview day when I met you in your casual dressing way until today where we have achieved our research goal. Paddy who is famous amongst students for his teaching uniqueness provided me the opportunity to learn and think along with him to tackle the challenges in research as well as at personal front. I still remember those long technical discussions especially the one walking by steps from the ground floor to the 13th floor of the EI Laboratory during an fire evacuation drill. One thing I would like to mention about Paddy was his motivation at various stages of the project to present the results to the outside world and receive feedback. This was facilitated by attending various conferences/lectures/workshops/debates etc. and the subsequent interaction with different people in the audiology world. The same applied internally at the cleanroom to perform various tests and runs to prove the proposed hypothesis. Special thanks to Dafina (Paddy's wife) for the encouragement whenever we met and allowing Paddy to be available even beyond working hours.

My second equivalent thanks note goes to my second promotor Prof. J. H. M. Frijns and Dr. J. J. Briaire (LUMC, Leiden) for their support and guidance shown in this PhD research to understand and realize the medical challenge associated with it. Johan's boldness to allow me to observe the CI surgery gave an idea how medical and engineering professionals perform at a common platform while addressing a common problem. His immense knowledge both in engineering and CI surgery, which is rare to have, helped me to get a closer look at surgery issues and associated

engineering difficulties. Jeroen being my daily supervisor during my initial days at LUMC practically supported for the CI workflow procedure and helped to channelize the intermediate goals. I would like to thank him for his timely guidance and those fruitful medical/technical discussions on the CI electrode array designs to nurture the development path of MEAs. I would like to thank all my colleagues (Randy Kalkman for his simulations, Jory Koolwijk for his *in-vitro* and *in-vivo* measurements and Dirk Vellinga for those medical discussions) and the supporting staff of LUMC, Leiden. Thanks Johan de Vos for arranging and performing the *in-vitro* and *in-vivo* experiments, the demonstration of the deafened guinea pig with my demonstrator device, research articles and for the final support to complete the characterisation part of my thesis.

My PhD consists of working at four different locations; ENT department at LUMC in Leiden, EI Laboratory of EWI faulty and DIMES (now Else Kooi Lab) in Delft and the last part at Sonion Nederland B.V. in Hoofddorp. Coming to Delft, Electronic Instrumentation Laboratory (EI Lab) and DIMES, my two working playgrounds where there are so many people to thank for this final day. From EI Lab my thanks goes to all the professors, technicians, secretaries and my fellow colleagues that were available to support me at different stages of my PhD making EI Lab a nice place to work at. Prof. Kofi Makinwa (thanks for your constant push to get to the end), prof. Gerard Meijer (thanks for your Dutch translation and PhD structural support), Joyce Siemers and Karen van Busschbach for your administration support, Piet Trimp, Jereon Bastemeijer (thanks for the Dutch translation help), Zu Yao Chang for the technical discussions to build experimental setups and building PCB's. Lukasz Pakula for all those long technical cleanroom discussions on processing. Thanks to my old roommates from 13th floor: Sharma Mokkapati, Chung Kay Yang (CK), Yue Chen, where sharing, working, discussing and arranging parties, drinks was the part of our so called "corrupted room" and my current roommates from 15th floor: Ugur Sonmez, Xiaoligang Ge and Dr. G Wan. These thanks extend to my former colleagues: Agung Purniawan, Arvin Emadi, Berenice, Devendiran, Mahdi Kashmiri, Caspar van Vroonhoven and my fellow colleagues of EI Lab. Also thanks to the MSc students: Danielle and Maria, Joost van Driel, Çilem and Valerio for being part of the Smac-*it* project.

My second playground, DIMES where I spend my time to bring my ideas to reality. Inside the cleanroom, I would like to thank to all the DIMES engineers, my past and fellow colleagues and the technical support staff for their advice, help and encouragement as and when required during my processing which made DIMES an enjoyable place to work at. The list Mario Laros, Charles de Boer (for introducing me to the cleanrooms: C100 and C10000), Silvana Milosavljević, Tom Scholtes, Wim van der Vlist, Jan Cornelis Wolff, Koos van Hartingsveldt, Hugo Schellevis, Cassan

Visser, Jan Groeneweg, Ruud Klerks, Wim Wien, Loek Steenweg, Johan van der Cingel, Johannes Wingerden, Peter Swart, Alex van den Bogaard, Robert Verhoeven. A special thanks to Mario Laros (super-Mario) who is there at any time to help out with processing and machine issues with an incredible knowledge on various machines in C100. Also a special thanks to Dr. Henk van Zeijl and Dr. Gregory Pandraud (the big boss/rector) for those never ending technical discussions, the long cleanroom working nights and the prompt help at any point of the processing which helped me to achieve my research goals. The marathon cleanroom run of 26 hours at a stretch with Mario and Dr. Henk is a unforgettable experience. Along with this list an another DIMES friends list whom I would like to thank for being with me in the cleanroom in those white and blue suits. Bruno Morena, Fábio Rodrigues, Sebastian Sosin, Thomas Moh, Theodoros Zoumpoulidis, Gianpaolo Lorito, Chenggang Shen, Jia Wei, Benjamin Mimoun, Cinzia Silvestri, Aslihan Arslan, Manjunath Ramachandrappa Venkatesh, Sten Vollebregt, Miki Trifunovic, Hugo Perez Garza, Pengfei Sun. I hope I have covered all of them. Also thanks to the ones not in this list but have supported me equally during these years. Outside DIMES I also thank prof. Lina Sarro, prof. Ronald Dekker, prof. Lis Nanver and all of those missing in this list. I would like to thank Ruud Hendrik, Dr. Arjan Mol and Agnieszka Kooijman from the Department of Materials Science and Engineering of 3ME faculty for carrying out XRD measurements at their laboratory.

I would like to thank my Smac-*it* consortium colleagues Wannaya Ngankham, (Wan), Ghazaleh Nazarian, Cees Jeroen Bes for their equal support and meeting discussions. Good luck Wan and Ghazaleh for rounding up your last PhD things. Also thanks to my other TU friends, Manjunath, Venkatesh, Girish. Thanks Manju for our long measurement nights and answering my questions. Outside Netherlands I would like to thank Dr. Filiep Vanpocuke for his support shown as a user committee member until the mid-phase of the project and then to Dr. Paddy Boyle for his external guidance and his valuable comments on the thesis manuscript. I extend my thanks to Tim Nauwelaers from the European Research Centre (ERC) of Advanced Bionics in Hannover, Germany for his intermediate support and feedback during the tenure of the project. I would like to thank all my professional mates working at Sonion Nederland B.V. A special thanks to Mr. Aart van Halteren for his continuous support and motivation shown in completing my PhD alongside my job. Thanks to Ricardo Muijtjens for his help on the assembly and packaging aspect of the devices.

Life outside PhD was equally fun with all my friends in The Netherlands and Germany. They are just like an extended part of my family. This journey would not have been so enjoyable without them. I have innumerable and precious memories with them where I had small trips around Europe and also spend hilarious and fun packed weekends with them. Get-togethers, dinner parties, clubbing and partying all

A night, playing various games, bike riding, healthy debates on endless topics, organising and attending events and many more activities with all these friends was like a detoxification process. I greatly value our friendship bond. I also want to thank each and every friend back home in India and who are spread all over the globe. Thank you to all, the people who influenced and passed on their positivity to me. Special thanks to Hrishikesh, for the proofreading help and to Girish and Dr. Vasant Wagh for the Marathi translations.

I also take this opportunity to thank my family whom we generally take for granted and don't thank formally. I am especially grateful to my eternal solid support system, my parents Shankar and Padmini Lawand, my brother Nitin and his family, my sister, my in laws Balasaheb and Alka Jadhav, all the relatives and cousins back in India.

Lastly I want to thank my soulmate Sayali who's support was worth more than I can express on paper. She inspired me to follow my dreams and believed in me throughout. When she entered my life we decided that as I am from the technical field I will handle technicalities and she is from a creative field so she will handle the aesthetic part of our life. So thank you for giving a new dimension and making my life aesthetically beautiful !!

September, 2015
Nishant S. Lawand.

Abbreviations and medical terms

HA: Hearing Aid; HI: Hearing Instrument;
CI: Cochlear Implant; CI's: Cochlear Implants;
ChR2: channelrhodopsin 2;
SGNs: spiral ganglion neurons;
BTE: behind-the-ear;
RIC: receiver-in-the-Canal;
ITE: in-the-ear;
ITC: in-the-canal;
CIC: completely-in-canal;
RF link: Radio Frequency link;
Smac-*it*: Smart Cochlear Implants;
TU Delft: Delft University of Technology:
EI Lab: Electronic Instrumentation Laboratory;
LUMC: Leiden University Medical Centre;
STW: Dutch Technology Foundation;
MEA: microelectrode array; MEAs: Microelectrode arrays;
TiN: Titanium Nitride;
FEA: finite element analysis;
BiCMOS: Bipolar Complementary Metal-Oxide Semiconductor;
FDA: Food and Drug Administration;
EAC: external auditory canal;
TM: tympanic membrane;
RW: Round window;
SV: scala vestibule;
SM: scala media;
ST: scala tympani;
RM: Reissner's membrane;
BM: basilar membrane;
IHC: inner hair cells;
OHC: outer hair cells;
dB: decibels;
SNHL: Sensorineural hearing loss;
SPL: Sound pressure level;
BCDs: Bone-conduction devices;
BAHA: Bone-anchored hearing aid;
FMT: floating mass transducer;
VORP: Vibrating Ossicular Prosthesis;

BCI: bone conduction implant;
AP: audio processor;
BBC: bridging bone conductor;
AFE: Audio Front End;
AGC: automatic-gain-control;
IDR: internal dynamic range;
A-to-D converter: Analogue to Digital converter;
MEDs: middle ear devices;
MET: Middle Ear Transducer;
Vrms: Voltage root mean square;
MEMS: Micro-Electrical-Mechanical-Systems;
Pt: Platinum; Ti: Titanium; Ir: Iridium; Al: Aluminium; Ta: tantalum;
Cr: Chromium; Cu: Copper; Ni: nickel; TiN: Titanium Nitride; TiO_2: Titanium Oxide; Al_2O_3: Aluminium Oxide; AlN: Aluminium nitride;
WIMS: Wireless Integrated Microsystems Engineering Research;
PTFE: PolyTetraFluoroEthylene;
PVD: Physical vapour deposition;
CNS: central nervous system;
Si: Silicon; nitric acid: Silicon dioxide; Si_3N_4: Silicon Nitride; SiC: Silicon Carbide;
SOI: silicon-on-insulator;
PDMS: polydimethylsiloxane;
SIROF: sputtered iridium oxide;
PPX: polyparaxylylene;
BPDA-PPD: biphenyltetracarboxylic dianhydride – p-phenylene diamine;
PNS: peripheral nervous system;
IC: integrated circuits;
RIE: Reactive-Ion-Etching;
DRIE: Deep Reactive-Ion-Etching;
LIGA: German acronym for x-ray lithography;
HNA: hydrofluoric acid + nitric acid + acetic acid;
XeF_2: Xenon difluoride;
KOH: potassium hydroxide;
TMAH: tetra-methyl-ammonium-hydroxide;
$SF_6 + C_4F_8$: Sulfur hexafluoride + Perfluoroisobutylene;
NF_3: nitrogen trifluoride; Cl_2: Chlorine; F_2: Fluorine
UV: Ultraviolet;
PAC: photoactive compound;
O_2: Oxygen; N_2: Nitrogen; CF_4: Carbon Tetrafluoromethane;

PECVD: plasma enhanced chemical vapour deposition;
CVD: chemical vapour deposition;
APCVD: atmospheric pressure chemical vapour deposition; LPCVD: low pressure chemical vapour deposition;
TCR: Temperature Coefficient of resistance;
DIMES: Delft Institute of Microelectronics and Submicron Technology, currently referred to as Else Kooi Laboratory;
AOS: Advance-Off Stylet;
RF: Faradaic resistance;
RE: electrolyte resistance;
GSA: geometric surface area; ESA: electrochemical surface area;
Au: gold; Pd: palladium; Rh: rhodium;
XRD: X-ray diffraction; XRS: X-ray stress analysis;
AFM: Atomic force microscopy;
PCB: printed circuit board;
EM: electromigration;
MTTF: Mean-Time-To-Failure;
PTC: Positive Temperature Coefficient; NTC: Negetive Temperature Coefficient;
NaCl: kitchen salt;
EIS: Electrochemical Impedance Spectroscopy;
DRIE: deep reactive ion etching;
FS: front side of the silicon wafer; BS: back side of the silicon wafer;
CH_3COOH: concentrated acetic acid; HNO_3: nitric acid; H_3PO_4: phosphorus acid;
C_2F_6: Hexafluoroethane; CHF_3: Trifluoromethane;
DAC: Digital-to-Analogue converter.
PI: Polyimide
FEM: finite element method;
F2R: Flex-to-Rigid
WIMS: Wireless Integrated Microsystems Engineering Research;
EDP: Ethylene-diamine pyrocatechol;
ASIC: application specific integrated circuit;
NMP: N-Methylpyrrolidone;
PES: an etching chemical with a combination of phosphoric acid (H_3PO_4; 85%), nitric acid (HNO_3; 65%) and concentrated acetic acid (CH_3COOH; 100%)
SiOx : oxides of silicon; SixNy: nitrides of silicon
CTE: coefficient of thermal expansion;
TMAOH: Tetramethylammonium hydroxide;
ICP: Inductively Coupled Plasma;
TEOS: tetraethyl orthosilicate;

DI: deionized;
ESC: Electrostatic Clamping;
He: Helium; HBr: Hydrogen Bromide; CF4: carbon tetrafluoride; SF6: Sulphur hexafluoride;
HOCl: hypochlorous acid;
QDR: quick-dump-rinse;
CSC: cathodic charge storage capacity;
Qinj: charge injection capacity;
MDD: medical device directive;
AIMD: medical device directive;
RVA: rectangular variable aperture;
CV: cyclic voltammetry;
PBS: phosphate buffered saline;
SCE: standard calomel electrode;
WE: working electrode; CE: counter electrode;
DAQ: data acquisition;
IPA: isopropyl alcohol;
AIROF- activated iridium oxide
AC: alternating current;
OCP: open-circuit potential;
SNR: signal to noise ratio;
VT: voltage transient;
EABR: evoked auditory brain stem response;
eCAPs: evoked compound action potentials;
NRT: Neural Response Telemetry; NRI: Neural Response Imaging;
AGF: Amplitude Growth Function;
ER: Etymotic Research;
IPI: inter pulse intervals;
EFI: electric field imaging
VLSI: Very large scale integration;
Pt-Ir: Platinum-Iridium;
NF2: neurofibromatosis type 2;
ABI: auditory brainstem implant;

Propositions

accompanying the dissertation

Micromachining technologies for future Cochlear Implants

(Human Ear, Materials and Microtechnologies)

Nishant Shankar Lawand

15th September 2015

1. With cochlear implants, one can make a severely-to-profoundly deaf person able to hear again, the capability of listening however lies within the person itself. Here, no implant can be developed to help repair the damaged listening capability. *(Chapter 2)*
2. MEMS[1] have a promising future to replace the traditional manufacturing of the cochlear implant electrode arrays. However, due to process reliability and cost benefit ratio concerns, convincing the investors will be the challenge. *(Chapter 3)*
3. Investigating a material's (TiN[2]) characteristics, makes one believe that you are close to understanding it. However one still has to search for properties that are suitable for the chosen application. *(Chapter 4)*
4. Designing micro devices does not need micro thinking, rather it requires macro vision to expand your working boundaries. *(Chapter 5)*
5. Photolithography transfers two-dimensional sketch ideas onto silicon or polymer substrates and micromachining adds a third dimension to it. *(Chapter 6)*
6. Fabrication of the "Flexi-Stiff" devices is a challenging procedure. Assembly, packaging and characterisation have equal weight in achieving the desired functionality. *(Chapter 7 and Chapter 8)*
7. For successful PhD research, imagination is more important than knowledge but without knowledge you cannot imagine.
8. Cleanroom work is like the cricket game: Substantial net practice, experience and dedication is necessary to develop a process recipe for the day's play. To grant success, it is vital to adapt the recipe to the continuously changing environment.
9. Apart from hearing, humans have developed speaking and listening capabilities along with the ability to comprehend and respond to what a person feels or needs. New age technologies can never replace these traditional communication methods.
10. It is necessary to present your ideas to the world during a conference. It is equally essential to interact with people and gather the gist of their information in order to enhance your understanding of the books. This method of working is equivalent to a honey bee which extracts only the nectar from all the flowers but does not collect the flowers themselves.
11. "It is better to live your own destiny imperfectly than to live an imitation of somebody else's life with perfection." *(Bhagwat Gita, Chapter 3, Version 35)*
12. Life is at its weakest when there are more doubts than trust, life is at its strongest when you learn how to trust yourself despite of the doubts you have.

These propositions are regarded as opposable and defendable, and have been approved as such by the supervisors, Prof. P. J. French and Prof. J. H. M. Frijns.

---

[1]MEMS: Micro-electrical mechanical systems; [2]TiN: Titanium Nitride.

Stellingen

behorende bij het proefschrift

Micromachining technologies for future Cochlear Implants

(Human Ear, Materials and Microtechnologies)

Nishant Shankar Lawand

15th September 2015

1. Met een cochleair implantaat, kan men een slechthorend tot zelfs doof persoon, de mogelijkheid geven om weer te horen, echter de mogelijkheid om te luisteren wordt bepaald door de persoon zelf. Er kan geen implantaat ontwikkeld worden om een luisterbeschadiging te verhelpen. *(Hoofdstuk 2)*
2. MEMS[1] hebben een veelbelovende toekomst als vervanging voor de traditioneel vervaardigde cochleaire implantaten. Echter, vanwege zorgen om de betrouwbaarheid van de produktie en de kosten-batenverhouding, is het een uitdaging om de investeerders te overtuigen. *(Hoofdstuk 3)*
3. Onderzoek naar materiaal-eigenschappen (TiN^2), zorgt ervoor dat men gelooft dat je het bijna begrijpt. Echter, men moet nog steeds zoeken naar eigenschappen die geschikt zijn voor de gekozen toepassing. *(Hoofdstuk 4)*
4. Voor het ontwerpen van micro-inrichtingen hoeft men niet micro (klein) te denken, het vereist ruimdenkendheid om de grenzen van het werkterrein te verleggen. *(Hoofdstuk 5)*
5. Fotolithografie zet twee-dimensionaal geschetste ideeën over op silicium of polymeer substraten, micromachining voegt een derde dimensie toe. *(Hoofdstuk 6)*
6. Fabricage van de "Flexi-Stiff" inrichtingen is een uitdagende procedure. Assemblage, inkapseling en karakterisatie hebben een gelijk gewicht om de gewenste functionaliteit te bereiken. *(Hoofdstuk 7 en hoofdstuk 8)*
7. Voor een succesvol promotie-onderzoek is verbeelding belangrijker dan kennis, maar zonder kennis kan men niets inbeelden.
8. Cleanroom werk is als het cricket-spel: Behoorlijk wat kooi-oefeningen, ervaring en toewijding zijn noodzakelijk om een recept (strategie) te ontwikkelen voor het spel van de dag. Om succesvol te zijn, is het noodzakelijk het recept aan te passen aan een continue veranderende omgeving.
9. Buiten het horen, hebben mensen spreek- en luistermogelijkheden ontwikkeld tezamen met de mogelijkheid om te begrijpen en te reageren op wat een persoon voelt of nodig heeft. Nieuwe technologieën kunnen deze traditionele communicatiemethoden nimmer vervangen.
10. Het is noodzakelijk om je ideeën te presenteren aan de wereld tijdens een conferentie. Het is net zo noodzakelijk om interactie te hebben met mensen en de essentie uit hun informatie te halen en kennis uit boeken op te doen. Deze interactie is vergelijkbaar met een honingbij die wel de nectar van de bloemen verzameld maar de bloemen zelf niet.
11. Het is beter om je eigen (levens) weg te bewandelen op een niet perfecte manier, dan een perfecte imitatie van een (levens) weg van een ander. *(Bhagwat Gita, hoofdstuk 3, vers 35)*
12. Leven is op z'n zwakst wanneer er meer twijfels zijn dan zekerheden, het leven is op z'n sterkst wanneer je leert op jezelf te vertrouwen ondanks de twijfels die je hebt.

Deze stellingen worden opponeerbaar en verdedigbaar geacht en zijn als zodanig goedgekeurd door de promotoren, Prof. P. J. French en Prof. J. H. M. Frijns.